A Hybrid Quantum System of Ultracold Polar Molecules and Rydberg Atoms

DANIEL KENNETH RUTTLEY

A Hybrid Quantum System of Ultracold Polar Molecules and Rydberg Atoms

Daniel K. Ruttley

A thesis submitted in partial fulfilment of the requirements for the degree of Doctor of Philosophy

Quantum Light and Matter
Department of Physics
Durham University

2024

Abstract

Hybrid quantum systems aim to leverage the strengths of different platforms to advance quantum science. This thesis presents the development of a hybrid system of ultracold molecules and Rydberg atoms. We assemble individually trapped ^{87}Rb^{133}Cs molecules and interface them with ^{87}Rb Rydberg atoms. This platform is a foundation for applications that seek to exploit the rich internal structure of molecules and the strong interactions of Rydberg atoms.

We introduce a new method for assembling weakly bound molecules in which optical tweezers are used to associate pairs of atoms. We compare this method to the well established technique of magnetoassociation and find that their efficiencies are comparable. We transfer arrays of up to eight weakly bound molecules to their rovibrational and hyperfine ground state. The overall efficiency of the formation and transfer process is 48(2)%.

We develop a toolbox of techniques for the control and readout of these molecules. We demonstrate global microwave control of multiple rotational states and use auxiliary tweezers to implement site-resolved addressing and state control. We show how the internal state of molecules can be mapped onto the position of atoms and use this capability to readout multiple rotational states in a single experimental run. Further, using a scheme for the mid-sequence detection of molecule-formation errors, we perform rearrangement of assembled molecules to prepare small defect-free arrays.

We study long range interactions between Rb atoms and RbCs molecules. To engineer these interactions, we prepare the atoms in highly excited Rydberg states and use species-specific tweezers to precisely control the separation between particles. We demonstrate blockade of Rydberg excitation due to these interactions for sub-micrometre atom-molecule separations. The development of this hybrid platform opens up prospects for transferring quantum information between individually trapped molecules using Rydberg atoms.

Contents

Declaration

I confirm that no part of the material offered has previously been submitted by myself for a degree in this or any other university. Where material has been generated through joint work, the work of others has been indicated.

Daniel Kenneth Ruttley
Durham, 27th March 2024

Amended 16th August 2024

The Durham University crest on the title page was created by imaging individually trapped caesium atoms in an array of optical tweezers using the apparatus described in this thesis.

This work was funded by a Durham Doctoral Studentship granted by the Faculty of Science, Durham University.

The data presented in this thesis are available at https://doi.org/10.15128/r25t34sj617.

Acknowledgements

A PhD is not a solo effort and this thesis would not have been possible without the significant contributions and support of many people. I wish to thank all those who have helped me along the way.

Firstly, I would like to thank my supervisor, Simon. I consider myself very fortunate to have been supervised by Simon, whose drive and attention to detail is second to none. I know that I am better researcher because of his guidance and I am deeply grateful for his support. Thanks also to my co-supervisor, Stuart, for his insightful suggestions of research avenues that we could explore.

I have been incredibly lucky to work with numerous talented and dedicated researchers in *Team Tweezer*. I must thank Alex for his deep expertise of AMO physics and his dedication to pushing the experiment forward. Thanks to Vincent and Stefan who showed me the ropes and whose work provided the foundation for mine. I am grateful to everyone else involved in the experiment prior to my arrival. I'd like to thank newer students Tom, Fritz, Erkan, Claus, Albert, and Ce for being such a pleasure to work with in the lab. I've had a lot of fun muddling through the experiment together. Thanks for your hard work and for putting up with my '00s music. I am confident that the experiment will be in good hands going forward.

The contribution of the door between the tweezer and microscope labs cannot be overstated. Many a time, I have snuck through that door and "borrowed" a post holder or mirror. Even more importantly, Adarsh, Jonathan, Alex, Ben, Sarah, and Andrew were always able to lighten my mood when the experiment (or I) decided that enough work had been done for the day and, for them, I am very thankful.

My time in Durham has been enriched immeasurably by being part of the Quantum Light and Matter (QLM) section. QLM is an extremely supportive and enjoyable place to work. I have enjoyed many a Friday seminar in the Vic, some fantastic cakes at FAtMol, and some brilliant board games at MolOploy. In addition to those I've already mentioned, I'd like to particularly thank Luke, Joe, Mitch, Bethan, Jack, Joe, Dani, Liam, Tobi, Matt, Archie, and Ifan for their friendship. Adarsh and Luke: you each owe me four pints.

The support staff at Durham Physics are world class and without them the research in this thesis would not have been possible. My huge thanks to all in the technical and administrative teams, who were always willing to answer my questions no matter how inane or repetitive they became.

Thank you to our theory collaborators – Robbie, Jeremy, Ruth, Rosario, Pablo, and Hossein – for explaining what was actually going on in our lab.

My friends outside of work have been a great source of fortitude. To the Sneks – Joe, Rob, Lucy, Zach, and Holly – thank you for the times we have spent together. I have learnt so much from all of you, including the fastest way to sacrifice a dozen bombards to a few gendarme and methods for making scrambled eggs with the maximum number of pans. Joe: consider this my one (and only) acknowledgement that you came up with the owl. I am grateful to my friends from undergrad – Fran and David, Harry and Emily, Lewis, and Akhil – who have made the long trip up north. Matt and Melissa: I'm sure one day we'll be able to drag you up here too. Thanks to the Dune Crew – Adarsh, Ali, Mike, Eoin, Joe, Sam, Ali, Bex, and Vis – for thoroughly degrading my trust every time we play. I hope to betray all of you again in the future.

I am grateful to those who introduced me to this wonderful subject. Thank you to Mr Sears, Mr Brackstone, and Mr Mills, who taught me the foundations and successfully persuaded me not to become a mathematician. Thanks to Rob, Anna, Milan, Lucas, and Péter for giving me a taste of AMO physics and showing me that not all labs are like the ones in the basement of the DW.

I am grateful for my extended family who mean so much to me. In particular, thank you to Grandma, Grandma and Granddad, and Granddad and Grannie. You have always been an incredible source of love and support. I am very fortunate and thankful to have acquired a wonderful second family via Katie. Hudson: hurry up and read your book so that you can move onto this.

Mum, Dad, and James: I have only made it to this point due to your unwavering support, belief, and love. I will be forever grateful for everything that you have done for me. Thank you. In return, I might even go easy on you when we next play *Ticket to Ride*.

Katie: my deepest thanks, of course, go to you. This journey would not have been possible without you. You are my closest friend and my fiercest advocate, and you have cheered me on every step of the way. I love you, and I can't wait to embark on many more adventures together.

For Granddad Ken.

1 Introduction

Understanding the behaviour of matter at the smallest scales is critical for future advances is science and technology. This behaviour is governed by the laws of quantum mechanics. Quantum mechanics is complex. Particles can exist in superpositions, where the same particle occupies multiple states at once. Furthermore, particles can be entangled, such that they cannot be considered as separate systems and cannot be described independently. This means that, for a system of N particles with two possible states each, the number of parameters needed to describe the system at a given moment increases exponentially as 2^N. Similarly, the number of operations needed to simulate the evolution of the system with time rises exponentially. This makes modelling the dynamics of such a system with more than a few tens of particles on a classical computer impractical.

Quantum simulation offers a solution that makes the study of complex quantum systems tractable [1–5]. It is motivated by a simple idea: rather than trying to work out what nature will do, why not just observe it? This is, of course, easier said than done. However, it is possible, with a system of individually controllable quantum particles that interact with each other, to construct a *quantum simulator* that mimics the behaviour of the system to be studied. The Hamiltonian of the simulator is engineered such that is can be directly mapped onto the studied system [6].

Quantum computing is a different technique. Rather than trying to simulate the dynamics of a complex quantum system, it exploits the exponential amount of information contained within a system of *quantum bits* (qubits) to drastically speed up certain calculations [5, 7, 8]. Popular examples are the prime factoring of large integers [9] or the searching of an unsorted database [10]. The requirement for experimental implementation is similar to that for quantum simulation: namely a system of individually controllable quantum particles that can interact with each other.

The matter for the experimental physicist then becomes: what system should be used to construct this network of quantum particles? The system must easily scale

and be made up of particles that support long coherence times and a universal set of quantum gates (for quantum computing) or the ability to create a Hamiltonian that is mappable to the problem Hamiltonian (for quantum simulation). The system must be able to be initialised in a given state, and its states must be able to be readout with high fidelity [11]. These criteria can be, at least somewhat, realised in a wide range of experimental settings. Quantum simulation and computation have been demonstrated using a variety of physical systems [5, 12], including trapped ions [13–16], superconducting qubits [17–19], photons [20–25], and quantum dots [26–32]. In recent years, there has been a surge in experiments that seek to implement quantum computation and simulation using dipolar systems [33–35]. Such systems include particles that possess magnetic dipoles, such as magnetic atoms [36–39], or electric dipoles, such polar molecules [40–47] or neutral atoms excited to Rydberg states [48–53].

Ultracold polar molecules offer a versatile platform for quantum science [41, 45–47], with applications spanning from quantum simulation [33, 34, 40, 42–44] and quantum information processing [54–60] to ultracold chemistry [61–63] and precision measurement [64–68]. Molecules have rich internal structures with ladders of rotational states that have long radiative lifetimes. Dipole-dipole interactions can be engineered by preparing molecules in a superposition of rotational states. These properties make rotational states ideal to encode quantum information [69, 70] or pseudo-spins in a quantum simulator [71–73]. Moreover, the abundance of these states unlocks possibilities such as synthetic dimensions in the rotational degree of freedom [74], realisation of *qudits* (higher-dimensional quantum systems as opposed to traditional two-level qubits) [60] or the implementation of quantum error-correcting codes in the molecule's internal states [59].

Rydberg atoms exhibit even stronger interactions that can be exploited to engineer quantum entanglement and multi-qubit gates [48, 53, 75–79]. Typically approaches exploit the Rydberg blockade mechanism, where strong van der Waals interactions between neighbouring Rydberg atoms prevent simultaneous excitation of multiple nearby atoms. This architecture is inherently scalable, with the number of qubits in state-of-the-art experiments typically limited by the laser power available to trap atoms. For quantum computing purposes, groups of individually trapped atoms have been combined to form *logical qubits* to provide error redundancy [8, 80–82], and experiments with tens of such logical qubits have been demonstrated [83].

Hybrid quantum systems, where multiple architectures are combined into a single system, allow the disadvantages of each to be mitigated [84–92]. For example, the short lifetimes of Rydberg states ($\sim 100\,\mu s$) [50] makes them non-ideal for simulating itinerant models where particles are not pinned to specific sites [39, 93]. However,

their interactions are very strong and can be much greater than the megahertz scale for micrometre separations [50]. In contrast, ultracold molecules have radiative lifetimes of many seconds which means that they can support long lived quantum coherence [94–98] but offer only kilohertz-scale interactions at micrometre separations [47]. A hybrid system composed of polar molecules and Rydberg atoms offers a way to combine the advantages of both platforms [99–102]. In such a system, the fast high-fidelity interactions and readout possible with Rydberg atoms [79, 103] are utilised alongside the long coherence times and lifetimes of polar molecules. One can envisage, for example, a quantum simulator where itinerant molecules move around an optical lattice, and interactions between molecules are effectively switched on and off at selected lattice sites by exciting atoms to Rydberg states. Alternatively, quantum information could be encoded in molecular states and multi-qubit gates could be implemented by mediating interactions between molecules with Rydberg atoms. Furthermore, this hybrid system offers new capabilities, such as non-destructive readout of molecular states [104–106], cooling of molecules using Rydberg atoms [107, 108], and photoassociation of giant polyatomic Rydberg molecules [109–112]. This thesis documents the creation of such a hybrid system.

1.1 Ultracold polar molecules

Ultracold polar molecules are attractive candidates for quantum science due to their rich internal structure, controllable long range interactions, and long coherence times. However, their rich structure makes them harder to laser cool to ultracold temperatures than alkali atoms, which have been successfully laser cooled for nearly a half-century [113]. To bring an atom or molecule from room temperature to ultracold temperatures typically requires $> 10^4$ photon-scattering events [114]. For alkali atoms, this requirement is not onerous. They typically have closed cycles, on which many photons can be scattered before an atom decays to a different state than its initial one. Even when such an atom decays out of this closed cycle, a single additional laser is typically sufficient to return it. The same is not true for molecules, which have a much more complex internal structure. As well as electronic structure, there are rotational and vibrational degrees of freedom. Generally, there are no selection rules on vibrational transitions, which means that cooling cycles typically only scatter a few photons before molecules are lost. Furthermore, the molecules are typically lost to many other states, so an often impractical number of additional lasers are needed to return them to the cooling cycle.

Methods for the production of ultracold molecules generally fall into one of two

approaches. The *direct approach* involves searching for candidate molecules that have near-closed transitions. These occur for molecules that posses an electronic transition where the excited electron does not participate in the molecular bond. The ground and excited electronic potentials for such a transition are similar so a vibrational wavefunction in one potential only has a significant overlap with the state in the other potential with the same vibrational quantum number [114]. These molecules can be cooled with techniques that mirror those used to cool atoms. Examples of molecules that have been directly cooled include diatomic molecules, such as SrF [115–122], YO [123, 124], CaF [69, 70, 125–136], and YbF [137], and polyatomic molecules, such as SrOH [138], CaOH [139], YbOH [140] and $CaOCH_3$ [141], among others [114, 142, 143].

In contrast, the *indirect approach* involves first laser-cooling atoms, then assembling ultracold molecules from these atoms. Molecules are typically formed in weakly bound states [144, 145] then optically transferred to their rovibrational ground state [146]. Most hetero-alkali dimers have been formed with this approach, including KRb [146, 147], RbCs [148–150], NaK [151–154], NaRb [155], NaLi [156], and NaCs [157, 158].[1] Experiments that indirectly cool molecules already have the capability to cool and trap atoms, as these are prerequisites for molecule formation. Therefore, they are ideally suited to developing a hybrid system of molecules and atoms. In this work, we form ground state ^{87}Rb^{133}Cs (hereafter RbCs) molecules, and interface them with ^{87}Rb (hereafter Rb) atoms that are excited to Rydberg states.

1.2 Rydberg atoms

A Rydberg atom is an atom in an excited state where one (or more) of its electrons has been promoted to a high energy level [161]. The excited electrons occupy orbits that are much further from the nucleus compared to their ground-state configurations, which can lead to several properties of the atom, such as the electric dipole moment and sensitivity to external fields, being greatly exaggerated [50]. The large dipole moments of Rydberg atoms means that they strongly interact with each other at long range, with the dominant interaction mechanism being van der Waals at large separations and dipole-dipole at smaller distances [48]. These interactions are switchable by selectively exciting certain atoms to Rydberg states, which makes them ideal candidates for implementing quantum gates and generating controllable entanglement [48, 53, 75–79].

[1] Homo-alkali dimers, such as Rb_2 [159] and Na_2 [160], have also been formed. However, the symmetry of these molecules means that they are not polar, so we do not discuss them further here.

For quantum computing and simulation, alkali atoms are often excited to Rydberg states due to their relatively simple atomic structure and the ease with which they can be manipulated using lasers. Alkali atoms essentially have a single electron, which can be promoted a Rydberg level. Rydberg-mediated gates and entanglement have been demonstrated with, for example, Rb [77–79] and Cs [103]. However, these architectures have some drawbacks, such as the inability to form attractive optical potentials for the interacting particles [162] or correlated errors in the control of storage and interaction qubits [163–169]. In this work we develop a hybrid quantum system of polar molecules and Rb Rydberg atoms that could overcome these disadvantages. We note that alternative approaches to address these problems are under development, such as the engineering of a dual-alkali architectures [170–173], where a second species is used as auxiliary qubits that are unaffected by the control of the first species, or the use of alkaline earth atoms, such as Sr [174–177] and Yb [178, 179], which offer the ability form attractive optical potentials for Rydberg atoms.

1.3 Single particle trapping and control

For quantum computing and simulation, the capability to confine and manipulate single particles is crucial. Within atomic, molecular, and optical (AMO) physics experiments, the primary tool for achieving this level of control is the optical tweezer [35]. Optical tweezers are laser beams focused to micrometre scales. This is small enough that *collisional blockade* can be engineered, where pair loss is induced to enable the trapping of single particles at the foci of the tweezers [180–182]. Arrays of tweezers are dynamically reconfigurable, allowing flexible connectivity [183] and the preparation of states with low configurational entropy through rearrangement of particles [184–187].

Optical tweezers not only provide the means to trap single particles but also enable the selective manipulation of their internal states. Through the exploitation of the ac Stark shifts induced by optical tweezers, individual particles can be controlled. For instance, adjusting the depth of the tweezer containing a specific qubit can bring it, and only it, into resonance with a driving field, such as microwave radiation [188–195]. This approach remains applicable even when particles are primarily trapped with alternative methods, such as in an optical lattice [190, 196].

In tweezer platforms, long range interactions between trapped particles have been utilised to simulate complex quantum systems [51, 197, 198]. The architecture's inherent scalability [83, 199] provides a promising avenue for constructing arrays

with an even greater number of particles, and arrays of over 10^4 tweezers have been demonstrated [200].

1.4 Outline of this thesis

This thesis details the development of a hybrid quantum system of RbCs molecules and Rb Rydberg atoms. We begin with individually trapped Rb and Cs atoms in optical tweezers, and convert these to molecules and Rydberg atoms. We explore how these particles can be controlled and study the interactions between them. The remainder of the thesis is structured as follows:

Chapter 2 describes the experimental apparatus utilised in this work and outlines recent upgrades.

Chapter 3 details the formation of weakly bound RbCs molecules from atom pairs. We discuss two distinct methods for molecule creation, both involving traversing an avoided crossing between atomic and molecular states, either through varying magnetic fields or adjusting the separation of two optical tweezers.

Chapter 4 details the optical transfer of the weakly bound molecules to their rovibrational and hyperfine ground state. We explore how optical tweezers can be used to enhance the quantum control of individual molecules. We implement global and local control of the molecular states, a multi-state readout scheme, and molecule rearrangement to prepare defect-free arrays.

Chapter 5 explores Rydberg atoms. We characterise the Rydberg excitation in our experiment. We detail measurements of the Stark shifts of Rydberg atoms and study interactions between Rydberg atoms.

Chapter 6 details measurements of the charge-dipole interaction between polar molecules and Rydberg atoms. We discuss the theory of this interaction, show how the optical tweezers can prepare the two particles with sub-micrometre separations, and present measurements of Rydberg blockade caused by this interaction.

Chapter 7 explores resonant dipole-dipole interactions between polar molecules and Rydberg atoms. We describe how to choose molecular and atomic states and tune their transitions in order to engineer these interactions. Following this, we present initial measurements of Rydberg blockade caused by this interaction.

Chapter 8 summarises the results of this thesis and provides an outlook towards future work. This includes the trapping of molecules in magic tweezers, the implementation of an optical lattice to realise smaller particle separations, scaling to larger arrays of traps, and mediating the detection and interactions of molecules with Rydberg atoms.

1.5 Contributions of the author

Over the course of my PhD, I have been fortunate to work with many talented researchers within *Team Tweezer*, without whom the research presented here would not have been possible. During my time in the team, I have worked closely with PhD students Vincent Brooks, Stefan Spence, and Tom Hepworth and postdoctoral research associate Alex Guttridge. We have had the assistance of master's students Mitch Walker, Albert Tao, Ce Li, Imogen Forbes, Archie Baldock, and Fritz von Gierke and summer students Kevin Roice, Claus Yang, and Erkan Nurdun. I am grateful for the contributions of those who were significantly involved in the development of the experiment prior to my arrival, including (in alphabetical order) Alex Alampounti, Phil Gregory, Lewis McArd, Ana Rakonjac, Rahul Sawant, Wendy Tomboza, and Jie Zhang. The project has been supervised by Simon Cornish throughout. Stuart Adams co-supervised the experiments involving Rydberg atoms.

When I arrived, Vincent, Stefan, Alex, and the previous team members had successfully trapped and imaged individual Rb and Cs atoms. Vincent and Ana designed the initial optical setup for the tweezers. This was later modified by Stefan and Alex when the 2D AOD was installed and by Vincent and me when the SLM was installed. The SLM was characterised prior to installation by Mitch and me. Fritz is leading the development of the magic tweezers that we hope to install in the experiment soon. Alex and I set up and characterised the bias and jump magnetic field coils. Stefan led the implementation of the Raman sideband cooling protocol for atomic cooling, and Vincent led the Feshbach spectroscopy of Cs atom pairs and the development of the atomic rearrangement protocol. Vincent, Stefan, Alex, and I characterised the beam waists of the optical tweezers, with assistance from Imogen.

Stefan developed `PyDex`, the main experimental control application. Kevin improved the `PyDex` user experience and I modified `PyDex` so that it can efficiently analyse images of arrays of tweezers. I wrote the Python applications that interface with `PyDex` to control the AWGs, SLM, and MWGs and Lewis wrote the Python application that controls the DDSs. The SLM application is based on code developed by Mitch, and the AWG application is based on code developed by Alex A., Vincent,

and Stefan. Tom modified the AWG code to allow for more flexible rearrangement.

I designed and implemented the STIRAP and Rydberg laser systems. Alex and Lewis helped me with the vacuum setup of the ULE cavity. Albert assisted me with the setup and characterisation of the STIRAP lasers and Ce assisted me with the Rb vapour cell spectroscopy.

Alex and I characterised the association methods used to form weakly bound molecules, with assistance from Stefan for the initial measurements. Alex and I performed optical spectroscopy of the molecules and developed the sequence used to transfer them to the ground state. I led the experiments with ground state molecules, with assistance from Alex, Tom, and Erkan.

Alex and I characterised the Rydberg excitation of Rb and measured the charge-dipole interactions between atoms and molecules. Archie simulated the dynamics of this system. I developed the code to find pairs of states to engineer resonant dipole-dipole interactions between atoms and molecules, initially with assistance from Claus, and performed the measurements of these interactions.

I am grateful to the theory collaborators that I have had the pleasure of working with. The theoretical calculations of the weakly bound molecular states and mergoassociation were performed by Robbie Bird, Ruth Le Sueur, and Jeremy Hutson of the Cold Molecules Theory Research Group at Durham University. The charge-dipole theoretical calculations were performed by Rosario González-Férez (Universidad de Granada) and Hossein Sadeghpour (ITAMP). The resonant dipole-dipole theoretical calculations for the pair of states that I identified were performed by Pablo Fernández-Mayo Yelo and Rosario González-Férez, both of Universidad de Granada.

1.6 List of publications

Significant parts of this thesis are presented in:

[201] D. K. Ruttley*, A. Guttridge*, S. Spence, R. C. Bird, C. R. Le Sueur, J. M. Hutson, and S. L. Cornish, *Formation of ultracold molecules by merging optical tweezers*, Phys. Rev. Lett. **130**, 223401 (2023).

[202] A. Guttridge*, D. K. Ruttley*, A. C. Baldock, R. González-Férez, H. R. Sadeghpour, C. S. Adams, and S. L. Cornish, *Observation of Rydberg blockade due to the charge-dipole interaction between an atom and a polar molecule*, Phys. Rev. Lett. **131**, 013401 (2023).

[203] D. K. Ruttley, A. Guttridge, T. R. Hepworth, and S. L. Cornish, *Enhanced quantum control of individual ultracold molecules using optical tweezer arrays*, PRX Quantum **5**, 020333 (2024).

The author also contributed to:
[204] R. V. Brooks*, A. Guttridge*, M. D. Frye, D. K. Ruttley, S. Spence, J. M. Hutson, and S. L. Cornish, *Feshbach spectroscopy of Cs atom pairs in optical tweezers*, New J. Phys. **24**, 113051 (2022).

[205] S. Spence, R. V. Brooks, D. K. Ruttley, A. Guttridge, and S. L. Cornish, *Preparation of ^{87}Rb and ^{133}Cs in the motional ground state of a single optical tweezer*, New J. Phys. **24**, 103022 (2022).

** denotes equal contribution.*

2 Experimental apparatus

The experimental apparatus used for the science presented in this thesis have been described in detail in the theses of Brooks [206] and Spence [207]. We direct the reader to these works for detailed explanations of the design choices and characterisation measurements. Here, we briefly summarise the apparatus and provide an overview of recent upgrades relevant to this work.

2.1 Vacuum system

For the study of atoms and molecules at ultracold temperatures, it is necessary to prepare them in an ultrahigh vacuum environment. This prevents significant collisions with room-temperature particles, which would usually impart enough kinetic energy to eject particles that are optically trapped. For this reason, our experiments take place in a custom vacuum chamber that maintains a pressure of $< 1 \times 10^{-10}$ mbar. Although the majority of the chamber is metal, for good optical access we perform experiments in a glass science cell[1] mounted at the front of the chamber. The science cell is anti-reflection (AR) coated to avoided standing waves being formed. Alkali-metal dispensers[2] release Rb and Cs into the vacuum chamber and we operate these continuously so that that background pressure is high enough to be able to easily load atomic magneto-optical traps (MOT), but sufficiently low that the vacuum-limited lifetime for individually trapped atoms is $\gtrsim 30$ s. A render of the vacuum chamber is shown in Fig. 2.1(a), where we define the coordinate system used in this work.

We highlight the in-vacuum electrodes in our apparatus which extend to the science cell. These electrodes were designed to orient molecules in the laboratory frame by generating large dc electric fields. The four electrodes are positioned in a 9.6 mm $\times$ 5.6 mm rectangular array centred around the optical tweezers: this aspect ratio ($\sqrt{3} : 1$) increases the uniformity of applied fields by eliminating the field curvature along the x-axis [208]. However, we find that the electrodes are a

[1] ColdQuanta CQDU0010
[2] Rb: SAES 5G0010, Cs: SAES 5G0050

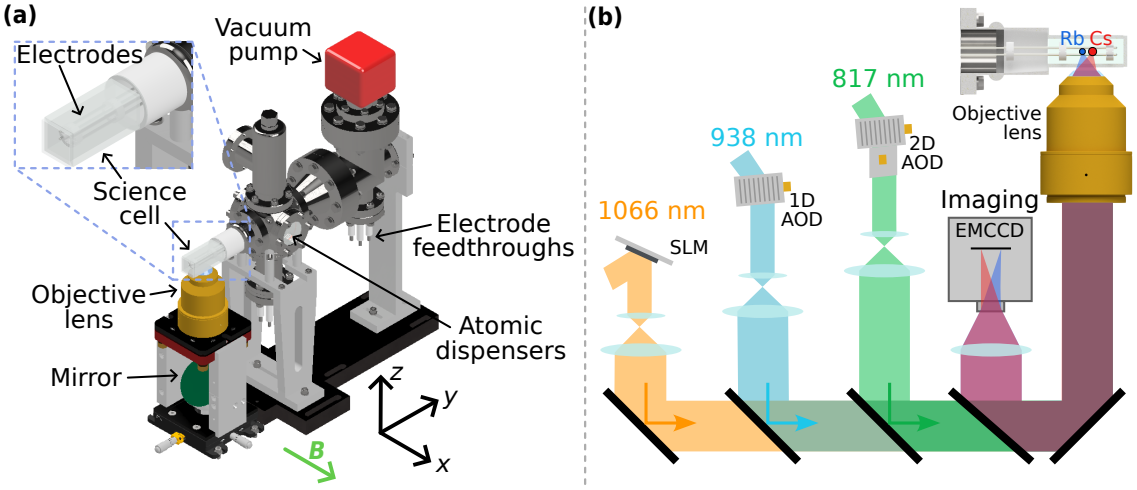

Figure 2.1: Experimental apparatus used in this work. (a) Render of the vacuum system. We highlight the in-vacuum electrodes which are used for microwave control of RbCs molecules. **(b)** A simplified setup showing the vacuum cell, objective lens, and key elements of the optical setup. Arrays of 1066 nm tweezers are created with an SLM, arrays of 938 nm tweezers are created with a 1D AOD, and arrays of 817 nm tweezers are created with a 2D AOD. Trapped atoms are detected by imaging atomic fluorescence onto an EMCCD.

good antenna for the $\sim$GHz frequency radiation that is resonant with rotational transitions in RbCs. Therefore, we use the electrodes to produce linearly polarised microwave radiation of high purity to drive coherent transfer between molecular states.

Six sets of magnetic field coils surround the vacuum chamber. Four of these sets produce magnetic fields oriented along the x-axis. These are the:

Quadrupole coils Coils in the anti-Helmholtz configuration, which produce a uniform magnetic field gradient at the centre of the vacuum chamber. This is used during the loading of atomic MOTs for which the field gradient is set to 8.47 G/cm.

Shim coils These coils generate a small field to provide a quantisation axis for atomic cooling and state preparation. Typically we operate them so that the generated field in the centre of the vacuum chamber is 4.78 G.

Bias coils These coils provide a large field which is used for experiments with RbCs molecules. Typically we operate with these coils so they produce a field of approximately 177 G so that, when combined with the shim field, the total field at the molecules is $B = 181.699(1)$ G. The magnetic field noise at typical operating fields is ~ 30 mG.

Jump coils These coils provide a field of up to ~ 40 G. The inductance of these coils is small to allow the magnetic field to be changed quickly. These coils are

used to associate atom pairs into molecules by sweeping the magnetic field.

The other two pairs of coils are shim coils that are oriented to give fields along the y- and z-axes. We typically operate these coils to produce fields $< 1\,\mathrm{G}$ to null stray fields in these directions. This sets the resultant field (and the quantisation axis) along the x-axis, as indicated in Fig. 2.1(a). All coils are made of copper and the quadrupole, bias, and jump coils are hollow to allow for water cooling. The coils are mounted in G-10, a fibreglass laminate, which is strong, electrically neutral, and has low thermal expansion.

We calibrate the magnetic fields by driving hyperfine transitions in Rb and Cs. The transitions are driven with microwave radiation produced by two antennae (one for each species) [209, 210]. The antennae are stub-tuned so that their resonant frequencies are approximately 6.8 GHz and 9.2 GHz for the Rb and Cs antenna respectively, and the bandwidth of each antenna is approximately 200 MHz. They are mounted outside the vacuum chamber approximately 12 mm along the x-axis from the centre of the science cell and are driven with a microwave source[3] which we amplify with a high-power amplifier[4]. For example, with the shim and bias coils switched on, we measure the frequency of the hyperfine transition $|5\mathrm{s}_{1/2}, f = 1, m_f = +1\rangle \rightarrow |5\mathrm{s}_{1/2}, f = 2, m_f = +2\rangle$ in Rb to be 7223.152(1) MHz. With the Breit-Rabi formula [211], we extract the magnetic field $B = 181.699(1)\,\mathrm{G}$.

2.2 Optical tweezers

We trap atoms and molecules in tightly-focused optical dipole traps called optical tweezers [35]. The potential depth for a particle in an optical tweezer is [180]

$$U = \frac{1}{2\varepsilon_0 c}\alpha_\lambda I\,, \tag{2.1}$$

where I is the intensity of the trapping light and α_λ is the particle's polarisability, which is a function of the trapping wavelength λ.[5,6] Typically, the particles are cold enough that they reside close to the centre of the trap. Here, we assume that

[3] Either Anritsu MG3692C or Windfreak Technologies SynthHD (v2)

[4] MiniCircuits ZVE-3W-183+

[5] The sign convention in Eq. (2.1) is such that $U > 0$ for a trapped particle.

[6] Strictly speaking, the polarisability is a complex tensor $\boldsymbol{\alpha}_\lambda$ that describes how particles respond to different polarisations of light [212]. Generally, this response is anisotropic because different polarisations couple different internal states. It is common to write $\boldsymbol{\alpha}_\lambda = \alpha_\lambda + c_1\boldsymbol{\alpha}_\lambda^{(1)} + c_2\boldsymbol{\alpha}_\lambda^{(2)}$ where α_λ, $\boldsymbol{\alpha}_\lambda^{(1)}$, and $\boldsymbol{\alpha}_\lambda^{(2)}$ are the scalar, vector, and tensor polarisabilities respectively and c_1 and c_2 are scalars [213]. $c_1 \propto \mathcal{V}\boldsymbol{k}\cdot\boldsymbol{B}$, where $\boldsymbol{k}$ is the tweezer wavevector, $\boldsymbol{B}$ is the magnetic field, and $\mathcal{V}$ is the fourth Stokes parameter that quantifies the circular polarisation of the light. We can largely ignore $\boldsymbol{\alpha}_\lambda^{(1)}$ in our system (because $\boldsymbol{k}$ and $\boldsymbol{B}$ are approximately orthogonal and our tweezers are formed from linearly polarised light), but, as will be discussed shortly, a small vector light

the optical tweezers are well described as Gaussian beams. At the centre of the tweezer, the intensity $I = 2P/\pi w_x w_y$. Here P is the total power in the beam and w_i is the trap waist along axis i (the distance at which the intensity falls to $1/e^2$ of the maximum). We have allowed for the fact that the beam may be elliptical at the focal point with different waists along the two radial directions. For our experiment, the radial directions are along the x- and y-axes as the optical tweezers propagate through the objective lens along the z-axis (see Fig. 2.1(a)).

Optical tweezers have trap waists on the micrometre scale which is small enough that collisional blockade can be engineered for trapped particles [181, 182]. Here, near-resonant light is applied which causes light-assisted collisions and pairwise loss. The result is parity projection, whereby if the number of particles initially loaded is even, all particles will pair up and be lost. However, if the number of particles initially loaded is odd, one particle will remain after all pairs have been lost. Therefore, a single atom or molecule can be prepared in a tweezer. As the same event (the loading of an additional particle) causes the parity to change, the mean occupation of a tweezer after parity projection is approximately half when the loading is saturated.

An atom close to the centre of a tweezer experiences a harmonic restoring force. Its motion along each axis is well described by the eigenstates of a quantum harmonic oscillator. The energy of a motional quantum is $h\nu_i$, where ν_i is the trap frequency along axis i.[7] For the radial directions (the x- and y-axes), the trap frequencies are

$$\nu_i = \frac{1}{2\pi}\sqrt{\frac{4U_0}{mw_i^2}}\,, \tag{2.2}$$

where U_0 is the potential depth at the centre of the tweezer and m is the mass of the particle. Along the direction of tweezer light propagation (the axial direction, i.e. the z-axis), the trap frequency is

$$\nu_z = \frac{1}{2\pi}\sqrt{\frac{2U_0}{mz_R^2}}\,, \tag{2.3}$$

shift can be formed near the tweezer foci. Further, we can ignore $\boldsymbol{\alpha}_\lambda^{(2)}$ because, for ground-state alkali atoms, it affects U by less than one part per million [214]. For molecules, the anisotropic polarisability is more significant (see Eq. (4.2)) but α_λ is still dominant. The imaginary part of α_λ quantifies dissipative effects of the light; for this work we ignore these and refer to the real part as the polarisability.

[7] In this thesis we favour linear frequencies ν, measured in hertz (Hz), over angular frequencies ω, measured in radians per second (rad/s). We follow the approach of Mohr and Philips [215], and explicitly define one hertz as equal to one cycle per second. The numerical value of the angular frequency (in rad/s) is equal to the numerical value of the linear frequency (in Hz) multiplied by 2π. For equations involving ν, we assume that the numerical value of ν measured in Hz is used; strictly speaking, this should be written as ν/cycle [215, 216]. We note that, for example, the Rabi frequency Ω of a transition driven at one cycle per second is sometimes written as $\Omega/2\pi = 1\,\text{Hz}$ or $\Omega = 2\pi \times 1\,\text{Hz}$; in the notation adopted for this work we write $\Omega = 1\,\text{Hz}$.

Table 2.1: Calculated polarisabilities for the different species in our experiment at the wavelengths of our optical tweezers. All polarisabilities are for absolute ground states. We do not give the polarisability for RbCs at 938 nm because this is within a dense group of molecular transitions [217].

Species	α_{817} $(4\pi\varepsilon_0 a_0^3)$	α_{938} $(4\pi\varepsilon_0 a_0^3)$	α_{1066} $(4\pi\varepsilon_0 a_0^3)$	$\alpha_{1066}/\alpha_{817}$
RbCs [217]	4.0×10^2	–	1.8×10^3	≈ 4.5
Rb [218]	4307	1039	687	$\approx 1/6.3$
Cs [218]	-3477	2890	1163	$\approx -1/3.0$

where z_R is the Rayleigh range.

A key aspect of our experimental setup is the use of distinct wavelengths of optical tweezers which enables species-specific trapping and independent control of the atoms and molecules. We primarily use two wavelengths of light to form optical tweezers. For particles in their ground state, tweezers at wavelength 1065.512 nm are attractive to all species in our experiment, whereas tweezers at 816.848 nm are strongly attractive for Rb, weakly attractive for RbCs, and repulsive for Cs. For convenience, we refer to these wavelengths as 1066 nm and 817 nm respectively. Additionally, a third set of tweezers at 938 nm is exclusively used to move Cs atoms in the initial stages of experiments.[8] Table 2.1 lists the polarisabilities at our tweezer wavelengths for the species we study. The listed polarisabilities are for atoms or molecules in the electronic ground state.

We source the tweezer light from lasers on a separate optical bench (the "laser table") to the bench that holds the vacuum apparatus (the "experiment table"). On the laser table, each beam is passed through an acousto-optic modulator (AOM) which allows the intensity of the tweezers to be stabilised with a homebuilt feedback circuit. The light is then fibre coupled and sent to the experiment table. The 817 nm and 938 nm light is sourced from bare diodes[9]. The beams are passed through laser line filters[10] prior to the AOMs. We obtain ~ 100 mW of light at each wavelength. The 1066 nm light is sourced from a distributed Bragg reflector laser[11] that is amplified with a fibre amplifier[12] prior to the AOM. With this, we can obtain

[8] This is primarily for historical reasons. When the experimental apparatus was being developed, the 938 nm tweezers were initially used to trap Cs because $\alpha_{938}^{\mathrm{Cs}} > \alpha_{1066}^{\mathrm{Cs}}$. However, 938 nm is close to the Cs D1 transition, so the 938 nm tweezers cause significant Raman scattering of Cs. Furthermore, 938 nm is within a dense group of transitions in RbCs [217]. For these reasons, we do not trap Cs atoms in the 938 nm tweezers for a signficant amount of time. Nevertheless, we opted to keep the 938 nm tweezers in the experiment because the AOD in their beam path allows them to be dynamically moved. We exclusively use these tweezers during the initial stages of the experiment when we rearrange atoms (see Sec. 2.3.1).

[9] 817 nm: Thorlabs L820P200, 938 nm: Thorlabs M9-940-0200

[10] 817 nm: Semrock Maxline LL01-830-12.5, 938 nm: Semrock Maxline LL01-976-12.5

[11] Thorlabs DBR1064PN

[12] Azurlight Systems ALS-IR-50-A-CP-SF

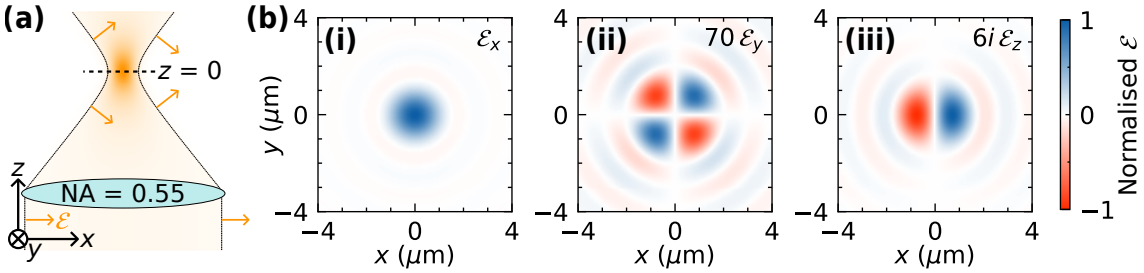

Figure 2.2: Polarisations of tweezers near their foci. (a) Ray optics diagram of a tweezer polarised along the x-axis. Near the focus ($z = 0$) significant polarisation components are generated along the other axes. **(b)** Calculated electric fields $\mathcal{E}$ at the focal plane (the xy-plane) along the **(i)** x- **(ii)** y- and **(iii)** z-axes. To plot all components on the same scale, we multiply $\mathcal{E}_y$ ($\mathcal{E}_z$) by 70 ($6i$).

up to 50 W of power at 1066 nm, but we typically operate with ~ 1 W.

The tweezers are overlapped with a series of dichroic mirrors and aligned through a high numerical aperture (NA) objective lens[13] (NA = 0.55) that is underneath the science cell. This is shown in Fig. 2.1(b). An additional dichroic mirror separates the light with which we image the atoms (see Sec. 2.3.1). The lens is designed to minimise the chromatic focal length shift between the different tweezer wavelengths and it produces traps that are near-diffraction limited.[14] We verify this by measuring ν_x, ν_y, and ν_z for tweezers of known optical power [220] from which we extract values of w_x, w_y, and z_R respectively. The beam waists $\{w_x, w_y\}$ are $\{0.925(1), 0.825(1)\}$ µm for the 817 nm tweezers, $\{1.285(5), 1.156(2)\}$ µm for the 938 nm tweezers, and $\{1.16(1), 1.05(1)\}$ µm for the 1066 nm tweezers. The Rayleigh ranges are $z_R^{817} = 3.29(1)$ µm, $z_R^{938} = 5.17(2)$ µm, and $z_R^{1066} = 4.17(7)$ µm respectively; these differ slightly from the ideal cases due to aberrations.

Each tweezer is linearly polarised along x-axis prior to the objective lens. However, near the tweezer foci, the tight focusing creates significant components of polarisation along the other axes. This leads to vector light shifts equivalent to a small fictitious magnetic field [205, 221–223]. We typically use the shim coils to apply a magnetic field of 4.78 G to minimise the impact of this fictitious field. For completeness, here we estimate the scale of the various polarisation components at the focal plane. Fig. 2.2(a) shows the system in the ray-optics framework. After refraction through the lens, the polarisation of each ray (orange arrows) remains transverse to its direction, and so has a component along the z-axis. We estimate the polarisation components along each axis by following the approach of Richards & Wolf [219, 224].

[13] SpecialOptics custom design

[14] The Abbe diffraction limit states that the smallest detail resolvable by an objective lens has size $\Delta x = \lambda/(2\,\mathrm{NA})$ [219]. Therefore, we expect the tweezer waists to be approximately 0.8 µm if they were diffraction limited. As we image atoms with light of similar wavelengths using the same objective lens (see Sec. 2.3.1), we expect that the resolution of the imaging system of similar scale.

We assume that the objective lens is illuminated with a cylindrically symmetric Gaussian beam of wavelength 1066 nm and beam waist $w_x = w_y = 15$ mm and take the beam waist to be at the front surface of the lens. We take the focal length of the objective lens to be 35.34 mm [206] and ignore refraction from the walls of the science cell. Figures 2.2(b)(i)-(iii) show the calculated electric field components $\mathcal{E}_x$, $\mathcal{E}_y$, and $\mathcal{E}_z$ along the x-, y-, and z-axes respectively. The values are relative to the maximum value of $\mathcal{E}_x$; to make all components visible, we scale $\mathcal{E}_y$ and $\mathcal{E}_z$ by factors of 70 and $6i$ respectively.[15]

Optical elements in the beam paths of the tweezers allow their positions to be controlled. We control the positions of traps that we wish to move around during an experimental sequence with acousto-optic deflectors (AOD) [186, 187]. The 817 nm tweezers are controlled with a two-dimensional AOD (2D AOD)[16] and the 938 nm tweezers are controlled with a one-dimensional AOD (1D AOD)[17], as shown in Fig. 2.1(b). The AODs slightly deflect the paths of the tweezer light prior to the objective lens, which changes the position of the traps at the focal plane. The deflection angle is proportional to the frequency with which the AODs are driven: changing this frequency moves the trap. The AODs are aligned so that an 817 nm trap can be moved in the xy-plane and a 938 nm trap can be moved along the x-axis. The AODs are driven with arbitrary waveform generators (AWG)[18], the output of which are amplified with radiofrequency (RF) amplifiers[19]. If multiple RF tones are applied, regular arrays of traps are formed.

Whilst AODs provide a simple and convenient way to form arrays of optical tweezers, they do have some drawbacks. A 1D AOD can only deflect light along a single axis, and 2D AODs can form only rectangular arrays because each axis operates independently. Furthermore, as AODs are diffractive optical elements, each tweezer along a given axis is at a slightly different frequency because the frequency of the RF tone used to create it is added or subtracted to the frequency of the input light (depending on the diffraction order used). This can introduce dephasing or differential light shifts between sites, which is particularly undesirable if a specific wavelength of tweezer is required for applications such as the magic trapping of molecules to obtain increased coherence times [98]. Furthermore, if two tweezers get close enough to form a beat, trapped particles can be significantly heated if the beat frequency is of the same order of magnitude as the trap frequencies [220].

[15] The polarisation component along the z-axis has a phase of $\pi/2$ relative to the components along the x- and y-axes. For this reason, the scale factor used when plotting $\mathcal{E}_z$ is imaginary.

[16] AA Opto-Electronic DTSXY-400-810

[17] IntraAction ATD-1803DA2.850

[18] 938 nm: Spectrum Inst. M4i.6622-x8, 817 nm: Spectrum Inst. M4i.6631-x8

[19] 938 nm: AA Opto-Electronic AMPA-B-34-20.425, 817 nm: AA O-E AMPB-B-34-10.500

Spatial light modulators (SLM) allow arrays of tweezers to be generated without suffering from these drawbacks. SLMs are liquid-crystal screens composed of a rectangular grid of pixels, each of which can be set to a different voltage. Applying a voltage to a pixel causes its crystals to rotate to a certain angle, modifying its refractive index. When light reflects off of (or is transmitted through) the SLM screen, it will acquire a phase that depends on the pixels' refractive indices. This allows an arbitrary phase (modulo 2π) to be encoded onto an input wavefront. By changing the pattern (the "hologram") on the SLM screen, different optical elements, such as a Fresnel lens or a diffraction grating, can be simulated by applying the phase shift that the real optical element would cause. This allows for the position of the tweezer focus to be moved in three dimensions. Furthermore, as the effect of the objective lens is to Fourier transform the input light, arbitrary array patterns in the focal plane can be realised by encoding phases onto an SLM that are calculated with Gerchberg-Saxton algorithms [225–228]. However, SLMs have their own drawback: the liquid-crystal nature of their displays means that their refresh rate is typically slow ($\sim$ 10 to 100 Hz) so it is impractical to use them to form tweezers that dynamically move particles.

We follow the approach of multiple experimental groups [229, 230] and use a hybrid solution involving AODs and an SLM[20]. As shown in Fig. 2.1(b), the SLM is in the 1066 nm beam path and controls the position of an array of 1066 nm tweezers, which is not changed during an experimental run. We use the AODs in the 817 nm and 938 nm beam paths to dynamically move tweezers that contain particles. By overlapping these arrays with the 1066 nm array, we can pick up particles from sites in the 1066 nm array and drop them off at other sites.

2.3 Lasers that drive atomic transitions

In this section, we introduce the lasers that we use to drive transitions in Rb and Cs.

2.3.1 Initial cooling and imaging

To cool Rb and Cs, we use two lasers for each species. Both lasers are slightly red detuned of hyperfine transitions on the D2 lines. For Rb (Cs), the "cooling" laser drives the closed transition $|5s_{1/2}, f = 2\rangle \rightarrow |5p_{3/2}, f' = 3\rangle$ ($|6s_{1/2}, f = 4\rangle \rightarrow |6p_{3/2}, f' = 5\rangle$) and the "repump" laser returns any atoms lost from this cycle (due to off-resonant scattering) by driving the transition $|5s_{1/2}, f = 1\rangle \rightarrow |5p_{3/2}, f' = 2\rangle$ ($|6s_{1/2}, f = 3\rangle \rightarrow |6p_{3/2}, f' = 4\rangle$). Here, the states are labelled $|n\ell_j, f\rangle$, where n is the principal quantum number, ℓ is the orbital angular momentum of the alkali

[20] Boulder Nonlinear Systems, PDM512-1064-DVI

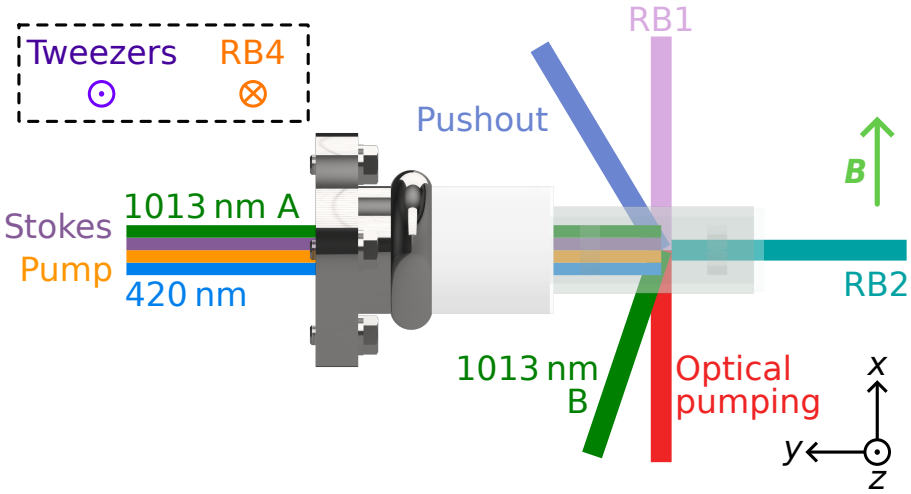

Figure 2.3: Overview of the beams in the science cell. The beams that are parallel to the y- or z-axes are linearly polarised. The other beams (RB1, pushout, 1013 nm B, and optical pumping) are circularly polarised to drive σ^+ transitions. For simplicity, the MOT beams are not shown and the tweezers and RB4 are offset from the centre of the cell. The 420 nm, pump, Stokes, and 1013 nm A beams are offset for clarity; in reality they are overlapped.

electron, j is its total angular momentum, and f is the quantum number of angular momentum resulting from the coupling of j with the nuclear spin i.[21] The projection of f along the quantisation axis is denoted m_f and will become relevant shortly. The frequency of these lasers are stabilised on the laser table by referencing them to atomic vapour cells. They are combined and coupled through optical fibres to the experiment table. The light is divided between three near-orthogonal beams that are circularly polarised and shone through the science cell, which are retroreflected to provide cooling in all six directions.

To load atoms into tweezers, we switch on the quadrupole coils and the cooling and repump light. This forms atomic MOTs in the science cell. During this time, the tweezer arrays are switched on so that their depth is sufficient to trap some atoms: we trap Rb (Cs) in an array of 817 nm tweezers (1066 nm tweezers). The favourable polarisability ratios $\alpha_{1066}/\alpha_{817}$ (see Table 2.1) mean that we do not trap a species in the other's array. The quadrupole coils are then switched off. The cooling and repump light further cools the atoms and induces light-assisted collisions to prepare single atoms. We load the species sequentially so that the shim coils can be used to best overlap each MOT with the corresponding tweezer array. We typically saturate tweezer loading when loading the MOTs for ~ 100 ms.

Atoms are imaged using the cooling and repump light. The atoms are excited on the D2 line and spontaneously decay. The resultant fluorescence has no preferred direction and some of it is oriented toward the objective lens underneath the science

[21] We use spectroscopic notation where $\ell = 0, 1, 2, 3, \ldots$ is denoted $\mathrm{s, p, d, f, \ldots}$.

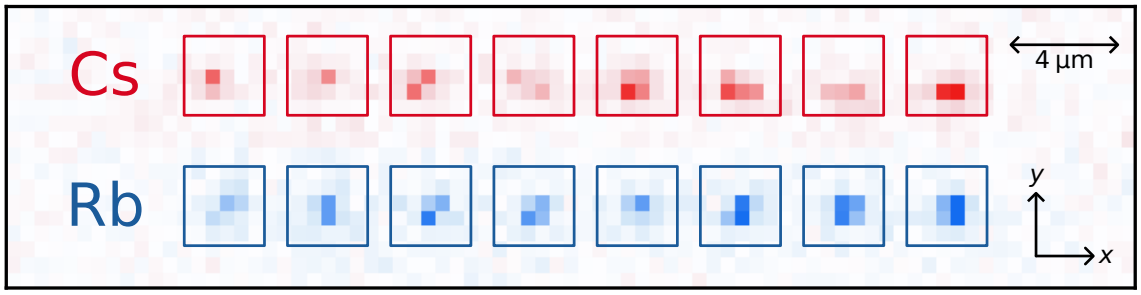

Figure 2.4: Defect-free arrays of eight Cs atoms and eight Rb atoms. The Cs atoms (red, top row) are trapped in an array of 1066 nm tweezers formed by the SLM. The Rb atoms (blue, bottom row) are trapped in an array of 817 nm tweezers formed by the 2D AOD. The height and width of each pixel is approximately 500 nm and the experimental coordinate system is labelled.

cell. This light is imaged onto an electron-multiplying charge-coupled device (EMCCD)[22]. High counts on the EMCCD correspond to the presence of an atom, and we distinguish between occupied and unoccupied sites with a fidelity $\gg 99\%$ whilst causing negligible loss of atoms.

We use data obtained from an initial image to form defect-free atomic arrays by correcting for sites where no atoms were loaded [186, 187]. First, we load the traps and measure their occupancy. Then, the 817 nm and 938 nm tweezers are used to shuttle Rb and Cs atoms respectively in order to form small one-dimensional defect-free arrays. The tweezer positions are swept by chirping the RF frequencies applied to the respective AODs. The Rb atoms are prepared in a final 817 nm array formed by the 2D AOD. Therefore, for the rearrangement of Rb atoms, we simply extinguishing unoccupied traps and shuttle occupied ones to one side of the array. The Cs atoms are moved around the array of 1066 nm traps sequentially with a single 938 nm tweezer.[23] The movement orders are calculated so that no atoms collide as they are moved. A second image verifies the occupancy of the arrays after rearrangement. The probability of loading an atom on a given site is well described by the cumulative binomial distribution [206]. We begin with nine 1066 nm traps and 14 817 nm traps so, on average, we load approximately five Cs atoms and seven Rb atoms. However, we can post-select to consider only experiments where an exact number of atoms were loaded, at the cost of increasing the time it takes to acquire experimental statistics. Fig. 2.4 shows an image obtained after this rearrangement procedure has prepared defect-free arrays of eight Rb atoms and eight Cs atoms. The extension of this procedure to prepare defect-free arrays of molecules is discussed in Sec. 4.8.

For experiments presented in Sec. 4.8, we image Rb atoms at high mag-

[22] Andor iXon 897 Ultra

[23] This is because we do not have sufficient power at 938 nm to move all Cs atoms simultaneously.

netic field (181.699(1) G). The atoms are imaged on the closed transition $|5s_{1/2}, f = 2, m_f = +2\rangle \rightarrow |5p_{3/2}, f' = 3, m'_f = +3\rangle$ with resonant circularly polarised light. The use of the closed transition prevents atoms decaying to states that are dark to the imaging light due to the large Zeeman shifts. This imaging light is sourced from a dedicated laser[24] which is frequency stabilised relative to the main cooling laser with a beat note lock [210] to be resonant with the imaging transition at the high magnetic field. This light is delivered to the science cell along the path labelled optical pumping in Fig. 2.3.

2.3.2 State preparation

To form RbCs molecules from Rb and Cs atoms, it is necessary to prepare them in the correct internal (i.e. hyperfine) and external (i.e. motional) states. The reasons for this are explored further in Ch. 3. To prepare Rb (Cs) atoms in the requisite hyperfine state $|\downarrow\rangle \equiv |5s_{1/2}, f = 1, m_f = +1\rangle$ ($|6s_{1/2}, f = 3, m_f = +3\rangle$) and the three-dimensional motional ground state, we implement a Raman sideband cooling protocol, as detailed by Spence [207]. We briefly summarise this protocol here. It uses the hyperfine states $|\downarrow\rangle$ and $|\uparrow\rangle \equiv |5s_{1/2}, f = 2, m_f = +2\rangle$ ($|6s_{1/2}, f = 4, m_f = +4\rangle$) in the ground manifold and states in the excited manifold $5p_{3/2}$ ($6p_{3/2}$) that we access when driving the D2 transition. The first component of the cooling protocol is an optical pumping beam. This beam is circularly polarised with high purity and drives σ^+ transitions on the D2 line. Over many absorption and emission events, this causes population to accumulate in the state $|\uparrow\rangle$. The second component is a two-photon Raman transition that, via a virtual state detuned from excited manifold, performs the coherent transfer $|\uparrow\rangle \rightarrow |\downarrow\rangle$ whilst removing one or more quanta of motion from the atom. We then optically pump back to $|\uparrow\rangle$ whilst maintaining the motional state. Over many cycles, this prepares atoms in the three-dimensional motional ground state in the hyperfine state $|\uparrow\rangle$. A final Raman transfer $|\uparrow\rangle \rightarrow |\downarrow\rangle$ prepares the atoms in the desired state.

To couple to the three separable directions of atomic motion, we use three "Raman" beams. These beams, along with the optical pumping beam, are shown in Fig. 2.3. To be consistent with Spence [207], the beams are labelled RB1, RB2, and RB4. The amplitude and frequency of the beams are controlled with AOMs and electro-optic modulators (EOM) on the laser table. RB1 and RB2 are used for the Raman transitions that couple to the two radial directions of the tweezers and RB1 and RB4 are used for the Raman transitions that couple to the axial direction. Previously, an additional beam (RB3) was used that propagated in the opposite

[24] Toptica DL pro

direction to RB2. This would be necessary if the tweezers were circular ($w_x = w_y$) due to the degeneracy of the two radial axes. However, we find that the elliptical nature of the tweezers means that the combination of RB1 and RB2 can couple to both radial axes. The sequence of pulses used for Raman sideband cooling is therefore the same as described by Spence [207], with the exception that RB3 pulses are replaced with RB2 pulses. Furthermore, we now Raman sideband cool Rb in an array of 817 nm tweezers and Cs in an array of 1066 nm tweezers. The trap frequencies during Raman sideband cooling are $\{\nu_x^{\mathrm{Rb}}, \nu_y^{\mathrm{Rb}}, \nu_z^{\mathrm{Rb}}\} = \{117(1), 148(1), 22.5(5)\}$ kHz for Rb and $\{\nu_x^{\mathrm{Cs}}, \nu_y^{\mathrm{Cs}}, \nu_z^{\mathrm{Cs}}\} = \{98(1), 148(1), 18.7(5)\}$ kHz for Cs. The frequencies of the pulses are adjusted from those in Ref. [207] accordingly and we typically play the pulse sequence twice to saturate cooling.

2.3.3 State-sensitive detection

A fraction of the atomic cooling light is coupled into an additional fibre to be used for state-sensitive detection. This light forms the "pushout" beam shown in Fig. 2.3. We use this to measure the probability that, for example, a Rb atom is in the state $|5\mathrm{s}_{1/2}, f = 1\rangle$ at the end of an experimental routine. The pushout beam is resonant with the transition $|5\mathrm{s}_{1/2}, f = 2\rangle \rightarrow |5\mathrm{p}_{3/2}, f' = 3\rangle$. This light causes rapid heating and loss of atoms in the state $|5\mathrm{s}_{1/2}, f = 2\rangle$ whilst not affecting atoms in the state $|5\mathrm{s}_{1/2}, f = 1\rangle$. Therefore, the state $|5\mathrm{s}_{1/2}, f = 1\rangle$ is mapped onto atomic survival and the state $|5\mathrm{s}_{1/2}, f = 2\rangle$ is mapped to atomic loss. The protocol for Cs is similar, mapping the state $|6\mathrm{s}_{1/2}, f = 3\rangle$ to atomic survival and ejecting atoms in the state $|6\mathrm{s}_{1/2}, f = 4\rangle$.

2.3.4 Rydberg excitation

In Ch. 5, we discuss the excitation of Rb atoms to highly excited Rydberg states. Here, we introduce the lasers that we use to perform this excitation. We transfer atoms from the ground manifold $5\mathrm{s}_{1/2}$ to Rydberg states with a two-photon excitation scheme. A laser at wavelength 420 nm drives transitions to the manifold $6\mathrm{p}_{3/2}$ and a laser at 1013 nm drives transitions from that manifold to the Rydberg states. The Rydberg beams are incident on the atoms as shown in Fig. 2.3. The lasers are housed on a separate optical bench (the "STIRAP table") to the main experiment and light is transferred to the experiment table with optical fibres.

The science cell is not AR coated for the 420 nm light and we therefore propagate this beam through an uncoated viewport along the long axis of the vacuum chamber (the y-axis). The setup we use to deliver the beam along this path is shown in

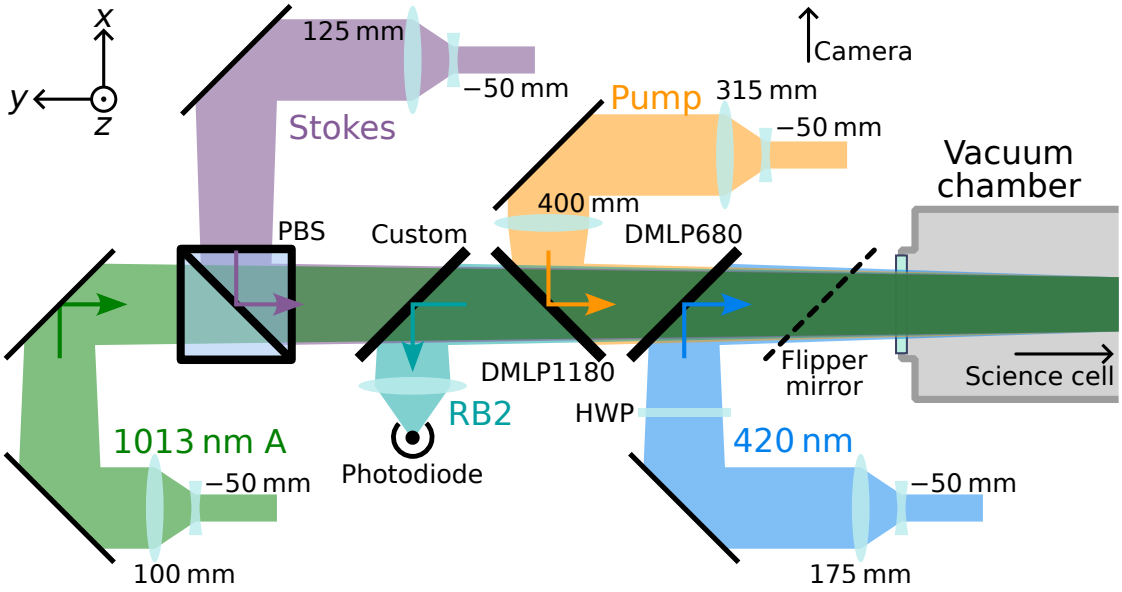

Figure 2.5: Optics to combine the beams that propagate along the long axis of the vacuum chamber. The beams are overlapped on a series of dichroic mirrors. Starting furthest from the vacuum chamber, the 1013 nm beam path A passes through and the Stokes light is reflected from a PBS. RB2 (which propagates through the chamber from the other side) is separated from these beams with a custom dichroic mirror from LaserOptik. The RB2 light is sent to a photodiode for power monitoring. A Thorlabs DMLP1180 dichroic mirror is used to overlap the pump beam. A Thorlabs DMLP680 dichroic mirror then overlaps the 420 nm light. Finally, there is a flipper mirror that is used to redirect the beams when profiling them. Each beam has its own set of focusing lenses (the focal lengths are labelled) which allow us to achieve the beam waists given in the text.

Fig. 2.5. The light passes through a focusing telescope, and it is overlapped with the counter-propagating RB2 beam and the lasers that address molecular transitions (see Sec. 2.4) with a series of dichroic mirrors. The beam is at a slight vertical angle (approximately 2°) to avoid a standing wave being formed at the focus of the optical tweezers. It is linearly polarised and a half-wave plate (HWP) allows its polarisation to be rotated in order to drive either π transitions when the polarisation is parallel to the magnetic field or $\sigma^{\pm}$ transitions when the two are perpendicular. At the atoms, we achieve a $1/e^2$ waist of 52(6) µm. This waist is measured by diverting the beam with a flipper mirror before it reaches the vacuum chamber and profiling it with a camera.

The science cell is AR coated for the 1013 nm light. Therefore, we can pass this beam through the science cell. We deliver the 1013 nm light to the atoms via one of two beam paths. The reasons for using these two beam paths are discussed further in Sec. 5.2. The first beam path, 1013 nm A, co-propagates with the 420 nm light as shown in Figs 2.3 and 2.5. This light is transmitted through a polarising beam splitter (PBS) so that its polarisation is parallel with the magnetic field and it drives

π transitions. The second beam path, 1013 nm B, propagates approximately parallel with the magnetic field and passes through the science cell, as shown in Fig. 2.3. This beam is circularly polarised to primarily drive σ^+ transitions. With beam path A we achieve a waist of 105(2) µm and with beam path B we achieve a waist of 35(2) µm.

2.4 Lasers that drive molecular transitions

The formation of molecules is discussed in detail in Chs 3 and 4. For now, we state that when a molecule is formed, it is formed and transferred to the weakly bound state $|F\rangle$. Ultimately, we aim to prepare molecules in the rovibrational ground state $|G\rangle$. We perform the molecular transfer $|F\rangle \rightarrow |G\rangle$ via the intermediate state $|E\rangle$ with two-photon stimulated Raman adiabatic passage (STIRAP) (see Sec. 4.2). For this, we use light resonant with the "pump" transition $|F\rangle \rightarrow |E\rangle$ and the "Stokes" transition $|E\rangle \rightarrow |G\rangle$. We refer to these two beams as the STIRAP light and here we discuss the laser system that prepares and delivers this light to the experiment.

The STIRAP lasers are housed on the STIRAP table alongside the Rydberg lasers and are delivered to the experiment table via optical fibres. The wavelength of the pump light is 1557 nm and the wavelength of the Stokes light is 977 nm. The science cell is not AR coated for the pump wavelength and we therefore propagate the beams through an uncoated viewport along the y-axis, as shown in Figs 2.3 and 2.5. We co-propagate the beams to minimise molecular heating (see Sec. 4.2). Each beam passes through an expansion telescope and they are overlapped on dichroic mirrors with the other beams that propagate along this axis. Both beams are linearly polarised. The polarisation of the pump light is parallel to the magnetic field so that it drives π transitions. The polarisation of the Stokes light is perpendicular to the magnetic field so that it drives $\sigma^{\pm}$ transitions. As with the 420 nm light, the pump light is at a slight vertical angle to avoid a standing wave being formed at the focus of the optical tweezers. We achieve a beam waist of 80(2) µm for the pump light and a beam waist of 70(2) µm for the Stokes light.

2.5 Frequency stabilisation of the STIRAP and Rydberg lasers

The STIRAP and Rydberg lasers require an artificial frequency reference to which we can frequency stabilise ("lock") them. For the STIRAP lasers, this is necessary because we do not have the convenience of a molecular vapour cell from which to

Table 2.2: Quantities relevant to the frequency stabilisation of the STIRAP and Rydberg lasers, as detailed in the text.

Laser		ULE cavity		PDH lock
		$\mathcal{F}$	ν_{FSR} (MHz)	ν_{PDH} (MHz)
STIRAP	Stokes ($\lambda = 977$ nm)	$2.00(8) \times 10^4$	1498.8123(9)	20.21
	pump ($\lambda = 1557$ nm)	$1.70(2) \times 10^4$	1498.796(3)	15.51
Rydberg	$\lambda = 420$ nm	$> 8 \times 10^2$	~ 1500	25.00
	$\lambda = 1013$ nm	$2.8(1) \times 10^4$	1498.8117(6)	11.31

derive an error signal. For the Rydberg lasers, this is necessary as we excite atoms to Rydberg states via a virtual level detuned from the intermediate manifold. In this section, we discuss the setup on the STIRAP table with which we lock these lasers.

We lock the STIRAP and Rydberg lasers to a single ultra-low expansion (ULE) cavity[25] using a Pound-Drever-Hall (PDH) scheme [231]. The cavity is temperature stabilised at its zero expansion temperature to avoid significant drifts in its length. It generally reflects incident light, apart from light resonant with one of the longitudinal cavity modes that occur at multiples of the free spectral range $\nu_{\mathrm{FSR}} = c/2L$ for cavity length L. An error signal can be derived from the change in reflectance around these modes, allowing the cavity to be used as an arbitrary frequency reference to which the lasers can be locked. To derive this error signal, each beam is phase modulated prior to the cavity at frequency $\nu_{\mathrm{PDH}} \sim 10\,\mathrm{MHz}$. The reflected light is incident on a photodiode and the interference between the carrier and sidebands gives rise to an error signal at ν_{PDH} that can be demodualated and be used for laser feedback. The performance of the cavity is quantified by the finesse $\mathcal{F} = \nu_{\mathrm{FSR}}/\Delta\nu$. Here $\Delta\nu$ is the linewidth of the cavity modes and a cavity constructed with higher reflectivity mirrors will have higher finesse. The finesse and free spectral range of our cavity at the different wavelengths used are tabulated in Table 2.2.[26] Additionally, we give the values of ν_{PDH} used when all four lasers are locked simultaneously to the cavity.

Although the ULE cavity provides an *arbitrary* frequency reference, on its own it does not provide a *tuneable* frequency reference. Cavities for which the resonant frequencies can be tuned after manufacturing (for example, by tuning the cavity length with a piezo stack [232] or tuning the refractive index of the cavity [233]) exist, but this tuneablity comes with the drawback that the length of the cavity can significantly drift over time. Additionally, with this approach, it is not possible to modify only a single laser's locking frequency. Instead, we use the approach of

[25] Stable Laser Systems custom specification

[26] The coating of the mirrors that make up the ULE cavity is complex in order to give a high finesse for all four specified wavelengths. Light at these different wavelengths reflects from different parts of the coating. This means that the cavity length L and the free spectral range ν_{PDH} are wavelength dependent.

Thorpe *et al.* [234] where each beam passes through a high-bandwidth fibre EOM prior to the cavity. The bandwidths of the fibre EOMs are greater than the free spectral range of the cavity. By adding a set of frequency sidebands to the light at an offset frequency ν_{offset}, and stabilising one of these sidebands to the cavity mode, the laser can be stabilised to an arbitrary frequency. The frequency at which a laser is locked can then be tuned by changing ν_{offset}.

The optical setup used to stabilise the STIRAP light and deliver it to the experiment is shown in Fig. 2.6(a). The setup is based on the design of Gregory *et al.* [235] which is used in the bulk-gas RbCs experiment at Durham. The light is sourced from diode lasers[27]; the 1013 nm light is amplified with a tapered amplifier[28]. From each beam path, we pickoff a small amount of light to monitor the frequency on a wavemeter[29]. A sample of each beam is then delivered to the cavity setup (Fig. 2.6(a), shaded region) with an optical fibre. For the STIRAP beams and the 1013 nm light, the relevant fibre EOM[30] serves as this optical fibre. We use these to phase modulate the light at both ν_{PDH} (to extract the PDH error signals) and ν_{offset} (to tune the lasers to an arbitrary frequency). Two independent function generators[31] produce the driving tones for these sidebands before they are combined with a power splitter[32] and sent to the modulator. The demodulation of the PDH error signal and laser feedback is performed by fast laser-locking modules[33]. We were not able to source an affordable near-ultraviolet (UV) fibre EOM. Therefore, for the 420 nm light, we use a free-space EOM[34] prior to a patchcord and modulate the light only at ν_{PDH}.[35] A telescope after each fibre matches the Gaussian beam curvature of each beam with the curvature of the cavity mirrors [236, 237]. Each beam is transmitted through a PBS and a quarter-wave plate (QWP) and the beams are overlapped with a series of dichroic mirrors[36]. The beams reflect from the cavity, pass through the QWPs for a second time, and reflect from the PBSs onto photodiodes[37] from which the error signals are extracted. An affordable dichroic mirror with a cutoff wavelength between the Stokes light (at 977 nm) and the 1013 nm light was not

[27] Toptica DL pro

[28] Toptica TA pro

[29] Bristol Instruments 671A-NIR

[30] Pump: Thorlabs LN65S-FC, Stokes: EOSpace PM-0S5-10-PFA-PFA-980, 1013 nm: EOSpace PM-0S5-10-PFA-PFA-1013

[31] PDH modulation: Rigol DG822, offset modulation: Windfreak Technologies Synth HD

[32] Minicircuits ZAPD-2-252-S+

[33] Toptica FALC pro

[34] Photonics Technologies EOM-02-25-U

[35] The resonant frequency of the EOM used for the 420 nm light is 25 MHz and its bandwidth is only a few megahertz; this precludes arbitrary tuning of the 420 nm frequency.

[36] As labelled in Fig. 2.6(a), D1 is Thorlabs DMLP650 and D2 is Thorlabs DMLP1180.

[37] STIRAP and 1013 nm: Thorlabs PDA05CF2, 420 nm: Thorlabs PDA8A2

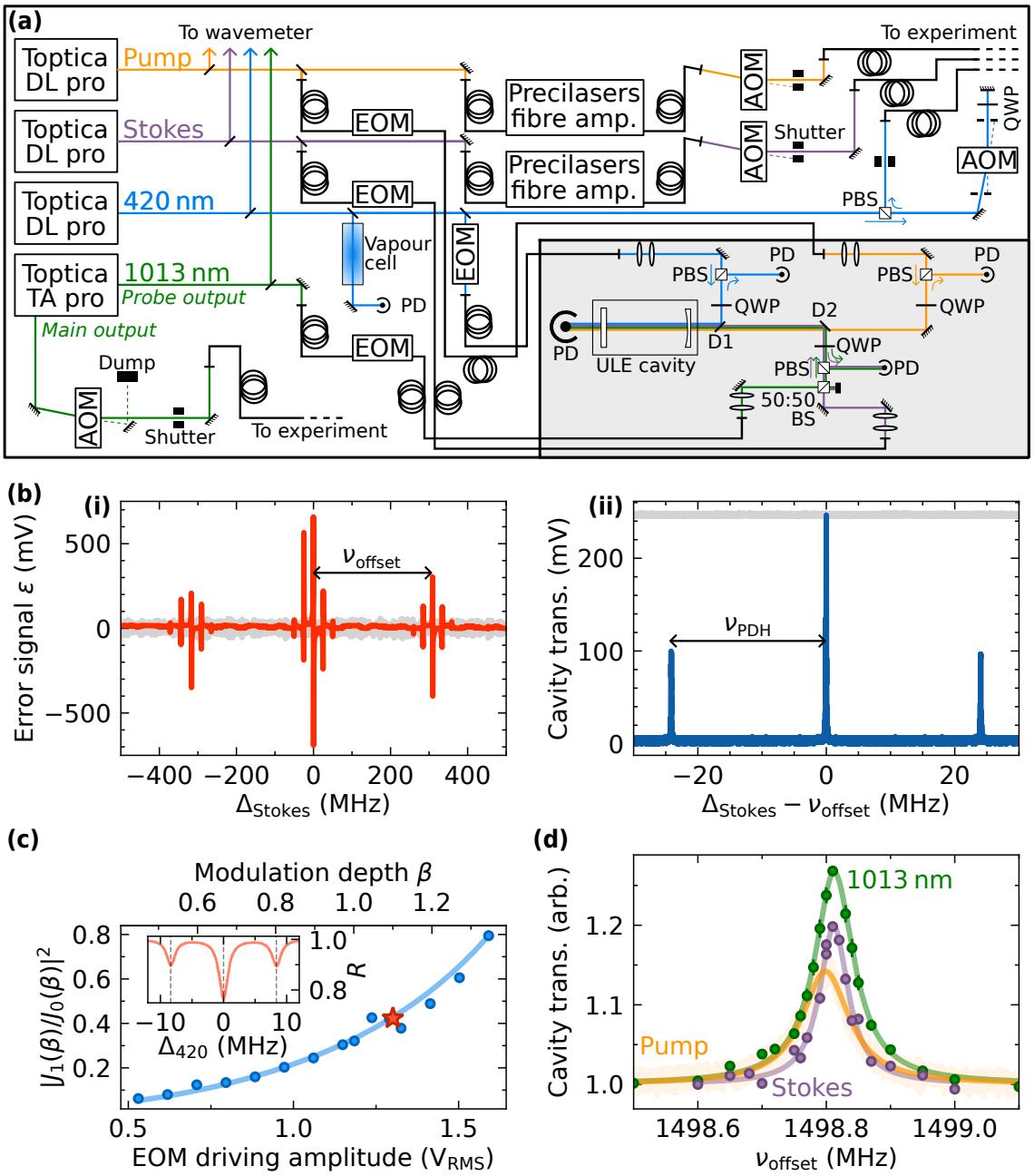

Figure 2.6: PDH locking setup used to stabilise the STIRAP and Rydberg lasers. (a) Simplified diagram of the optical setup on the STIRAP table as described in the text. The shaded region shows the region relevant for the PDH lock. **(b)** The error signal (panel **(i)**) and cavity transmission (panel **(ii)**) for the Stokes laser as a function of laser frequency. The shaded grey data show the deviation over 20 ms when the laser is locked at $\Delta_{\text{Stokes}} = \nu_{\text{offset}}$ Here, $\nu_{\text{PDH}} = 24.1\,\text{MHz}$ and $\nu_{\text{offset}} = 313\,\text{MHz}$. **(c)** Ratio between the amplitudes of the sidebands and the carrier as a function of the driving amplitude for a homebuilt 420 nm EOM modulated at 8.37 MHz. The inset shows the cavity reflectivity R at the red star. **(d)** Measurement of ν_{FSR} for the STIRAP and 1013 nm lasers. When $\nu_{\text{offset}} = \nu_{\text{FSR}}$ there is an increase in light transmitted through the cavity. The pump data were obtained with a continuous frequency sweep of ν_{offset}; the Stokes and 1013 nm data were obtained by measuring the cavity transmission at distinct values of ν_{offset}. The dark lines show fits to Lorentzians from which we extract ν_{FSR} and $\mathcal{F}$ of the cavity at each wavelength.

available. Therefore, these beams are overlapped on a 50 : 50 non-polarising beam splitter prior to their PBS. The difference in ν_{PDH} between the two (see Table 2.2) allows their error signals to be extracted independently. We ensure that there are a sufficient number of degrees of freedom so that each beam can be independently aligned to the cavity; this is important to preclude excited transverse modes.

Figure 2.6(b)(i) shows a typical error signal that we derive from the cavity setup. For this example, we show the error signal as the frequency of the Stokes laser is scanned. The detuning Δ_{Stokes} is relative to a cavity mode. Here, $\nu_{\mathrm{offset}} = 313\,\mathrm{MHz}$ and $\nu_{\mathrm{PDH}} = 24.1\,\mathrm{MHz}$. Fig. 2.6(b)(ii) shows the cavity transmission when $\Delta_{\mathrm{Stokes}} \approx \nu_{\mathrm{offset}}$. In both plots, the data shown in grey shows how the error signal and transmission vary over 20 ms when the laser is locked at $\Delta_{\mathrm{Stokes}} = \nu_{\mathrm{offset}}$.

The amount of modulation performed by an EOM is characterised by the modulation depth β. The electric field of light after it has passed through a phase-modulating EOM being driven at frequency ν_m with modulation depth β_m is of the form $\sqrt{P}\exp\{i\left[2\pi\nu_0 t + \beta_m \sin\left(2\pi\nu_m t\right)\right]\}$, where P is the power in the beam, and ν_0 is the frequency of the input light [234]. For the STIRAP and 1013 nm lasers, we modulate the light at ν_{PDH} with modulation depth β_{PDH} and at ν_{offset} with modulation depth β_{offset}. It can be shown that, at a detuning $\Delta = \nu_{\mathrm{offset}}$ from the cavity mode, the derivative of the error signal with respect to laser frequency is [234]

$$\left.\frac{d\epsilon}{d\nu}\right|_{\Delta=\nu_{\mathrm{offset}}} \propto J_1^2(\beta_{\mathrm{offset}})J_0(\beta_{\mathrm{PDH}})J_1(\beta_{\mathrm{PDH}})\,. \tag{2.4}$$

Here, J_n is the nth-order Bessel function of the first kind. For the 420 nm light, we modulate the light at only ν_{PDH} with modulation depth β_{PDH}. At the cavity mode ($\Delta = 0$), we have [234]

$$\left.\frac{d\epsilon}{d\nu}\right|_{\Delta=0} \propto J_0(\beta_{\mathrm{PDH}})J_1(\beta_{\mathrm{PDH}})\,. \tag{2.5}$$

To obtain the narrowest linewidths possible, we maximise $d\epsilon/d\nu$ so that the locking hardware is as sensitive to fluctuations in the laser frequency as possible. In both cases this occurs when $\beta_{\mathrm{PDH}} \approx 1.082$ and, when relevant, $\beta_{\mathrm{offset}} \approx 1.841$.

We characterise the modulation depths of the EOMs in order to maximise $d\epsilon/d\nu$. We vary the amplitude with which we drive an EOM and, for each driving amplitude, find the ratio between the amplitudes of the sidebands and carrier. In Fig. 2.6(c) we show data obtained by performing this characterisation with a homebuilt 420 nm EOM driven at 8.37 MHz. The solid line shows a fit to the expected ratio $|J_1(\beta)/J_0(\beta)|^2$, where we have assumed that β is proportional to the driving amplitude. The inset shows the carrier and sidebands when the modulation depth is near optimum ($\beta \approx 1.082$).

The values of $\mathcal{F}$ given in Table 2.2 are obtained by measuring ν_{FSR} and $\Delta\nu$ for each laser. We measure these by locking each laser to a carrier and varying ν_{offset} around ν_{FSR}. When $\nu_{\mathrm{offset}} = \nu_{\mathrm{FSR}}$, both the carrier and the sidebands are transmitted through the cavity because they coincide with neighbouring longitudinal modes. This measurement for the STIRAP and 1013 nm lasers is shown in Fig. 2.6(d). We fit a Lorentzian to each feature to extract ν_{FSR} and $\Delta\nu$; the ratio of these is the finesse $\mathcal{F}$. We cannot perform this measurement with the 420 nm laser because its EOM is in free space and has a small bandwidth. Instead, we estimate these quantities based on the cavity linewidth and position of the PDH sidebands on the error signal.

The majority of the light from each laser is sent to the experiment. We amplify the STIRAP light with fibre amplifiers[38] so that each beam contains approximately 50 mW. Each beam passes through an AOM[39] (see Fig. 2.6(a)) that we use to control the frequency and amplitude of pulses. The 420 nm beam is double passed through its AOM to so that we can access a larger frequency range (as this laser cannot be locked to an arbitrary frequency). For the other beams, we single pass the AOMs to maximise the available power. The AOMs are driven with by homebuilt direct digital synthesisers (DDS)[40] that can shape pulses with up to 4 ns resolution. Each beam passes through a low vibration shutter[41] and is coupled to the experiment table via optical fibres. Additionally, a small amount of 420 nm light is picked off and transmitted through a heated Rb vapour cell that we typically operate at about 60 °C. This is used for vapour-cell spectroscopy on the transition $|5s_{1/2}\rangle \rightarrow |6p_{3/2}\rangle$ (see Sec. 5.3).

2.6 Experimental control

AMO experiments typically require precise control of dozens of pieces of equipment with microsecond timing resolution. Our experiment is no different. The main application that controls our apparatus is `PyDex`[42], a custom Python application that is used for experimental control and data analysis. `PyDex` runs on the main control computer, which interfaces with other computers on our laboratory network. To acquire statistics from an optical tweezer experiment, it is necessary to repeat an experimental sequence many (typically ~ 100) times because each experimental run gives only a few bits of data (whether or not a given tweezer is occupied at the end

[38] Both STIRAP fibre amplifiers are supplied by Precilasers

[39] Pump: ISOMET M1205-P80-L-0.6, Stokes and 1013 nm: ISOMET 1205C-843, 420 nm: ISOMET M1250-T250L-0.45

[40] Based on Anologue Devices AD9910

[41] Stanford Research Systems SR475

[42] https://github.com/ssquantum/PyDex

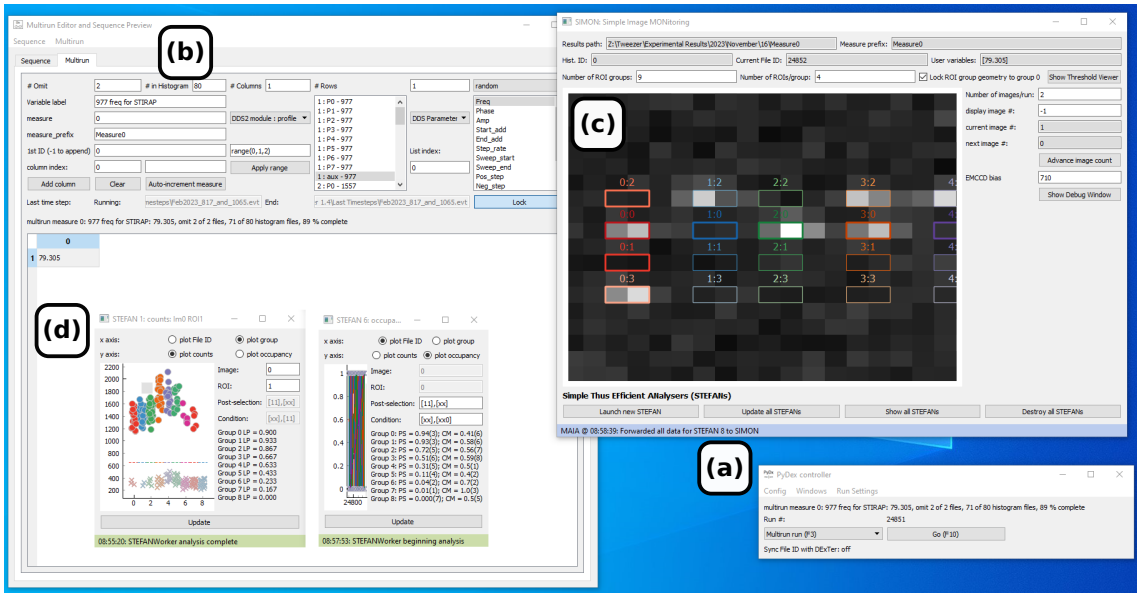

Figure 2.7: `PyDex` **interface used for experimental control and near real-time analysis.** **(a)** Main control window. **(b)** Multirun Editor control window that we use to queue experiments. **(c)** The `SIMON` window that we use to view near real-time experimental images and set the ROIs used when assigning atom occupancy. **(d)** Example of the `STEFAN` modules that we use for simple mid-experiment analysis. The left window shows EMCCD counts obtained for different ROIs over multiple runs of the experiment, the right window shows results from a simple analysis of these counts based on user-defined criteria.

of an experimental sequence). `PyDex` handles this repeated operation and performs real-time processing of the acquired data.

The majority of equipment in our laboratory is controlled by a few voltage inputs. Therefore, an experimental sequence is mainly a table of timesteps and a list of each voltages to set at each timestep. `PyDex` automatically constructs experimental sequences from a predefined list of parameters. These sequences are then passed to a custom LabView application called `DExTer` [238]. `DExTer` interfaces with an FPGA card[43] to output analogue and digital voltages when required and runs on its own dedicated computer. Equipment which requires more complex control (such as the AWGs, the SLM, and programmable microwave generators (MWG)) are each controlled via with custom Python applications[44] that interface with commercial application programming interfaces on dedicated computers.

Figure 2.7 shows a typical mid-experiment view of `PyDex`. The main control window is shown in Fig. 2.7(a). An experiment is run by queuing a list of parameters to vary in the Multirun Editor window, which is shown in Fig. 2.7(b). During an

[43] National Instruments PCI-7833R

[44] AWGs: https://github.com/danielruttley/awg,
SLM: https://github.com/danielruttley/slm,
MWGs: https://github.com/danielruttley/mwcontrol

the running of an experimental sequence, `PyDex` receives images from the EMCCD. Imaged are analysed in near real-time after being placed into a first-in, first-out (FIFO) queue. When processor load allows, an image is removed from the queue by the Multi Atom Image Analyser (`MAIA`) module. This module assigns a binary occupancy to each tweezer by comparing the EMCCD counts in a pre-defined region of interest (ROI) to a threshold. If the counts are above the threshold, the trap is deemed to be occupied. Furthermore, each image is passed to the Simple Image Monitor (`SIMON`) module, shown in Fig. 2.7(c), to be displayed to the user. The images and occupancies are written to disk to allow for future retrieval and analysis. For simple analysis during an experiment, we use the Simple Thus Efficient Analyser (`STEFAN`) modules, examples of which are shown in Fig. 2.7(d). These allow the user to set a list of criteria to monitor in real-time. For example, we can check that molecules are still being formed as an experiment is being run. If, say, a laser in the laboratory mode hops, we can quickly detect and correct this without waiting until an entire experiment is complete.

The exception to this data flow is for images from the EMCCD that we use for rearrangement of atoms or molecules. This is because these images are required to be processed as quickly as possible in order to provide feedback to the experiment. When images used for rearrangement are received, as well as being added to the FIFO queue, they are immediately passed to the Atom Loading Enhancement for Experiment (`ALEX`) module and the processing of the FIFO queue is suspended. `ALEX` determines the occupancy of the tweezers as quickly as possible, then immediately passes this information to the AWG control scripts that move their respective tweezers in order to rearrange the particles. This processing takes $\sim 10\,\text{ms}$ and after this processing of the FIFO queue resumes.

2.7 Summary

We have introduced the experimental apparatus that is used in the following chapters. The optics and lasers used for trapping and control of individual atoms have been discussed. We have highlighted recent changes in the experimental apparatus, including the installation of beams used for molecular state transfer and the Rydberg excitation of Rb atoms. Furthermore, we have described recent changes to the experimental control and analysis software that have been implemented for the efficient control and readout of small arrays of optical tweezers.

3 Weakly bound molecules

The majority of the results in this chapter have been published in Ref. [201]. Some of the results have been published in Refs [202, 203].

We form RbCs molecules from ultracold Rb and Cs atoms that are individually trapped in species-specific optical tweezers. The first step of molecule production is the association of Rb+Cs atom pairs into weakly bound molecules.

In this chapter, we present methods that we use to form these weakly bound molecules. We begin by briefly introducing the molecular bound states that we access. Following this, we discuss two methods for converting atom pairs into molecules in this manifold. We detail spectroscopy of these weakly bound molecular states and show how the atom to molecule conversion processes can be experimentally controlled.

3.1 Feshbach molecule structure

The electronic energy levels of RbCs molecules are shown in Fig. 3.1(a). We follow the approach of Brown & Carrington [239] and label each potential with the moleculear term symbol $^{2S+1}\Lambda^{\pm}$. Here, Λ is the electronic orbital angular momentum, S is the electronic spin angular momentum, and the $\pm$ superscript refers to the symmetry under inversion in a plane containing the internuclear axis.[1] The index prior to the term symbol orders the potentials by increasing energy, similar to the principal quantum number for atomic states. For singlet states ($S = 0$), we count up from lowest energy with $\mathrm{X}, \mathrm{A}, \mathrm{B}, \mathrm{C}, \ldots$. For triplet states ($S = 1$), we enumerate the potentials with $\mathrm{a}, \mathrm{b}, \mathrm{c}, \mathrm{d}, \ldots$. In this notation, the electronic ground state has the label $\mathrm{X}^1\Sigma^+$.

Ultimately, we aim to prepare molecules in the rovibrational ground state $|G\rangle$ of the manifold $\mathrm{X}^1\Sigma^+$. Molecules in this manifold have significant molecule-frame dipole moments and long radiative lifetimes that make them ideal for quantum information

[1] We use spectroscopic notation where $\Lambda = 0, 1, 2, 3, \ldots$ is denoted $\Sigma, \Pi, \Delta, \Phi, \ldots$.

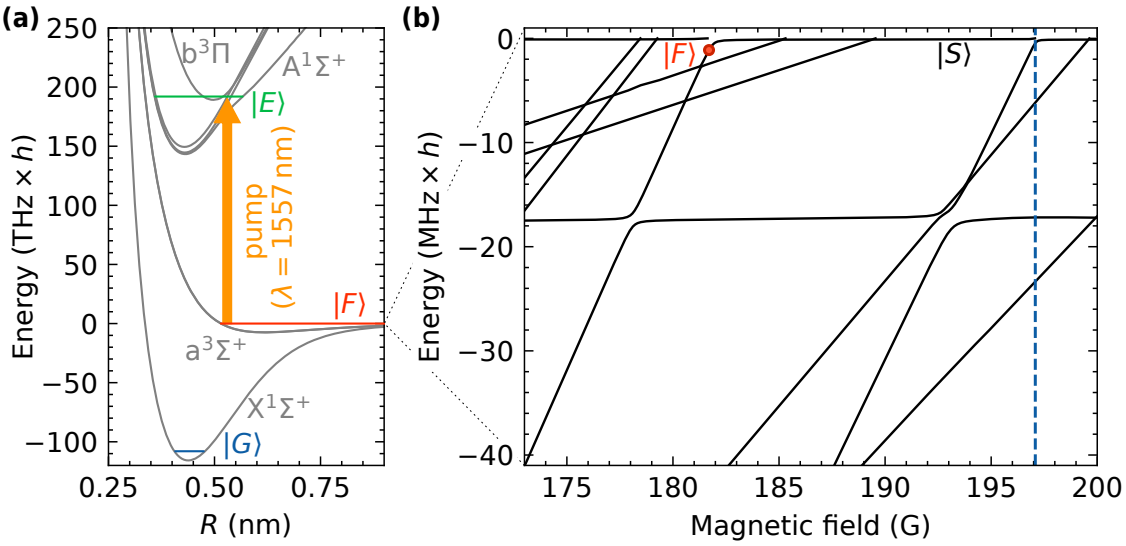

Figure 3.1: Energies of RbCs molecules. (a) Electronic potential curves for RbCs molecules. The orange arrow shows the pump transition $|F\rangle \rightarrow |E\rangle$. (b) Bound-state spectrum of weakly bound RbCs molecules in the Feshbach manifold surrounding the state $|F\rangle$ (red point). Energies are given relative to the dissociation threshold and come from coupled-channel calculations using the RbCs interaction potential of Takekoshi *et al.* [148].

and simulation applications. However, we are not able to directly associate atom pairs into molecules in the state $|G\rangle$ due to the vanishing wavefunction overlap between it and an atom pair state. Therefore, we adopt a two step approach that has been widely used to assemble heteronuclear polar molecules in their rovibrational ground state [146, 149, 151, 155, 156, 240]. We first convert atom pairs to weakly bound molecules in the state $|F\rangle$ which has mostly $a^3\Sigma^+$ character. This state is chosen because it has strong coupling to an excited state $|E\rangle$ of the coupled $A^1\Sigma^+ + b^3\Pi$ manifold that also has strong coupling to the state $|G\rangle$.[2] This enables the transfer $|F\rangle \rightarrow |G\rangle$ with two-photon techniques (see Ch. 4). For the remainder of this chapter, we will explore how atom pairs can be converted into molecules in the state $|F\rangle$.

The energies of bound states surrounding the state $|F\rangle$ as a function of magnetic field are shown in Fig. 3.1(b). The energies are relative to the dissociation threshold. This group of states is typically termed the *Feshbach manifold*, and the states within it are the *Feshbach states*. The states relevant to the discussion here have binding energies ~ 0.1 to $10\,\mathrm{MHz} \times h$. The bound-state spectrum is calculated with coupled-channel methods using the RbCs interaction potential of Takekoshi *et al.* [148].[3] We highlight the state $|F\rangle$ at a magnetic field equal to 181.699 G (red point) and the

[2] We give quantum numbers for the state $|E\rangle$ in Sec. 4.1.

[3] The binding energies of states in the Feshbach manifold were calculated by C. Ruth Le Sueur and Jeremy M. Hutson. The details are beyond the scope of this thesis and can be found in Ref. [148].

least-bound state $|S\rangle$ which has a binding energy equal to $110(2)\,\mathrm{kHz} \times h$ for most of the field range shown here. States in the Feshbach manifold are typically labelled as $|n\,(f_{\mathrm{Rb}}, f_{\mathrm{Cs}})\,L\,(m_{\mathrm{Rb}}, m_{\mathrm{Cs}})\rangle$, where n is the vibrational quantum number relative to the supporting threshold and L is the rotational quantum number around the centre of mass.[4] In this notation, $|S\rangle \equiv |-1(1,3)\mathrm{S}(+1,+3)\rangle$ and $|F\rangle \equiv |-6(2,4)\mathrm{D}(+2,+4)\rangle$.

3.2 Association pathways

We assemble molecules in the state $|S\rangle$ by exploiting coupling between this state and the unbound atom pair state $|5\mathrm{s}_{1/2}, f=1, m_f=+1\rangle_{\mathrm{Rb}}\,|6\mathrm{s}_{1/2}, f=3, m_f=+3\rangle_{\mathrm{Cs}}$ (hereafter $|1,+1\rangle_{\mathrm{Rb}}|3,+3\rangle_{\mathrm{Cs}}$). First, we consider the general case where the energies of these two states depend on a parameter that can be externally controlled. When the energies of the states would otherwise cross, the coupling between them can give rise to an avoided crossing. A cartoon of such a crossing is shown in Fig. 3.2. By slowly varying the control parameter, we are able to adiabatically follow the eigenstates of the system.[5] Explicitly, in the situation shown in Fig. 3.2, we would start with the control parameter high and prepare atom pairs in the state $|1,+1\rangle_{\mathrm{Rb}}|3,+3\rangle_{\mathrm{Cs}}$. We would then slowly decrease the control parameter, as indicated by the arrow. Provided that the rate of change of the control parameter is sufficiently slow, we would adiabatically convert an atom pair in the state $|1,+1\rangle_{\mathrm{Rb}}|3,+3\rangle_{\mathrm{Cs}}$ to a molecule in the state $|S\rangle$. In contrast, if the rate of change of the control parameter was too fast, we would follow the blue dashed diabat and maintain an atom pair in the state $|1,+1\rangle_{\mathrm{Rb}}|3,+3\rangle_{\mathrm{Cs}}$.

In this section, we detail two different mechanisms for generating and traversing such an avoided crossing. First, we discuss an avoided crossing where the control parameter is an external magnetic field, which has been widely used in bulk-gas experiments to form molecules [144, 145]. Second, we describe a novel avoided crossing where the control parameter is separation of two optical tweezers that each trap either a single Rb or Cs atom.

3.2.1 Magnetoassociation

Magnetoassociation is a technique that exploits the differential magnetic moment between an atom pair state and molecular state to assemble molecules. The differential magnetic moment means that the energy separation between the states

[4] We use spectroscopic notation where $L = 0, 1, 2, 3, \ldots$ is denoted $\mathrm{S}, \mathrm{P}, \mathrm{D}, \mathrm{F}, \ldots$.

[5] We will give a more concrete definition of "slowly" when discussing the specific methods used for association.

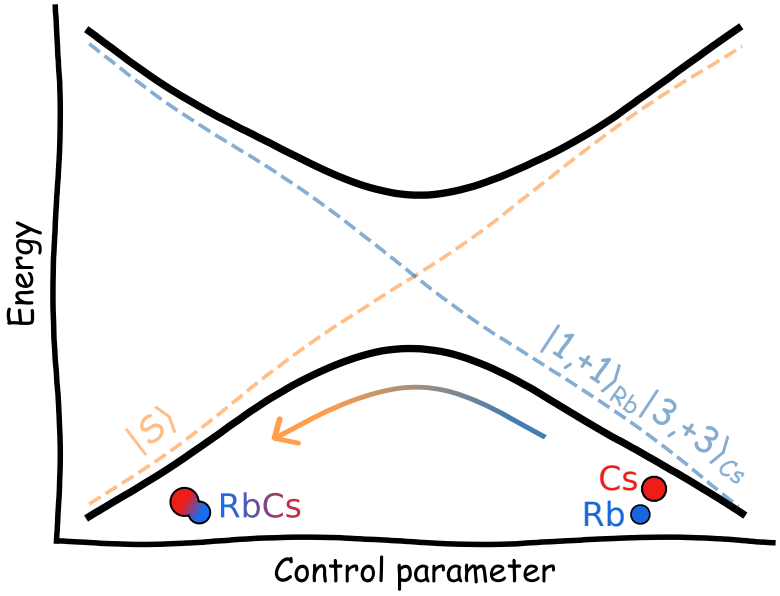

Figure 3.2: Forming molecules by adiabatically traversing an avoided crossing. We engineer avoided crossings between the atom pair state $|1,+1\rangle_{\mathrm{Rb}}|3,+3\rangle_{\mathrm{Cs}}$ and the least-bound molecular state $|S\rangle$ in our experiment. We adiabatically traverse these avoided crossing by changing a control parameter to convert atom pairs into molecules. By reversing the process, we convert molecules in the state $|S\rangle$ back to atom pairs.

can be tuned with a magnetic field. The field at which the atomic and molecular state would have the same energy corresponds to a Feshbach resonance. At this field, there is an avoided crossing caused by coupling between the two states. During magnetoassociation, this avoided crossing is adiabatically traversed to convert atom pairs into molecules that occupy a single quantum state [144, 145].

Bulk-gas experiments that assemble RbCs molecules have used magnetoassociation to convert atom pairs into molecules in the state $|S\rangle$ [148, 241]. In these experiments, atoms are cooled to obtain a high phase-space density and prepared in the atom pair state $|1,+1\rangle_{\mathrm{Rb}}|3,+3\rangle_{\mathrm{Cs}}$. The magnetic field is then swept across a Feshbach resonance arising from the state $|-6(2,4)\mathrm{D}(+2,+3)\rangle$ at 197.08(2) G (see Fig. 3.1(b), blue dashed line) and atom pairs follow the associated avoided crossing to be converted into molecules in the state $|S\rangle$. We follow the same procedure to form individually trapped molecules in the state $|S\rangle$.

In Fig. 3.3(a)(i) we show energies of atomic and molecular states around a Feshbach resonance in our system. The energies are given as a function of $-1/a$, where a is the s-wave scattering length [242, 243]. We calculate these energies by following the approach of Spence [207]. We assume that the atom pairs are individually trapped in cylindrically symmetric tweezers and, for now, take them to be in the ground state of centre-of-mass motion. We assume that the centre-of-mass

and relative motions are separable.[6] The trap frequency for relative motion of the atom pair along axis i is

$$\nu_i = \sqrt{\frac{m_{\mathrm{Cs}}\nu_{\mathrm{Rb},i}^2 + m_{\mathrm{Rb}}\nu_{\mathrm{Cs},i}^2}{m_{\mathrm{Rb}} + m_{\mathrm{Cs}}}}\,, \tag{3.1}$$

where atom j has mass m_j and trap frequency $\nu_{j,i}$ along axis i. As the tweezers are cylindrically symmetric, along the radial axes the trap frequencies of relative motion are equal and we denote them as $\nu_r = \nu_x = \nu_y$. We consider the case where the ratio between ν_r and the axial trap frequency for relative motion ν_z is $\nu_r/\nu_z = 6$.[7] The state energies are obtained by solving a Fermi pseudopotential interaction [244–246], where we make the simplification that the background scattering length $a_{\mathrm{bg}} = 0$.[8]

In the limit $a \to 0$ (i.e. $-1/a \to \pm\infty$), the eigenstates are those of a non-interacting atom pair in a three-dimensional harmonic potential. Relative to the ground state of relative motion, the energies of these states are $h(n_{\mathrm{rel}}^x\nu_r + n_{\mathrm{rel}}^y\nu_r + n_{\mathrm{rel}}^z\nu_z)$, where n_{rel}^i is the number of relative motional quanta along axis i. For the energy range shown in Fig. 3.3(a)(i), the states have $n_{\mathrm{rel}}^x = n_{\mathrm{rel}}^y = 0$. The coloured dashed lines show the energies these states. For finite $-1/a$, the effect of pseudopotential is to couple states with even n_{rel}^z to states where n_{rel}^z differs by ± 2. We plot $-1/a$ in units of $1/\beta_{\mathrm{rel}}^z$, where $\beta_{\mathrm{rel}}^z = (1/2\pi)\sqrt{h/\mu\nu_z}$ is the confinement length for relative motion in the axial direction of the tweezer and $\mu = m_{\mathrm{Rb}}m_{\mathrm{Cs}}/(m_{\mathrm{Rb}} + m_{\mathrm{Cs}})$ is the reduced mass of the atom pair.

The three-dimensional ground state of relative motion (and *only* this state) is coupled to a molecular bound state. The three-dimensional ground state of relative motion is that with $n_{\mathrm{rel}}^x = n_{\mathrm{rel}}^y = n_{\mathrm{rel}}^z = 0$, and is shown as the dotted blue line in Fig. 3.3(a)(i). An atom pair prepared in this state can be converted into a molecule by adiabatically sweeping $-1/a$ to follow the red arrow shown in in Fig. 3.3(a)(i).

We control $-1/a$ by using a magnetic field. Fig. 3.3(b)(i) shows the behaviour of a in the relevant magnetic field range. The effect of a single Feshbach resonance on the scattering length is given by [247]

$$a = a_{\mathrm{bg}}\left(1 - \frac{\Delta}{B - B_0}\right)\,, \tag{3.2}$$

[6] This is true if the trap frequencies for each species are equal. We magnetoassociate atom pairs trapped in 1066 nm tweezers. At this wavelength, the trap frequencies of Cs atoms are approximately a factor of 1.05 larger than those of Rb atoms, so this is a reasonable approximation to make.

[7] Ideally, for an optical tweezer with waist w_0 and wavelength λ, $\nu_r/\nu_z = 2\pi w_0/\lambda$. The mean waist of the 1066 nm tweezers is approximately 1.15 µm, which gives $\nu_r/\nu_z \approx 7$. However, measurements of the trap frequencies give $\nu_r/\nu_z \approx 6$, which we use here. We believe this is lower than the ideal case due to aberrations in the focusing of the tweezers.

[8] A treatment for $a_{\mathrm{bg}} \neq 0$ can be found in Ref. [207].

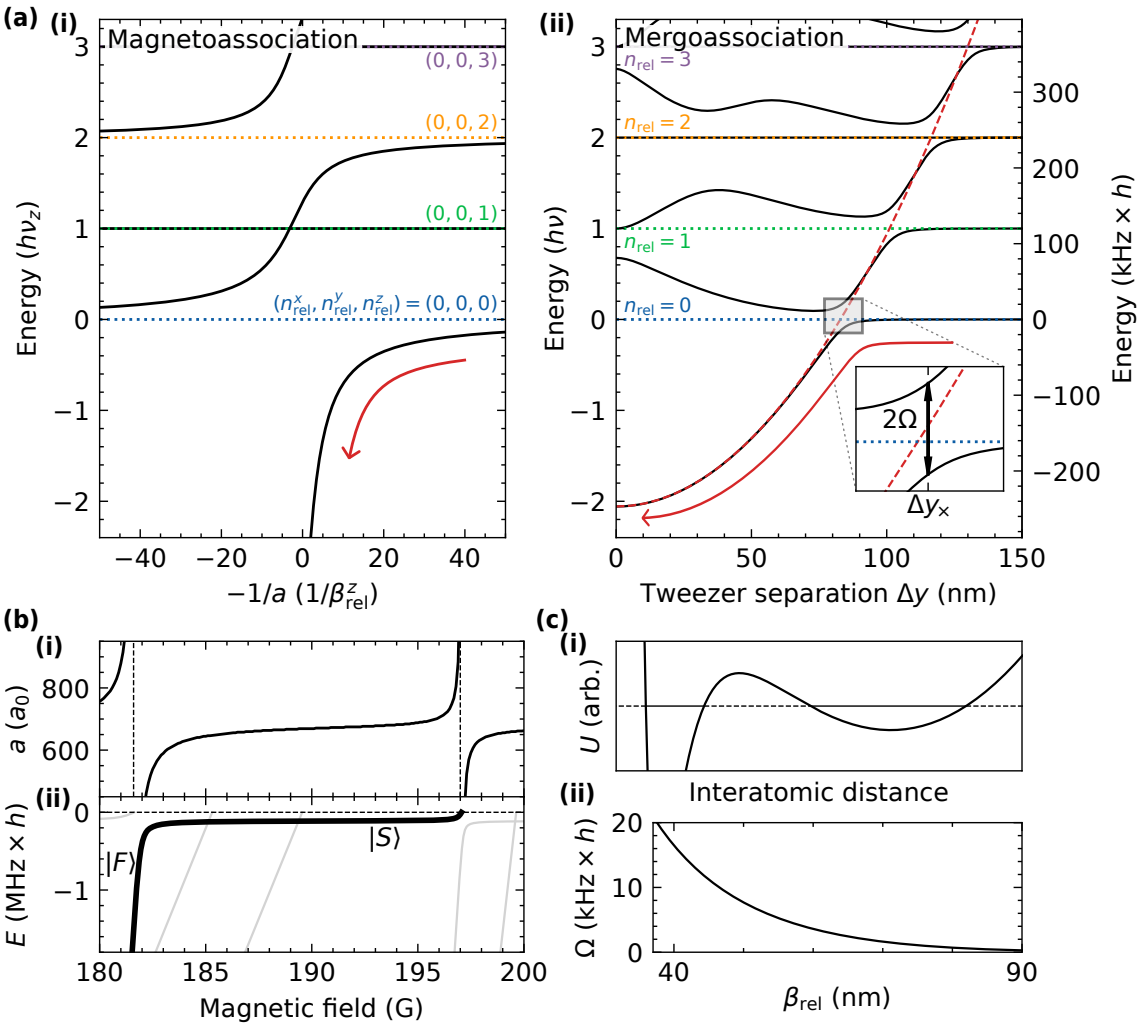

Figure 3.3: Association pathways for forming weakly bound molecules. **(a)** Energy levels used for the assembly of weakly bound molecules. Energies are given relative to the ground state of relative motion (blue dotted lines). Atom pairs in the ground state of relative motion can be associated into molecules by following the red arrows. **(i)** Energy levels used during magnetoassociation. We assume the atom pair is in a cylindrically symmetric tweezer where $\nu_r/\nu_z = 6$. **(ii)** Energy levels used during mergoassociation. We assume the tweezers are spherically symmetric. The red dashed line shows the harmonic trapping experienced by a molecule in the absence of tunnelling. The inset shows a zoom to the avoided crossing used during mergoassociation. **(b)** Properties relevant to magnetoassociation. **(i)** Dependence of the scattering length a on magnetic field for a Rb+Cs atom pair. **(ii)** Energies of molecular states in the Feshbach manifold. The bold line shows the path followed as the magnetic field is adiabatically swept from high to low. **(c)** Properties relevant to mergoassociation. **(i)** Cartoon of the interaction energy as a function of interatomic distance when $\Delta y = \Delta y_\times$. **(ii)** The effective matrix element Ω between the lowest-energy atom-pair and molecular states as a function of β_{rel}.

where Δ is the width of the Feshbach resonance, B_0 is the pole of the resonance, and $a_{\rm bg}$ is the background scattering length far from the resonance. For the Rb+Cs system, $a_{\rm bg} = 645(60)\,a_0 \approx 34.1(3)\,\text{nm}$ [148]. There are two poles in Fig. 3.3(b)(i), resulting from the Feshbach resonance at 197.08(2) G and an additional resonance arising from the state $|F\rangle$ at approximately 182 G.

We magnetoassociate atom pairs into molecules by ramping the magnetic field from ~ 205 G to 181.699 G. During this process, we follow the path in the Feshbach manifold shown by the bold line in Fig. 3.3(b)(ii). First, we cross the Feshbach resonance at 197.08(2) G which has width $\Delta = 90(10)$ mG. The field ramp sweeps $-1/a$ from high to low, crossing $-1/a = 0$ at the pole of the resonance. This converts atom pairs into molecules in the least-bound state $|S\rangle$. The field ramp then continues over the second Feshbach resonance. We traverse the resultant avoided crossing so that the molecules are transferred into the state $|F\rangle$.

We now relax the assumption that the atom pairs are in the ground state of centre-of-mass motion. As the centre-of-mass and relative motions are separable, the centre-of-mass motion causes repeats of the energy levels shown in Fig. 3.3(a)(i), with the energy levels shifted by energy $h(n^x_{\rm com}\widetilde{\nu}_r + n^y_{\rm com}\widetilde{\nu}_r + n^z_{\rm com}\widetilde{\nu}_z)$. Here,

$$\widetilde{\nu}_i = \sqrt{\frac{m_{\rm Rb}\nu^2_{{\rm Rb},i} + m_{\rm Cs}\nu^2_{{\rm Cs},i}}{m_{\rm Rb}+m_{\rm Cs}}} \tag{3.3}$$

is the trap frequency for centre-of-mass motion and $n^i_{\rm com}$ is the number of centre-of-mass motional quanta, both along axis i. Crucially, this means that an atom pair in the ground state of relative motion can be associated into a molecule, regardless of the centre-of-mass motion. The molecule will then inherit the motional state of the centre-of-mass.

A molecule will be formed in the motional ground state if the atom pair was in the ground state of relative motion (so that the molecule could be formed) and in the ground state of centre-of-mass motion (that the molecule inherits). The probability that an atom pair is in the ground state of relative motion along axis i is [248]

$$P(n^i_{\rm rel}=0) = \frac{P(n_{{\rm Rb},i}=0)P(n_{{\rm Cs},i}=0)}{1-\frac{m_{\rm Rb}}{m_{\rm Rb}+m_{\rm Cs}}\frac{\bar{n}_{{\rm Rb},i}}{\bar{n}_{{\rm Rb},i}+1}-\frac{m_{\rm Cs}}{m_{\rm Rb}+m_{\rm Cs}}\frac{\bar{n}_{{\rm Cs},i}}{\bar{n}_{{\rm Cs},i}+1}}\,, \tag{3.4}$$

where $\bar{n}_{j,i}$ is the average number of motional quanta (along axis i) of atom j and $P(n_{j,i}=0) = 1-\bar{n}_{j,i}/(\bar{n}_{j,i}+1)$ is the probability of that atom being in the motional ground state along axis i. The form of $P(n_{j,i}=0)$ assumes that the population of motional levels follows a thermal distribution. The probability of the atom pair being in the three-dimensional ground state of relative motion is

$$P(n^{\rm 3D}_{\rm rel}=0) = P(n^x_{\rm rel}=0)P(n^y_{\rm rel}=0)P(n^z_{\rm rel}=0)\,. \tag{3.5}$$

The probability that a formed molecule occupies the ground state of motion along axis i is [248]

$$P(n^i_{\mathrm{mol}}=0)=1-\frac{m_{\mathrm{Rb}}}{m_{\mathrm{Rb}}+m_{\mathrm{Cs}}}\frac{\bar{n}_{\mathrm{Rb},i}}{\bar{n}_{\mathrm{Rb},i}+1}-\frac{m_{\mathrm{Cs}}}{m_{\mathrm{Rb}}+m_{\mathrm{Cs}}}\frac{\bar{n}_{\mathrm{Cs},i}}{\bar{n}_{\mathrm{Cs},i}+1}\,, \tag{3.6}$$

and probability of that molecule being in the three-dimensional ground state is

$$P(n^{\mathrm{3D}}_{\mathrm{mol}}=0)=P(n^x_{\mathrm{mol}}=0)P(n^y_{\mathrm{mol}}=0)P(n^z_{\mathrm{mol}}=0)\,. \tag{3.7}$$

The avoided crossings traversed when sweeping the magnetic fields can be well described using a Landau-Zener model. The probability of adiabatically traversing the avoided crossing used for association is [145, 248]

$$P_{\mathrm{magneto}}=1-\exp\left(-\frac{2\pi\hbar n_2}{2\mu}\left|\frac{a_{\mathrm{bg}}\Delta}{dB/dt}\right|\right)\,. \tag{3.8}$$

The two parameters that can be controlled experimentally are n_2, the density of an atom pair trapped in a single tweezer, and dB/dt, the rate at which the magnetic field is swept across the resonance. The form of Eq. (3.8) means that we are more likely to form a molecule by magnetoassociation when the pair density n_2 is large or the magnetic field ramp speed dB/dt is small.

3.2.2 Mergoassociation

We have so far neglected coupling of motional states caused by the tightly confining tweezers in our experiment. We are able to safely do this as long as the confinement of the traps is weak enough such that it can be safely ignored. However, confinement-related effects can become significant when the confinement length β_{rel} for relative motion approaches the value of the background scattering length a_{bg}. Effects like elastic [249, 250] and inelastic [251, 252] confinement-induced resonances (CIR) have been observed experimentally in a number of different systems and dimensionalities [253–257]. These confinement-related effects offer new ways to form molecules. Using pairs of fermions in strongly confined in one-dimension, inelastic CIRs have been used to form molecules coherently in an optical trap [258]. In addition, molecules have been formed coherently utilising spin-motion coupling in a strongly focused optical tweezer with large polarisation gradients [259].

In contrast, there has been little experimental investigation of the interactions of two particles in separate optical potentials with tuneable separation [260, 261], despite the existence of theoretical work in this area [262, 263]. Stock *et al.* [262] predicted the existence of avoided crossings between molecular and confined-atom states at critical values of the separation of two optical potentials: so called trap-induced shape resonances. These avoided crossing offers an unexplored path to the

formation of molecules by merging together two optical potentials; a process we refer to as *mergo*association.[9]

Figure 3.3(a)(ii) shows the energies of two atoms in separate but overlapping tweezers as a function of the separation between the tweezers. Each tweezer is assumed to trap only its own atom and the energies are calculated with coupled-channel methods that take the tweezers to be spherically symmetric: the trap frequency for relative motion in all three axes is ν.[10] Nevertheless, we denote the separation between the atoms as Δy to be consistent with the orientation of the experiments that will be discussed in later in this chapter. This calculation is for the Rb+Cs system with $\beta_{\mathrm{rel}} \equiv (1/2\pi)\sqrt{h/\mu\nu} = 40\,\mathrm{nm}$. We assume that there is negligible coupling between relative and centre-of-mass motion and show only energy levels for which the atom pair is in the ground state of centre-of-mass motion. At large separation, the energies of the separately confined atom pairs are almost independent of Δy and, relative to the ground state of relative motion, are given by $h\nu n_{\mathrm{rel}}$ for $n_{\mathrm{rel}} \equiv n^x_{\mathrm{rel}} + n^y_{\mathrm{rel}} + n^z_{\mathrm{rel}}$. However, there can also be a molecular state that is weakly bound at $\Delta y = 0$. For RbCs, this bound state is the state $|S\rangle$. The energy of this state increases quadratically with Δy due to the harmonic tweezer potentials and there is an avoided crossing with the atomic ground state of relative motion at a critical separation $\Delta y_\times$.

The strength of the avoided crossing at $\Delta y_\times$ depends on the height and width of the barrier between the atomic and molecular wells, as shown in Fig. 3.3(c)(i). The avoided crossing is strongest when the bound state is close to threshold, corresponding to a large positive value of a_{bg}, and when β_{rel} is comparable to a_{bg}. The effective matrix element coupling the two states is Ω: this leads to a minimum energy separation at the avoided crossing equal to 2Ω. The value of $\Delta y_\times$ is approximately $\beta_{\mathrm{rel}}\sqrt{3 + \beta^2_{\mathrm{rel}}/a^2_{\mathrm{bg}}}$, so the crossing occurs at larger interatomic separations for weaker confinement. This leads to a reduction in tunneling through the barrier and in the strength of the avoided crossing: Fig. 3.3(c)(ii) shows the dependence of Ω on β_{rel} for the system considered here. We note that the effects of this avoided crossing were not observed in previous demonstrations of molecule formation in lattices [73, 264, 265] and tweezers [248, 259], probably because $a_{\mathrm{bg}} \ll \beta_{\mathrm{rel}}$ for the systems investigated.

Conceptually, the conversion of atom pairs into molecules during mergoassociation is very similar that which occurs during magnetoassociation. The difference is that

[9] A not insignificant amount of effort was spent trying to find a suitable Latin root word for this association technique that does not contain a soft g. However, we couldn't think of one and the hardness of the g when pronouncing mergoassociation is left to the discretion of the reader.

[10] These coupled-channel calculations were performed by Robert C. Bird, C. Ruth Le Sueur, and Jeremy M. Hutson. The details of these calculations are beyond the scope of this thesis; more details can be found in Ref. [201].

the control parameter for mergoassociation is the distance between the two tweezers rather than a magnetic field. As with magnetoassociation, we associate only atom pairs in the ground state of relative motion and are insensitive to the centre-of-mass motion. The molecule inherits the center-of-mass motion of the atom pair, and the probability of a formed molecule occupying the three-dimensional motional ground state is given by Eq. (3.7).

Like magnetoassociation, mergoassociation is described well by a Landau-Zener model, where the probability of traversing the avoided crossing adiabatically is

$$P_{\mathrm{mergo}} = 1 - \exp\left(-\frac{4\pi^2\Omega^2}{h\,|(d_{\mathrm{mol}} - d_{\mathrm{at}})(d\Delta y/dt)_\times|}\right). \tag{3.9}$$

Here, d_{mol} and d_{at} are the gradients of the molecular and atom pair states with respect to Δy at $\Delta y_\times$ in the absence of coupling. To a good approximation, $d_{\mathrm{at}} = 0$ and $d_{\mathrm{mol}} = 4\pi^2\mu\nu^2\Delta y_\times = (h^2\Delta y_\times)/(4\pi^2\mu(\beta_{\mathrm{rel}}^\times)^4)$. The speed at which the avoided crossing is traversed is $(d\Delta y/dt)_\times$ and $\beta_{\mathrm{rel}}^\times$ is the confinement length of relative motion at this moment. Experimentally we can directly control $(d\Delta y/dt)_\times$ (by changing the speed at which we move the tweezers together) or $\beta_{\mathrm{rel}}^\times$ (by changing the intensities of the tweezers). The form of Eq. (3.9) means that we are more likely to form a molecule by mergoassociation when $(d\Delta y/dt)_\times$ is small or the trap confinement is strong (i.e. $\beta_{\mathrm{rel}}^\times$ is small, resulting in small d_{mol} and large Ω).

3.3 Optical spectroscopy

In order to characterise magnetoassociation and mergoassociation, we need a method to detect when a molecule has been formed. Fig. 3.4(a) shows the experimental sequence used to associate, probe, and dissociate molecules. A single Rb atom and a single Cs atom are prepared in species-specific tweezers with a separation of 3.7 µm along the y-axis. Fluorescence imaging of the atoms is performed to determine the trap occupancy; when analysing data we post-select to only consider experimental runs in which both a Rb and Cs were initially loaded. Following this, the atoms are prepared predominantly in the motional ground state and transferred to the hyperfine state $|1,+1\rangle_{\mathrm{Rb}}|3,+3\rangle_{\mathrm{Cs}}$. The traps are merged together at magnetic field B_{merge}. The field is then ramped down to B_{spec}. Atom pairs can either be mergoassociated during the merging step if the tweezer confinement is sufficiently strong or magnetoassociated if the magnetic field ramp crosses a Feshbach resonance and is sufficiently slow. We then apply a spectroscopy pulse of pump light. This light is linearly polarised and drives π transitions from the Feshbach manifold to the excited state $|E\rangle$ (see Fig. 3.1(a), orange arrow) from which the molecule can

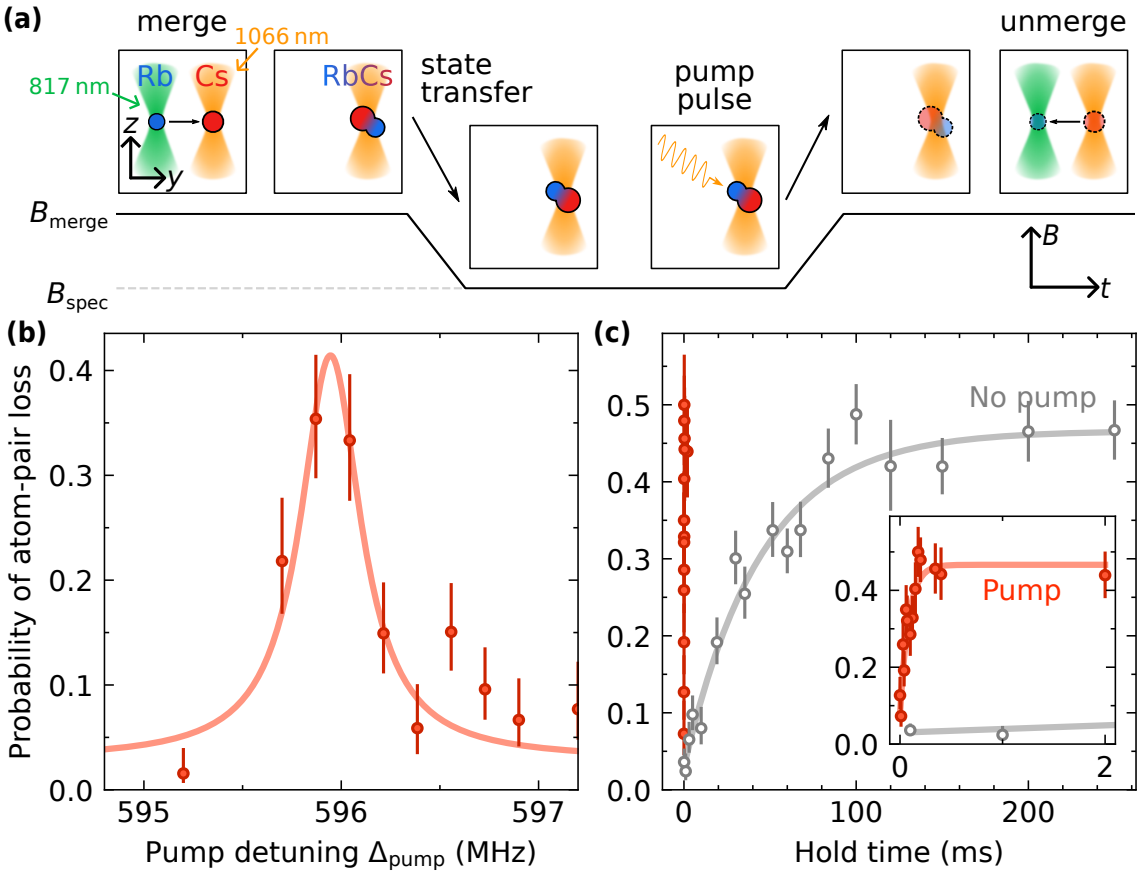

Figure 3.4: Molecule loss caused by driving the pump transition. When the laser frequency is resonant with the transition, molecules are lost from the Feshbach manifold and atom pairs are not recovered after the reversing the association stages of the experimental routine. **(a)** Sequence for molecule formation and detection. **(b)** Lineshape of the pump transition for molecules in the state $|F\rangle$ at magnetic field 181.699(1) G. **(c)** Lifetime measurement of molecules in the state $|F\rangle$ with the resonant pump light at the same intensity as in (b) (red filled points) and without the pump light (grey empty points).

subsequently decay to a number of different states. This pump light is sourced from the 1557 nm laser that is stabilised the ULE cavity as described in Sec. 2.4. The frequency of this light is 192572.11(4) GHz, as measured by a wavemeter[11] with a quoted accuracy of ±0.2 parts per million. Then, the field ramps are reversed and the traps are unmerged. Fluorescence imaging of the atoms is performed to determine the trap occupancy. When the pump light is resonant with a molecular transition, loss to other molecular states results in no atoms being reimaged [149, 150, 240, 266].

Figure 3.4(b) shows an example of molecule loss caused by driving the the pump transition. For this measurement, we merge the tweezers at $B_{\mathrm{merge}} = 205\,\mathrm{G}$. We set the tweezer confinement to be weak; this means that the mergoassociation probability P_{mergo} during the merging step is negligible (see Eq. (3.9)) and the

[11] Bristol Instruments 671A-NIR

merging step prepares a co-trapped atom pair. We then ramp the magnetic field down to $B_{\mathrm{spec}} = 181.699(1)\,\mathrm{G}$. We use a sufficiently slow magnetic field ramp to saturate the magnetoassociation probability P_{magneto} (see Eq. (3.8)). During this field ramp, we follow the state path that is highlighted in Fig. 3.3(b)(ii) to prepare molecules in the state $|F\rangle$. When the light is resonant with the pump transition, the loss of molecules to other states (which causes no atoms to be reimaged at the end of the routine) increases. The detuning Δ_{pump} of the pump light is relative to the cavity mode to which we stabilise it. During the spectroscopy pulse, the molecules are trapped in a 1066 nm tweezer of intensity 12.7(2) $\mathrm{kW/cm^2}$ and the intensity of the pump light is $1.7(2)\,\mathrm{W/cm^2}$. We choose a pulse length such that we avoid saturating the transition: here a pulse time of 150 µs is used.

The data in Fig. 3.4(b) are obtained by repeating the experimental sequence many times in order to measure the average probability of atom-pair loss. In each repeat of the experiment, we attempt to load a single atom pair. We post-select the data to consider only repeats in which this initial loading was successful. The data points show the average probability of losing the atom pair; this probability is calculated from approximately 60 experimental repeats for each value of Δ_{pump}. The vertical bars show the 1σ binomial confidence intervals, calculated using the Jeffreys prior [267–269]. We use this method to calculate the confidence intervals for all experimental probabilities shown in this work and the size of the error bars reflect the number of experimental repeats used for each datapoint.

Figure 3.4(c) shows the timescale on which the pump light causes loss of molecules from the state $|F\rangle$ at 181.699(1) G. The tweezer intensity is the same as for the measurement in Fig. 3.4(b). The red filled points show data obtained when resonant pump light is applied at $1.7(2)\,\mathrm{W/cm^2}$. The $1/e$ lifetime is 80(20) µs. In the absence of pump light, the lifetime of the molecules in the tweezers are limited by scattering of the tweezer light. The grey empty points show data obtained when no pump light is applied: here the extracted $1/e$ time is 45(7) ms. We expect the tweezer-limited lifetimes of all Feshbach states to be of similar magnitude, with the important exception of the state $|S\rangle$, for which we observe no significant loss on the timescale of the experiment. This is consistent with measurements of the same state for isolated molecules in deep optical lattices [270].

We measure binding energies of molecules in the Feshbach manifold by tracking the resonance frequency of the pump transition as a function of B_{spec}. Fig. 3.5 shows these measured binding energies. For this measurement, we form molecules by mergoassociation by increasing the tweezer confinement to saturate P_{mergo} (see Eq. (3.9)). This allows us to access the state $|S\rangle$ at an arbitrary magnetic field B_{merge}. Molecules formed when merging the traps at $B_{\mathrm{merge}} = 205\,\mathrm{G}$ follow the path

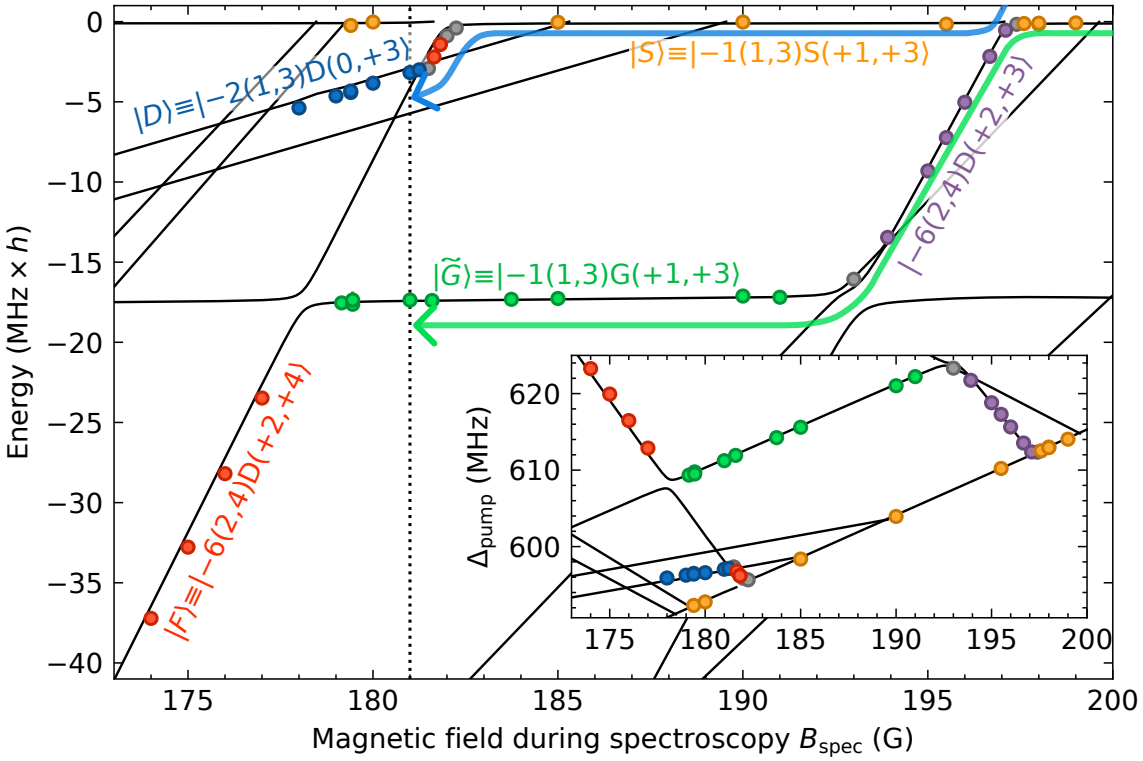

Figure 3.5: Bound-state spectrum of weakly bound RbCs molecules. The main figure shows the energy (relative to threshold) of RbCs molecules measured with optical spectroscopy. Colours and their corresponding labels indicate different molecular states; points in grey indicate measurements in the region of avoided crossings between states. The data points are obtained by fitting the pump lineshape, an example of which is shown in Fig. 3.4(b), at different magnetic fields. The error bars show the 1σ confidence intervals from these fits and are typically smaller than the data points. Solid black lines are the calculated state energies. The inset shows the same data with energies expressed as the laser detuning Δ_{pump} above the cavity mode to which we stabilise the pump laser.

indicated by green arrow when the field is ramped to B_{spec}. Entry into the state $|S\rangle$ by mergoassociation above the Feshbach resonance at 197.08(2) G allows us to approach this resonance from the molecular side and subsequently to occupy states not accessible in magnetoassociation experiments from this starting field [240, 241]. By mergoassociating with B_{merge} below this resonance, but above the resonance at ~ 182 G, we instead follow the path indicated by blue arrow as the field is ramped.

In Fig. 3.5 we group the points by the accessed molecular states. Different molecular states are shown as different colours and points in grey indicate measurements in the region of avoided crossings between states. The solid black lines are the calculated state energies and are the same as shown in Fig 3.1(b). We identify the molecular states that have been populated by comparing the measured and theoretical binding energies. The inset shows Δ_{pump} at which the pump light is resonant with a transition to $|E\rangle$. Different states have different coupling strengths to $|E\rangle$ and we experimentally set the pump power for each state so that the transition

is not saturated. More energy is required to drive the pump transition for states that are more bound. The points in the inset are mapped onto the main plot, where we show the state energies relative to that of the atomic pair state $|1,+1\rangle_{\mathrm{Rb}}|3,+3\rangle_{\mathrm{Cs}}$, by fitting the orange points from the state $|S\rangle$ to the corresponding theoretical energies. The only free parameter in this fit is the magnetic moment of the excited state $|E\rangle$, which we extract as $-0.452(2)\mu_{\mathrm{B}}$.

3.4 Controlling association probabilities

In this section, we investigate how the probabilities of forming molecules from magnetoassociation or mergoassociation can be experimentally controlled. We characterise the two association methods and show that their maximum efficiencies are comparable.

3.4.1 Magnetoassociation

First, we investigate the experimental parameters relevant to the formation of molecules with magnetoassociation. The probability P_{magneto} of traversing the relevant avoided crossing adiabatically, and therefore forming molecules, is given by Eq. (3.8). Experimentally, we can control the density n_2 of the trapped atom pair and the rate dB/dt at which the magnetic field is ramped to traverse the avoided crossing between atomic and molecular states.

In Fig. 3.6 we show the effect of varying dB/dt during the magnetoassociation sweep across the Feshbach resonance at 197.08(2) G. For this measurement, we start with arrays loaded with up to four Rb and four Cs atoms, each in their own tweezer. The initial experimental geometry is shown in Fig. 3.6(a)(i). The array for each species is oriented along the x-axis and the approximate spacing between adjacent traps is 4 µm. The arrays are separated from each other by 3.7 µm along the y-axis. After imaging the atoms to determine the initial trap occupancies, we prepare the atoms predominantly in the motional ground state and the hyperfine state $|1,+1\rangle_{\mathrm{Rb}}|3,+3\rangle_{\mathrm{Cs}}$. The 817 nm tweezers (which contain Rb atoms) are swept along the y-axis to the position of their corresponding 1066 nm tweezers (which contain Cs atoms) and are ramped off. During this merging step, the tweezer confinement is weak (to avoid a significant number of molecules being formed via mergoassociation) and the magnetic field is $B_{\mathrm{merge}} = 205$ G. This prepares up to four individually trapped atom pairs, as shown in Fig. 3.6(a)(ii). After the merging is complete, we ramp the magnetic field over the Feshbach resonance at 197.08(2) G. In the event that magnetoassociation is successful, forms molecules in the state $|S\rangle$.

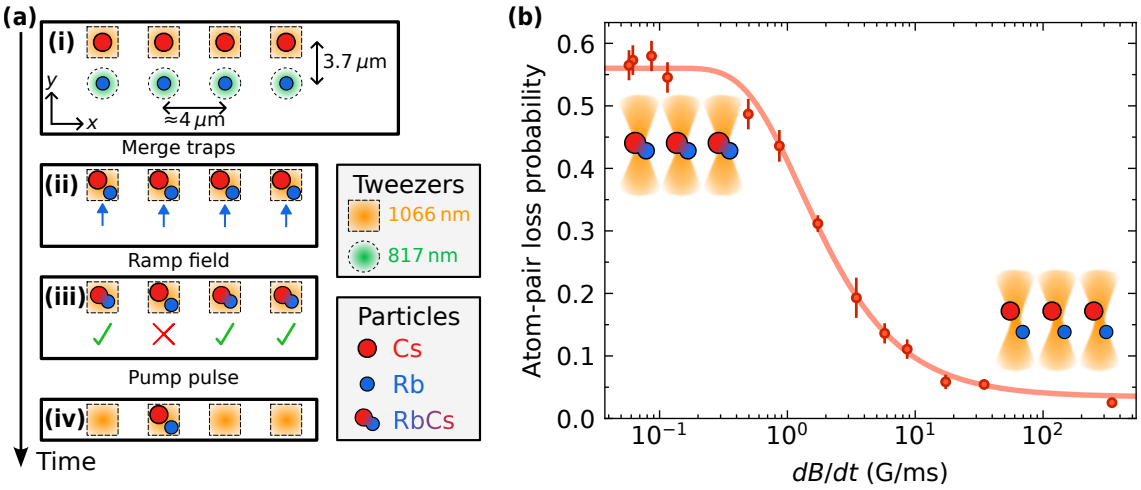

Figure 3.6: Controlling the probability of magnetoassociation. (a) Sequence for molecule formation and detection. We use an array of up to four atom pairs. **(b)** Probability of losing atom pairs as a function of the magnetic field ramp speed dB/dt over the avoided crossing at 197.08(2) G. Molecule loss is induced by subsequently sweeping the magnetic field to 181.699(1) G and applying pump light.

We then continue the magnetic field ramp to 181.699(1) G which transfers molecules to the state $|F\rangle$. For the second part of the field ramp, we always use a ramp speed that is sufficiently slow for the transfer $|S\rangle \rightarrow |F\rangle$ to be adiabatic. Fig. 3.6(a)(iii) shows the system at this point: the 1066 nm tweezers will be occupied by either a Rb+Cs atom pair or, if molecule formation was successful, a molecule in the state $|F\rangle$. We wait for 10 ms to allow the field to stabilise and then apply the pump light at intensity 290(30) W/cm^2 for 1 ms. This intensity is approximately 170 times that used for the measurements in Fig. 3.4, so the light-induced loss of molecules is extremely saturated. Therefore, we expect that all formed molecules to be lost (see Fig. 3.6(a)(iv)). Following this, we reverse the magnetic field ramps with a ramp speed slow enough that any remaining molecules would be adiabatically converted back to atom pairs and separate and reimage the atom pairs.

Figure 3.6(b) shows the probability of atom pair loss using this routine. We vary the magnetic field ramp speed dB/dt during the magnetoassociation sweep across the Feshbach resonance at 197.08(2) G. At high dB/dt, the avoided crossing between the atomic and molecular states is traversed diabatically and molecules are not formed. The pump light then has no effect and atom pairs are recovered at the end of the sequence in 97(1)% of experimental runs. Here the background loss of 3(1)% is from atom pairs that occupy an excited hyperfine state. The infidelity in the initial preparation of each species in the correct hyperfine state is approximately 1% prior to merging. However, significant Raman scattering of Rb caused by the 817 nm tweezer during the merging process means that atom pairs in the correct

hyperfine state are prepared in 93(2)% of runs. The remaining 7(2)% of atom pairs are prepared in excited hyperfine states and can be lost due to inelastic collisions following merging [271]. For this measurement, the length of the experimental sequence before unmerging is not sufficient to saturate this collisional loss. This results in 3(1)% of atom pairs being loss. When a slower magnetic field ramp is used, we adiabatically transfer first to the state $|S\rangle$ then to the state $|F\rangle$ and molecules are lost once the pump light is applied.

The solid line in Fig. 3.6(b) shows the result of fitting a Landau-Zener model to the data. The probability of traversing the avoided crossing adiabatically is given by P_{magneto} (see Eq. (3.8)). We scale P_{magneto} to match the experimental contrast in the atom-pair loss and add a small offset to account for the experimental background. Accordingly, the free parameters in our model are the atom-pair density n_2 and the probability of atom-pair loss in the limits of large and small dB/dt. From this model we extract $n_2 = 1.7(1) \times 10^{13}\,\text{cm}^{-3}$. When dB/dt is large enough to make the adiabatic conversion probability negligible, the probability of atom-pair loss is equal to the background loss value of 3(1)%. As dB/dt is decreased, corresponding to a more adiabatic ramp, the observed atom-pair loss is the sum of the background loss and the loss of formed molecules. In the small dB/dt limit, P_{magneto} saturates and we fit the atom-pair loss to be 56(1)%, corresponding to a molecule formation efficiency of 53(1)%.

The efficiency of molecule formation is primarily limited by the efficiency with which we can prepare atom pairs in the ground state of relative motion prior to magnetoassociation. We measure the ground-state occupation of the traps with sideband thermometry [272]. Heating caused during the merging of the traps is measured by performing thermometry either before or after the traps are merged and unmerged. We estimate the motional energy at the point of association by assuming uniform heating during the merging and unmerging routines and using the mean energy of these two measurements. At the point of association, we estimate that the mean number of motional quanta along each confining axis is $\left\{\bar{n}_x^{\text{Rb}}, \bar{n}_y^{\text{Rb}}, \bar{n}_z^{\text{Rb}}\right\} = \{0.35(3), 0.08(6), 0.27(6)\}$ for Rb and $\left\{\bar{n}_x^{\text{Cs}}, \bar{n}_y^{\text{Cs}}, \bar{n}_z^{\text{Cs}}\right\} = \{0.10(6), 0.20(14), 0.29(10)\}$ for Cs. Using Eq. (3.5), we estimate that the probability of the atom pair occupying the three-dimensional ground state of relative motion is 56(4)%. Magnetoassociation requires atom pairs in the ground hyperfine state *and* the ground state of relative motion. The probabilities for preparing atom pairs in these states are 93(2)% and 56(4)%, respectively. Therefore, for sufficiently slow magnetic field ramps, we expect to convert an atom pair to a molecule in 52(4)% of experimental runs, which is in excellent agreement with the fitted conversion efficiency. Using Eq. (3.7), we predict that 58(6)% of formed molecules will be in the three-dimensional motional ground

state.

The value of the atom-pair density that we extract from the fit is approximately that which we independently estimate from the parameters of the traps used for this routine. The atom-pair density is [273]

$$n_2 = \int_{-\infty}^{+\infty}\int_{-\infty}^{+\infty}\int_{-\infty}^{+\infty} n_{\mathrm{Rb}}(x,y,z)\, n_{\mathrm{Cs}}(x,y,z)\, dx\, dy\, dz\,, \tag{3.10}$$

where n_j is the probability density of atom j. For simplicity, we consider all atoms to be in the motional ground state. Then, [274]

$$n_j(x,y,z) = \prod_{i=x,y,z} \left| \left(\frac{4\pi m_i \nu_{j,i}}{h}\right)^{1/4} \exp\left(\frac{-2\pi^2 m_i \nu_{j,i}}{h} i^2\right)\right|^2 . \tag{3.11}$$

For this measurement, the trap frequencies after the atom pairs have been prepared in the 1066 nm tweezers are $\{\nu_{\mathrm{Rb},x}, \nu_{\mathrm{Rb},y}, \nu_{\mathrm{Rb},z}\} = \{8.5(1), 9.3(1), 1.67(3)\}$ kHz for Rb and $\{\nu_{\mathrm{Cs},x}, \nu_{\mathrm{Cs},y}, \nu_{\mathrm{Cs},z}\} \approx 1.05 \times \{\nu_{\mathrm{Rb},x}, \nu_{\mathrm{Rb},y}, \nu_{\mathrm{Rb},z}\}$ for Cs. From this, we obtain $n_2 \sim 2.5 \times 10^{13}/\mathrm{cm}^3$ which is within a factor of two of the fitted value.

For the rest of this work, we use sufficiently small dB/dt to saturate P_{magneto} such that we expect that over 99% of atom pairs in the correct states are transferred adiabatically to the molecular state $|F\rangle$ when performing magnetoassociation field ramps.

3.4.2 Mergoassociation

We now investigate how the probability of mergoassociation can be controlled. The probability P_{mergo} of traversing the relevant avoided crossing adiabatically, and therefore forming molecules, is given by Eq. (3.9). Experimentally, we can directly control the speed $(d\Delta y/dt)_\times$ at which the avoided crossing is traversed (by changing the speed at which we move the tweezers together) and the confinement length for relative motion $\beta_{\mathrm{rel}}^\times$ as the avoided crossing is traversed (by changing the intensities of the tweezers).

As the formation of ultracold molecules by mergoassociation has not previously been studied, we choose to use an experimental sequence that will allow us to compare the relative efficiencies of mergoassociation and magnetoassociation. We expect the maximum efficiency of both association methods to be set by the efficiency of the atom-pair state preparation. The initial experimental geometry is like that shown in Fig 3.6(a)(i), but here we only use a single trap for each species. The atoms are loaded into species-specific tweezers spaced by 3.7 µm along the y-axis, imaged, then prepared in the hyperfine and motional ground states. We sweep the Rb trap to overlap with the Cs trap in 2.7 ms, and then ramp off the intensity of the Rb trap in

10 ms. During this merging procedure the magnetic field is $B_{\text{merge}} = 205\,\text{G}$. If the trap confinement is strong enough, atom pairs will be mergoassociated into a molecule during the merging procedure. Following this, the magnetic field is jumped down to 199 G and then ramped down to 196.8 G in 3 ms; this final step magnetoassociates any remaining atom pairs in the ground state of relative motion. The magnetic field is then ramped to $B_{\text{spec}} = 181\,\text{G}$ in 3 ms where it is held for 4 ms during which a 2 ms pulse of pump light is applied. The association routine is then reversed to dissociate any remaining molecules, the traps are separated, and the atoms reimaged.

For the purposes of this investigation, we utilise the difference in the binding energies of molecules formed by mergoassociation or magnetoassociation to tell them apart. With this routine, molecules formed by mergoassociation will enter the state $|S\rangle$ at $B_{\text{merge}} = 205$ G, then follow the path indicated by green arrow in Fig. 3.5 as the field is ramped to B_{spec} (black dotted line). The molecule will occupy the state $|\widetilde{G}\rangle \equiv |-1(1,3)\text{G}(+1,+3)\rangle$ at B_{spec}, of which the binding energy is approximately $18\,\text{MHz} \times h$. In contrast, if an atom pair in the ground state of relative motion is not converted into a molecule via mergoassociation, it will be converted into a molecule via magnetoassociation when the field is swept across the Feshbach resonance at 197.08(2) G. This molecule will follow the path indicated by the blue arrow in Fig. 3.5 and will occupy the state $|D\rangle \equiv |-2(1,3)\text{D}(0,+3)\rangle$ at B_{spec}. The binding energy of $|D\rangle$ is approximately $3\,\text{MHz} \times h$. Therefore, the frequency of the pump light at which we observe light-induced loss distinguishes between molecules formed by these two methods. These two states were chosen for the comparison between mergoassociation and magnetoassociation because they posses similar transition strengths to $|E\rangle$. The panels in Fig. 3.7(a)(i)-(iii) show pump spectra for strong, intermediate, and weak confinement during merging. For these measurements, we set the pump power to avoid saturating the transitions. For strong confinement, we observe high occupation of the state $|\widetilde{G}\rangle$ as the majority of atom pairs in the ground state of relative motion are mergoassociated. As the confinement is reduced, fewer atom pairs are mergoassociated, resulting in high occupation of the state $|D\rangle$.

Figure 3.7(b) shows the probability of molecule loss caused by the pump light as a function of $\beta_{\text{rel}}^{\times}$ during merging of the traps. We use the pump intensity $290(30)\,\text{W/cm}^2$ to heavily saturate the light-induced loss of molecules. Green filled points show loss when the pump frequency is set to be resonant with the transition $|\widetilde{G}\rangle \rightarrow |E\rangle$ which causes loss of molecules formed by mergoassociation. Blue empty points show the light-induced loss of molecules formed by magnetoassociation by driving the transition $|D\rangle \rightarrow |E\rangle$. We emphasise that P_{magneto} is saturated for all points shown, but less atom pairs are converted into molecules via magnetoassociation when P_{mergo} is large, as they have already been mergoassociated. We clearly observe

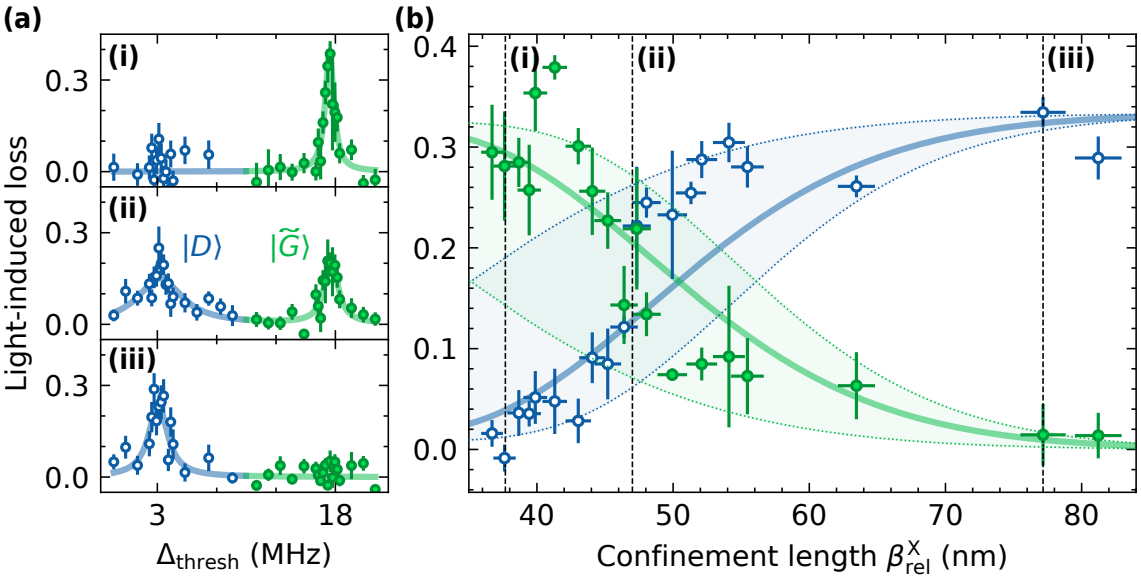

Figure 3.7: Controlling the probability of mergoassociation. (a) Spectroscopic identification of molecules formed by mergoassociation (green filled points) and magnetoassociation (blue empty points) for confinement lengths $\beta^{\times}_{\text{rel}}$ of (i) 37.7(8) nm, (ii) 47(1) nm, and (iii) 77(2) nm. Light-induced loss is measured as a function of the detuning Δ_{thresh} from the transition between the atomic threshold and $|E\rangle$ at 181 G. (b) The probability of light-induced loss of molecules formed by mergoassociation (green filled points) and magnetoassociation (blue empty points) as a function of $\beta^{\times}_{\text{rel}}$. Each data point is measured with approximately 450 experimental repeats. The theory curves show the calculated Landau-Zener probabilities scaled to match the light-induced loss. The shaded regions indicate the experimental uncertainty in the merging speed.

a change in the probability of mergoassociation from high to low as the confinement is reduced (i.e. $\beta^{\times}_{\text{rel}}$ is increased). The similarity in the peak probabilities of the mergoassociation and magnetoassociation data points indicates that the efficiency of the two techniques is similar. The dashed lines in Fig. 3.7(b) correspond to the values of $\beta^{\times}_{\text{rel}}$ used for the spectroscopy presented in Fig. 3.7(a).

The control parameter used in mergaossociation is the separation between the two atoms. Therefore, to model the system studied in Fig. 3.7(b), we must consider the merging procedure in detail. The merging procedure has two distinct stages. First, the 817 nm tweezer (which contains Rb) is swept along the y-axis to the position of the 1066 nm tweezer (which contains Cs). For this sweep, we use a hybrid-jerk trajectory $y(t)$ which is defined as [275]

$$y(t) - y_0 = \begin{cases} y_{\text{mj}}(t, 2\Delta\widetilde{y}, 2\Delta t) & \text{for } 0 \leq t \leq \Delta t\,, \\ \frac{15}{4}\frac{\Delta\widetilde{y}}{2\Delta t} & \text{for } \Delta t \leq t \leq T_{\text{s}} - \Delta t\,, \\ y_{\text{mj}}(t - T_{\text{s}} + 2\Delta t, 2\Delta\widetilde{y}, 2\Delta t) + \alpha T_{\text{s}}\frac{15}{4}\frac{\Delta\widetilde{y}}{2\Delta t} & \text{for } T_{\text{s}} - \Delta t \leq t \leq T_{\text{s}}\,, \end{cases} \tag{3.12}$$

where the minimum-jerk trajectory [275]

$$y_{\mathrm{mj}}(t,d,T) = d\left[10\left(\frac{t}{T}\right)^3 - 15\left(\frac{t}{T}\right)^4 + 6\left(\frac{t}{T}\right)^5\right]. \tag{3.13}$$

The hybrid-jerk trajectory has minimum jerk at the start and end, and a linear trajectory in the middle. The hybridicity α is the fraction of the trajectory that is linear motion (i.e. $\alpha = 1$ is a linear sweep, and $\alpha = 0$ is a minimum-jerk trajectory). y_0 is the starting position of the tweezer, $y_0 + \Delta y$ is end position, and T_s is the time taken to perform the sweep. $\Delta\widetilde{y} = \Delta y/\left[2 + (15/4)\alpha/(1-\alpha)\right]$ and $\Delta t = T_\mathrm{s}(1-\alpha)/2$ are the distance covered and time elapsed, respectively, during each minimum-jerk portion. We use the hybrid-jerk trajectory to strike a balance between heating caused by a sharp change in the acceleration of the atom (favouring the minimum-jerk trajectory) and technical heating caused by resonances in the AOD with which we control the tweezer position (favouring a linear trajectory of constant velocity) [205, 207, 275]. Second, after the Rb tweezer has reached the end point of the sweep, we ramp its intensity to zero with the profile

$$I(t) = I_0\frac{k^{(1-t/T_\mathrm{r})} - 1}{k-1}. \tag{3.14}$$

Here k is the index of the ramp, T_r is the ramp duration, and I_0 is the intensity of the tweezer used during the sweep. We choose to use $k = 20$: this creates an intensity profile that is qualitatively similar to an exponential ramp with $1/e$ time $\sim T_\mathrm{r}/3.5$, but switches the trap completely off in finite time T_r.

We set the merging parameters experimentally to minimise heating of the atoms [205, 207]. For the trap sweep, we use $\Delta y = 3.7\,\mu\mathrm{m}$, $T_\mathrm{s} = 2.7\,\mathrm{ms}$ and $\alpha = 0.95$. We aim to end with the 817 nm perfectly overlapped with the 1066 nm tweezer. During the trap sweep, the ratio between the intensities of the 1066 nm and 817 nm tweezers is $I_{1066}/I_{817} = 5.2(1)$. For the intensity ramp, we use $T_\mathrm{r} = 10\,\mathrm{ms}$. Fig. 3.8(a) shows the position y_{817} of the 817 nm tweezer and Fig. 3.8(b) shows I_{817}/I_{1066} during the merging procedure.

Each data point in Fig 3.7(b) is assigned a value of $\beta^{\times}_{\mathrm{rel}}$ by performing numerical simulations of the tweezer merging procedure. The combined potential experienced by the atoms during this merging routine is simulated. Taking into account the effect of both tweezers on each atom is particularly important as the tweezers become overlapped. We calculate the trajectory of the atoms and, by fitting quadratic functions to the potential minima, the trap frequencies along the y-axis experienced by Rb and Cs. Here, we denote these trap frequencies as ν_{Rb} and ν_{Cs} respectively.[12]

[12] Our model only considers the atomic separation and confinement along the merging axis.

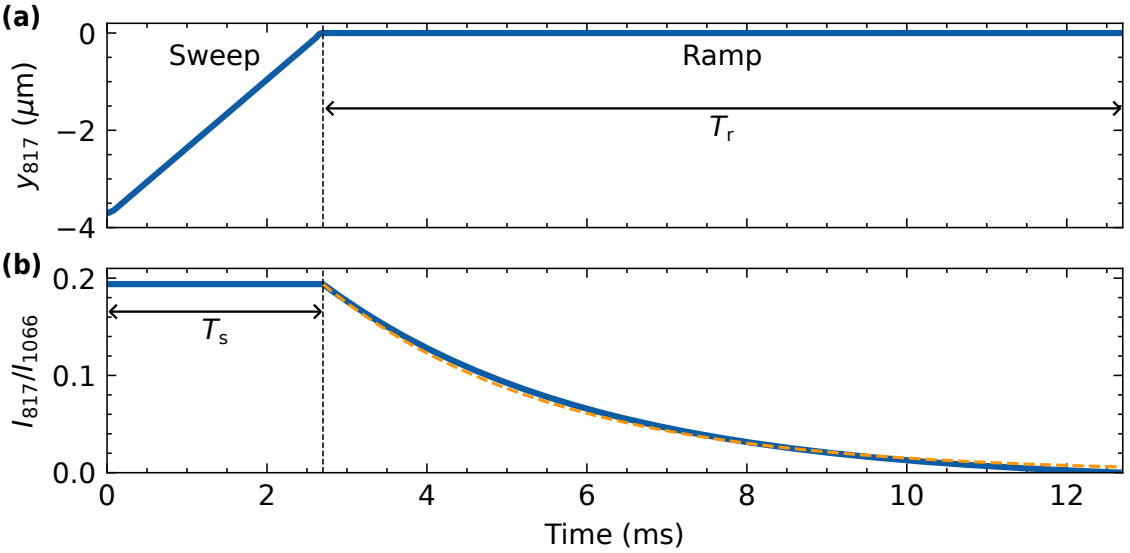

Figure 3.8: Trajectory of the 817 nm tweezer during the trap merging procedure. First, the 817 nm is swept to overlap with the 1066 nm tweezer at the origin in $T_s = 2.7$ ms. Then the trap ramps off in $T_r = 10$ ms. We show **(a)** the position y_{817} of the 817 nm tweezer and **(b)** the ratio I_{817}/I_{1066} between the intensities of the 817 nm and 1066 nm tweezers. The dashed orange line during the ramping step shows, for comparison, an exponential ramp with time constant $T_r/3.5$.

From these, we obtain the trap frequency for relative motion ν (see Eq. (3.1)) and β_{rel} as functions of time. For these simulations, we take the tweezers to be perfectly overlapped at the end of the sweep by placing the 1066 nm tweezer at the origin and setting the start point of the 817 nm tweezer at $y_0 = -3.7\,\mu$m. We assume that the tweezers remain overlapped in the x- and z-axes at all times during the merge. This means that the mergoassociation avoided crossing is traversed during the sweep part of the merging procedure. The separation between the *atoms* is $\Delta y = |y_{\mathrm{Rb}} - y_{\mathrm{Cs}}|$, where y_j is the position of atom j. We take the avoided crossing to occur when $\Delta y = \beta_{\mathrm{rel}}\sqrt{3 + \beta_{\mathrm{rel}}^2/a_{\mathrm{bg}}^2}$; this occurs at time $t_\times$ with atomic separation $\Delta y_\times$ and confinement length $\beta_{\mathrm{rel}}^\times$.[13] The results of this simulation for trap depths corresponding to $\beta_{\mathrm{rel}}^\times = 37.7$ nm are shown in Fig. 3.9. We note that as the tweezers become overlapped (see Fig. 3.9(a), inset), the Cs atom is strongly repelled by the 817 nm tweezer so the atomic separation Δy is larger than the separation between the *tweezers* Δy_{t}. The separation between the tweezer centres at the avoided crossing

In our experimental realisation, the merging axis is the y-axis. To avoid a string of sub- and superscripts, for the rest of this section, we drop subscripts y for these trap frequencies that were included in earlier sections.

[13] This is a semi-classical simulation: we assume that the atoms follow classical trajectories and then calculate their separations and trap frequencies to use for Eq. (3.9). This is valid because we are in the regime $|d\beta_{\mathrm{rel}}/d\Delta y| \ll 1$ (i.e. the potential energies of the particles vary slowly), so a fully quantum simulation is not required. This is analogous to the validity condition for the Wentzel-Kramers-Brillouin semi-classical approximation [276].

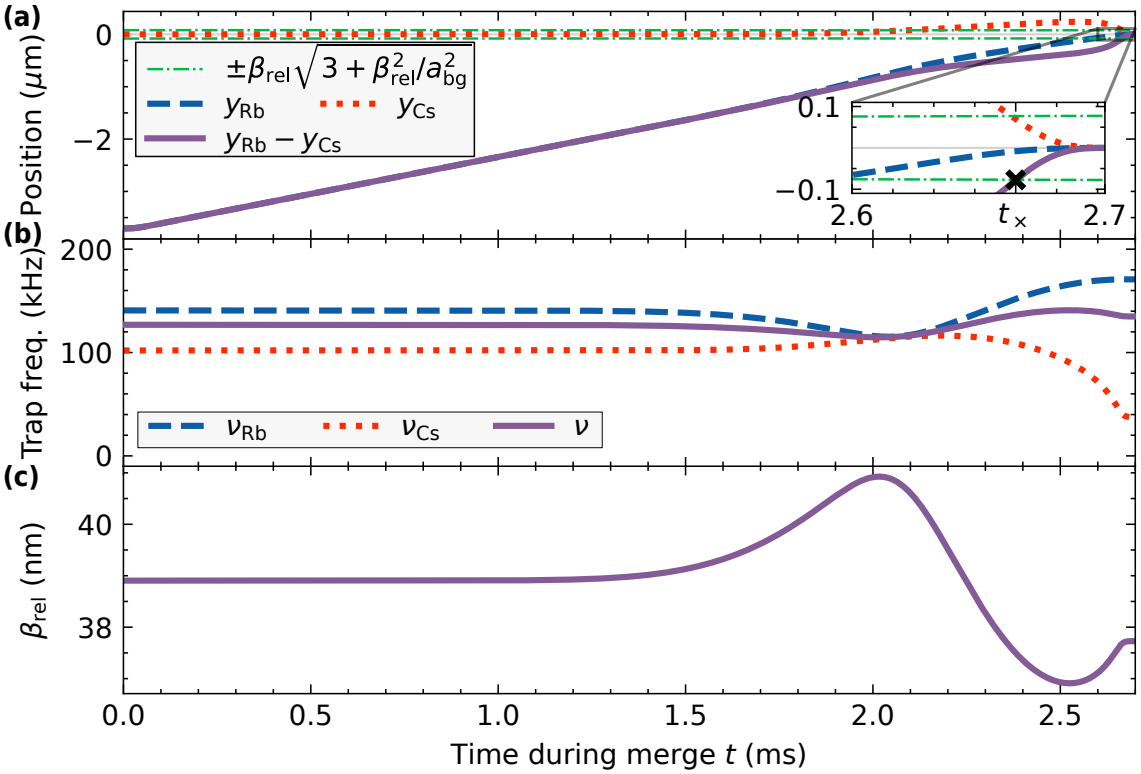

Figure 3.9: Numerical simulations of the trap merging routine. We show results for the merging routine for trap depths corresponding to $\beta_{\mathrm{rel}}^{\times} = 37.7$ nm, finishing with perfectly overlapped tweezers. **(a)** The position of the potential minima along the merging axis for the Rb atom, y_{Rb}, and the Cs atom, y_{Cs} and their difference. **(b)** The atomic trap frequencies and the frequency for relative motion. **(c)** The harmonic length for relative motion, β_{rel}.

is denoted as $\Delta y_{\mathrm{t}}^{\times}$.

The critical separation at which we traverse the avoided crossing is typically around $\Delta y_{\times} \sim 100\,\mathrm{nm}$. This is near the end of the merging routine, where small deviations in the trajectory significantly affect the speed $(d\Delta y/dt)_{\times}$ at which the avoided crossing is traversed. These deviations are caused by small fluctuations δ in the position of the 817 nm tweezer relative to the 1066 nm tweezer between experimental shots. δ is much less than the waists of the tweezers, so we always form either a co-trapped atom pair or a molecule in the 1066 nm tweezer at the end of the merging procedure. However, the dynamics of how the atoms come together depend significantly on the value of δ. We simulate these by offsetting the 817 nm tweezer by δ throughout the merging routine. After the sweep stage of the merging procedure, 817 nm tweezer is at $y = \delta$ so that the separation between the centre of the tweezers is δ. We find that three distinct regimes can exist depending on the value of δ. These regimes are illustrated in Fig. 3.10(a) and are:

Regime (i) $|\delta| \leq \delta_{\mathrm{c}}$. Here δ_{c} is a critical final separation and for $|\delta| \leq \delta_{\mathrm{c}}$ the tweezers are sufficiently overlapped for the avoided crossing to be traversed

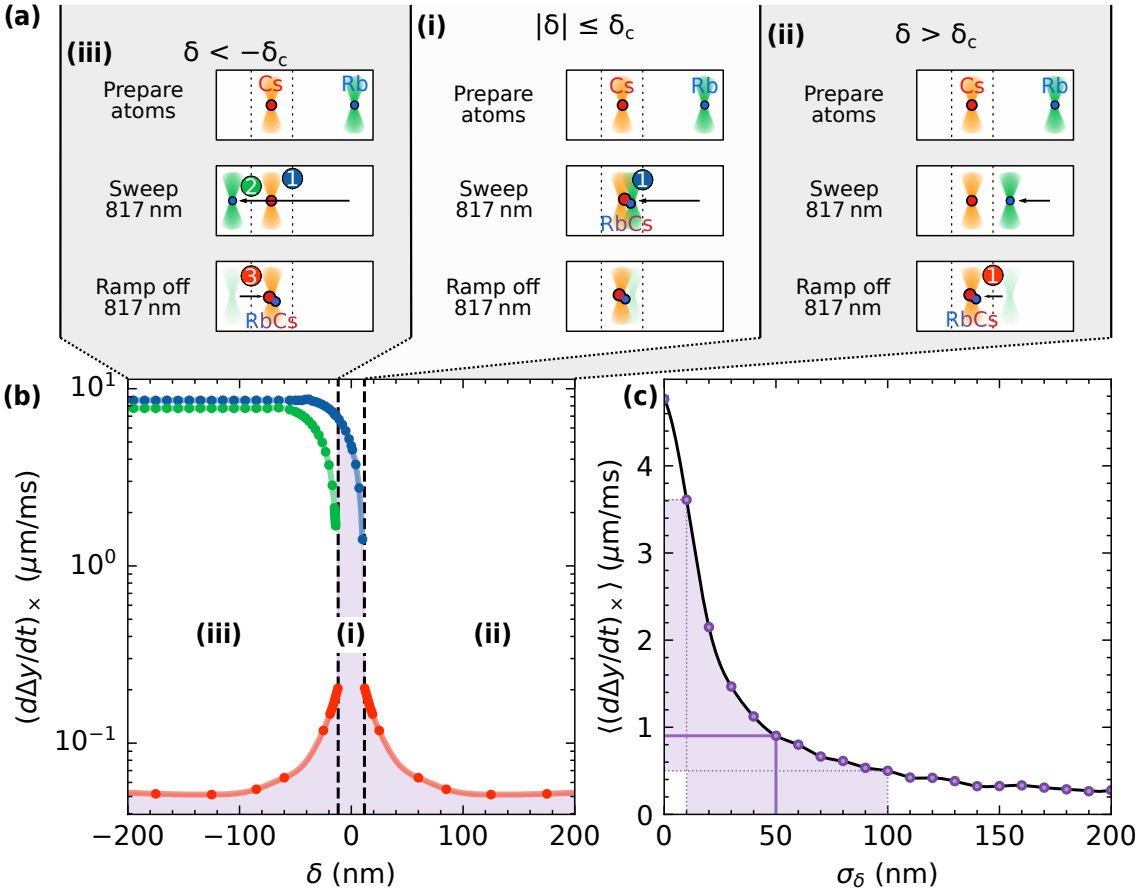

Figure 3.10: Effect of tweezer misalignments on the mergoassociation crossing speed. **(a)** Diagram of the merging procedure. The vertical dashed lines denote the critical positions of the 817 nm tweezer $\pm\delta_c$ at which the avoided crossing is traversed. We illustrate the three regimes as described in the text. The numbers indicate the number of times the avoided crossing is traversed. Blue and green points indicate traversal during the sweep stage, red points indicate traversal during the ramp stage. **(b)** Effect of δ on the speed $(d\Delta y/dt)_\times$ at which the avoided crossing is traversed. The vertical dashed lines show $\pm\delta_c$. The colours are as in (a). The purple shaded region shows the distribution of merging speeds from which we sample to obtain the mean. **(c)** The mean speed $\langle(d\Delta y/dt)_\times\rangle$ at which the avoided crossing is traversed as a function of the standard deviation of tweezer misalignments σ_δ. We obtain this distribution by sampling from the purple distribution in (b). The shaded region shows the range of $\langle(d\Delta y/dt)_\times\rangle$ used in Fig. 3.7.

during the sweep part of the merging procedure. For our merging parameters, we find that $\delta_c \approx 14$ nm. This crossing is shown in Fig. 3.10 in blue.

Regime (ii) $\delta > \delta_c$. The tweezers do not come sufficiently close for the avoided crossing to be traversed during the sweep stage, and it is traversed instead as the 817 nm tweezer is ramped off. This crossing is shown in Fig. 3.10 in red. The average crossing speed $(d\Delta y/dt)_\times$ is much slower than that in regime (i) because the atomic separation typically changes by ~ 100 nm in a few milliseconds.

Regime (iii) $\delta < -\delta_c$. Here the avoided crossing is traversed *three* times. The first crossing is as in regime (i). Then, as the 817 nm tweezer 'overshoots' the 1066 nm tweezer, the crossing is traversed *in the opposite direction*. This crossing is shown in Fig. 3.10 in green. A final crossing is made as in regime (ii) when the 817 nm tweezer ramps off. $(d\Delta y/dt)_\times$ is similar for the first and second crossing, so here we assume that they are either both diabatic (so the atom pair remains as an atom pair) or adiabatic (so the atom pair is mergoassociated into a molecule, which is then dissociated) such that only the speed of the third crossing is critical.

The speeds $(d\Delta y/dt)_\times$ during these traversals of the avoided crossing are shown in Fig. 3.10(b). The purple shaded region shows the distribution of $(d\Delta y/dt)_\times$ at the critical crossing (i.e. the only crossing for regimes (i) and (ii), and the final crossing for regime (iii)).

We account for variations in δ by performing Monte Carlo simulations where δ is sampled from a Gaussian distribution with mean equal to zero and standard deviation σ_δ. For each iteration of a simulation, we take a value of δ and find the corresponding speed $(d\Delta y/dt)_\times$ from the purple shaded distribution in Fig. 3.10(b). Fig. 3.10(c) shows the mean speed $\langle (d\Delta y/dt)_\times \rangle$ as a function of σ_δ, which we obtain by repeating the simulation many times with different values of δ_c.

We independently measure the relative tweezer drift with two methods. First, we fit images of the atomic fluorescence obtained during the experimental runs. We fit the atomic centres and use these to estimate the fluctuations in tweezer position. Second, we use a routine which ejects Cs atoms trapped in the 1066 nm tweezer by overlapping a 817 nm tweezer with this trap. The 817 nm tweezers are antitrapping for the Cs atoms (see Table 2.1) so they eject the atoms. By measuring the position of maximum loss over time, we can track the tweezer overlap with a precision of ~ 10 nm [271]. From these measurements, we observe that the drift is correlated with the change in humidity of the lab (roughly 10 nm per percentage point). The humidity changes significantly during a single air-conditioning cycle which typically lasts 20 mins. The standard deviation in the tweezer drifts is approximately $\sigma_\delta = 50^{+50}_{-40}$ nm. This results in the range of speeds $\langle (d\Delta y/dt)_\times \rangle = 0.9^{+2.7}_{-0.4}$ µm/ms, as highlighted by the shaded region in Fig. 3.10(c). We note that this analysis predicts a most likely speed similar to a much simpler analysis assuming a constant speed throughout the merging process 3.7 µm/2.7 ms $\approx$ 1.4 µm/ms.

The green solid line in Fig. 3.7(b) shows the expected probability P_{mergo} of forming a molecule via mergoassociation for our experimental parameters (calculated with Eq. (3.9)), scaled to the contrast of the experimental data. The shaded region shows

the uncertainty in P_{mergo} arising from the uncertainty in $\langle (d\Delta y/dt)_\times \rangle$. The blue solid line shows the expected probability $1 - P_{\text{mergo}}$ of a molecule not being formed by mergoassociation. A molecule is then formed by magnetoassociation over the Feshbach resonance at 197.08(2) G. Again, the contrast has been scaled to that of the experimental data and the shaded region shows the uncertainty resulting from the uncertainty in the crossing speed. The experimental results are in good agreement with our theoretical model, with the observed crossover point in $\beta_{\text{rel}}^{\times}$ within 10% of the theoretical prediction. This agreement was surprisingly good in view of the approximations made in the theoretical model as described here, particularly the assumption that the tweezers are spherically symmetric. In reality, our tweezers have an aspect ratio of 2:5 between the confinement lengths along the radial and axial directions. Recent theoretical work by Bird *et al.* [277] extends the model described here to non-spherical traps. This work shows that the agreement here is a coincidence: this aspect ratio happens to give similar results to spherical traps. Of course, this means that using the extended model with the correct aspect ratio would give similar results that agree well the experimental data presented here.

3.5 Microwave spectroscopy

An exciting prospect for mergoassociation its potential to be used for associating atoms in systems that do not possess Feshbach resonances suitable for magnetoassociation [278]. To this end, we use mergoassociation to form molecules at low magnetic fields, far from any Feshbach resonances, and without any magnetic field ramps. Mergoassociation is still possible in this regime, because it relies only on the presence of a bound state near threshold, which for RbCs exists over a large range of magnetic field.

We perform microwave spectroscopy to verify molecule formation at these low fields. The experimental sequence is similar to the one described earlier, but the magnetic field is held constant at the field applied during the cooling of the atoms, $B = 4.78\,\text{G}$, for the entirety of the molecule formation and detection portion of the sequence. A microwave pulse of frequency $\sim 6.84\,\text{GHz}$ is applied for $89\,\mu\text{s}$ in place of the pulse of pump light. This pulse length approximates a π pulse for a Rb atom on the hyperfine transition $|1, +1\rangle \rightarrow |2, +2\rangle$ and for a RbCs molecule on the transition $|S\rangle \rightarrow |S'\rangle$, where the state $|S'\rangle \equiv |-1(2, 3)\text{S}(+2, +3)\rangle$. Following the unmerging of the traps, state-sensitive detection is performed by using the pushout light to eject any Rb atoms in the state $|f = 2\rangle$ and any Cs atoms in the state $|f = 4\rangle$ prior to imaging (see Sec. 2.3.3).

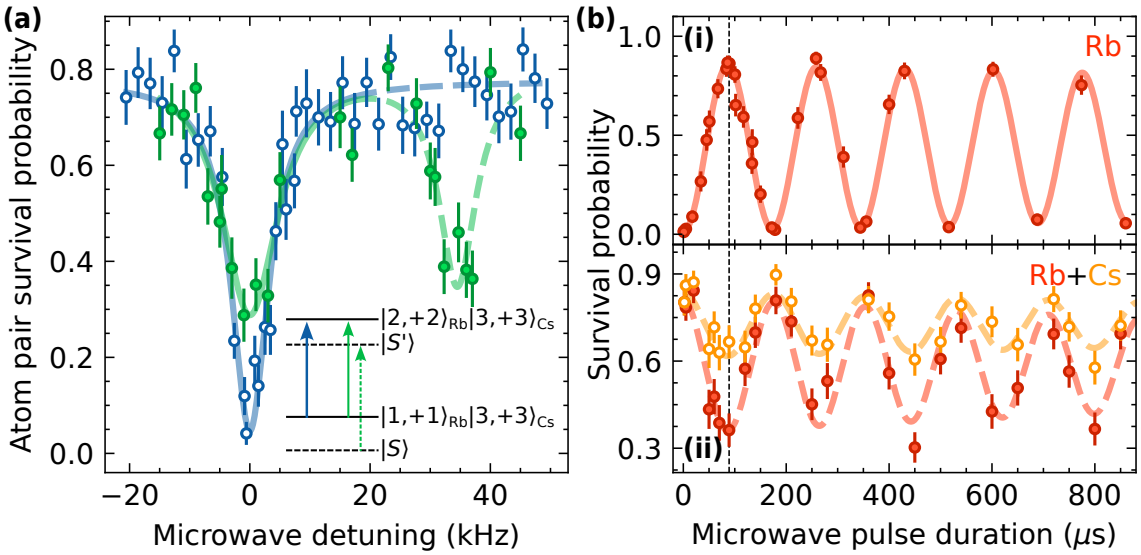

Figure 3.11: Microwave spectroscopy of RbCs molecules produced by mergoassociation at $B = 4.78\,\mathrm{G}$. (a) The probability of detecting both a Rb and Cs atom at the end of the sequence as a function of the microwave detuning from the transition $|1,+1\rangle \rightarrow |2,+2\rangle$ in atomic Rb for strong (filled green points) and weak (empty blue squares) confinement during merging: $\beta^{\times}_{\mathrm{rel}} = 39.4(9)\,\mathrm{nm}$ and $55(1)\,\mathrm{nm}$ respectively. When a molecule is formed, we observe the molecular transition $|S\rangle \rightarrow |S'\rangle$ at detuning $35(2)\,\mathrm{kHz}$. A pulse time of $89\,\mu\mathrm{s}$ is used. The inset shows the energy-level structure of the relevant states with atomic (molecular) states indicated with solid (dashed) lines. **(b)** Measurement of the Rabi frequencies of the transitions. Red filled points (orange empty points) show the survival probability of Rb (Cs) atoms. **(i)** Rb atoms are prepared in $|2,+2\rangle$ before the microwave pulse. **(ii)** Rb+Cs atom pairs are prepared in $|1,+1\rangle_{\mathrm{Rb}}|3,+3\rangle_{\mathrm{Cs}}$ and mergoassociated into the molecular state $|S\rangle$. The microwave pulse is applied at detuning $35\,\mathrm{kHz}$ relative to the Rb transition. The measured Rabi frequencies are $5.81(4)\,\mathrm{kHz}$ and $5.62(3)\,\mathrm{kHz}$ respectively. The black dashed lines show the $89\,\mu\mathrm{s}$ pulse duration used in (a) which is approximately a π pulse for both transitions.

The results of the microwave spectroscopy are shown in Fig. 3.11(a). The blue empty points show the results for weak confinement during merging, where the probability of mergoassociation is low and we expect to prepare an atom pair. We observe only a single feature in the probability of observing both a Rb and Cs atom at the end of the sequence; this is the feature corresponding to the hyperfine transition $|1,+1\rangle \rightarrow |2,+2\rangle$ in atomic Rb. In contrast, when the tweezers are merged with stronger confinement, as shown by the green filled points, we mergoassociate the atom pair to form a molecule. Consequently, we observe an additional feature in the survival probability of the atom pair, detuned by $35(2)\,\mathrm{kHz}$; this corresponds to the molecular transition $|S\rangle \rightarrow |S'\rangle$ illustrated in the inset. Both features are fitted with Lorentzians as shown by solid (dashed) lines for the atomic (molecular) transition. Using the RbCs interaction potential of Takekoshi *et al.* [148], the binding energy of the state $|S'\rangle$ at $4.78\,\mathrm{G}$ is calculated to be $80\,\mathrm{kHz} \times h$.[14] This value is smaller than

[14]The binding energies discussed here were calculated by Jeremy M. Hutson.

that of the state $|S\rangle$ ($122\,\mathrm{kHz} \times h$) and the calculated difference in binding energy ($42\ \mathrm{kHz} \times h$) is in reasonably good agreement with the experimental measurement. For this measurement, the atom pair is prepared in the required hyperfine states in 78(1)% of experimental runs leading to the offset of P_{11} from unity in Fig. 3.11(a).

We verify that the Rabi frequencies of the two transitions are similar by changing the pulse duration with which we resonantly drive the transitions. Fig. 3.11(b)(i) shows data from a routine in which only a Rb atom is loaded and prepared in the hyperfine state $|2,+2\rangle$. We then drive the transition $|2,+2\rangle \rightarrow |1,+1\rangle$. Fig. 3.11(b)(ii) shows the survival probabilities of Rb atoms (red filled points) and Cs atoms (orange empty points) under experimental conditions where we expect molecule formation by mergoassociation. Here we drive the transition $|S\rangle \rightarrow |S'\rangle$; the frequency of the microwave photon is detuned by 35(2) kHz relative to the Rb transition $|2,+2\rangle \rightarrow |1,+1\rangle$. We observe a correlated reduction in the Cs and Rb survival probabilities. In this experiment we do not drive a transition between Cs hyperfine states; by repeating the experiment without the resonant pushout pulse we verify that the change in survival probability for the atoms primarily reflects atomic loss rather than change of the hyperfine states. We do not observe loss of Cs atoms when the microwave frequency is tuned onto resonance with the atomic transition. This suggests either significant decay of the state $|S'\rangle$ for our experimental conditions or failure to break apart the spin-flipped molecule when unmerging the optical tweezers. We note that the binding energy of $|S'\rangle$ is smaller than that of $|S\rangle$, so that the latter explanation is less likely. We measure very similar Rabi frequencies for the two transitions: 5.81(4) kHz for the atomic transition and 5.62(3) kHz for the molecular transition. This means that the pulse time of 89 µs (dashed black line) used for the measurement Fig. 3.11(a) approximates a π pulse for both atomic and molecular transitions. Therefore, the molecule formation efficiency may then be inferred from the relative depths of the features in Fig. 3.11(a). These indicate that 46(8)% of these atom pairs are converted into molecules.[15]

3.6 Summary

We have detailed two methods by which we can associate individually trapped Rb+Cs atom pairs into RbCs molecules. We have performed spectroscopy of the

[15]The efficiencies of hyperfine state preparation and molecule formation are lower than in Sec. 3.4.1 because these data were collected first. Subsequently, we optimised the experimental routine to maximise the molecule formation efficiency. We improved the atomic hyperfine-state preparation with careful optimisation of the pulse times use for the final Raman transfer (see Sec. 2.3.2). Additionally, we slightly tuned the parameters used during the merging routine (i.e. relative trap positions and powers and merging speed) to further reduce atomic heating.

weakly bound molecular states that we can access with either magnetoassociation, where an avoided crossing is traversed by sweeping the magnetic field across a Feshbach resonance, or mergoassociation, where we use two tightly confining optical tweezers to create a strong avoided crossing that we traverse as the tweezers are brought together. We have discussed how the probability of adiabatically traversing the relevant avoided crossings can be tuned. Further, we have demonstrated that the efficiency of molecule formation by mergoassociation is comparable to that of magnetoassociation in this system. Finally, we have showed that mergoassociation can be performed in regimes far from Feshbach resonances, and expect that this method could be used in future to form new molecular species.

4 Ground-state molecules

Some of the results in this chapter have been published in Refs [202, 203].

For quantum science applications, particles need to be long lived and able to interact with other particles at long range. To meet these requirements, we transfer weakly bound molecules in the Feshbach manifold to states in the electronic ground manifold. These ground-state molecules have significant molecule-frame dipole moments and long radiative lifetimes that make them ideal for quantum information and simulation applications.

In this chapter, we detail how we transfer molecules to the rovibrational and hyperfine ground state and characterise the efficiency of this transfer. We then develop a toolbox of techniques for the control and readout of these molecules. Finally, we prepare defect-free arrays of molecules by rearranging them to correct for sites where molecule formation failed.

4.1 Optical spectroscopy

The electronic structure of RbCs molecules is shown in Fig. 4.1(a). In the previous chapter, we discussed the association of atom pairs into weakly bound molecules in the state $|F\rangle$ which has mostly $a^3\Sigma^+$ character. Ultimately, we aim to prepare molecules in the rovibrational and hyperfine ground state $|G\rangle$ of the $X^1\Sigma^+$ electronic manifold.

The structure of the electronic manifold $X^1\Sigma^+$ is rich and extends over a wide range of energy scales [239]. Within the manifold, first there are vibrational energy levels (see Fig. 4.1(b)) which are labelled with the quantum number v which counts up from the vibrational ground state $v = 0$. These energy levels come from the approximately harmonic restoring force between the molecular nuclei and are therefore approximately evenly spaced. The energy spacing between the vibrational levels with $v = 0$ and $v = 1$ for RbCs is $\approx 1.5\,\mathrm{THz} \times h$ [279], and for this work we always

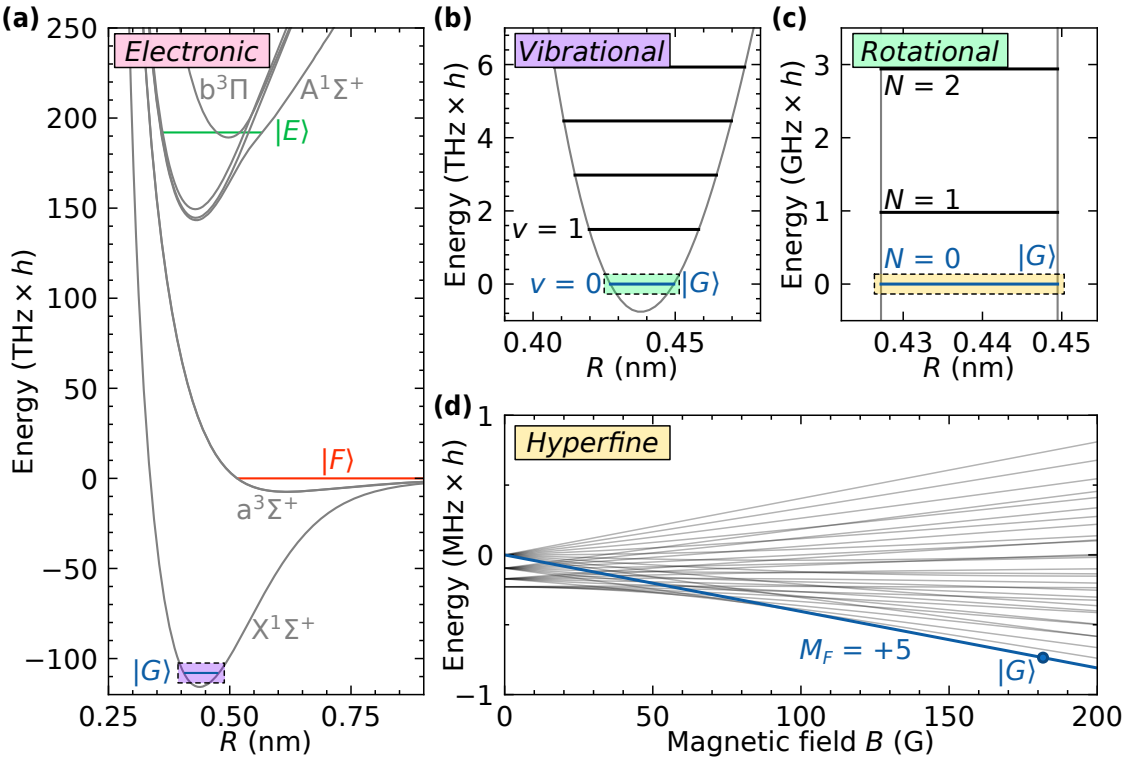

Figure 4.1: The rich internal structure of RbCs molecules. (a) Electronic energy structure. The ground state $|G\rangle$ is in the manifold $X^1\Sigma^+$. **(b)** Vibrational energy levels near the bottom of the manifold $X^1\Sigma^+$. **(c)** Rotational energy levels within the ground vibrational manifold. **(d)** Hyperfine energy levels within the ground rotational manifold. The point shows the energy of the state $|G\rangle$ at the molecule-formation field (181.699(1) G). For (a) energies are relative to the dissociation threshold, for other panels energies are relative to the state $|G\rangle$ in free-space.

remain in the ground vibrational level with $v = 0$.

In ground vibrational level, the molecules can be described by the rigid-rotor Hamiltonian. This Hamiltonian gives rise to rotational energy levels (see Fig. 4.1(c)). These are labelled by the rotational angular momentum N, which enumerates the levels from the rotational ground state with $N = 0$. The energies of the rotational levels are $hB_\nu N(N+1)$ such that the splitting between neighbouring rotational manifolds is in the microwave domain (for RbCs, $B_\nu \approx 490\,\mathrm{MHz}$) [280]. Each rotational level is $(2N+1)$-fold degenerate, where the degeneracy is caused by the projection M_N of the rotational angular momentum along the quantisation axis.

However, this picture ignores coupling between the rotational angular momentum and the nuclear spins of the constituent atoms ($i_{\mathrm{Rb}} = 3/2$ and $i_{\mathrm{Cs}} = 7/2$). This coupling causes each state $|N, M_N\rangle$ to split into $(2i_{\mathrm{Rb}}+1)(2i_{\mathrm{Cs}}+1) = 32$ hyperfine states. This hyperfine structure is illustrated in Fig. 4.1(d) for the ground rotational state. The highlighted state $|G\rangle$ is the rovibrational and hyperfine ground state for magnetic fields $B \gtrsim 100\,\mathrm{G}$. At typical magnetic fields in our experiment ($\sim 200\,\mathrm{G}$), the molecular eigenstates are generally superpositions of states of different m_{Rb}

and m_{Cs}, where m_{Rb} (m_{Cs}) is the projection of the Rb (Cs) nuclear spin along the quantisation axis. The only good quantum numbers that can be used to describe the eigenstates are N and $M_F \equiv M_N + m_{\mathrm{Rb}} + m_{\mathrm{Cs}}$. The exceptions to this are the stretched states with maximum $|M_F|$; for these states $|m_{\mathrm{Rb}}| = 3/2$, $|m_{\mathrm{Cs}}| = 7/2$ and M_N is a good quantum number. The state $|G\rangle$ is stretched, therefore can be written $|G\rangle \equiv |N = 0, M_N = 0, m_{\mathrm{Rb}} = +3/2, m_{\mathrm{Cs}} = +7/2\rangle$ or $|G\rangle \equiv |N = 0, M_F = +5\rangle$. Its value of $M_F = +5$ is unique in the ground rotational manifold.

We transfer molecules from the state $|F\rangle$ to the state $|G\rangle$ via the intermediate state $|E\rangle \equiv |v' = 29, N' = 1\rangle$ of the coupled manifold $\mathrm{A}^1\Sigma^+ + \mathrm{b}^3\Pi$. The state $|E\rangle$ is chosen because it has strong optical coupling to both the state $|F\rangle$ and the state $|G\rangle$. Therefore, the transfer $|F\rangle \rightarrow |G\rangle$ can be performed with two-photon methods. The two lasers that we use to perform this transfer are the pump laser that drives the transition $|F\rangle \rightarrow |E\rangle$ (see Ch. 3) and the Stokes laser that drives the transition $|E\rangle \rightarrow |G\rangle$. These two lasers are locked to the same ULE cavity (see Sec. 2.5) and the transitions that they drive are shown in Fig 4.2(a).

We perform two-photon spectroscopy to identify the Stokes transition. The experimental sequence is similar to that used for the measurement shown in Fig. 3.6, with the exception that the results shown here are for a single molecule. We form the molecule by magnetoassociation and transfer it to the state $|F\rangle$ at 181.699(1) G. We then apply the pump light. As with the measurements in Ch. 3, this light excites molecules to the state $|E\rangle$, from which the subsequently decay. This precludes atom-pair recovery at the end of the experimental sequence. Unlike the measurement shown in Fig. 3.6, here we apply only a small amount of the pump light (an intensity of 0.8(1) W/cm^2) so that the transition is not saturated and we use a pulse duration of 750 µs. Fig 4.2(b)(i) shows the effect of changing the detuning of the pump light. The detuning is relative to the fitted centre.

Fig 4.2(b)(ii) shows the effect of applying the Stokes light for the time when the pump light is applied. The relative pulse timings are shown in the inset. The intensity of the Stokes light is 210(10) W/cm^2, so it significantly perturbs the states of the system that we probe with the low-intensity pump light.[1] When the Stokes light is resonant with the transition $|E\rangle \rightarrow |G\rangle$, it causes a significant light shift to the state $|E\rangle$, which prevents the pump light exciting molecules to $|E\rangle$. Consequently, this means that more atom pairs are recovered at the end of the experimental routine. When resonant with the transition $|E\rangle \rightarrow |G\rangle$, the frequency of the Stokes laser is

[1]This spectroscopy method is called Autler-Townes spectroscopy and is ideal for three-level systems where the intermediate state is short-lived. The theory of Autler-Townes spectroscopy is explored thoroughly in Sec. 5.4 in the context of Rydberg atoms.

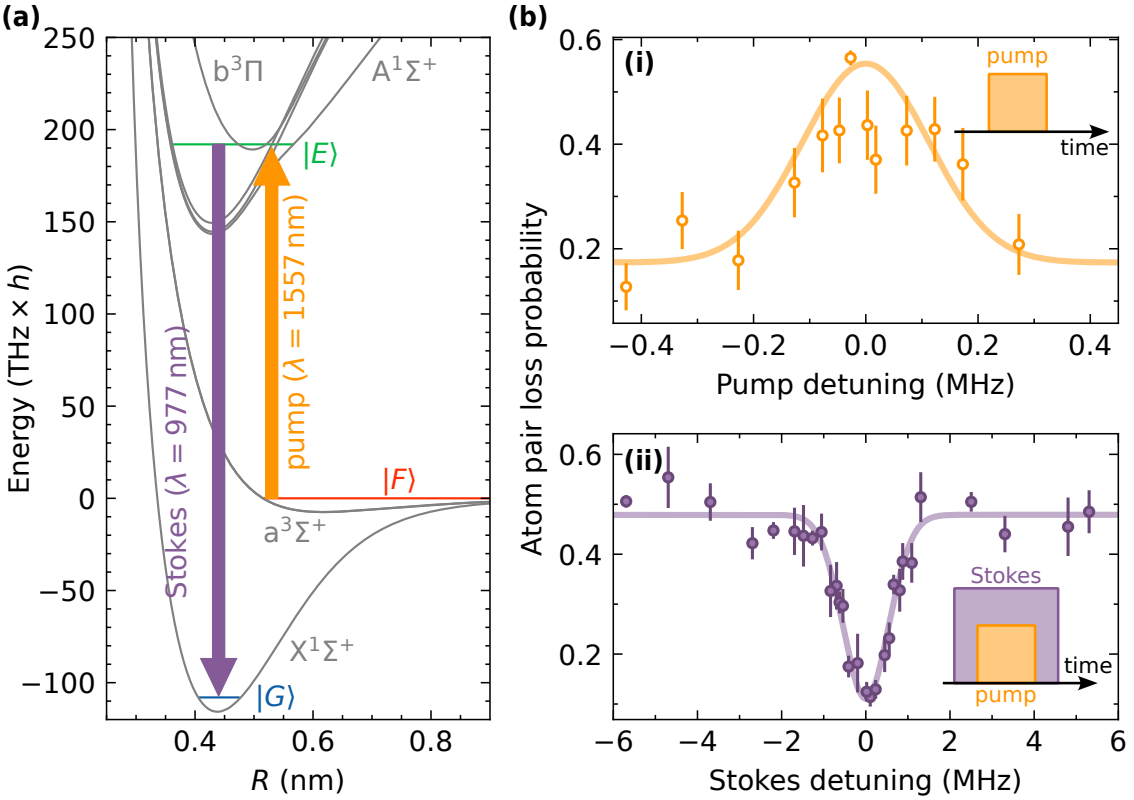

Figure 4.2: Spectroscopy of the Stokes transition. **(a)** RbCs electronic structure with the pump and Stokes transitions highlighted. **(b)(i)** One-photon spectroscopy of the pump transition. Molecules are prepared in $|F\rangle$. The pump light excites molecules to $|E\rangle$ which precludes atom-pair recovery. **(ii)** Two-photon spectroscopy of the Stokes transition. The Stokes beam is switched on before the pump light is applied. When the Stokes light is on resonance, the pump transition is significantly light shifted. This precludes molecules being excited out of $|F\rangle$, suppressing atom pair loss.

306830.42(6) THz, as measured by a wavemeter[2] with a quoted accuracy of ±0.2 parts per million.

4.2 Transfer to the ground state

We transfer molecules from the state $|F\rangle$ to the state $|G\rangle$ using stimulated Raman adiabatic passage (STIRAP) [281, 282]. Transfer with STIRAP uses the adiabatic evolution of an eigenstate of the three level system that contains the states $|F\rangle$, $|E\rangle$, and $|G\rangle$. When the pump and Stokes lasers are resonant, one of the eigenstates of this system is [281]

$$|\psi\rangle \equiv \cos(\theta)\,|F\rangle + \sin(\theta)\,|G\rangle\,, \tag{4.1}$$

where we have defined the mixing angle $\theta \equiv \arctan(\Omega_{\text{pump}}/\Omega_{\text{Stokes}})$ for the Rabi frequencies Ω_{pump} and Ω_{Stokes} with which we drive the pump and Stokes transitions

[2] Bristol Instruments 671A-NIR

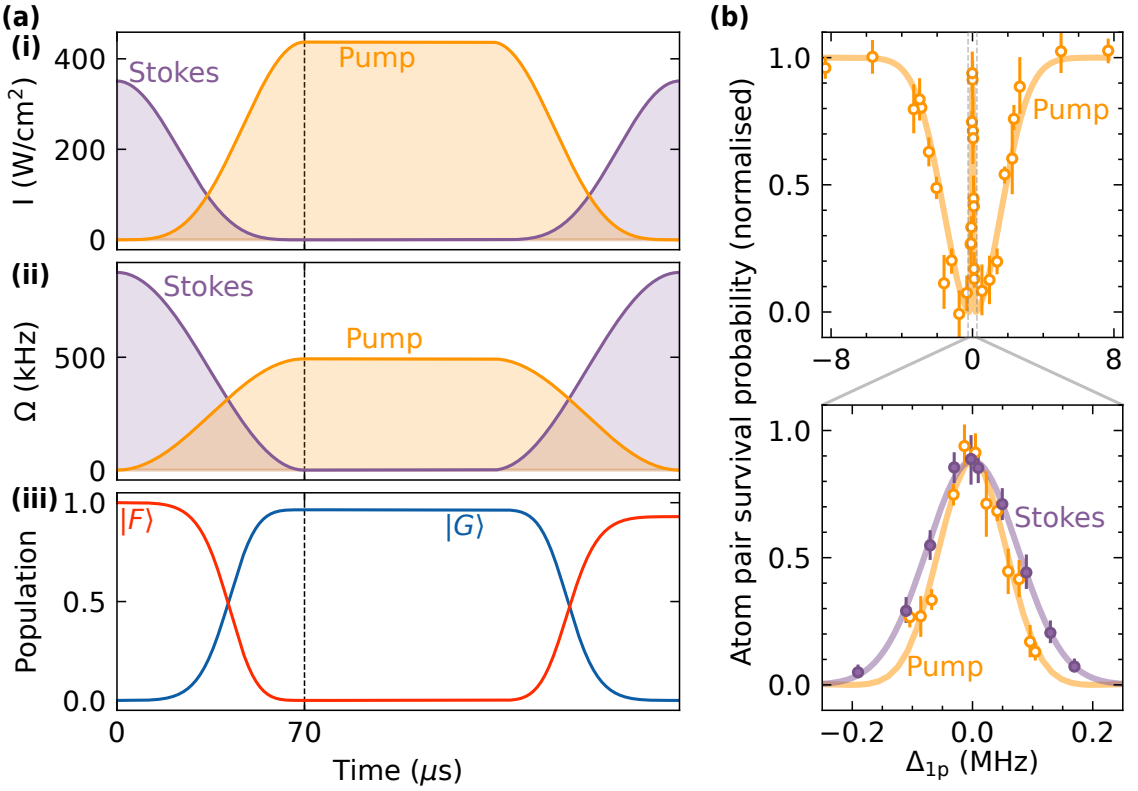

Figure 4.3: STIRAP to the rovibrational ground state. **(a)** Evolution of **(i)** the intensity of the STIRAP beams, **(ii)** the Rabi frequency of the transitions they drive, and **(iii)** the population of $|F\rangle$ and $|G\rangle$ during a round-trip STIRAP transfer. The time to complete the transfer $|F\rangle \rightarrow |G\rangle$ is 70 μs (black dashed line). **(b)** Atom-pair survival probability for a round trip $|F\rangle \rightarrow |G\rangle \rightarrow |F\rangle$ as a function of the one-photon detuning Δ_{1p} of either the pump (from the transition $|F\rangle \rightarrow |E\rangle$) or the Stokes (from the transition $|E\rangle \rightarrow |G\rangle$) lasers when the other laser is on resonance. The lower panel is a zoom to small values of Δ_{1p}

respectively. Crucially, $|\psi\rangle$ has no overlap with the state $|E\rangle$; this means that we can adiabatically transfer molecules from the state $|F\rangle$ to the state $|G\rangle$ whilst avoiding decoherence from the short lifetime of the state $|E\rangle$.

To evolve the state $|\psi\rangle$ from $|F\rangle$ to $|G\rangle$, we use a pulse sequence which begins with only the Stokes beam on and evolves to having only the pump beam on [281]. At the start of this sequence, $\theta = 0$ and $|\psi\rangle = |F\rangle$. We adiabatically evolve θ by ramping on the pump beam and ramping off the Stokes beam. Once the pump beam is completely off, $\theta = \pi/2$ rad and $|\psi\rangle = |G\rangle$. During the transfer, we modulate the intensity of the beams with profiles proportional to $\cos^4(\pi t/2\tau)$ for time $t \leq \tau$.[3] The intensity profiles during a round-trip transfer $|F\rangle \rightarrow |G\rangle \rightarrow |F\rangle$ are shown in Fig. 4.3(a)(i). The maximum intensity of the pump beam is 440(20) W/cm^2 and the maximum intensity of the Stokes beam is 350(20) W/cm^2. The pulse shapes are

[3]The pulse shapes used for STIRAP are not critical; we only require that θ varies adiabatically. We choose to use a $\cos^4$ profile so that the Rabi frequencies vary smoothly with $\cos^2$ profiles. More complex pulse shapes can maximise the adiabaticity with which θ varies [283].

controlled with the AOMs in the laser locking setup (see Sec. 2.5). We experimentally set the duration of the pulses to maximise the STIRAP efficiency, and the time to complete a one-way transfer $|F\rangle \rightarrow |G\rangle$ is $\tau = 70\,\mu s$ (black dashed line).

Figure 4.3(a)(ii) shows the evolution of the pump and Stokes Rabi frequencies during a round-trip transfer. The maximum pump Rabi frequency is 493(5) kHz and the maximum Stokes Rabi frequency is 876(4) kHz. The measurement of these Rabi frequencies is discussed in Sec. 4.3. Fig. 4.3(a)(iii) shows the expected population of the state $|F\rangle$ (red) and the state $|G\rangle$ (blue) during the transfer. Here, the efficiency of each one-way transfer has been set to 96.4(1)%, the measurement of which is presented in Sec. 4.4.

In Fig. 4.3(b) we show the probability of recovering an atom pair after a round trip $|F\rangle \rightarrow |G\rangle \rightarrow |F\rangle$ as a function of the one-photon detuning Δ_{1p} of either the pump or Stokes lasers, with the other laser held on one-photon resonance. The experimental sequence is the same as used for Fig. 4.2, but we apply the STIRAP pulses rather than the square pulses used for spectroscopy. The pulse sequence is as shown in Fig. 4.3(a)(i) but we set the duration between the forward transfer $|F\rangle \rightarrow |G\rangle$ and the reverse transfer $|G\rangle \rightarrow |F\rangle$ to a few microseconds. When both lasers are resonant, molecules successfully undergo the round-trip transfer $|F\rangle \rightarrow |G\rangle \rightarrow |F\rangle$. This means that they reoccupy the state $|F\rangle$ and can be successfully disassociated into atoms which are reimaged at the end of the experiment. When the Stokes laser is not resonant (purple points), the pump laser causes loss to other molecular states via the state $|E\rangle$. Therefore, molecules are not successfully dissociated into atom pairs, so the probability of atom-pair loss increases. When the pump laser is not resonant (orange points), at small detunings ($|\Delta_{1p}| \sim 200\,kHz$) the two-photon detuning from the transition $|F\rangle \rightarrow |G\rangle$ is sufficiently large to prevent efficient STIRAP. However, the pump laser is still close enough to resonance that it causes significant loss to other molecular states via the state $|E\rangle$. As the laser is tuned further to $|\Delta_{1p}| \gtrsim 5\,MHz$, the rate with which molecules are off-resonantly excited to $|E\rangle$ decreases and molecules never transfer out of $|F\rangle$ during the pulse sequence. This causes the chance of the atom-pair survival to return to the background value, as seen in the upper panel at large values of $|\Delta_{1p}|$.

We briefly consider the effect of the trapping light on the molecules. The energy shift of molecular states is in the presence of optical light is known as the ac Stark effect. The ac Stark shift for a state $|i\rangle$ is

$$\Delta E_{ac} = -\frac{1}{2\varepsilon_0 c}\alpha_i(\theta) I\,, \tag{4.2}$$

where I is the tweezer intensity and $\alpha_i(\theta)$ is the polarisability of the state.[4] For

[4]Eq. (4.2) is essentially the same as Eq. (2.1), but here the sign convention is such that ΔE_{ac}

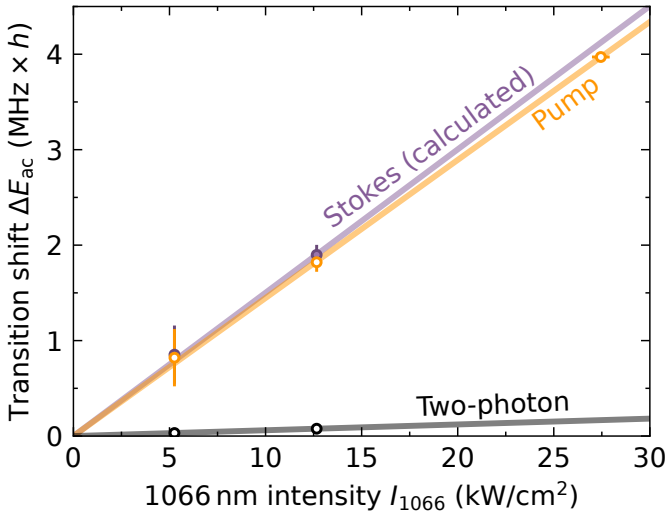

Figure 4.4: ac Stark shifts of the STIRAP transitions. We measure the frequency of the STIRAP transitions as a function of the intensity I_{1066} of the 1066 nm tweezers that trap the molecules. The pump and two-photon transition shifts can be directly measured, the Stokes shift is calculated from the sum of the two. We extract differential polarisabilities $\Delta\alpha_{\text{pump}} = -3089(6) \times 4\pi\varepsilon_0 a_0^3$, $\Delta\alpha_{\text{Stokes}} = -3220(20) \times 4\pi\varepsilon_0 a_0^3$, and $\Delta\alpha_{2p} = -130(20) \times 4\pi\varepsilon_0 a_0^3$.

molecules described by the rigid-rotor Hamiltonian, the polarisability depends on the angle θ between the polarisation of the trapping light and the internuclear axis and is given by $\alpha_i(\theta) = \alpha^{(0)} + \frac{1}{2}\alpha^{(2)}[3\cos^2(\theta) - 1]$ [284]. In practise, this means that different rotational states $|N, M_N\rangle$ in the manifold $X^1\Sigma^+$ experience different polarisabilities. $\alpha^{(0)}$ is the *isotropic polarisability* and its contribution to the total polarisability is the same for all rotational states. It therefore has no effect on frequencies of rotational transitions, but still provides a contribution to a trapping potential. $\alpha^{(2)}$ is the *anisotropic polarisability* and it causes differences in the polarisabilities of rotational states and can mix them. This will become relevant later when rotational transitions are introduced.

We measure the differential polarisabilities of the pump and Stokes transitions. The ac Stark shift for a transition $|i\rangle \to |j\rangle$ is given by the Eq. (4.2), but with α_i replaced by the differential polarisability $\Delta\alpha = \alpha_j - \alpha_i$. In Fig. 4.4, we show the ac Stark shifts for the STIRAP transitions when the molecules are trapped in 1066 nm tweezers of intensity I_{1066}. We measure these by repeating the measurements shown in Fig. 4.3(b) at different tweezer intensities. We can directly measure either the shift of the one-photon pump transition (orange) or of the two-photon transition $|G\rangle \to |F\rangle$ (black). The shift of the one-photon Stokes transition (purple) is the sum of these two. We fit the data with linear functions passing through the origin to obtain differential polarisabilities for the pump and Stokes transitions as $\Delta\alpha_{\text{pump}} = -3089(6) \times 4\pi\varepsilon_0 a_0^3$

is negative for a trapped particle.

and $\Delta\alpha_{\text{Stokes}} = -3220(20) \times 4\pi\varepsilon_0 a_0^3$ respectively. The differential polarisability of the two-photon transition is $\Delta\alpha_{2\text{p}} = -130(20) \times 4\pi\varepsilon_0 a_0^3$. We expect the polarisability of $|F\rangle$ to be approximately the sum of the polarisabilities of a Rb+Cs atom pair ($\alpha_F \approx \alpha_{\text{Rb}} + \alpha_{\text{Cs}} = 1.8(1) \times 10^3 \times 4\pi\varepsilon_0 a_0^3$) and find the ratio of the polarisabilities for the states $|G\rangle$ and $|F\rangle$ to be $\alpha_G/\alpha_F = (\alpha_F + \Delta\alpha_{2\text{p}})/\alpha_F = 1.07(1)$ at our tweezer wavelength. This means that these tweezers are approximately magic for the STIRAP transition. Our value of α_G/α_F is within error of the value of $\alpha_G/\alpha_F = 1.09(2)$ at 1064 nm reported by Blackmore [285].

It is important to understand how a molecule may be heated during STIRAP because fidelities of molecular gates are often limited by thermal motion [69, 70, 96]. The majority of molecules that are formed in our experiment (58(6)%, see Sec. 3.4.1) occupy the three-dimensonal motional ground state and maintaining this high ground-state fraction is desirable. We follow the approach of Cairncross *et al.* [157] and consider the chance that a molecule, starting in the state $|F\rangle$ in the three-dimensional motional ground state, is successfully transferred to the state $|G\rangle$ whilst remaining in the three-dimensional motional ground state. In our experiment, the STIRAP beams co-propagate along the radial axis of tightest tweezer confinement (the y-axis, see Sec. 2.4). During STIRAP, we hold the molecules in 1066 nm tweezers of intensity of $I_{1066} = 3.07(1)\,\text{kW/cm}^2$ so that the trap frequency along this axis for a molecule in $|G\rangle$ is $\nu_y = 6.9(2)\,\text{kHz}$. The first effect that can cause heating is the momentum kick $p = h\left(\lambda_{\text{pump}}^{-1} - \lambda_{\text{Stokes}}^{-1}\right)$ from the absorption of a pump photon and the emission of a Stokes photon during STIRAP. By equating the two-photon recoil energy $h\nu_{\text{recoil}} \equiv p^2/2m$, where m is the mass of the molecule, and the energy of a motional excitation $h\nu_y$, we find the in mean motional level after the momentum kick is $\widetilde{n} = 0.019(1)$. In the worse case, this corresponds to a 98.1(1)% probability of remaining in the motional ground state.

Secondly, the mismatch between the trap frequencies of the states $|F\rangle$ and $|G\rangle$ can cause heating as the wavefunction of $|F\rangle$ is projected onto the wavefunction of $|G\rangle$. The ratio between the trap frequencies is $f \equiv \sqrt{\alpha_G/\alpha_F} = 1.034(5)$, and the probability that a molecule remains in the three-dimensional motional ground state during the transfer $|F\rangle \rightarrow |G\rangle$ is [157]

$$P_{0\rightarrow 0} = \frac{8f^{3/2}}{(f+1)^3} \exp\left(-\frac{f\eta^2}{2f+2}\right), \tag{4.3}$$

where the Lamb-Dicke parameter $\eta \equiv \sqrt{\nu_{\text{recoil}}/\nu_y} = 0.138(2)$. We find that $P_{0\rightarrow 0} = 99.47(2)\%$. This is so close to unity precisely because the trapping wavelength is nearly magic for the STIRAP transition. In the worst case there is no cancellation between these two motional effects, and the chance for a molecule to remain in the

three-dimensional motional ground state after the STIRAP transfer is 97.58(7)%. We expect that 58(6)% of molecules in $|F\rangle$ are in the three-dimensional motional ground state (see Sec. 3.4.1) and therefore expect that 56(6)% of molecules in the rovibrational ground state $|G\rangle$ are in the three-dimensional motional ground state.

4.3 Molecule detection scheme

Generally, we wish to present and analyse data that are post-selected on initial experimental conditions. This allows us to ignore fluctuations in the experiment that are not relevant to the parameter being studied. For most experiments discussed so far, we have post-selected to consider only experimental runs where the correct number of atoms were initially loaded. For example, the data points presented in Fig. 4.2 show the probability that both a Rb and Cs atom are lost during a routine *given that* both are present at the start. Due to the stochastic nature of loading atoms into optical tweezers, in some experimental runs, we will fail to load both a Rb and Cs atom. We learn nothing useful from this particular shot of the experiment, and therefore discard it when processing data.

However, the lack of closed optical cycling transitions in RbCs precludes scattering enough photons from a single molecule in order to detect it with fluorescence imaging. This means that we cannot directly image a molecule in order to determine that it was successfully formed. The features in Fig. 4.2 saturate to approximately the efficiency of molecule formation (53(1)%, see Sec. 3.4.1) because in the other experimental runs, atoms are loaded but molecules are not formed. In Fig. 4.3 we illustrate a solution, where we fit the orange data and normalise them such that the contrast of the orange fit is unity. However, this solution is non-ideal, because it is unclear whether small fluctuations in the normalised probabilities are due to fluctuations in the probability of molecule *formation* (which we typically do not care about) or fluctuations in the probability of molecule *survival* given that a molecule was formed (which is typically what we are trying to measure). Furthermore, we obtain points where the normalised survival probability is above unity or below zero.

To overcome this, we map the success or failure of molecule formation onto atoms in specific tweezers and then use standard atomic fluorescence imaging of Rb and Cs. This allows us to detect sites of the array where molecule formation failed, similar to erasure conversion in neutral-atom arrays [286]. Fig. 4.5 shows a diagram of this detection scheme. The stages in the detection scheme are:

I. We prepare defect-free arrays of up to eight Rb and eight Cs atoms. We take a fluorescence image to measure the occupancy of the arrays. Atoms are then

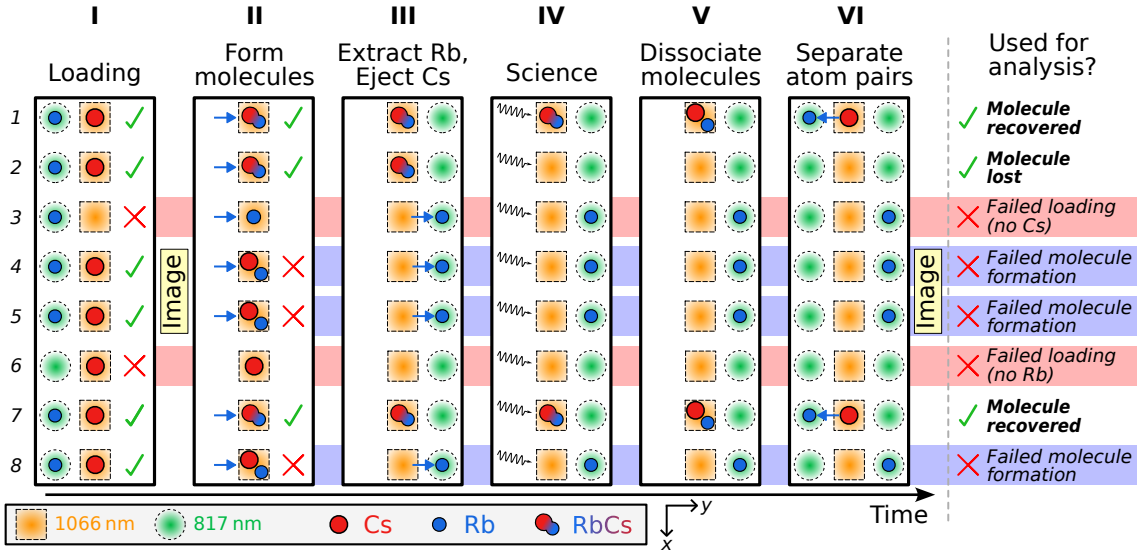

Figure 4.5: Stages of a typical experiment. **I** Initially Rb and Cs atoms are loaded and rearranged to prepare defect-free 1D arrays in species-specific tweezers. **II** The Rb tweezers are merged to overlap with the Cs tweezers. The atom pairs are magnetoassociated and the resultant molecules are transferred to the ground state using STIRAP. **III** Atom pairs remaining due to failed molecule formation are separated. The Cs is ejected and the Rb is stored in a separate row of tweezers. Detection of the Rb atom indicates failure to form a molecule in a particular site. **IV** An experiment is performed on the molecules. **V** The molecules are dissociated. **VI** The resulting atom pairs are separated into their original traps for imaging. The right hand column shows whether each site is used when determining P_r.

prepared in the requisite states for molecule formation.

II. We merge the arrays and attempt to form molecules. Formation errors result in atom pairs remaining in the 1066 nm tweezers after the molecules have been transferred to state $|G\rangle$.

III. We detect molecule-formation errors by extracting the remaining Rb atoms and storing them in a separate row of 817 nm tweezers (the "detection array"). In addition, we apply resonant light to remove any remaining Cs atoms.

IV. We perform the science relevant to the chosen experiment. This will often cause some molecule loss, which is what we want to measure.

V. We reverse the STIRAP sequence to transfer molecules back to state $|F\rangle$ before immediately reversing the association field ramps to convert the molecules back to atom pairs.

VI. Resulting atom pairs are separated by extracting the Rb atoms and returning them to their original traps. We take a fluorescence image of Rb and Cs to determine the occupancy of the *three* tweezer arrays: the original arrays con-

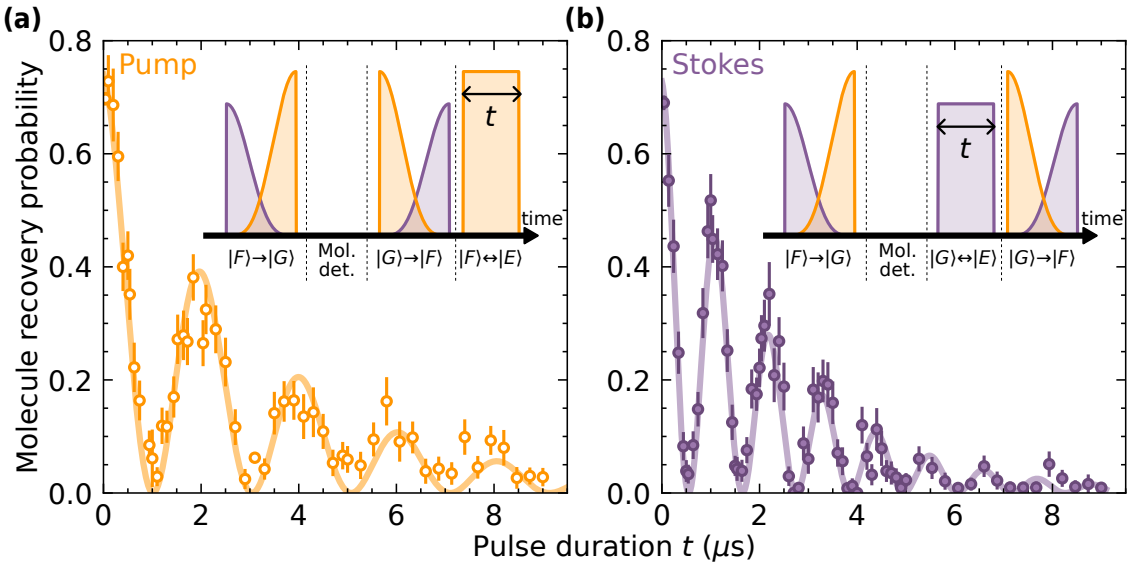

Figure 4.6: Rabi frequencies of the pump and Stokes transitions. (a) The pump light drives the transition $|F\rangle \rightarrow |E\rangle$. **(b)** The Stokes light drives the transition $|G\rangle \rightarrow |E\rangle$. Molecules in state $|E\rangle$ cannot be recovered. For both experiments, we begin by transferring the molecule to $|G\rangle$ to be able to post-select on successful molecule formation. The Rabi oscillations decay as population leaks to other molecular states. The insets show the relative intensities of the pump (orange) and Stokes (purple) beams during the experiment. We extract Rabi frequencies $\Omega_{\text{pump}} = 493(5)\,\text{kHz}$ and $\Omega_{\text{Stokes}} = 876(4)\,\text{kHz}$.

taining atoms recovered from the molecules *and* the detection array containing Rb atoms in sites where molecule formation failed.

From the final fluorescence image we determine the recovery probability P_r of the molecules as follows. First, using the initial fluorescence image, we ignore all sites in the array in which the requisite number of atoms were not loaded (Fig. 4.5, sites 3 and 6). Second, the presence of a Rb atom in the detection array indicates that molecule formation failed in the corresponding 1066 nm trap and we ignore that site when analysing statistics (Fig. 4.5, sites 4, 5, and 8). Conversely, if the detection trap is empty, we assume that a molecule was formed in that site and therefore consider the occupancy of the corresponding initial Rb and Cs traps (Fig. 4.5, sites 1, 2, and 7). A molecule is then deemed to be 'recovered' if both atoms that formed it are successfully imaged in their original traps at the end of a routine. Thus P_r is defined as the probability that we recover both a Rb and a Cs atom in their initial traps, ignoring sites in which the presence of a Rb atom in the detection array indicates that molecule formation failed. For the example shown in Fig. 4.5, we would measure $P_r = 2/3$.

Figure 4.6 shows examples of measurements using this detection scheme. We measure the Rabi frequencies of the pump transition $|F\rangle \rightarrow |E\rangle$ (Fig. 4.6(a)) and the Stokes transition $|G\rangle \rightarrow |E\rangle$ (Fig. 4.6(b)). The pulses of STIRAP light for

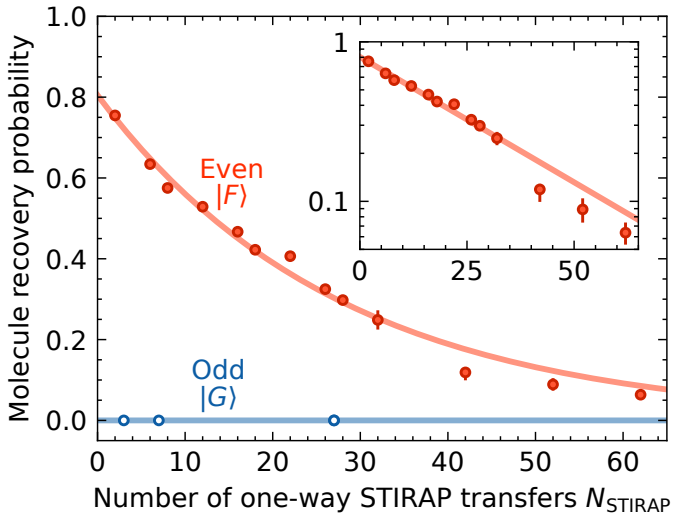

Figure 4.7: Repeated STIRAP transfers with a one-way efficiency of 96.4(1)%. An odd number of one-way transfers (blue empty points) leave the molecule in $|G\rangle$ from atom pairs are not recovered. An even number of one-way transfers (red filled points) leave the molecule in $|F\rangle$ from which we recover atom pairs. The inset shows the same data on a logarithmic scale.

each experiment are shown in the insets. For the measurement of the pump Rabi frequency, we transfer the molecule to $|G\rangle$, perform molecule detection, transfer the molecule back to $|F\rangle$, and pulse on the pump light for a varying duration. The transfer to $|G\rangle$ is necessary for the detection scheme to be effective as we require the lifetime of the molecular state to be significantly longer than the time it takes to remove the atom pair ($\sim 10\,\mathrm{ms}$), which is true for the state $|G\rangle$ but not the state $|F\rangle$ (see Sec. 4.4). The sequence for measuring the Stokes Rabi frequency is similar, but we pulse the Stokes light before the reverse STIRAP. We drive the transitions with square pulses that have intensity equal to the maximum intensity used during STIRAP. The data are fitted with damped cosine functions (solid lines) that decay towards zero, modelling the fact that molecules are lost when the state $|E\rangle$ decays. The shaded regions show the errors on the fits. The pump Rabi frequency is $\Omega_{\mathrm{pump}} = 493(5)\,\mathrm{kHz}$ and the Stokes Rabi frequency is $\Omega_{\mathrm{Stokes}} = 876(4)\,\mathrm{kHz}$.

4.4 Formation and detection efficiencies

The efficiency with which we prepare molecules in the state $|G\rangle$ (and subsequently recover them) is primarily limited by the STIRAP efficiency and the loss of molecules in the state $|F\rangle$. In this section, we quantify these losses using the detection scheme described in Sec. 4.3.

We measure the STIRAP efficiency by repeating N_{STIRAP} one-way transfers before reversing the association field ramps and measuring the molecule recovery

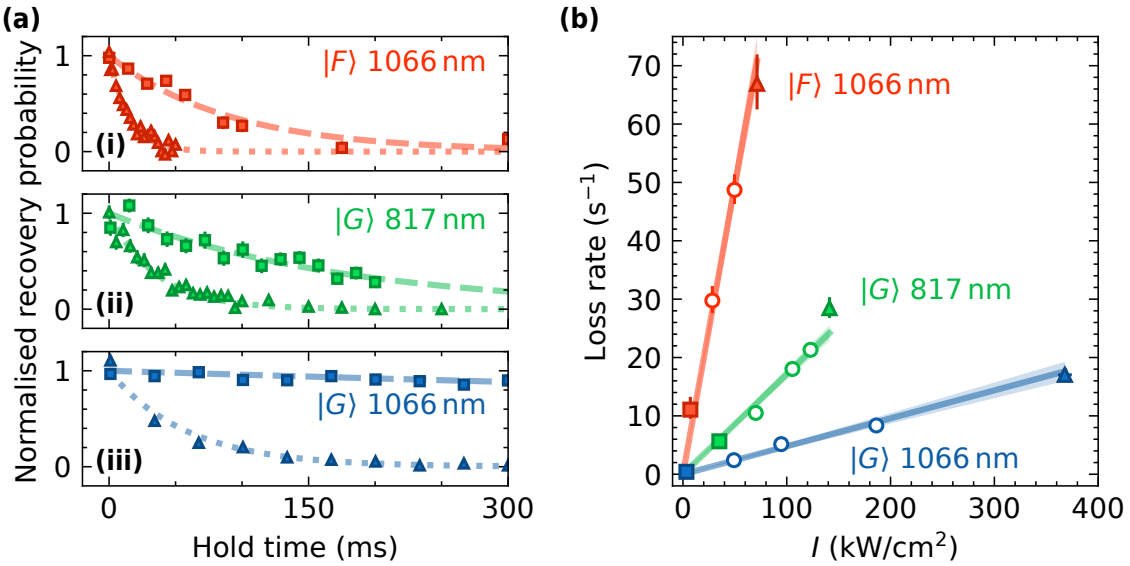

Figure 4.8: Lifetime of RbCs molecules in optical tweezers with wavelengths of 1066 nm and 817 nm. **(a)** Normalised recovery probabilities as a function of the hold time in the tweezers for molecules **(i)** in state $|F\rangle$ and 1066 nm, **(ii)** the ground state $|G\rangle$ and 817 nm and **(iii)** the ground state $|G\rangle$ and 1066 nm. In each panel results are shown for two different intensities with the values indicated by the corresponding symbols in (b). The axes have been rescaled to make the contrast of the fits equal to unity. The blue squares in (iii) show the loss of molecules in state $|G\rangle$ at our typical operating intensity. **(b)** Scaling of the molecule loss rates with tweezer intensity I. The solid lines show linear fits to the measured loss rates.

probability. The results are shown in Fig. 4.7. Ideally, an even number of one-way transfers (red filled points) leave molecules in the state $|F\rangle$, from which atom pairs can be recovered. An odd number of one-way transfers (blue empty points) transfer molecules to the state $|G\rangle$, from which expect to recover no atom pairs. Indeed, for points where N_{STIRAP} is odd, we never recover a molecule. We fit the points where N_{STIRAP} is even with an exponential decay from which we extract a one-way transfer efficiency of 96.4(1)%, assuming the efficiencies of the forward and reverse transfers to be the same. This efficiency is marginally better than the efficiencies reported for RbCs in bulk gases [150, 240] and comparable to the highest reported efficiencies for ground-state transfer of diatomic molecules [73, 287].

Figure 4.8 shows lifetime measurements of the states $|F\rangle$ and $|G\rangle$ for different tweezer intensities. We find that molecules in the weakly bound state $|F\rangle$ exhibit a much larger loss rate than ground-state molecules. We have previously observed a photoassociation resonance from the state $|F\rangle$ at 1063.91(7) nm with an estimated transition dipole moment (TDM) of $0.064(2) \times ea_0$ [207]. We believe that the tweezer light is driving a transition from the manifold $a^3\Sigma^+$ to the manifold $c^3\Sigma^+$ [288]. We can reduce the loss rate from photon scattering by operating far from this resonance; it is for this reason that we operate the molecule tweezers at a wavelength of

Table 4.1: Efficiencies of each stage of molecule formation. The values are measured experimentally unless stated otherwise.

Experimental stage	**Efficiency**
Preparation of atom-pair hyperfine state	0.93(2)
Occupancy of ground state of relative motion (following the merging of the traps)	0.56(5)
Magnetoassociation efficiency (calculated)	> 0.99
Atom pair $\rightarrow |F\rangle$ conversion	**0.53(1)**
$|F\rangle$ survival pre-STIRAP	0.95(1)
STIRAP transfer $|F\rangle \rightarrow |G\rangle$	0.964(1)
$|F\rangle \rightarrow |G\rangle$ conversion (calculated)	**0.91(1)**
Atom pair $\rightarrow |G\rangle$ conversion (calculated)	**0.48(2)**

1065.512 nm. At this wavelength, we determine the loss rate of molecules in state $|F\rangle$ to be 0.99(4) $\mathrm{s}^{-1}/(\mathrm{kW/cm}^2)$ from the fit to the red points in Fig. 4.8(b). To mitigate this loss, we operate at low tweezer intensities and minimise the time between the molecule entering state $|F\rangle$ and being transferred to state $|G\rangle$. Unfortunately, the narrow ($\sim$ 100 kHz) linewidths of the STIRAP transitions necessitate a 10 ms hold following the magnetoassociation ramps to achieve sufficient magnetic field stability ($\sim$ 50 mG) for efficient transfer. During this time the molecules in state $|F\rangle$ are held in tweezers with an intensity of 6 $\mathrm{kW/cm}^2$ such that 5(1)% are lost. We note that the molecular state $|S\rangle$ shown in Fig. 3.1(b), which is populated in the initial magnetoassociation ramp, has a much longer lifetime, consistent with that of the atom pair (> 10 s). However, STIRAP from this state is inefficient due to the weak coupling to state $|E\rangle$.

The loss rate of molecules in the ground state $|G\rangle$ is much lower than that of molecules in state $|F\rangle$. From the fits in Fig. 4.8(b), we determine loss rates for the state $|G\rangle$ of 0.171(8) $\mathrm{s}^{-1}/(\mathrm{kW/cm}^2)$ in tweezers with a wavelength of 816.848 nm and 0.047(4) $\mathrm{s}^{-1}/(\mathrm{kW/cm}^2)$ for a wavelength of 1065.512 nm. The linear relation observed between loss rate and intensity suggests that the lifetime is limited by photon scattering of the tweezer light, most likely Raman scattering. A single Raman-scattering event would appear as loss since we only detect molecules in the specific rotational and hyperfine state addressed by the STIRAP lasers. In light of this, we typically operate the tweezers at a low intensity where the lifetime of the state $|G\rangle$ is 2.7(4) s, corresponding to the blue squares in Fig. 4.8(a)(iii), and loss is negligible for the duration of most experiments. This lifetime is still limited by scattering of the trapping light; the vacuum lifetime of atoms in the experiment is > 30 s [206].

The efficiencies of each step of the molecule formation protocol are summarised

in Table 4.1. We successfully convert atom pairs to molecules in the state $|F\rangle$ with an efficiency of 53(1)%, limited by the initial state preparation of the atom pairs (see Sec. 3.4.1). Subsequently, 91(1)% of the molecules in the state $|F\rangle$ are successfully transferred to the ground state $|G\rangle$. The overall efficiency for the conversion of an atom pair to a rovibrational ground-state molecule is therefore 48(2)%.

The maximum probability of molecule recovery that we measure is $P_r = 75(1)\%$. This corresponds to the value after a single round-trip STIRAP in Fig. 4.7. If our scheme for detecting molecule formation was perfect, we would expect to measure 88(1)%, limited by the lifetime of the state $|F\rangle$ and the infidelity of a round-trip STIRAP. However, our detection scheme overestimates molecule formation due to loss of atom pairs prior to magnetoassociation. The overall probability that a detection trap is empty is 60(3)%; a combination of successful molecule formation (53(1)%) and loss of atoms prepared in the wrong hyperfine state (7(2)%, see Sec. 3.4.1). With our detection scheme, these two events are indistinguishable and we assume that a molecule has been formed in both cases. In reality, a molecule is only formed in 88(3)% of cases where the detection trap is empty. Accounting for this, we would expect to measure $P_r = 77(3)\%$, in agreement with our observations.

4.5 Global control of rotational states

The hyperfine structure of RbCs is shown in Fig. 4.9(a) for the lowest four rotational manifolds. Here, the energies of the states are shown as a function of the intensity I_{1066} of the 1066 nm tweezer and the magnetic field is 181.699 G. When performing STIRAP we form molecules in the rovibrational and hyperfine ground state $|G\rangle$ (lowest red line). The transitions that we drive between rotational levels are shown by vertical lines.

Transitions between rotational levels are driven using microwave fields to which strong coupling is facilitated by the molecule-frame electric dipole moment (for RbCs, $d = 1.225\,\mathrm{D}$) [149]. Allowed electric dipole transitions are those with $|\Delta N| = 1$ and $|\Delta M_N| \leq 1$. The strength of the transition is determined by the TDM $\mu_{i,j} = \langle\psi_i|\,\mu\,|\psi_j\rangle$, where the components $(\mu^z_{i,j}, \mu^+_{i,j}, \mu^-_{i,j})$ of $\mu_{i,j}$ describe the strength of π, σ^+, and σ^- transitions respectively. The nuclear spin is not addressed when driving rotational transitions such that we can only couple to hyperfine states with nuclear spins unchanged from those of $|G\rangle$; namely $m_{\mathrm{Rb}} = +3/2$ and $m_{\mathrm{Cs}} = +7/2$. For the work presented here, we drive transitions to either stretched states or hyperfine states with mixed character for which the component with $m_{\mathrm{Rb}} = +3/2$ and $m_{\mathrm{Cs}} = +7/2$ has the largest amplitude. This criterion selects the transitions with the highest

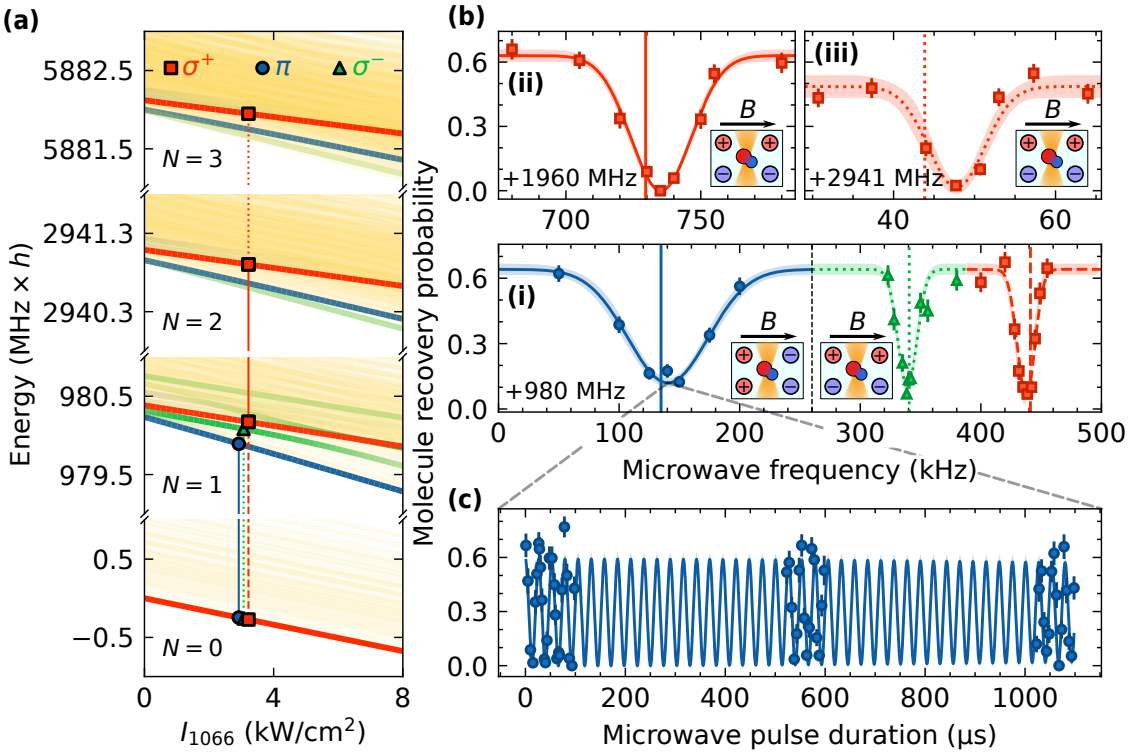

Figure 4.9: Excitation of RbCs molecules to higher rotational states. **(a)** Hyperfine energy structure of the first four rotational manifolds of RbCs as a function of 1066 nm tweezer intensity I_{1066} at a magnetic field of 181.699 G. Energies are given relative to the energy of $|G\rangle$ in free space. The red lines show the spin-stretched hyperfine states of each manifold, where the molecule is initially prepared in the ground state (lowest red line). σ^+, π, and σ^- transitions from each spin-stretched state are shown in red, blue, and green respectively. The yellow lines show other hyperfine states that we do not access. The color of the lines represents the TDM of a given transition: more intense lines have higher TDMs. **(b)** Spectroscopy of the $N = 1, 2, 3$ rotational manifolds for **(i)**,**(ii)**,**(iii)** respectively in a 3.07 kW/cm^2 tweezer. Changing the electrode configuration (insets) allows us to drive either π or $\sigma^{\pm}$ transitions. **(c)** Rabi oscillation on the π transition $|0, 0\rangle \rightarrow |1, 0\rangle$ for a single trapped molecule.

TDMs. For simplicity, we continue to label the states $|N, M_N\rangle$, but give the full state compositions in Table 4.2. Additionally, in Table 4.2, we give each state a label using the scheme of Blackmore *et al.* [289] where states are labelled $|N, M_F\rangle_k$. Here k is an index enumerating states in order of increasing energy such that $k = 0$ is the lowest energy state for given values of N and M_F. The state compositions are calculated for a molecule in a 1065.512 nm tweezer of intensity $I_{1066} = 3.07\,\mathrm{kW/cm^2}$ at a magnetic field of 181.699 G using the molecular constants and polarisabilities that will be introduced shortly. The components of the $N = 1$ states that we to couple with microwave radiation from the state $|G\rangle$ have $m_{\mathrm{Rb}} = +3/2$ and $m_{\mathrm{Cs}} = +7/2$ and are highlighted in bold.

We use the in-vacuum electrodes mounted inside the science cell (see Sec. 2.1) as a microwave antenna to drive coherent transfer between molecular rotational states.

Table 4.2: Rotational and hyperfine states of RbCs used in this work. We give the $|N, M_N\rangle$ label used in the text, the corresponding $|N, M_F\rangle_k$ label, and the state compositions in a 1065.512 nm tweezer of intensity $I_{1066} = 3.07\,\mathrm{kW/cm^2}$ at a magnetic field of 181.699 G. The state components with $m_{\mathrm{Rb}} = +3/2$ and $m_{\mathrm{Cs}} = +7/2$ are shown in bold.

$\lvert N, M_N\rangle$	$\lvert N, M_F\rangle_k$	$\lvert N, M_N, m_{\mathrm{Rb}}, m_{\mathrm{Cs}}\rangle$
$\lvert 0,0\rangle \equiv \lvert G\rangle$	$\lvert 0,+5\rangle_0$	$\mathbf{\lvert 0,0,+3/2,+7/2\rangle}$
$\lvert 1,-1\rangle$	$\lvert 1,+4\rangle_1$	$\mathbf{-0.827\,\lvert 1,-1,+3/2,+7/2\rangle}$
		$-0.438\,\lvert 1,0,+1/2,+7/2\rangle$
		$+0.293\,\lvert 1,+1,-1/2,+7/2\rangle$
		$-0.196\,\lvert 1,0,+3/2,+5/2\rangle$
		$-0.019\,\lvert 1,+1,+3/2,+3/2\rangle$
		$+0.011\,\lvert 1,+1,+1/2,+5/2\rangle$
$\lvert 1,0\rangle$	$\lvert 1,+5\rangle_0$	$\mathbf{-0.971\,\lvert 1,0,+3/2,+7/2\rangle}$
		$+0.236\,\lvert 1,+1,+1/2,+7/2\rangle$
		$-0.039\,\lvert 1,+1,+3/2,+5/2\rangle$
$\lvert 1,+1\rangle$	$\lvert 1,+6\rangle_0$	$\mathbf{\lvert 1,+1,+3/2,+7/2\rangle}$
$\lvert 2,+2\rangle$	$\lvert 2,+7\rangle_0$	$\mathbf{\lvert 2,+2,+3/2,+7/2\rangle}$
$\lvert 3,+3\rangle$	$\lvert 3,+8\rangle_0$	$\mathbf{\lvert 3,+3,+3/2,+7/2\rangle}$
$\lvert 4,+4\rangle$	$\lvert 4,+9\rangle_0$	$\mathbf{\lvert 4,+4,+3/2,+7/2\rangle}$

An additional external dipole Wi-Fi antenna is mounted approximately 10 cm from the vacuum chamber. Using this external antenna we can also drive transitions, albeit with much reduced polarisation control due to the presence of magnetic field coils around the cell.

We demonstrate rotational state control by driving coherent microwave transitions from the ground state $|G\rangle$ to higher rotational states. Excitation to higher rotational states is detected by the failure to recover atom pairs from the (excited) molecules at the end of the experimental sequence due to the state specificity of the reverse STIRAP. We selectively drive either $\sigma^{\pm}$ or π transitions by connecting the electrodes in different configurations to change the orientation of the electric field of the microwave radiation. When the electric field is parallel to the applied magnetic field we drive π transitions; when the two fields are orthogonal we drive $\sigma^{\pm}$ transitions.

Figure 4.9(b)(i) shows spectroscopy from state $|G\rangle$ to the $N = 1$ manifold, with the polarity of the connections to the electrodes shown inset. Here, the magnetic field is 181.699(1) G and the intensity of the 1066 nm tweezer is $I_{1066} = 3.07\,\mathrm{kW/cm^2}$. We measure the frequencies of the π, σ^-, and σ^+ transitions to be 980.140(2) MHz, 980.3391(9) MHz and 980.4374(5) MHz, respectively. The widths of the measured features are transform limited.

The vertical lines in Fig. 4.9(b) show the expected transition frequencies. We calculate these and the state energies shown in Fig. 4.9(a) by solving the molecular Hamiltonian, including the interactions with external optical and magnetic fields.

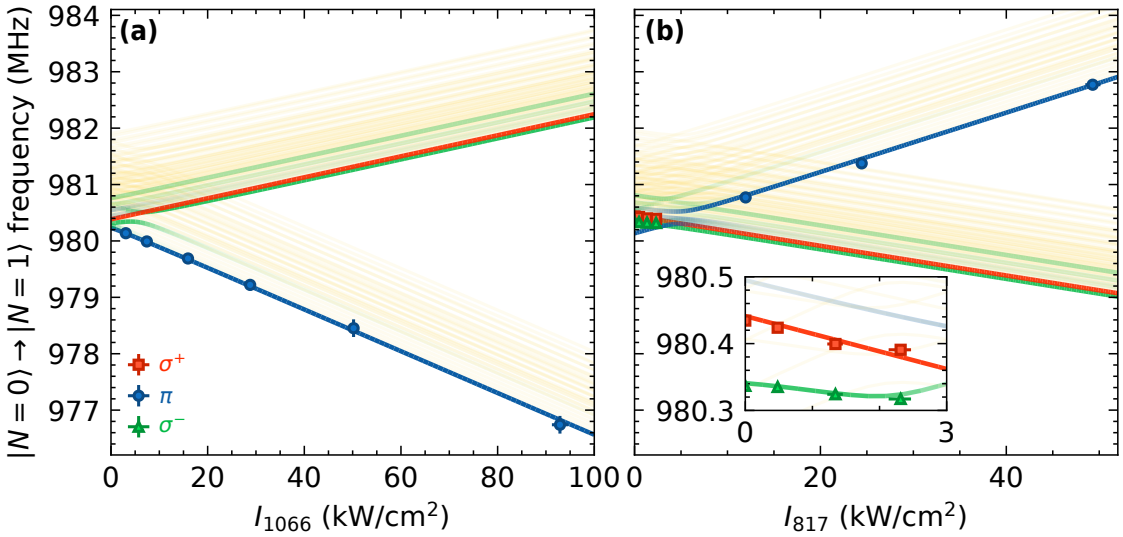

Figure 4.10: Measurements of the anisotropic polarisability of RbCs. Colours of the states are as in Fig 4.9(a). We measure the frequencies of the σ^+ (red squares), π (blue circles), and σ^- (green triangles) transitions from the state $|G\rangle$ for different tweezer intensities at a magnetic field of 181.699(1) G. **(a)** Data for molecules in 1066 nm tweezers of varying intensity I_{1066}. **(b)** Data for molecules in 1066 nm tweezers of intensity 3.07 kW/cm^2 that are addressed with additional 817 nm tweezers of varying intensity I_{817}. The inset shows a zoom to small values of I_{817}. Lines show the calculated state energies obtained by solving the molecular Hamiltonian. For both fits, we assume that the polarisation of the tweezer light is parallel to the quantisation axis set by the magnetic field.

We perform this calculation using the Python package `diatomic-py` [290]. We use the molecular constants determined in previous bulk-gas experiments [97, 280, 289]. The value of the isotropic polarisability $\alpha^{(0)}$ is scaled from that measured by Blackmore *et al.* [291] to account for the difference in trapping wavelengths [217]; here we use $\alpha^{(0)}_{1066} = 2000 \times 4\pi\varepsilon_0 a_0^3$. For this calculation, we need to know the anisotropic polarisability $\alpha^{(2)}_{1066}$, which we measure by performing spectroscopy on the π transition at different tweezer intensities I_{1066}, as shown in Fig. 4.10(a). We perform a least-squares fit on this data to extract $\alpha^{(2)}_{1066} = 1980(60) \times 4\pi\varepsilon_0 a_0^3$, which we use for the calculations shown in Fig. 4.9. For comparison, Blackmore *et al.* measured the anisotropic polarisability at 1064 nm to be $\alpha^{(2)}_{1064} = 1997(6) \times 4\pi\varepsilon_0 a_0^3$ [291]. Using our value of $\alpha^{(2)}_{1066}$, the measured transition frequencies in Fig. 4.9(b) are within 10 kHz of the calculated values; we expect that the discrepancy between the two is primarily caused by our simplifying assumption that the polarisation of the tweezer is exactly aligned to the quantisation axis of the magnetic field.

We observe coherent oscillations between states by changing the duration of the applied microwave pulses. For example, in Fig. 4.9(c) we show the effect of changing the pulse length with the microwave frequency set to that of the π transition $|0,0\rangle \rightarrow |1,0\rangle$ for a single trapped molecule. With a small RF power of -16 dBm

incident to the electrodes, we obtain a Rabi frequency of 37.96(2) kHz and observe no significant damping in the contrast after approximately 40 Rabi oscillations. The microwave field produced by the electrode array is highly linearly polarised. For example, with the field set to drive π transitions, we are not able to resonantly drive the σ^- transition, even when the Rabi frequency on the π transition is increased to 133.7(1) kHz. Setting a conservative upper bound on Rabi frequency with which we drive the σ^- transition of 1 kHz, we extract the linear polarisation purity of the microwave radiation emitted by the electrode array to be in excess of $10^4 : 1$. This enables high-fidelity control of the rotational states.

We probe higher rotational manifolds in the molecule using successive microwave transitions [289]. Here, we restrict ourselves to σ^+ transitions so that we always occupy a stretched hyperfine state in each rotational manifold. For example, in Fig. 4.9(a)(ii) we present spectroscopy of the transition $|1, +1\rangle \rightarrow |2, +2\rangle$. This is measured by first performing a π pulse on the transition $|0, 0\rangle \rightarrow |1, +1\rangle$ to prepare the molecule in $|1, +1\rangle$ prior to the spectroscopy pulse. After the spectroscopy pulse, a third microwave pulse returns any molecules remaining in $|1, +1\rangle$ back to $|0, 0\rangle$ from which atom pairs can be recovered. Molecules that were excited to $|2, +2\rangle$ during the spectroscopy pulse are not returned back to $|0, 0\rangle$, resulting in atom pairs not being recovered. This is easily extended to higher manifolds; we generally prepare molecules in the stretched hyperfine state $|N, N\rangle$ with a series of N coherent π pulses before probing the transition $|N, N\rangle \rightarrow |N + 1, N + 1\rangle$ and returning molecules in $|N, N\rangle$ to $|0, 0\rangle$. For example, in Fig. 4.9(a)(iii), we perform similar spectroscopy of the transition $|2, +2\rangle \rightarrow |3, +3\rangle$ with this procedure. As before, the measured frequencies for these transitions are within 10 kHz of the predicted frequencies indicated by the vertical lines. Extension to more rotational states will allow the realisation of a large number of synthetic lattice sites with fully controllable synthetic inter-site tunnellings for engineering synthetic band structures [74].

4.6 Multi-state readout

Proposed quantum simulators composed of molecules often utilise the rotational states to encode pseudo-spins [42, 292]. The ability to detect multiple rotational states of a molecule in a single iteration of an experiment is therefore highly desirable, particularly given the finite efficiency of molecule formation. For example, without the ability to readout multiple molecular states, it is impossible to distinguish between a molecule which is lost and a molecule in a spin state which is not detected. Here, we describe a technique that can be used to detect the rotational state of a

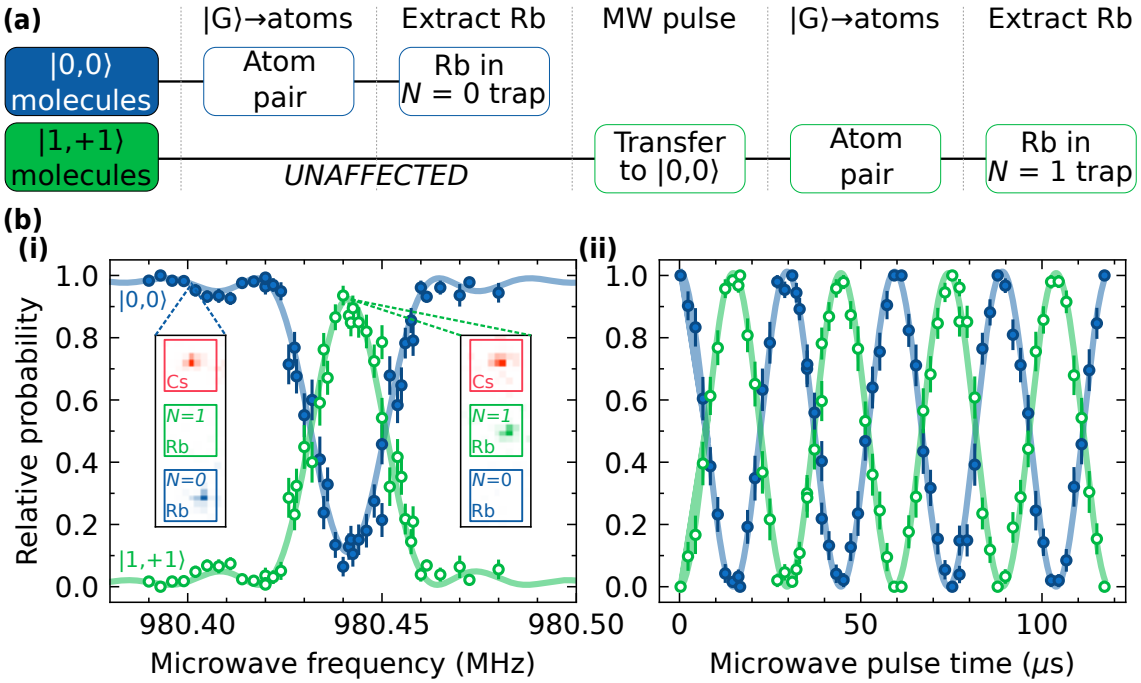

Figure 4.11: Readout of multiple rotational states whilst driving the transition $|0,0\rangle \rightarrow |1,+1\rangle$**. (a)** Flowchart of the detection procedure as described in the text. **(b)** Coherent transfer between $|0,0\rangle$ and $|1,+1\rangle$. The population in state $|0,0\rangle$ ($|1,+1\rangle$) is shown as blue filled (green empty) points. **(i)** Spectroscopy of the transition. The Rabi frequency is set to 11.92(6) kHz and a spectroscopy pulse of duration 39.6 μs (slightly less than a π pulse) is used. The readout π pulse is at 980.4415 MHz. The fitted centre is 980.4412(2) MHz. The insets show the Cs (red) and Rb (green and blue) traps with example fluorescence images obtained from a molecule in states $|0,0\rangle$ (left) and $|1,+1\rangle$ (right). **(ii)** Rabi oscillations on the transition. Here, the Rabi frequency is 33.69(3) kHz and the fitted contrast is consistent with unity.

molecule on a given site whilst avoiding errors caused by molecule loss.

We present an experimental scheme that maps the rotational state of the molecule onto atoms in spatially distinct tweezers, similar to the proposal of Covey *et al.* [293]. In our scheme, we detect the internal state of the molecule by mapping it onto the position of a Rb atom in the final fluorescence image. A flowchart of the detection scheme is shown in Fig. 4.11(a). We exploit the state specificity of the reverse STIRAP transfer: only molecules in the state $|G\rangle$ are converted into atom pairs during the reverse STIRAP pulses and dissociation magnetic field sweeps. Molecules in excited rotational states are unaffected by these stages of the experimental routine. After atom pairs are recovered from molecules that were in the state $|G\rangle$, they are separated and the Rb atoms are stored in a row of 817 nm tweezers. We then return to the usual operating magnetic field to transfer molecules in excited rotational states back to state $|G\rangle$ with a series of microwave pulses and repeat the dissociation steps. However, this time when separating the resultant atom pairs, we place the Rb atoms in a *different* row of 817 nm tweezers. After all the molecules have been dissociated

into atom pairs, the magnetic field is reduced to 4.78 G and a final fluorescence image is taken. With this image, we can detect the rotational state of the molecule prior to the readout procedure by observing which tweezer the Rb atoms populate. Using mid-sequence detection of Rb atoms would allow this procedure to be repeated multiple times. This would enable many internal molecular states to be readout in a single experimental run, ideal for implementations of qudits [60] or quantum error correction using the internal states of the molecule [59].

This detection scheme allows us to mitigate the effects of noise in our experimental data. Such noise can result from fluctuations in the molecule formation efficiency or molecule loss which reduces the recovery probability P_r. We are also able to eliminate leakage errors that occur when molecules leave a chosen set of energy levels. The lowest rotational levels of RbCs have lifetimes exceeding 1000 s limited by blackbody radiation [294]. Consequently, leakage errors due to off-resonant excitation during microwave transfers, for example, are much more likely than bit-flip errors for RbCs qubits. Using this detection scheme, we specify the energy level subspace that we wish to readout with the choice of microwave pulses prior to converting the molecules back to atom pairs.

In Fig. 4.11(b) we present example measurements performed with this detection scheme. Fig. 4.11(b)(i) shows spectroscopy on the σ^+ transition between the states $|0,0\rangle$ (blue filled circles) and $|1,+1\rangle$ (green empty circles). Here, we set the microwave power so that the Rabi frequency with which we drive the transition is 11.92(6) kHz. This avoids significant off-resonant excitation on the σ^- transition which is detuned by $-96(1)$ kHz, as shown in Fig. 4.9(b)(i). We use a square pulse of duration 39.6 µs, which is slightly less than that of a π pulse. After this pulse, molecules that remain in $|0,0\rangle$ are converted back to atom pairs from which Rb atoms are moved to the "$N = 0$ detection" traps (insets, blue square). Molecules in $|1,+1\rangle$ are then transferred back to $|0,0\rangle$ with a π pulse at 980.4415 MHz. We convert these molecules back to atom pairs and deposit the Rb atoms into the "$N = 1$ detection" traps (insets, green square). Cs atoms always remain in the 1066 nm traps in which the molecules are formed (insets, red square). We post-select data to consider only experimental runs in which both a Cs atom and a Rb atom (in either of the two detection traps) are successfully recovered from an initial atom pair. The relative occupation of Rb atoms in the detection traps is used to infer the state of the molecule before the detection procedure. This detection scheme allows us to resolve features that would otherwise be difficult to discern above the experimental noise, such as the sidelobes in the sinc-squared function with which we fit the data.

Figure 4.11(b)(ii) shows a Rabi oscillation when the microwaves are set to be resonant with the σ^+ transition. Here, the Rabi frequency with which we drive the

transition is 33.69(3) kHz: this is still low enough to avoid significantly driving the σ^- transition. The sequence is the same for the measurement shown in Fig. 4.11(b)(i), but the readout pulse duration is reduced so that it remains a π pulse at the higher Rabi frequency. The fitted contrast of the Rabi oscillations is consistent with unity and we do not observe dephasing over the range of pulse durations shown here.

The error bars in Fig. 4.11(b) represent the statistical uncertainties obtained from 100 repetitions of the experiment using an array of four molecules. The statistical uncertainty dominates over the systematic errors in the multi-state readout scheme. The primary source of systematic error is the preferential loss of molecules in a particular rotational state. This cannot cause a molecule to be detected in the wrong rotational state, but can skew the ratio of the relative populations in the two states. To assess the impact of loss on the relative populations, we analyse the raw molecule recovery probabilities for the data presented in Fig. 4.11(b)(ii). The peak recovery probability of molecules in the state $|0,0\rangle$ is 23.8(5)%, whereas the peak recovery probability of molecules in the state $|1,+1\rangle$ is 21.7(5)%. This corresponds to a relative recapture probability $r = 91(3)\%$ for molecules in state $|1,+1\rangle$ relative to molecules in the state $|0,0\rangle$. The detection error is maximised to a value of $[1/(1+r) - 1/2]$ when the true occupation of the two states is equal. Here, this corresponds to a maximum error of 2.3(8) %. As the true occupation of one of the states approaches unity, this resultant error decreases and eventually vanishes.

There are two main contributions to the preferential loss of molecules in the state $|1,+1\rangle$ that lead to the lower observed recovery probability. The first is loss due to scattering of the tweezer light during the time it takes to perform the readout of molecules in the state $|0,0\rangle$. The duration of this stage is dominated by the ~ 10 ms required for the magnetic field to settle after separating the atom pairs that result from the dissociation of molecules in the state $|0,0\rangle$. This leads to loss of approximately 1 % of the molecules in the state $|1,+1\rangle$. Additionally, if the field has not completely settled, the efficiency of the second STIRAP transfer can be slightly reduced. The second source of loss is off-resonant excitation from $|1,+1\rangle$ to states with $N' = 2$ in the excited electronic manifold $A^1\Sigma^+ + b^3\Pi$ [295] when the Stokes light is applied during the readout of molecules in the state $|0,0\rangle$.

Errors that would lead to the incorrect assignment of the molecular state are vanishingly rare. The selection rules governing the transitions used in STIRAP mean that the return transfer of molecules from the state $|1,+1\rangle$ is forbidden by parity [149], so these molecules cannot result in an atom in the $N = 0$ detection traps. For a molecule in the state $|0,0\rangle$ to be detected as a molecule in the state $|1,+1\rangle$ would require it to remain in the state $|0,0\rangle$ during the first dissociation stage and then be unaffected by the microwave π pulse used for readout of molecules in the state

$|1,+1\rangle$. This is extremely unlikely.

4.7 Local control of rotational states

Controlling the rotational states of individual molecules within an array is essential for a range of applications. For example, preparing reactants in distinct rotational states facilitates studies of state-controlled quantum chemistry [296]. Additionally, certain quantum computation architectures using ultracold molecules require the selective excitation of molecules to perform single qubit gates [54] or to execute entangling gates between chosen pairs of molecules using microwave fields [58]. The targeted transfer of subsets of molecules into non-interacting states allows them to be shelved for mid-circuit readout, enabling measurement-based quantum computation [297, 298] or the study of measurement-induced phase transitions [299].

We demonstrate site-resolved control of the rotational state using an additional array of 817 nm tweezers to address selected molecules. The additional tweezers cause a differential light shift between molecular states, altering the microwave transition frequency on the addressed sites. First, we characterise the differential light shift by measuring the frequency of the transitions from the state $|G\rangle$ to the states $|1,-1\rangle$, $|1,0\rangle$, and $|1,+1\rangle$ at different intensities of the addressing tweezers. This measurement is shown in Fig. 4.10(b) with the σ^-, π, and σ^+ transitions shown as green triangles, blue circles, and red squares respectively. For this measurement, molecules are trapped in the 1066 nm array with trap intensities $I_{1066} = 3.07\,\mathrm{kW/cm^2}$. We overlap the addressing array with this array and vary the intensity I_{817} of the addressing array. We fit the transition frequencies, taking into account the polarisabilities for both tweezers, to obtain $\alpha^{(2)}_{817} = -2814(12) \times 4\pi\varepsilon_0 a_0^3$.

An example of selectively addressing certain molecules is shown in Fig. 4.12(a). For this measurement, every other trap in an eight-trap array is addressed with an 817 nm tweezer, as indicated by the green rectangles in Fig. 4.12(b). The addressing tweezers are ramped up to an intensity of $2.18\,\mathrm{kW/cm^2}$ after the molecules have been prepared in the state $|G\rangle$. We then perform microwave spectroscopy on the array. Following this, the addressing light is removed such that all molecules are resonant with the microwave π pulse required for the multi-state readout (see Sec. 4.6) and the reverse STIRAP. The results in Fig. 4.12(a) show that the additional 817 nm tweezer light causes the frequency of the $|0,0\rangle \rightarrow |1,+1\rangle$ transition to shift by $-80(2)$ kHz in the addressed molecules (green filled circles) relative to the unaddressed molecules (purple empty circles). We note the increase in the size of the error bars for unaddressed molecules at a detuning of around -100 kHz. This results from these

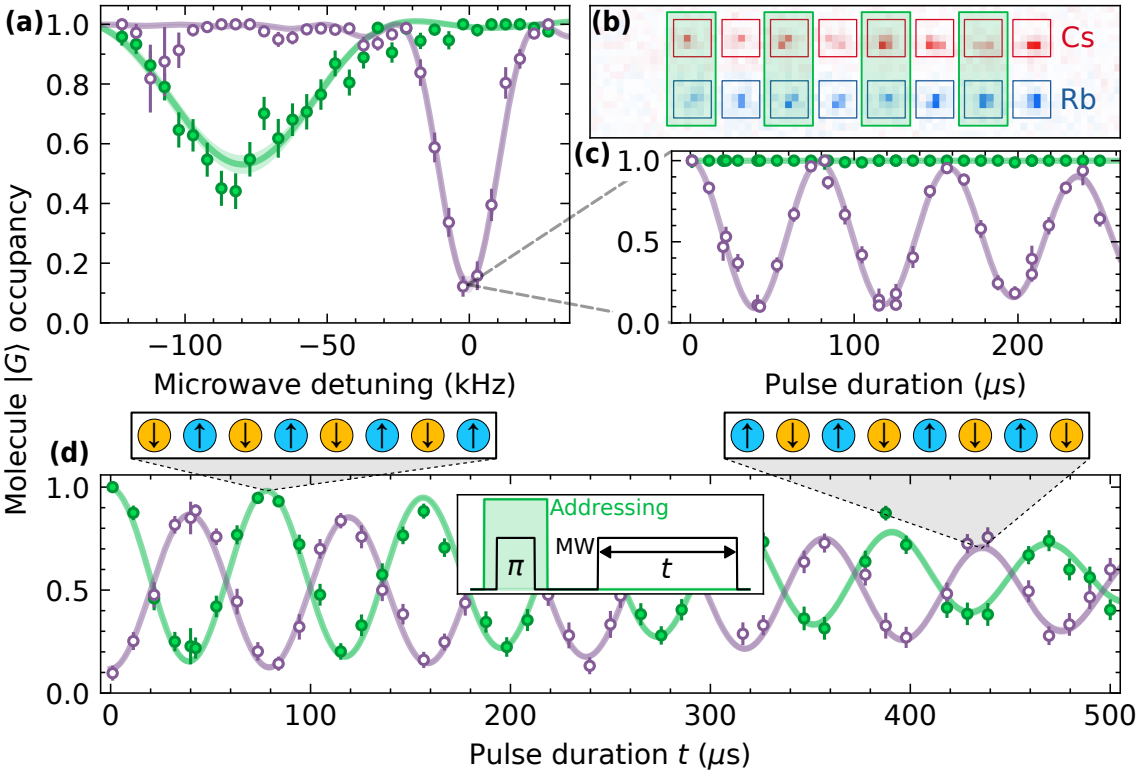

Figure 4.12: Local control of rotational states in an array of molecules. **(a)** Selected molecules are addressed with an additional 817 nm tweezer that light shifts the transition of these molecules (green filled points) relative to the unaddressed molecules (purple empty points). **(b)** Image of atoms that form the molecular array showing which sites are addressed (green highlight). **(c)** With an applied light shift of approximately -200 kHz $\times$ h applied to the addressed molecules, we drive a Rabi oscillation in only unaddressed molecules. **(d)** Preparation and manipulation of alternating spin chains of molecules. An initial π pulse transfers only unaddressed molecules to $|\uparrow\rangle$. The addressing is then removed to coherently rotate the spins of all molecules in the array.

molecules being excited on the σ^- transition such that the number of molecules remaining in the $\{|0,0\rangle, |1,+1\rangle\}$ subspace from which we sample is greatly reduced.

When the induced light shift is much larger than the Rabi frequency of our chosen transition, we are able to drive transitions in *only* the unaddressed molecules. We demonstrate this in Fig. 4.12(c) where we increase the intensity of the addressing tweezers such that the shift in the frequency of the transition due to the addressing light is approximately -200 kHz. We then apply microwave radiation that is resonant for the unaddressed molecules to drive a Rabi oscillation in only these molecules. After a π pulse, we observe no transfer of the addressed molecules out of the state $|G\rangle$ and place a 1σ upper bound of 1.0% on the probability of driving an undesired excitation. We choose to target unaddressed molecules as fluctuations in the relative alignment of the trapping and addressing tweezers cause variations in the induced light shift and broaden the transitions of the addressed molecules.

We dynamically switch the addressing on and off during the experimental sequence to change between driving molecular transitions locally and globally. As an example, Fig. 4.12(d) shows the result of an experiment where we form an alternating spin chain of molecules with $|\downarrow\rangle \equiv |0,0\rangle$ and $|\uparrow\rangle \equiv |1,1\rangle$ and then drive Rabi oscillations in the whole array. The molecule formation stages initialise the array in the state $|\downarrow\rangle$. As before, half of the molecules in the array are then addressed with 817 nm light. A π pulse on the $|\downarrow\rangle \rightarrow |\uparrow\rangle$ transition is then driven in only the unaddressed molecules to prepare an alternating spin chain. We then remove the addressing light such that a second microwave pulse drives the rotational transition for all molecules in the array. This pulse rotates all the spins in the chain such that two adjacent molecules are always out of phase with each other. The dephasing evident in Fig. 4.12(d) is primarily caused by different trap depths across the array of eight molecules. This leads to a variation in the differential light shifts along the spin chain, such that the microwave field is not exactly resonant with all the molecules. In future work, we plan to address this problem by using an array of tweezers at a magic wavelength, where $\alpha^{(2)}$ is zero, such that the differential light shift between the states $|\downarrow\rangle$ and $|\uparrow\rangle$ is eliminated [98].

4.8 Deterministic array preparation

We now demonstrate the preparation of defect-free arrays of molecules. The primary source of configurational entropy in our array is the finite conversion efficiency of atom pairs to molecules which leads to some tweezers not containing molecules. We remove this entropy by detecting the traps where molecule formation failed using the procedure described in Sec. 4.3. Unlike the experiments presented thus far, in this experiment we perform the detection mid-sequence and use the information to rearrange molecules to occupy sites where formation failed.

Mid-sequence detection of molecule formation errors requires imaging Rb atoms at the magnetic field of 181.699(1) G used for STIRAP. At the normal imaging field of 4.78 G, the state $|G\rangle$ is no longer the lowest in energy and the hyperfine levels are more closely spaced. Imaging at high magnetic field therefore avoids potential loss of molecules to other states due to sweeping the magnetic field through numerous level crossings. Rb atoms in the detection array are imaged on the closed transition $(5s_{1/2}, f = 2, m_f = +2) \rightarrow (5p_{3/2}, f' = 3, m'_f = +3)$ (hereafter $(2,+2)$ and $(3',+3')$, respectively).[5] This approach has previously been used for non-destructive hyperfine-state readout of individually trapped Rb atoms [300, 301]. As the Rb

[5]For this section, we label the state of Rb atoms as (f, m_f) and (f', m'_f) (in round brackets) to avoid confusion with molecular states labelled $|N, M_N\rangle$ (in kets).

atoms are initially in the state $(1,+1) \equiv (5s_{1/2}, f = 1, m_f = +1)$ required for molecule formation, they are transferred to the state $(2,+2)$ with microwave adiabatic rapid passage (ARP) before imaging. This ARP transfer is implemented using the loop antenna mounted outside the vacuum chamber (see Sec. 2.1). With this antenna we produce microwave radiation that couples the states $(1,+1)$ and $(2,+2)$ with a Rabi frequency of 7.6(3) kHz. We use a magnetic field sweep of 72 mG in 2.5 ms to adiabatically transfer the atoms into $(2,+2)$. For this Rabi frequency, the efficiency of the transfer is limited to 90% due to magnetic field noise. In future experiments we plan to increase the coupling strength to improve the transfer.

We then image the Rb atoms on the closed transition $(2,+2) \rightarrow (3',+3')$ with resonant circularly polarised light (see Sec. 2.3.1). The peak intensity of this light is $10I_{\text{sat}}$. The primary limitation to the achievable imaging fidelity is the loss of Rb atoms before the number of scattered photons that are detected is sufficient to differentiate occupied traps from the background. This loss is caused by the recoil momentum imparted by imaging photons heating atoms out of the traps. To combat this, we image the atoms in deep tweezers of peak depth $U_0 = 2.5(1)\,\text{mK} \times k_B$. We modulate the imaging and trapping light in antiphase; this avoids light shifts caused by the deep traps which would otherwise cause broadening of the signal histograms and loss from dipole-force fluctuations [302]. The duty cycle of the trapping (imaging) light is approximately 80% (10%) and we estimate that approximately 10^4 photons are scattered before the atoms are lost.

To enhance the preparation efficiency in (2,+2) beyond the 90% achievable with ARP alone, and consequently improve the Rb detection fidelity, we implement additional optical pumping methods. We apply the optical pumping light (see Sec. 2.3.1) which is resonant with the $(1,+1) \rightarrow (2',+2')$ transition at 4.78 G, but off-resonant at the magnetic field at which we form molecules (181.699(1) G). Further, we apply microwaves resonant with the $(1,+1) \rightarrow (2,+2)$ transition during imaging to continuously pump atoms from the dark state $(1,+1)$ to the bright state $(2,+2)$. We find these steps pump $> 99\,\%$ of the atoms into the bright state for imaging.

Figure 4.13(a) shows a histogram of camera counts from a single Rb trap obtained using the high-field imaging procedure. Trap occupancy is determined by comparing whether the observed counts are above or below a predefined threshold. The lines in Fig. 4.13(a) show the error in the occupancy assignment as this threshold is changed; the blue dashed line is the false-positive error ε_p and the red dashed line is the false-negative error ε_n. The black solid line is the average error probability ε, from which we extract a value of 3% when the threshold is optimised.

In Fig. 4.13(b) we verify the performance of the detection scheme by varying the ratio of tweezer intensities I_{817}/I_{1066} during the Rb extraction step. When I_{817} is too

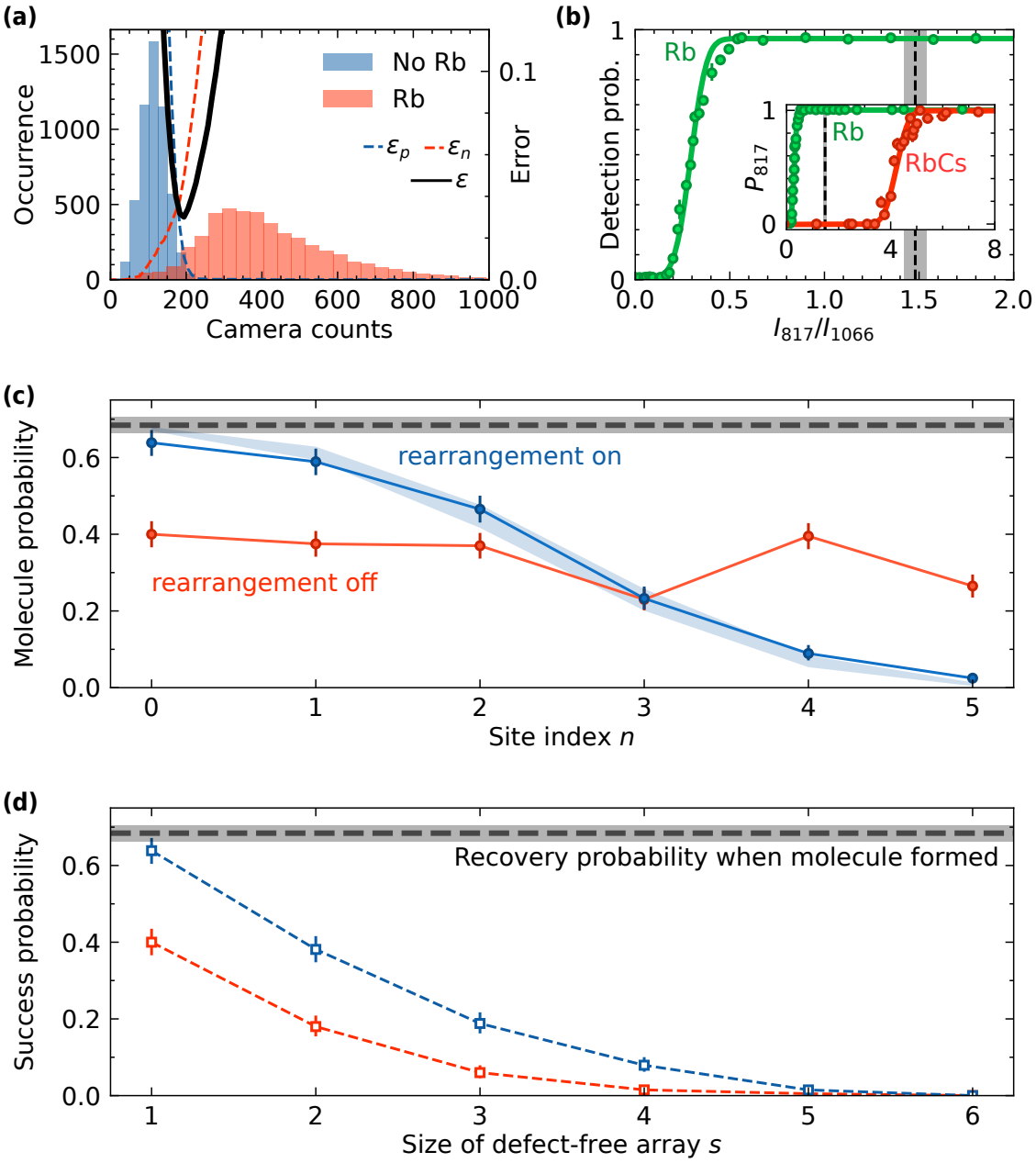

Figure 4.13: Rearrangement of assembled molecules. **(a)** Histogram of camera counts obtained using high-field imaging of Rb atoms. Red (blue) data are counts obtained when an atom is (is not) present. The blue and red dashed lines are the probabilities of false-positive (ε_p) and false-negative (ε_n) errors, respectively, as the occupancy threshold is changed. The black solid line is the average error ε. **(b)** The probability of detecting Rb in the detection trap as a function of the intensity ratio between the 817 nm and 1066 nm tweezers, I_{817}/I_{1066}, during the Rb extraction. The vertical dashed line indicates the value used in a typical sequence. The inset shows the probability P_{817} of extracting Rb (green) and RbCs (red) with the 817 nm tweezer for higher values of I_{817}/I_{1066}. **(c)** The probability of molecule recovery P_r^* for each site n of the array. Blue (red) points show data with (without) molecule rearrangement for an initial array of six atom pairs. No post-selection on successful molecule formation is performed; the black dashed line shows the measured recovery probability (0.68(2)) for a molecule that is formed and left in a single trap. The blue shaded region shows the prediction of a Monte Carlo simulation of the rearrangement. **(d)** The probability of successfully recovering defect-free arrays of size s, starting from site zero, with (blue) and without (red) rearrangement.

low, no Rb atoms are moved into the detection tweezers and a non-zero probability of detection corresponds to a false positive. Conversely, when I_{817} is high, all remaining Rb atoms are transferred to the detection tweezer and a probability below unity corresponds to a false negative. From the fit to Fig. 4.13(b) we find the combined procedure of Rb extraction and imaging gives a false-positive rate of 0.7(1)% and a false-negative rate of 3.6(1)%. The latter is dominated by a $\sim 2\%$ probability for loss of the Rb atom prior to imaging. This value is consistent with the trap lifetime of Rb atoms in the experiment ($\sim 30\,\mathrm{s}$) and the duration of a typical experimental routine after Rb has been loaded ($\sim 500\,\mathrm{ms}$). The vertical dashed line in Fig. 4.13(b) shows the intensity ratio of 1.48(6) used for mid-sequence detection. This value is chosen to saturate the Rb detection fidelity whilst leaving molecules in their original traps, as shown in the inset.

We use the real-time information obtained from the high-field image to identify traps in which molecule formation was successful and rearrange the molecules to one side of the array. Molecule occupancy is assigned by inverting the measured Rb occupancy in the corresponding traps of the detection array. Molecules are then transferred from the 1066 nm array to an overlapping 817 nm array and unoccupied molecule traps are extinguished. Occupied molecule traps are then shuttled to one end of the array before the molecules are transferred back into the 1066 nm array.

We show the molecule recovery probabilities P_r^* obtained using this rearrangement scheme in Fig. 4.13(c). Here, we do *not* post-select statistics based on successful molecule formation, unlike in the experiments presented in earlier sections. For these measurements, exactly six atom pairs are prepared in the 1066 nm array which we attempt to associate into molecules and transfer to state $|G\rangle$. For points with rearrangement enabled (blue), molecules are shuttled to the end of the array; for points with rearrangement disabled (red), the molecules are left in their original traps. We then reverse the association routine and image resultant atom pairs to determine P_r^*.

With rearrangement disabled, the molecule recovery across the array is approximately uniform with an average of 34(1)%. This is consistent with the 36(2)% that we expect from combining the typical molecule formation efficiency of 53(1)% with the molecule recapture probability $P_r = 68(2)\%$ obtained with this experimental routine when post-selecting on successful molecule formation. The molecule recapture probability is reduced from the value reported in Sec. 4.4 due to increased time spent in the tweezers during imaging and the additional time required for calculating the rearrangement sequence. Variations in P_r^* (the probability that a molecule is formed *and* recovered) across the array primarily stem from variations in the probability of molecule *formation*. Molecules are formed only from atom pairs in the ground

state of relative motion. Site-to-site differences in the intensities of the tweezers affect the cooling of the atoms to the motional ground state. Furthermore, angular misalignments across the array cause heating during the merging process. These effects cause variations in the probability of molecule formation, and therefore P_r^*, across the array.

When rearrangement is enabled, the average molecule recovery in the array remains 34(1)% but the distribution is no longer uniform, being weighted significantly towards the low-index sites in the array as intended. The observed recovery in the array agrees well with the prediction of a Monte Carlo simulation of the rearrangement, indicated by the blue shaded region in Fig. 4.13(c). In this simulation, we populate the initial array of molecules by generating a random number, x_n, between 0 and 1 for each site in the array. If x_n is lower than the measured molecule formation efficiency for that site, then the site is deemed to be occupied. Once the initial occupancy of the array is determined, all molecules are shuttled to fill the traps with the lowest site indices. We assume that no molecules are lost during this process. This is repeated for 500 initializations of the array, and the average occupancy of each site is determined. The site occupancies are then scaled by the measured value of P_r. The shaded region shows the 1σ bounds on the simulation results, obtained by repeating it 500 times using different values of the molecule formation efficiency and P_r, both sampled from Gaussian distributions centered about their measured values with standard deviations equal to their experimental uncertainties.

Figure 4.13(d) shows the probability of successfully observing a defect-free array of size s. With rearrangement enabled, this probability scales as $(P_r)^s$ due to the loss of molecules prior to the final fluorescence image.

4.9 Summary

In this chapter, we have detailed how we transfer weakly bound molecules, which are individually trapped in optical tweezers, to their rovibrational ground state. We have quantified the efficiency of each step in this process: overall we convert 48(2)% of atom pairs into ground-state molecules. We have established a suite of experimental techniques for the quantum control of these molecules. We have described an adaptable technique for detecting molecule formation errors. Further, we have demonstrated global and local control of multiple rotational states of the molecules and have combined this with a technique for the detection of multiple rotational states in a single experimental run. Finally, using mid-sequence detection of formation errors, we have demonstrated rearrangement of assembled molecules.

5 Rydberg atoms

Some of the results in this chapter have been published in the Supplemental Material of Ref. [202].

In this chapter, we detail how we excite Rb atoms in the ground state to Rydberg states with high principal quantum number. Rydberg atoms are highly tuneable and possess large dipole moments that allow them to interact strongly with each other and other dipolar systems at long range. This makes them ideal candidates to mediate the transfer of quantum information between polar molecules.

We start with a brief introduction to Rydberg physics. We then detail the characterisation of Rydberg excitation in our experiment. We explore how specific atoms can be excited to Rydberg states and study interactions between Rydberg atoms. These techniques provide the foundation to study interactions between Rb Rydberg atoms and RbCs molecules.

5.1 Introduction to Rydberg atoms

A Rydberg atom is an atom in an excited state where one (or more) of its electrons has been promoted to an energy level with a high principal quantum number $n \gg 1$ [161, 303]. Here, we consider alkali atoms that have a single electron that can be excited to a Rydberg level. In free space, the binding energy E^{B} of the excited electron is given by [161]

$$E^{\mathrm{B}} = -\frac{\mathcal{R}}{(n-\delta_\ell)^2}\,. \tag{5.1}$$

Here, n is the principal quantum number of the Rydberg state, $\mathcal{R}$ is the Rydberg constant,[1] and δ_ℓ is the quantum defect of the state that strongly depends on ℓ.[2]

[1] Strictly speaking, $\mathcal{R} = \mathcal{R}_\infty M/(M+m_e)$ is the *mass-corrected* Rydberg constant that accounts for the mass M of the nucleus. Here, $\mathcal{R}_\infty = e^4 m_e/(8\varepsilon_0^2 h^2) \approx 13.6\,\mathrm{eV} \approx 3290\,\mathrm{THz} \times h$ [304]. For heavy alkalis, like Rb and Cs, $\mathcal{R} \approx \mathcal{R}_\infty$.

[2] The screened Coulomb potential experienced by the excited electron in an alkali Rydberg atom does not follow a $1/r$ dependence with distance r from the ionic core [161]. This causes the dependence of δ_ℓ on ℓ and, to higher orders, n and j. Values of quantum defects in alkali atoms

This structure is similar to the energy levels of a hydrogen atom, where the principal quantum number has been replaced by an effective principal quantum number $n^* \equiv n - \delta$.

Rydberg atoms display highly exaggerated properties that depend strongly on n [50]. The average radius of a Rydberg atom scales with n^2, and can reach $\sim 100\,\text{nm}$ for typically-used Rydberg levels (those with $50 \lesssim n \lesssim 100$). The large distance between the negatively charged electron and positively charged core means that the Rydberg atoms can exhibit very large electric dipole moments and are highly sensitive to external fields. Rydberg atoms can interact with other Rydberg atoms and polar molecules at long range, and typical interaction energies can be on the megahertz (or larger) scale for particle separations on the micrometre scale [50, 101, 102]. Two Rydberg atoms that are resonant with each other can interact via a dipole-dipole interaction,[3] which scales with the interatomic distance R_{aa} as R_{aa}^{-3}. The strength of this dipole-dipole interaction scales as n^4. The dominant interaction between two non-resonant Rydberg atoms is van der Waals, scaling with distance as R_{aa}^{-6} and with principal quantum number as n^{11}. Additionally, the relatively small wavefunction overlap between Rydberg states and atomic ground states means that they are long lived, with typical radiative lifetimes of $\sim 100\,\mu\text{s}$ that scale as n^3. These properties make Rydberg atoms attractive candidates for constructing quantum simulators and computers.

5.2 Excitation scheme

We transfer Rb atoms from the ground manifold $5s_{1/2}$ to the Rydberg states with a two-photon excitation scheme. A diagram of this scheme is shown in Fig 5.1(a). The scheme uses a laser at wavelength 420 nm that drives the transition $|5s_{1/2}\rangle \rightarrow |6p_{3/2}\rangle$ and a 1013 nm laser that drives the transitions from the manifold $6p_{3/2}$ to a variety of Rydberg states.[4] These two lasers are locked to the same ULE cavity as the STIRAP lasers, and their frequency stabilisation is discussed in Sec. 2.5.

We choose to use a two-photon excitation scheme as opposed to a one-photon excitation scheme for two reasons. Firstly, using two-photons allows us to access a wider range of Rydberg states, as we can either excite to s ($\ell = 0$) or d ($\ell = 2$)

have been measured experimentally [305–315] and programs like `ARC` [304] and `pairinteraction` [316] tabulate these values.

[3] By "resonant" we mean that there exists two dipole-coupled pair states have equal energy. This can occur for two atoms of the same or different species. The extension of this principle to a system of a Rydberg atom and a polar molecule is discussed in Ch. 7.

[4] To access various Rydberg states, we tune the wavelength of the second laser between 1012 nm and 1015 nm. For convenience, we always refer to this laser as the 1013 nm laser.

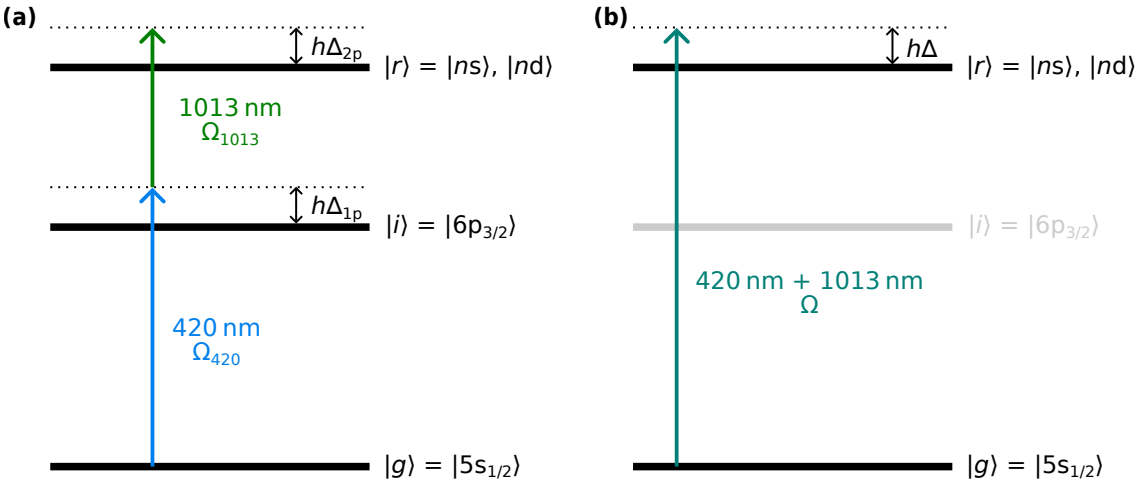

Figure 5.1: Energy levels used during Rydberg excitation of Rb atoms. (a) Bare atomic energy levels. **(b)** Effective two-level system after the adiabatic elimination of the intermediate level.

states versus the p ($\ell = 1$) states that we would be able to access with one photon. This wider choice of states is advantageous when engineering resonant interactions between atoms and molecules (see Ch. 7). Second, if we were to use a one-photon excitation scheme, the wavelength of that laser would be in the UV region. For example, to access the Rydberg state $|83\text{p}\rangle$, we would need a photon of wavelength 297 nm. This wavelength range is much more difficult to work with than the visible and near-infrared (IR) lasers that we use. Additionally, the TDMs between ground and Rydberg states are small and scale as $n^{-3/2}$ [50], which means that a lot of optical power ($\sim$ W) is needed to drive transitions at reasonable ($\sim$ MHz) Rabi frequencies, which is hard to source at UV wavelengths.

We consider the Hamiltonian of the system shown in Fig. 5.1(a). There are three states in this system: the ground state $|g\rangle$, the intermediate state $|i\rangle$, and the Rydberg state $|r\rangle$. The Rabi frequency with which we drive the first stage ($|g\rangle \rightarrow |i\rangle$) is Ω_{420} and the Rabi frequency of the second stage ($|i\rangle \rightarrow |r\rangle$) is Ω_{1013}. We allow the lasers to be off-resonant with the bare atomic transitions. The one-photon detuning of the 420 nm laser is $\Delta_{1\text{p}}$ and the two-photon detuning (i.e. the difference between the combined energy of the two lasers and the energy of the transition $|g\rangle \rightarrow |r\rangle$) is $\Delta_{2\text{p}}$. The Hamiltonian describing this system is

$$\hat{H} = \frac{h\Omega_{420}}{2}(|g\rangle\langle i| + |i\rangle\langle g|) + \frac{h\Omega_{1013}}{2}(|i\rangle\langle r| + |r\rangle\langle i|) - h\Delta_{1\text{p}}|i\rangle\langle i| - h\Delta_{2\text{p}}|r\rangle\langle r| \ . \quad (5.2)$$

Typical one-photon Rabi frequencies obtained with resonable laser powers are on the order of 10 MHz. The dominant source of decoherence in this system is spontaneous emission from the intermediate state $|i\rangle$, which, for typical systems, has a radiative decay rate $\Gamma_i \sim$ MHz. The typical radiative decay rate of the Rydberg state $|r\rangle$ is

on the order of kHz, so Rydberg decay occurs on timescales much slower than the excitation and can be ignored.

We operate in the regime where $\Delta_{1p} \gg \{\Omega_{420}, \Omega_{1013}, \Gamma_i\}$. In this regime we can adiabatically eliminate the state $|i\rangle$ [317] and create an effective two-level system where the state $|g\rangle$ is coupled with the state $|r\rangle$. This system is shown in Fig. 5.1(b) and is described by the Hamiltonian [317]

$$\hat{H} = \frac{h\Omega}{2}(|g\rangle\langle r| + |r\rangle\langle g|) - h\Delta\,|r\rangle\langle r|\,. \tag{5.3}$$

Here, the two-photon Rabi frequency is

$$\Omega = \frac{\Omega_{420}\Omega_{1013}}{2\Delta_{1p}}\,, \tag{5.4}$$

and the effective detuning is

$$\Delta = \Delta_{2p} + \delta\,, \tag{5.5}$$

where

$$\delta = \frac{\Omega_{420}^2 - \Omega_{1013}^2}{4\Delta_{1p}} \tag{5.6}$$

is the differential ac Stark shift caused by the excitation lasers. Working in this regime does not completely remove decoherence caused by the off-resonant coupling to and subsequent decay of the state $|i\rangle$, but the effective decay rate Γ_i' is significantly reduced to [318]

$$\Gamma_i' = \frac{\Omega_{420}^2 + \Omega_{1013}^2}{4\Delta_{1p}^2}\Gamma_i\,. \tag{5.7}$$

The excitation scheme that we use, where we excited via a virtual state close to the manifold $6p_{3/2}$, is commonly called the *inverted* Rb excitation scheme. This is opposed to exciting via a virtual state close to the the manifold $5p_{3/2}$ (or the manifold $5p_{1/2}$) which requires a 780 nm (795 nm) photon for the first stage and a 480 nm (475 nm) photon for the second stage. The inverted excitation scheme offers several advantages over schemes using the manifold $5p_{3/2}$. Firstly, the radiative lifetimes of the states in the manifold $6p_{3/2}$ are approximately five times longer than those in the manifold $5p_{3/2}$ so the spontaneous decay rate is significantly reduced ($\Gamma_{6p_{3/2}} \approx 1.3\,\text{MHz}$ [319] and $\Gamma_{5p_{3/2}} \approx 6.0\,\text{MHz}$ [211]). Furthermore, the laser that drives the second stage transition $|i\rangle \to |r\rangle$ is at 1013 nm rather than 480 nm. Due to the small overlap in the wavefunctions of the intermediate and Rydberg states, it is advantageous to have as much laser power as possible for the second stage, and high-power laser technology is more developed (and cheaper) at this larger wavelength.

From the manifold $6p_{3/2}$ (where $\ell = 1$), the selection rule $|\Delta\ell| = 1$ means we can access either s ($\ell = 0$) or d ($\ell = 2$) Rydberg states. There is no selection rule on the

principal quantum number n and we can tune the frequency of the 1013 nm laser to access Rydberg manifolds of different n. In Fig. 5.2(a), we show the excitation pathways that we use to access the two Rydberg manifolds that we use for the majority of this work, namely $52s_{1/2}$ and $83d_{5/2}$. These manifolds are chosen because they have favourable properties for interactions between Rb Rydberg atoms and RbCs molecules; these properties are covered in detail in Chs 6 and 7.

For the magnetic fields used in this work ($\lesssim 200$ G), the ground manifold $5s_{1/2}$ is in the Zeeman regime where f and m_f are good quantum numbers [211]. We typically excite Rb atoms to Rydberg states from the states $|f, m_f\rangle = |1, +1\rangle$ or $|2, +2\rangle$ in this manifold. In contrast, the hyperfine coupling for Rydberg states is weak enough that it can be ignored and the good quantum numbers are m_j and m_i.[5] We do not resolve the hyperfine splitting and typically label the Rydberg states as $|n\ell_j, m_j, m_i\rangle$.

Most of the experiments in which we excite to the manifold $52s_{1/2}$ were performed first. For these experiments, we excite from the ground state $|5s_{1/2}, f = 1, m_f = +1\rangle$ using the excitation scheme shown in Fig. 5.2(a)(i). Both lasers are linearly polarised with their electric field parallel to the applied magnetic field so that they drive π transitions. They are propagated along the long-axis of the vacuum chamber (the y-axis). This is shown in Fig. 2.3, with the 1013 nm light travelling down the beam path labelled A. The 420 nm laser couples the ground state to the states $|f', m_f'\rangle = |1', +1'\rangle$ and $|2', +1'\rangle$ in the manifold $6p_{3/2}$. The 1013 nm laser couples to states in the Rydberg manifold with $m_j + m_i = +1$. We usually excite to the state $|s\rangle \equiv |52s_{1/2}, m_j = -1/2, m_i = +3/2\rangle$.

In order to excite atoms to the manifold $83d_{5/2}$, we changed the 1013 nm beam so that it propagates along beam path B shown in Fig. 2.3. This was done for two reasons. First, the Rabi frequency with which we can couple to Rydberg states from the ground state scales as $n^{-3/2}$ [50]. Therefore, if all else were equal, changing from $n = 52$ to $n = 83$ would reduce the Rabi frequency by approximately a factor of two. Beam path A propagates along the long axis of the vacuum chamber, which means that its final lens is over half a metre away from the atoms. This limits the beam waist (105(2) µm) that we can achieve. We realise a smaller waist by propagating the light down beam path B, where we can place the final lens much closer to the cell (a distance of ~ 20 cm) and achieve a beam waist of 35(2) µm. This mitigates the reduction in Rabi frequency caused by exciting to states with higher n. Second,

[5] Colloquially, this is because the Rydberg electron is sufficiently far from the nucleus that the coupling between electronic and nuclear spins is very weak. Tauschinsky *et al.* [321] measured the hyperfine splitting in ^{87}Rb between the states $|f = 1\rangle$ and $|f = 2\rangle$ in the Rydberg manifold $ns_{1/2}$ to be $37.1(2)\,\text{GHz} \times (n - \delta)^{-3}$ at zero magnetic field. Therefore, we expect the zero-field hyperfine splitting for the Rydberg manifolds that we access to be $\sim 100\,\text{kHz} \times h$.

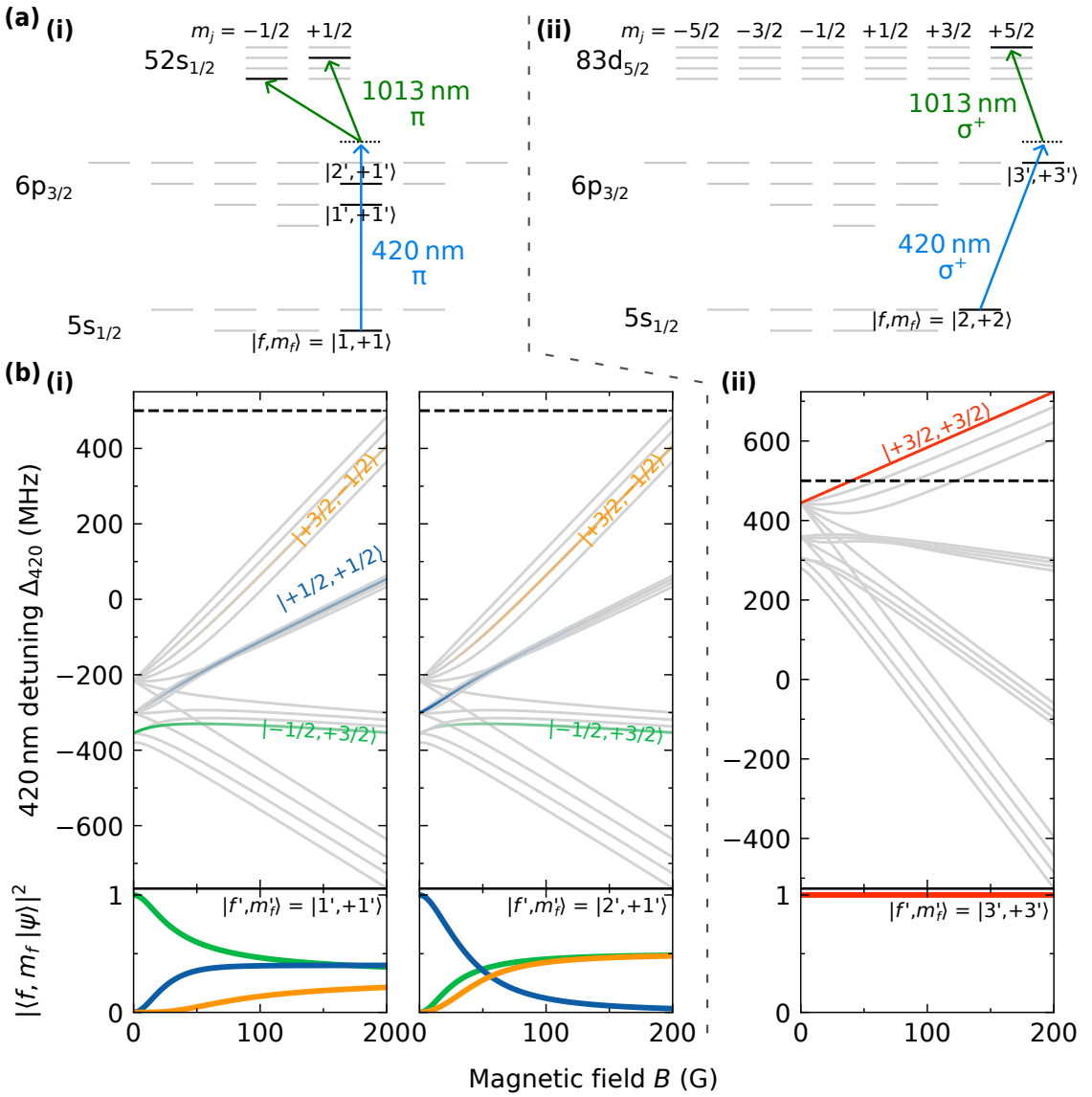

Figure 5.2: Pathways for Rb Rydberg excitation. **(a)** Energy levels used for most of experiments presented in this work. Atoms in the manifold $5s_{1/2}$ are excited to the Rydberg manifold via a virtual level blue-detuned from the manifold $6p_{3/2}$. **(i)** The pathway coupling the ground state $|f, m_f\rangle = |1, +1\rangle$ to the manifold $52s_{1/2}$ with two photons that drive π transitions. **(ii)** The pathway coupling the state $|2, +2\rangle$ to the manifold $83d_{5/2}$ with two photons that drive σ^+ transitions. **(b)** Upper panels: Frequencies of transitions to the manifold $6p_{3/2}$ calculated with the magnetic dipole and electric quadrupole constants of Glaser *et al.* [320]. We show the detuning Δ_{420} of the transitions from the states $|1, +1\rangle$ (panels **(i)**) and $|2, +2\rangle$ (panel **(ii)**) as a function of magnetic field. The detuning is relative to the nearest cavity mode to which we can stabilise the 420 nm laser. Colours and lower panels: the overlaps $|\langle f', m'_f|\psi\rangle|^2$ for the labelled states $|f', m'_f\rangle$ in the manifold $6p_{3/2}$ used during Rydberg excitation with the states $\{|\psi\rangle\}$ that evolve from the high-field states $|m'_j, m'_i\rangle = |-1/2, +3/2\rangle$ (green), $|+1/2, +1/2\rangle$ (blue), $|+3/2, -1/2\rangle$ (orange), and $|+3/2, +3/2\rangle$ (red).

the manifold $83d_{5/2}$ was chosen due to resonant properties that Rydberg atoms in this state have with RbCs molecules. These are discussed in detail in Ch. 7, but for now we state that it is advantageous for the atom to be in a stretched state with maximal $|m_j + m_i|$ (i.e. $m_j = \pm j$ and $m_i = \pm i$ or equivalently, in the low-field regime, $|m_f| = f = j + i$). To access a stretched state in the manifold $83d_{5/2}$, we must excite from a stretched state in the manifold $5s_{1/2}$ on two $\sigma^{\pm}$ transitions. Propagating the 1013 nm beam along beam path B (parallel to the magnetic field) allows us to achieve a higher Rabi frequency on σ^+ transitions by setting the polarisation of the beam to be circular. We note that it would also be desirable to do this for the 420 nm beam, but the AR coating of the science cell prevents this. Instead, we rotate the linear polarisation of the 420 nm light by 90° using the HWP shown in Fig. 2.5 so that it can drive $\sigma^{\pm}$ transitions.

The excitation scheme used to access the manifold $83d_{5/2}$ is shown in Fig. 5.2(a)(ii). We excite from the state $|5s_{1/2}, f = 2, m_f = +2\rangle$ with 420 nm light that drives σ^+ transitions to a virtual state detuned from the state $|f', m'_f\rangle = |3', +3'\rangle$ in the manifold $6p_{3/2}$. The 1013 nm light then couples this virtual state to the Rydberg state $|d\rangle \equiv |83d_{5/2}, m_j = +5/2, m_i = +3/2\rangle$.

For the intermediate manifold $6p_{3/2}$, the crossover point between the Zeeman (weak-field) and Paschen-Back (strong-field) regimes is approximately ~ 50 G. We usually excite to Rydberg states at the low field used to when cooling atoms (4.78 G) or the high field used when forming molecules (~ 200 G), so it is important to understand how the states in the manifold $6p_{3/2}$ change with magnetic field. The good quantum number that is conserved between the two regimes is $m'_f = m'_j + m'_i$. The upper panels in Fig. 5.2(b) show the frequency of transitions to the manifold $6p_{3/2}$ from the states $|5s_{1/2}, f = 1, m_f = +1\rangle$ (panels (i)) and $|5s_{1/2}, f = 2, m_f = +2\rangle$ (panel (ii)). The detuning Δ_{420} is relative to the nearest cavity mode to which we can stabilise the 420 nm light (see Sec. 2.5). The zero point in panel (ii) is five cavity modes (a frequency difference of $-5\nu_{\mathrm{FSR}} \approx -7.5$ GHz) lower than in panels (i) due to the hyperfine splitting of the ground manifold. The colours and lower panels show the overlaps $\left|\langle f', m'_f|\psi\rangle\right|^2$ between the low-field states $|f', m'_f\rangle$ that we couple to with the 420 nm light and the eigenstates $\{|\psi\rangle\}$ that evolve from the high-field states $|m'_j, m'_i\rangle = |-1/2, +3/2\rangle$ (green), $|+1/2, +1/2\rangle$ (blue), $|+3/2, -1/2\rangle$ (orange), and $|+3/2, +3/2\rangle$ (red). Table 5.1 lists the composition of the low-field states $|f', m'_f\rangle$ in the high-field $|m'_j, m'_i\rangle$ basis. These compositions are important because the Rydberg excitation projects the ground states (described by the basis $|f, m_f\rangle$) to Rydberg states (described by the basis $|m_j, m_i\rangle$) via the manifold $6p_{3/2}$, as discussed in Sec. 5.4.

Table 5.1: Composition of relevant $|f', m_f'\rangle$ states in the $6p_{3/2}$ manifold in the $|m_j', m_i'\rangle$ basis.

$\lvert f', m_f'\rangle$	$\lvert m_j', m_i'\rangle$
$\lvert 1', +1'\rangle$	$-\sqrt{3/10}\,\lvert +3/2, -1/2\rangle + \sqrt{2/5}\,\lvert +1/2, +1/2\rangle - \sqrt{3/10}\,\lvert -1/2, +3/2\rangle$
$\lvert 2', +1'\rangle$	$+\sqrt{1/2}\,\lvert +3/2, -1/2\rangle - \sqrt{1/2}\,\lvert -1/2, +3/2\rangle$
$\lvert 3', +3'\rangle$	$\lvert +3/2, +3/2\rangle$

5.3 First stage spectroscopy

Figure 5.3(a) shows a Doppler-broadened absorption spectrum obtained with the 420 nm light through a natural-abundance Rb vapour cell. The light is tuned to be resonant with the transitions $|5s_{1/2}\rangle \rightarrow |6p_{3/2}\rangle$. A small amount ($< 1$ mW) of the light is sent down the spectroscopy path; the remainder is split between the frequency stabilisation setup (~ 1 mW) and the path leading to the main experiment (~ 40 mW). No magnetic field is applied to the vapour cell and it is heated to approximately 60 °C. We see four features corresponding to transitions from the two different values of f in the ground manifold of each isotope ($f = 1, 2$ for ^{87}Rb and $f = 2, 3$ for ^{85}Rb). The hyperfine states in the manifold $6p_{3/2}$ are not sufficiently separated to be resolved. The dashed lines show the expected detunings relative to the transitions from $|5s_{1/2}, f = 3\rangle$ in ^{85}Rb which we assume to be at the minimum of the deepest feature in the spectrum [320].

The frequency axis in Fig. 5.3(a) is calibrated using the PDH error signal obtained from the laser-locking setup (see Sec. 2.5). This error signal is shown in Fig. 5.3(b). The separation between the sharp peaks is set by the free spectral range of the ULE cavity, which we measure to be approximately 1.5 GHz at 420 nm. The detuning Δ_{420} is given relative to the cavity mode closest to the transitions from $|5s_{1/2}, f = 1\rangle$ in ^{87}Rb. At this cavity mode, the wavelength of the light is 420.295(1) nm as measured with a HighFinesse WS5 wavemeter. This is the same zero-point as in Fig. 5.2(b)(i). The zero-point in Fig. 5.2(b)(ii) is the cavity mode at $\Delta_{420} \approx -7.5$ GHz which is the closest mode to the transitions from $|5s_{1/2}, f = 2\rangle$ in ^{87}Rb.

The 420 nm light is delivered to the experiment after being passed through an AOM, as shown in Fig. 2.6. The AOM gives control over the frequency and intensity of the pulses of light the delivered to the experiment. We use an AOM with a high resonant frequency (250 MHz) and bandwidth (100 MHz) to maximise the range of frequencies that the light at the experiment can have, because, unlike the other lasers stabilised to the ULE cavity, the 420 nm laser cannot be locked to an arbitrary frequency due to the lack of a fibre EOM in the locking setup.

We perform finer spectroscopy using the 420 nm light to optically pump atoms in

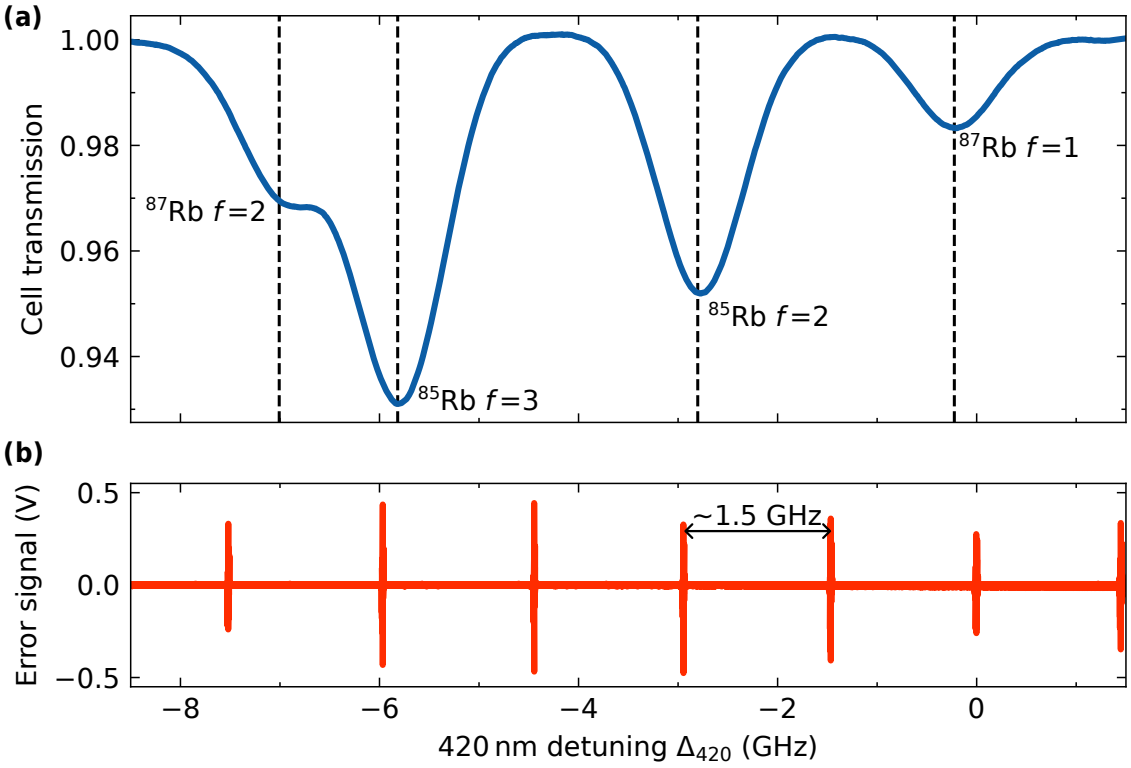

Figure 5.3: Absorption spectrum for 420 nm light resonant with the transitions $|5s_{1/2}\rangle \rightarrow |6p_{3/2}\rangle$**. (a)** The transmission through a natural abundance Rb vapour cell. Doppler-broadened absorption features are visible for ^{87}Rb (outer features) and ^{85}Rb (inner features). Labels for each transition show the Rb isotope and the quantum number f for the states in the manifold $5s_{1/2}$. The dashed vertical lines show the transition spacings as measured by Glaser *et al.* [320]: the frequency of the transitions from $f = 3$ in ^{85}Rb has been set to the minimum of the spectrum. **(b)** The PDH error signal obtained with the locking setup described in Sec. 2.4. We can stabilise the frequency of the light to one of the cavity modes, seen here as the sharp peaks. Detunings are referenced to the cavity mode nearest to the transitions from $f = 1$ in ^{87}Rb.

the main experiment. From the measurement presented in Fig. 5.3, we know that the transitions from $|5s_{1/2}, f = 1\rangle$ in ^{87}Rb are detuned by approximately $-300\,\text{MHz}$ from a cavity mode to which we can stabilise the 420 nm laser. Therefore, for this spectroscopy, we single-pass the light through the AOM and operate it in the -1 diffraction order which removes energy from the light. We load Rb atoms in an array of 817 nm tweezers and optically pump them into the state $|f, m_f\rangle = |2, +2\rangle$ in the ground manifold at magnetic field $B = 4.78\,\text{G}$. We transfer the atoms to the state $|1, +1\rangle$ with ARP and hold them in tweezers of peak depth $U_0 = 3.5\,\text{MHz} \times h$. A small amount of 420 nm light at intensity $130(10)\,\mu\text{W/cm}^2$ is then applied. This light can drive transitions to the states $|f', m_f'\rangle = |1', +1'\rangle$ and $|2', +1'\rangle$ in the manifold $6p_{3/2}$. Atoms will spontaneously decay from these states and eventually return to the states $|f = 1\rangle$ or $|f = 2\rangle$ in the ground manifold. Atoms in the state $|f = 1\rangle$ can be excited again. However, the 420 nm light is approximately 7 GHz detuned of the

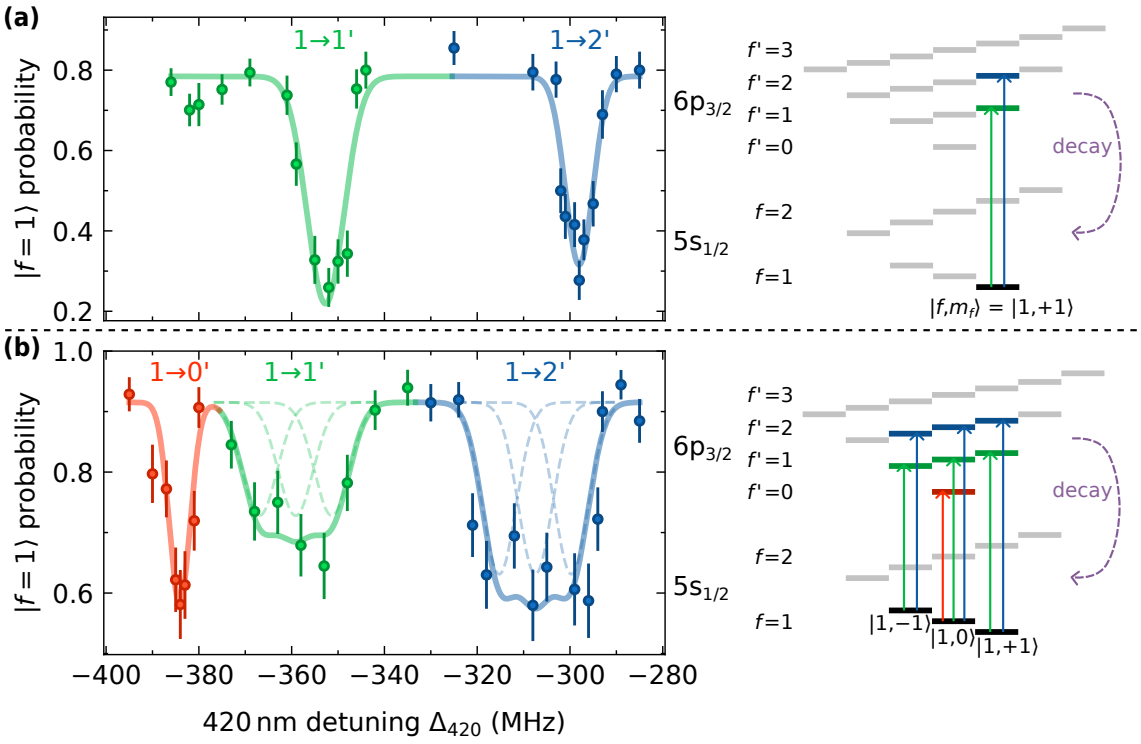

Figure 5.4: Optical pumping with the 420 nm light on the transitions $|5s_{1/2}, f = 1\rangle \rightarrow |6p_{3/2}\rangle$**.** Atoms are prepared in the hyperfine state $|f, m_f\rangle = |1, +1\rangle$ (panel **(a)**) or evenly across the states $|1, m_f\rangle$ (panel **(b)**) in the manifold $5s_{1/2}$. The 420 nm light drives π transitions to the manifold $6p_{3/2}$ from which atoms can subsequently decay to the states $|f = 1\rangle$ or $|f = 2\rangle$ in the ground manifold. Atoms that have been pumped into the state $|f = 2\rangle$ are ejected at the end of the experimental routine. The detuning of the 420 nm light is relative to the same cavity mode as in Fig. 5.3.

transition $|5s_{1/2}, f = 2\rangle \rightarrow |6p_{3/2}\rangle$, so atoms in the state $|f = 2\rangle$ are not re-excited. Therefore, population is optically pumped into the state $|f = 2\rangle$. Finally, we pushout atoms in the state $|f = 2\rangle$ (see Sec. 2.3.3) and reimage the remaining atoms.

Figure 5.4(a) shows the probability that Rb atoms are retained as a function of the frequency of the 420 nm light. The detuning Δ_{420} is given relative to the same cavity mode as in Fig. 5.3. We apply the excitation light for 5 ms which avoids saturating the features and observe two peaks corresponding to the transitions $|1, +1\rangle \rightarrow |1', +1'\rangle$ (green) and $|1, +1\rangle \rightarrow |2', +1'\rangle$ (blue). The solid lines show Gaussian fits to the peaks. Fig. 5.4(b) shows the spectrum obtained when routine is modified to replace the ARP transfer $|2, +2\rangle \rightarrow |1, +1\rangle$ with a pulse of cooling light that depumps the atoms to distribute them approximately uniformly across the states $|1, m_f\rangle$. For this measurement, the 420 nm intensity is reduced to approximately half that used in Fig. 5.4(a) to avoid saturation. The data is fitted with triple Gaussians for the transitions to the states $|1', m'_f\rangle$ and $|2', m'_f\rangle$, where the splitting between the three Gaussians is set to the expected splitting $(7/6)\mu_B B/h \approx 7.81$ MHz [211]. We extract

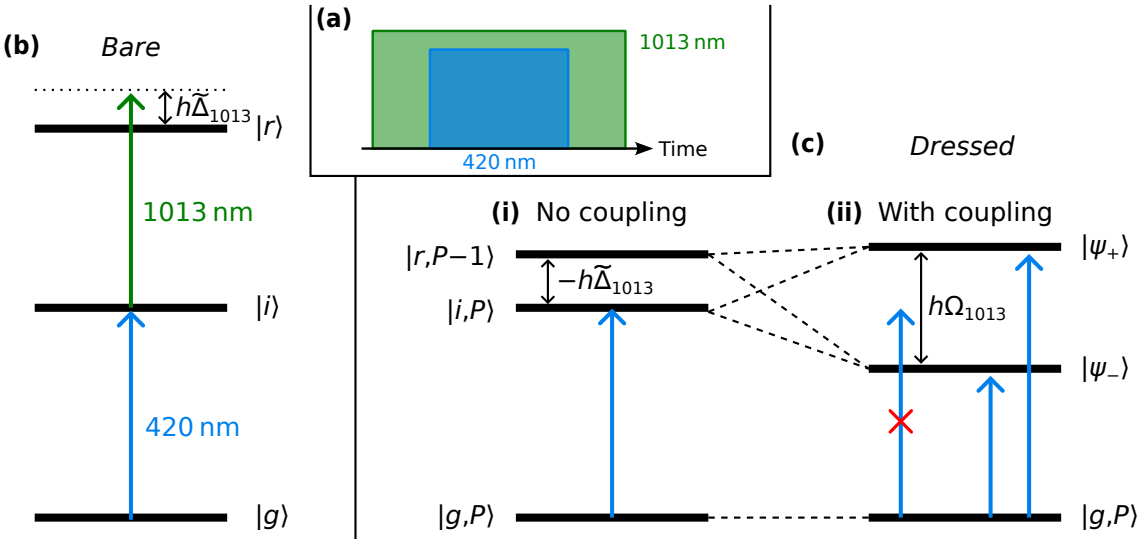

Figure 5.5: Energy states relevant in measurements of Autler-Townes splitting. (a) The pulses of excitation light used in the experimental sequence. **(b)** The bare atomic energy levels. **(c)** Energy levels in the dressed state picture. **(i)** Energy levels when the coupling between states $|i, P\rangle$ and $|r, P-1\rangle$ is ignored. **(ii)** Energy levels when the coupling between these states is included for $\widetilde{\Delta}_{1013} = 0$.

the splitting between the states $|1', 0'\rangle$ and $|2', 0'\rangle$ to be $51(2)\,\text{MHz} \times h$, in agreement with the expected value of $51\,\text{MHz} \times h$ [320]. Similarly, the splitting between the states $|0', 0'\rangle$ and $|2', 0'\rangle$ is $77(2)\,\text{MHz} \times h$, in comparison with the expected value of $75\,\text{MHz} \times h$ [320].

5.4 Second stage spectroscopy

We perform Autler-Townes spectroscopy to characterise the coupling between the intermediate and Rydberg states. The experimental sequence is similar to that used for the measurement shown in Fig. 5.4, with the modification that before switching on the 420 nm light, we turn on the 1013 nm light. The 1013 nm light remains on throughout the 420 nm pulse. A diagram of these pulse timings is shown in Fig. 5.5(a).

As with the 420 nm light, the 1013 nm light is delivered to the experiment after passing through an AOM that we use to control its intensity and frequency (see Fig. 2.6). Due to the fibre EOM prior to the ULE cavity, we are able to lock the 1013 nm laser to an arbitrary frequency. This is especially important because the 420 nm light cannot be locked to an arbitrary frequency: the 1013 nm fibre EOM allows us to set the combined energy of the two photons so that the effective detuning Δ is zero.

We briefly consider the theory of this Autler-Townes experiment. The bare atomic

energy levels are shown in Fig. 5.5(b). We assume that the 420 nm laser is on single-photon resonance. For this experiment, we operate in the regime $\Omega_{420} \ll \Omega_{1013}$; in this regime the 420 nm light does not significantly affect the eigenstates of the system whilst the 1013 nm light *dresses* the energy levels. Here, we follow the approach of Pokorny [322]. The relevant eigenstates of the dressed state picture, in the absence of coupling, are shown in Fig. 5.5(c)(i). These are $\{|g,P\rangle, |i,P\rangle, |r,P-1\rangle\}$, where P is the number of photons in the dressing (1013 nm) field. The energy difference between states $|r,P-1\rangle$ and $|i,P\rangle$ is equal to $-h\widetilde{\Delta}_{1013}$, where $\widetilde{\Delta}_{1013}$ is the single-photon detuning of the 1013 nm laser from the bare transition $|i\rangle \rightarrow |r\rangle$.[6] When including the 1013 nm coupling, the Hamiltonian in the basis $\{|g,P\rangle, |i,P\rangle, |r,P-1\rangle\}$ is

$$\hat{H} = \frac{h}{2}\begin{pmatrix} 2E_g/h & 0 & 0 \\ 0 & 0 & \Omega_{1013} \\ 0 & \Omega_{1013} & -2\widetilde{\Delta}_{1013} \end{pmatrix}, \tag{5.8}$$

where we have taken state $|i,P\rangle$ to be at zero energy and E_g is the energy of state $|g\rangle$. The eigenvectors of this system are $|g,P\rangle$ and $|\psi_\pm\rangle$. $|\psi_\pm\rangle$ are linear combinations of $|i,P\rangle$ and $|r,P-1\rangle$ with eigenvalues

$$E_\pm = (h/2)\left(-\widetilde{\Delta}_{1013} \pm \sqrt{\Omega_{1013}^2 + \widetilde{\Delta}_{1013}^2}\right). \tag{5.9}$$

When the 1013 nm light is on resonance ($\widetilde{\Delta}_{1013} = 0$), the difference in energy between these two eigenstates is $h\Omega_{1013}$. The energy levels in this case are shown in Fig. 5.5(c)(ii).[7]

We use the 420 nm laser to weakly probe the dressed system shown in Fig. 5.5(c)(ii). As the coupling of the 420 nm laser is weak ($\Omega_{420} \ll \Omega_{1013}$), it does not significantly affect the eigenstates of the system. In this regime, if the 420 nm light is tuned to the bare transition $|g\rangle \rightarrow |i\rangle$, it is not resonant with a dressed transition. However, if the frequency of the 420 nm laser is changed by $\pm\Omega_{1013}/2$, it can drive the transition $|g\rangle \rightarrow |\psi_\pm\rangle$ as both states $|\psi_\pm\rangle$ have some $|i\rangle$ character. This allows us to measure Ω_{1013} by measuring energy difference between these transitions.

We show examples of such measurements in Fig. 5.6. Here, we use the 420 nm light to couple the state $|g\rangle = |1,+1\rangle$ in the manifold $5s_{1/2}$ to a state $|i\rangle \in \{|2',+1'\rangle, |1',+1'\rangle\}$ in the manifold $6p_{3/2}$. The 1013 nm light couples the state

[6] We denote the single-photon detuning of the 1013 nm laser from the bare transition $|i\rangle \rightarrow |r\rangle$ as $\widetilde{\Delta}_{1013}$. This is to avoid confusion with Δ_{1013} that will soon be introduced, which is the detuning of the 1013 nm light above the cavity mode to which we lock the laser. When the 420 nm light is resonant with the bare transition $|g\rangle \rightarrow |i\rangle$ (i.e. $\Delta_{1p} = 0$), $\widetilde{\Delta}_{1013} = \Delta_{2p}$.

[7] We note that far from resonance ($|\Delta_{1013}| \gg \Omega_{1013}$), we can expand the square root in $E_\pm$ to see that each state experiences a shift $\pm(h\Omega_{1013}^2)/(4\Delta_{1013})$. This is the ac Stark shift that was introduced in Eq. (5.6).

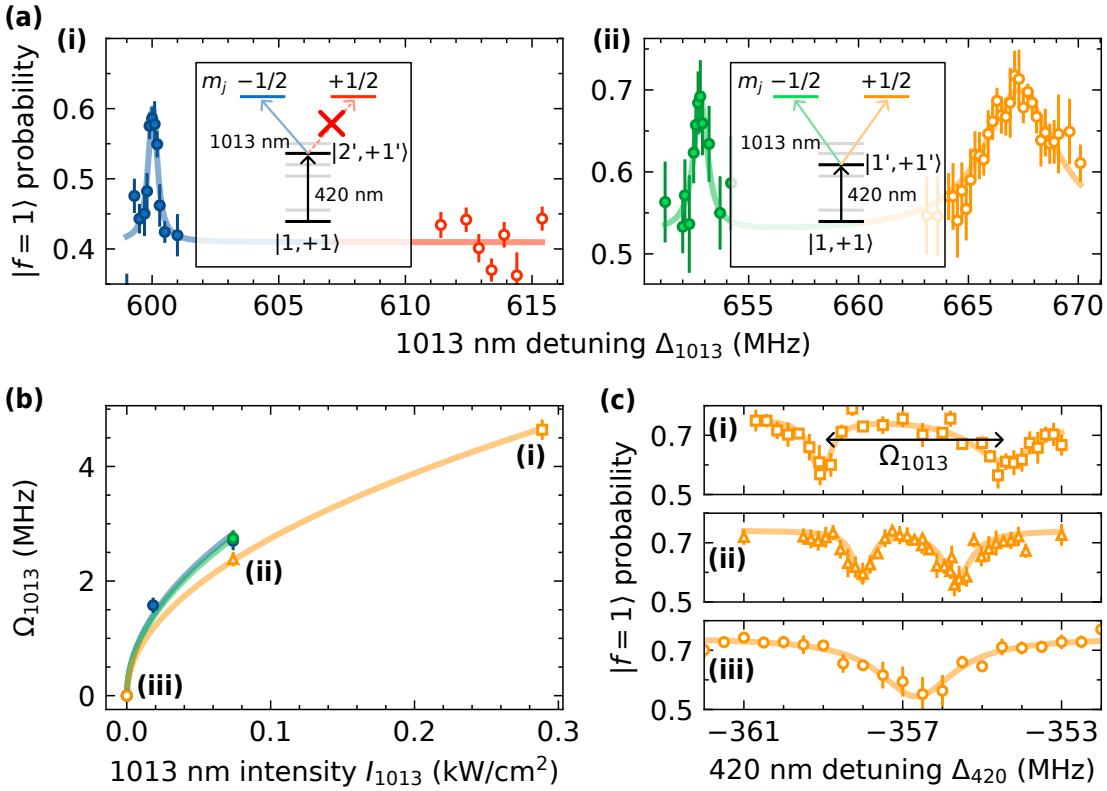

Figure 5.6: Autler-Townes splitting of the transitions $|5s_{1/2}\rangle \rightarrow |6p_{3/2}\rangle$. (a) When the 1013 nm light is resonant, optical pumping by the 420 nm light out of the state $|f, m_f\rangle = |1, +1\rangle$ is prevented. The 420 nm light is resonant with the transition to the state $|f', m_f'\rangle = |2', +1'\rangle$ (panel **(i)**) and the state $|1', +1'\rangle$ (panel **(ii)**) in the manifold $6p_{3/2}$ **(b)** Scaling of Ω_{1013} with I_{1013}. The colours are consistent with **(a)** and lines show a fit to the expected square root scaling. **(c)** Measurements of Ω_{1013} by setting the 1013 nm light to resonant and scanning the 420 nm detuning. The labels in panel (b) show I_{1013} for each measurement.

$|i\rangle$ to states in the manifold $52s_{1/2}$. For this measurement, both coupling lasers drive π transitions and the magnetic field $B = 4.78\,\mathrm{G}$.

Figure 5.6(a) shows the effect of tuning the frequency of the 1013 nm laser when the 420 nm laser is resonant with the bare transitions $|1, +1\rangle \rightarrow |2', +1'\rangle$ (panel (i)) and $|1, +1\rangle \rightarrow |1', +1'\rangle$ (panel (ii)). The frequency of the 1013 nm laser is 295.364(1) THz as measured with a HighFinesse WS5 wavemeter and we reference the detuning Δ_{1013} to the frequency of the cavity mode to which we lock the laser. The relative pulse timings are shown in Fig. 5.5(a). When the 1013 nm light is resonant with a transition $|i\rangle \rightarrow |r\rangle$, the dressing of the intermediate states precludes the 420 nm light optically pumping the atoms out of $|1, +1\rangle$. This means that more atoms remain in $|f = 1\rangle$ and are recaptured at the end of the sequence. For each peak, we set the intensity 1013 nm light to give a clear feature whilst avoiding saturation.

When the 420 nm light is resonant with the bare transition $|1, +1\rangle \rightarrow |1', +1'\rangle$

(panel (ii)), we see two clear features corresponding to the coupling from $|1', +1'\rangle$ to the Rydberg states $|s\rangle \equiv |52\mathrm{s}_{1/2}, m_j = -1/2, m_i = +3/2\rangle$ (green filled points) and $|s'\rangle \equiv |52\mathrm{s}_{1/2}, m_j = +1/2, m_i = +1/2\rangle$ (orange empty points). The splitting between the two peaks is 14.5(1) MHz which is slightly larger than the expected splitting of $2g_j m_j \mu_\mathrm{B} B/h \approx 13.4\,\mathrm{MHz}$.[8]

In contrast, when the 420 nm light is resonant with the bare transition $|1, +1\rangle \rightarrow |2', +1'\rangle$, we observe only coupling to the Rydberg state $|s\rangle$ (blue filled points). The state $|2', +1'\rangle$ has no component for which $m_j' = +1/2$ (see Table 5.1), and the π transitions that we drive with the 1013 nm laser do not change m_j. Consequently, we are unable to access a Rydberg state with $m_j = +1/2$, like the state $|s'\rangle$, via this intermediate state. This results in the two-photon Rabi frequency with which we can drive transitions to $|s'\rangle$ being lower than that for transitions to $|s\rangle$, because we only couple via one intermediate state.

In Fig. 5.6(b) we show the effect of changing the intensity I_{1013} of the 1013 nm light. The Rabi frequency shows the expected scaling $\Omega_{1013} = k\sqrt{I_{1013}}$ and we extract $k \sim 9\,\mathrm{MHz}/(\mathrm{kW/cm^2})^{1/2}$ for the three observed transitions. This measurement is performed by scanning the frequency of the 420 nm light when the 1013 nm light is resonant. We measure the frequency splitting of the dressed states which is equal to Ω_{1013}. Fig. 5.6(c) shows an example this for three different value of I_{1013} for the transition $|1', +1'\rangle \rightarrow |s'\rangle$. The intensities for each panel are as labelled in Fig. 5.6(b).

The measured value of k is of the same order of magnitude as those expected from calculations using the Python package `ARC` [304]. We calculate the scaling constant for the transitions $|6\mathrm{p}_{3/2}, m_j = \pm 1/2\rangle \rightarrow |52\mathrm{s}_{1/2}, m_j = \pm 1/2\rangle$ as $10.5\,\mathrm{MHz}/(\mathrm{kW/cm^2})^{1/2}$. Using the state compositions listed in Table 5.1, we map these to the relevant low-field states and expect to measure k in the range $5.7\,\mathrm{MHz}/(\mathrm{kW/cm^2})$ to $8.5\,\mathrm{MHz}/(\mathrm{kW/cm^2})$.

5.5 Rydberg excitation

We coherently excite to the Rydberg manifold by simultaneously applying both excitation lasers to the atoms. We drive transitions from a state $|g\rangle$ in the manifold $5\mathrm{s}_{1/2}$ to a Rydberg state $|r\rangle$ via a virtual level detuned by $\Delta_{1\mathrm{p}}$ from the intermediate manifold. The state $|g\rangle$ is either the state $|5\mathrm{s}_{1/2}, f = 1, m_f = +1\rangle$ (hereafter $|1, +1\rangle$) or the state $|5\mathrm{s}_{1/2}, f = 2, m_f = +2\rangle$ (hereafter $|2, +2\rangle$). We operate in the regime described in Sec. 5.2 where $\Delta_{1\mathrm{p}} \gg \{\Omega_{420}, \Omega_{1013}\}$ and $\Delta = 0$. The two-photon Rabi frequency Ω is given by Eq. (5.4).

[8] We take the Landè factor to be $g_j = 1 + (j(j+1) + s(s+1) - \ell(\ell+1)) / (2j(j+1))$. For states in the $52\mathrm{s}_{1/2}$ manifold, $g_j = 2$.

A sensible choice of Δ_{1p} is critical for maximising coherence during the Rydberg excitation. A large value of Δ_{1p} minimises scattering from states in the intermediate manifold but reduces Ω. We choose to use $\Delta_{1p} \sim 1\,\text{GHz}$ which we set by the frequency at which we operate the 420 nm laser. To give reasonable value of Δ_{1p} for both the transition $|1,+1\rangle \rightarrow |s\rangle$ and the transition $|2,+2\rangle \rightarrow |d\rangle$, we double-pass the 420 nm light through its AOM, as shown in Fig. 2.6. We operate the AOM in the +1 diffraction order around its centre frequency of 250 MHz, which increases the frequency of the light by $\approx 500\,\text{MHz}$ (Fig. 5.2(b), dashed horizontal lines). Δ_{1p} is given by the difference between the frequency of the light and the frequency of the transition to the intermediate manifold. For the transition $|1,+1\rangle \rightarrow |s\rangle$ we couple via the state $|6p_{3/2}, m_j' = -1/2, m_i' = +3/2\rangle$ (Fig. 5.2(b), green state) and $\Delta_{1p} \approx 800\,\text{MHz}$. For the transition $|2,+2\rangle \rightarrow |d\rangle$ we couple via the state $|6p_{3/2}, m_j' = +3/2, m_i' = +3/2\rangle$ (Fig. 5.2(b), red state). For this transition, if the 420 nm light were locked to the cavity mode at $\Delta_{420} = 0$ in Fig. 5.2(b), we would have $\Delta_{1p} \approx 0$. Therefore, we therefore lock to the neighbouring cavity mode (at higher frequency) such that $\Delta_{1p} \approx 1.6\,\text{GHz}$.[9]

Figure 5.7 shows coherent excitation on the transition $|2,+2\rangle \rightarrow |d\rangle$. To perform this excitation, we switch on the 1013 nm light and wait for 1 ms. This allows the 1013 nm intensity experienced by the atoms to stabilise. No excitation is performed in this time as the atoms are still in the ground state which does not couple to the 1013 nm light. We then switch off the tweezer traps for approximately 10 µs so that the atoms are in free space. During this time, we apply a square pulse of 420 nm light. The duration of the 420 nm pulse sets the time for which we drive the two-photon transition between the ground and Rydberg states, so we refer to this as the two-photon pulse duration. After this pulse, the traps are switched back on and the 1013 nm light turned off. During the excitation, the intensity of the 420 nm light is approximately $100\,\text{W/cm}^2$ and the intensity of the 1013 nm light is approximately $30\,\text{kW/cm}^2$.

In Fig. 5.7(a) we show the effect of varying the effective detuning Δ (by varying Δ_{420}) using a two-photon pulse with a duration less than that of a π pulse on the two-photon transition. The programmed pulse duration is 600 ns, but we expect that due to the finite rise time of the 420 nm AOM the actual pulse time is approximately 500 ns. When the excitation lasers are resonant with the two-photon transition (i.e. Δ is zero), atoms are transferred to the state $|d\rangle$. The data are fitted with a Gaussian of which the full width at half maximum is 1.9(2) MHz; this width is transform limited.

[9] This is the cavity mode at $\Delta_{420} \approx -6\,\text{GHz}$ in Fig. 5.3.

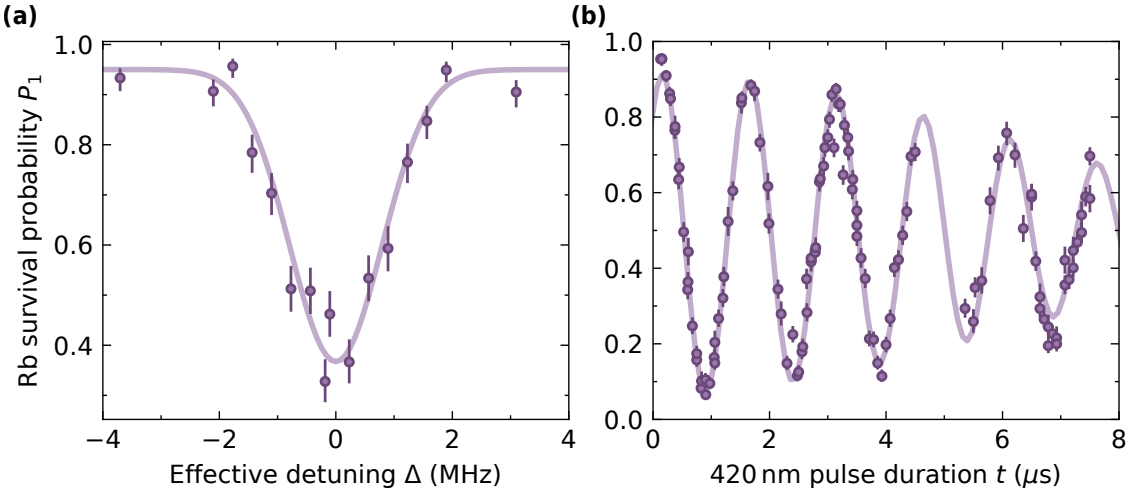

Figure 5.7: Rydberg excitation on the transition $|2,+2\rangle \rightarrow |d\rangle$ **(a)** Spectroscopy of the transition performed with a pulse duration (~ 600 ns) less than that of a π pulse. **(b)** Coherent Rabi oscillations on the transition when Δ is zero. For both measurements, the one-photon detuning $\Delta_{1p} \approx 1600$ MHz and the magnetic field is 181.699(1) G.

Figure 5.7(b) shows the effect of changing the duration of the two-photon pulse when on two-photon resonance. The data are fitted with the function

$$P_1 = A \exp\left[(2\pi\sigma t)^2/2\right] \cos\left(2\pi\langle\Omega\rangle t + \phi\right) + c\,. \tag{5.10}$$

Here, we account for the fact that the two-photon Rabi frequency experienced by the atoms may change in each shot of the experiment, which leads to the damping of the Rabi oscillations seen at long pulse durations. We assume that the two-photon Rabi frequency Ω is sampled from a Gaussian distribution with mean $\langle\Omega\rangle$ and standard deviation σ. We fit $\langle\Omega\rangle = 669(2)$ kHz and $\sigma = 26(1)$ kHz. A and c scale the amplitude and offset of the oscillations respectively and ϕ accounts for the phase offset caused by the finite rise time of the AOM.

For these measurements we map Rydberg excitation onto atom loss using the optical tweezers. The polarisability of alkali Rydberg atoms is well-approximated by that of a free electron [162, 323]

$$\alpha_r(\lambda) = -\frac{e^2}{m_e}\left(\frac{\lambda}{2\pi c}\right)^2, \tag{5.11}$$

where λ is the wavelength of the trapping light. We usually trap Rb in 817 nm tweezers for which $\alpha_r = -3.2 \times 10^2 \times 4\pi\varepsilon_0 a_0^3$. However, we note that, for *any* wavelength, α_r is negative and the tweezers are repulsive to Rydberg atoms. This means that when we switch on the tweezers after the 420 nm pulse, if the atom is in a Rydberg state, it is rapidly ejected and lost.

Figure 5.8 shows a measurement of the trap-limited lifetime of Rydberg atoms in the state $|s\rangle$. For this measurement, we first excite to the Rydberg state with a

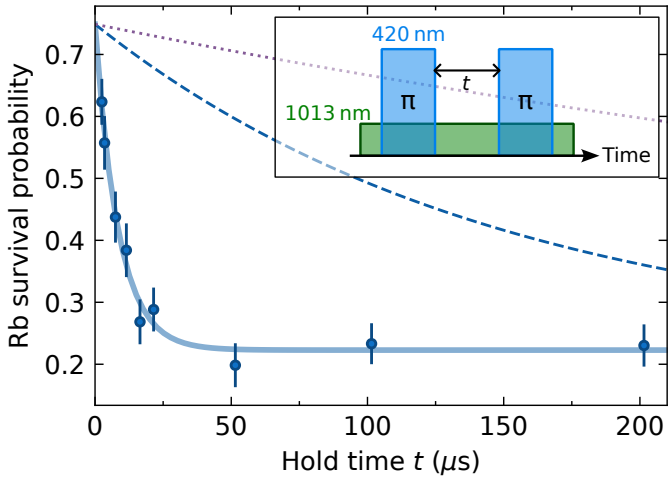

Figure 5.8: Lifetime of the Rydberg state $|s\rangle$ in 817 nm tweezers. A π pulse excites the atom to the Rydberg state. After a variable hold time a second π pulse returns the atom to the ground state. The lifetime of the Rydberg atom in the tweezer is 8.5(1.1) µs. The atom is excited to the Rydberg state when trapped in an 817 nm optical tweezer of intensity 35 kW/cm^2. For comparison, we show the expected behaviour if the Rydberg atom was not ejected and survived for the zero-temperature lifetime of $\tau_s^{(0)}$ (blue dashed line) or $\tau_d^{(0)}$ (purple dotted line).

two-photon π pulse whilst the atoms are trapped in tweezers of intensity 35 kW/cm^2. After a waiting for a variable time, during which the Rydberg atoms can be ejected from the tweezer, we perform a second π pulse to bring surviving atoms back to the ground manifold. For this measurement, we extract the lifetime τ of the Rydberg atoms to be 8.5(1.1) µs. For comparison, we calculate the radiative lifetimes of the states $|s\rangle$ and $|d\rangle$ with the Python package `ARC` [304]. At zero temperature, the lifetimes are calculated to be $\tau_s^{(0)} = 150\,\mu$s and $\tau_d^{(0)} = 590\,\mu$s and the blue and purple dashed lines in Fig. 5.8 show the expected decay if these lifetimes were dominant, scaled to the contrast of the experimental data. The Rydberg detection fidelity $\mathcal{F} = \exp(-\tau/\tau^{(0)})$ is limited by atoms that decay from Rydberg states before they can be ejected. For example, for this trap intensity, we expect that $\mathcal{F}_s = 94.5(7)\%$ and $\mathcal{F}_d = 98.6(2)\%$. Although the effect of blackbody radiation from the room-temperature environment (≈ 300 K) is to couple our chosen states to other Rydberg states [161], approximately halving their lifetimes to $\tau_s^{(300)} = 70\,\mu$s and $\tau_d^{(300)} = 240\,\mu$s, this does not affect the detection fidelity as these other Rydberg states also will be ejected from the tweezers.

In order to maximise the Rydberg excitation fidelity for a given value of Δ_{1p}, we maximise the relative ratio between the two-photon Rabi frequency Ω (Eq. (5.4)) and the intermediate-state effective decay rate (Eq. (5.7)) which is

$$\frac{\Omega}{\Gamma'_{6p_{3/2}}} = 2\frac{\Omega_{420}\Omega_{1013}}{\Omega_{420}^2 + \Omega_{1013}^2}\frac{\Delta_{1p}}{\Gamma_{6p_{3/2}}}. \tag{5.12}$$

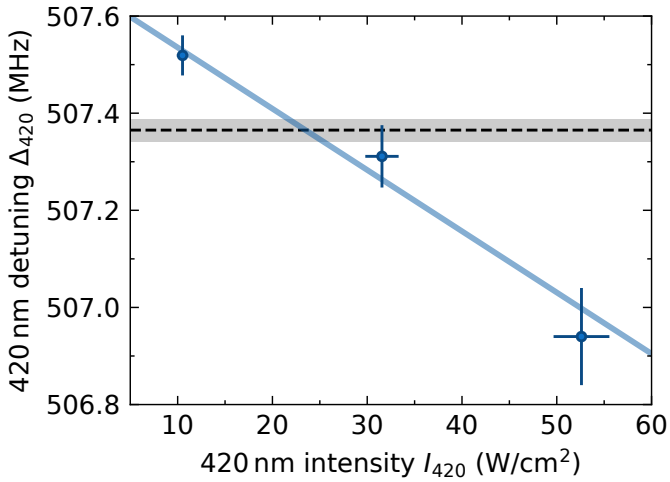

Figure 5.9: Matching the single-photon Rabi frequencies Ω_{420} and Ω_{1013}. We measure at what 420 nm detuning Δ_{420} the effective detuning is zero for the transition $|1,+1\rangle \rightarrow |s\rangle$ as a function of the 420 nm intensity I_{420}. The detuning is relative to the same cavity mode as in Fig. 5.3. For blue data points, $I_{1013} = 2.0(2)\,\mathrm{kW/cm^2}$. The dashed line shows the transition position when the intensities of the excitation beams are reduced to $I_{420} = 5.3(3)\,\mathrm{W/cm^2}$ and $I_{1013} = 400(40)\,\mathrm{W/cm^2}$, the shaded region shows the error.

This ratio is maximised when $\Omega_{420} = \Omega_{1013}$. We use the differential ac Stark shift of the excitation lasers (Eq. (5.6)) to equalise the light shifts. When $\Omega_{420} = \Omega_{1013}$, the differential ac Stark shift δ becomes zero and Eq. (5.5) simplifies to $\Delta = \Delta_{2p}$.

Figure 5.9 shows an example of the measurement we perform to equalise the excitation Rabi frequencies. We set the intensity I_{1013} of the 1013 nm excitation light to $I_{1013} = 2.0(2)\,\mathrm{kW/cm^2}$, and vary the intensity I_{420} of the 420 nm light. For each value of I_{420}, we perform spectroscopy of the transition $|1,+1\rangle \rightarrow |s\rangle$ by changing the 420 nm AOM frequency and measuring a loss feature such as that shown in Fig. 5.7(a). We plot the detuning Δ_{420} of the 420 nm laser at which we realise two-photon resonance for each value of I_{420} (blue points). At resonance, the effective detuning $\Delta = \Delta_{2p} + \delta = 0$ so that $\Delta_{2p} = -\delta = -(\Omega_{420}^2 - \Omega_{1013}^2)/(4\Delta_{1p})$. Therefore, the value of Δ_{420} required to stay resonant depends linearly on $-\Omega_{420}^2 \propto -I_{420}$ and we fit a linear function with a negative gradient to the data (blue line). We then significantly reduce the intensity of the two beams significantly to $I_{420} = 5.3(3)\,\mathrm{W/cm^2}$ and $I_{1013} = 400(40)\,\mathrm{W/cm^2}$ such that $\delta \approx 0$ and $\Delta \approx \Delta_{2p}$. We perform spectroscopy with these powers and measure the transition position which is shown as the dashed line (the grey region shows the error). The intersection of the two lines shows the 420 nm intensity required ($I_{420} = 23(2)\,\mathrm{W/cm^2}$) to set $\Omega_{420} = \Omega_{1013}$ when $I_{1013} = 2.0(2)\,\mathrm{kW/cm^2}$ and we maintain the ratio $I_{1013}/I_{420} = 87$ when scaling the powers to change Ω for this transition.

5.6 dc Stark shifts of Rydberg atoms

The dc polarisability of Rydberg atoms scales with n^7, which makes them highly sensitive to externally applied electric fields [50]. Whilst this property makes Rydberg atoms ideal for the construction of sensors for dc and ac electric fields [324–330], this heightened sensitivity can often cause issues in experiments seeking to coherently excite and control Rydberg atoms. Electric fields fluctuating during an experiment can shift the Rydberg transitions, leading to changes in Δ and decoherence of Rabi oscillations. Two distinct methods can be used to overcome this problem: either the cancellation of the stray fields with an externally applied field [331] or the engineering of the Rydberg atoms such that their transitions are less sensitive to the external fields [332, 333]. This second approach relies on careful mixing of multiple Rydberg states with microwave radiation; we choose here to use the first approach due to its simplicity.

The energy shift of a Rydberg atom in an external electric field is [334]

$$\Delta E_{\mathrm{dc}} = -\frac{1}{2}\alpha_{\mathrm{dc}}\mathcal{E}^2\,, \tag{5.13}$$

where $\mathcal{E}$ is the electric field strength and α_{dc} is the dc polarisability.[10] It is the quadratic nature of this energy shift that motivates the cancellation of stray fields: $\partial(\Delta E_{\mathrm{dc}})/\partial\mathcal{E} = -\alpha_{\mathrm{dc}}\mathcal{E}$ such that the magnitude of energy shift caused by a given electric field fluctuation is proportional to the background field.

Accumulation of alkali-metal vapour on the chamber walls is a major cause of stray electric fields in ultra-high vacuum experiments using alkalis. To overcome this, experiments often use a light-induced atomic desorption (LIAD) technique where a pulse of UV light is applied between experimental runs [198, 337, 338]. This non-resonant light causes atoms that have been adsorbed onto the surface of the vacuum chamber to be released, much like the photoelectric effect. Prior to measuring the stray electric field in our experiment, we applied light at 375 nm to the glass cell to remove alkali buildup from the approximately four years of prior experimental operation. We do not currently apply this light between experimental runs and in future will remeasure the stray field to determine the timescale over which the alkali buildup becomes significant.

We measure the stray electric field by measuring the dc Stark shift of the Rydberg state $|\sigma\rangle \equiv |85\mathrm{s}_{1/2}, m_j = +1/2, m_i = +1/2\rangle$. We choose to use this state because its high value of n provides enhanced sensitivity to $\mathcal{E}$ (as $\alpha_{\mathrm{dc}} \propto n^7$), but we remain

[10] Here we ignore the tensor polarisability and use only the scalar polarisability. For s states, the tensor polarisability is much smaller than the scalar polarisability and results from the (negligible) hyperfine structure. For states with $\ell \geq 1$, the tensor polarisability is more significant and leads to splittings in the Stark map. For more details, see Refs [334–336].

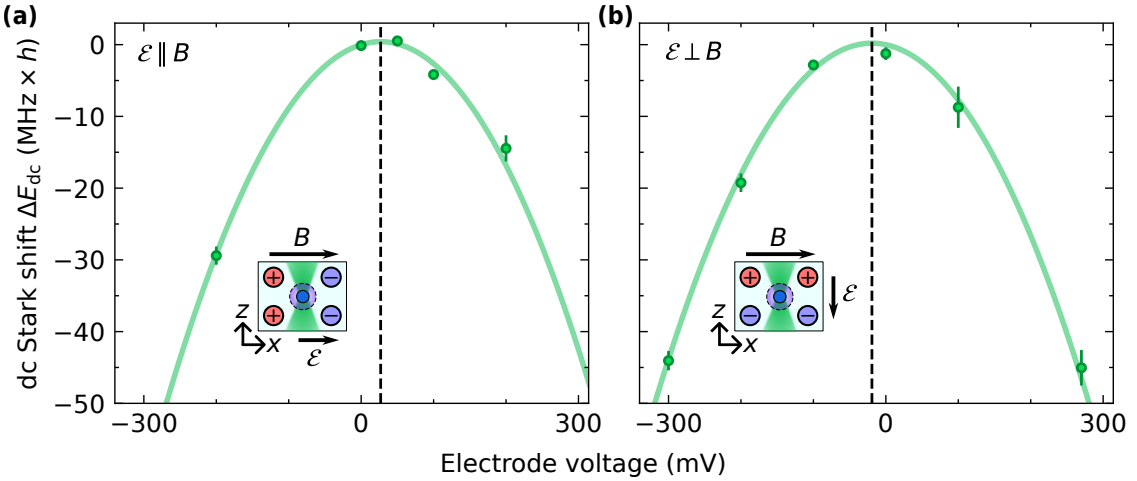

Figure 5.10: dc Stark shifts of the state $|\sigma\rangle$. We apply an electric field parallel (panel **(a)**) or perpendicular (panel **(b)**) to the magnetic field $B = 4.78\,\mathrm{G}$ by applying a voltage to the in-vacuum electrodes. To null the stray electric fields, we need to apply a voltage of $V_0^x = 29(5)\,\mathrm{mV}$ and $V_0^z = -19(4)\,\mathrm{mV}$ respectively (dashed vertical lines). The insets show the electrode configurations used to create these electric fields.

in the simpler Stark map of the s states. We drive the transition $|1, +1\rangle \rightarrow |\sigma\rangle$ by driving a σ^- transition with the 420 nm light and a σ^+ transition with the 1013 nm light, with the 1013 nm light propagating along beam path B shown in Fig. 2.3.

We use the in-vacuum electrodes mounted inside the science cell (see Sec. 2.1) to control the electric field at the atoms. For this measurement, the electrodes are connected to a 20-bit digital-to-analogue converter (DAC)[11] which can output voltages up to ±15 V. We connect the electrodes in two different configurations, either to create an electric field parallel to the magnetic field or perpendicular to it.[12]

Figure 5.10 shows the dc Stark shift of the state $|\sigma\rangle$ when a voltage is applied to the electrodes to generate an electric field. This is measured by performing a spectroscopy scan like that shown in Fig. 5.7(a) and tracking the resonance feature a function of the applied voltage. Panel (a) shows the data when $\boldsymbol{\mathcal{E}} \parallel \boldsymbol{B}$ (i.e. the electric field is along the x-axis) and panel (b) shows the data when $\boldsymbol{\mathcal{E}} \perp \boldsymbol{B}$ (i.e. the electric field is along the z-axis). The insets show cartoons of the field and tweezer orientations. We are unable to control the field along the direction of the electrodes (the y-axis) with this four-electrode array.

The data in Fig. 5.10 are fitted with Eq. (5.13). For this fit, we use $\alpha_{\mathrm{dc}}/h = 2040(40)\,\mathrm{MHz}/(\mathrm{V/cm})^2$, which we extract from a Stark map calculated for the state $|\sigma\rangle$ with the Python package `pairinteraction` [316]. We assume that the dc Stark

[11] Analogue Devices AD5791 mounted onto Analogue Devices EVAL-AD5791SDZ evaluation board

[12] These are, respectively, the configurations used when driving π or $\sigma^{\pm}$ rotational transitions in RbCs with microwave radiation emitted from the electrodes, as described in Ch. 4.

shift of the state $|1,+1\rangle$ is negligible. ΔE is relative to the maximum value of this fit. We fit a conversion factor $\kappa = |\mathcal{E}|/|V|$ for each of the two orientations to convert from applied voltage to electric field and obtain $\kappa_x = 0.75(4)\,(\mathrm{V/cm})/\mathrm{V}$ and $\kappa_z = 0.75(3)\,(\mathrm{V/cm})/\mathrm{V}$ for the x- and z-axes respectively. The agreement of these two factors is somewhat surprising considering that the electrode array has the aspect ratio $\sqrt{3}:1$.[13] The voltages required to cancel the stray fields in each direction are $V_0^x = 29(5)\,\mathrm{mV}$ and $V_0^z = -19(4)\,\mathrm{mV}$ (Fig. 5.10, dashed vertical lines) corresponding to stray fields of $\mathcal{E}_0^x = -22(5)\,\mathrm{mV/cm}$ and $\mathcal{E}_0^z = 14(4)\,\mathrm{mV/cm}$. We have no reason to expect that the stray field along the y-axis is significantly different, and therefore expect that the magnitude of the total stray field $|\mathcal{E}_0| = 32(6)\,\mathrm{mV/cm}$.[14] This corresponds to a dc Stark shift of $\Delta E_{\mathrm{dc}} = -1.0(3)\,\mathrm{MHz} \times h$ for the state $|\sigma\rangle$ relative to the energy at zero electric field.

For the remainder of this work, we do not cancel the stray electric field as we prioritise using the electrodes as microwave antennae to drive molecular transitions with high fidelity. However, hardware to allow us to do both at the same time is currently under development. We will use an eight-electrode array mounted outside the experimental chamber to cancel the stray field along all three axes while maintaining the ability to use the in-vacuum electrodes as microwave antennae.

5.7 ac Stark shifts of Rydberg atoms

To selectively excite certain Rydberg atoms in our tweezer array, we exploit the ac Stark shifts of the two-photon transitions to Rydberg states. This technique is very similar to the molecular addressing discussed in Sec. 4.7, but we perform atomic trapping and addressing with the same set of tweezers. Rather than switching off all tweezers when attempting to excite to the Rydberg state, we keep certain tweezers on. The energy shift caused by the ac Stark effect for a given state is given by Eq. (4.2). To calculate the ac Stark shift of the Rydberg transition, we replace α in Eq. (4.2) with the transition's differential polarisability $\Delta\alpha$. Then, if ΔE_{ac} is larger than the linewidth of transition, we can selectively excite *either* the atoms in free space *or* the atoms in the tweezers by tuning the frequency of the excitation lasers.

[13] A possible cause for this agreement is the fact that the DAC has a buffered output (used for the $\mathcal{E} \parallel B$ measurement) and an unbuffered output (used for the $\mathcal{E} \perp B$ measurement), which potentially causes different voltages across the electrodes for the two different configurations. Another possibility is that there is a difference in the capacitance of the two configurations; a finite-element simulation of the electrodes and vacuum chamber could be used to calculate this. For our purposes however, it is sufficient to measure this calibration and apply whatever voltage is needed to cancel the stray field.

[14] Here we have assumed that the stray electric field in the third direction is approximately $\frac{1}{2}(|\mathcal{E}_0^{\parallel}| + |\mathcal{E}_0^{\perp}|) = 18(3)\,\mathrm{mV/cm}$.

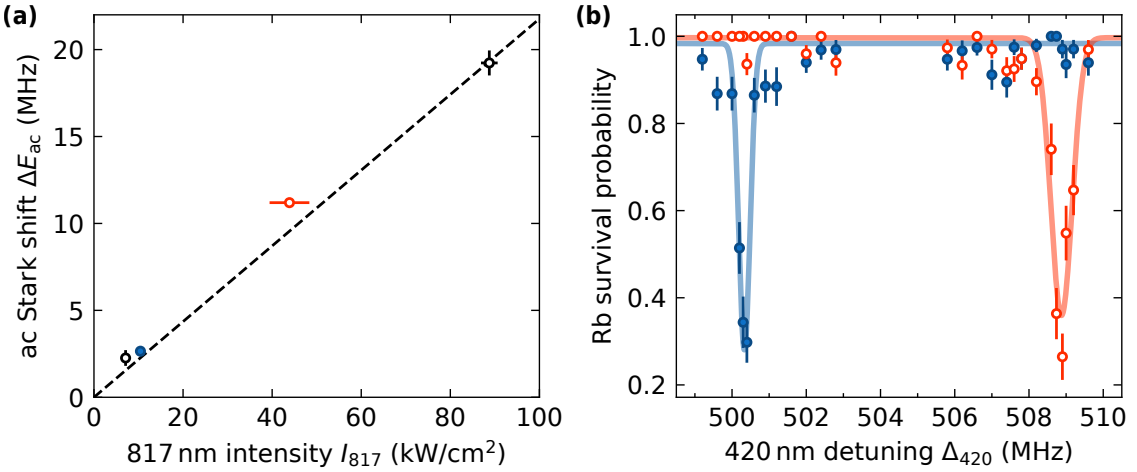

Figure 5.11: Local control of Rydberg excitation. (a) ac Stark shift ΔE_{ac} of the transition $|1,+1\rangle \rightarrow |s\rangle$ as a function of the 817 nm tweezer intensity I_{817}. Transition frequencies are given relative to the frequency in free space. The dashed line shows the expected shift. **(b)** Selective Rydberg excitation by trapping atoms in tweezers of different depths. By trapping some atoms in deeper tweezers, we can selectively excite only those atoms. The tweezer intensities used are shown in panel (a) as points of the same colours.

Alternatively, if we wish to keep all ground-state atoms trapped (such as during the experiments discussed in Ch. 6), we simply make the traps of the atoms we wish to excite a different depth to the rest of the array and tune excitation lasers to be resonant with the target atoms.

Figure 5.11(a) shows a measurement of this light shift for the two-photon transition $|1,+1\rangle \rightarrow |s\rangle$. The transition energies are shown relative to the energy of the transition in free space. For a Rb atom in an 817 nm tweezer, the differential polarisability of the transition is $\Delta\alpha = \alpha_r - \alpha_g = -4.7 \times 10^3 \times 4\pi\varepsilon_0 a_0^3$, where $\alpha_r = -3.2 \times 10^2 \times 4\pi\varepsilon_0 a_0^3$ is the polarisability of the Rydberg state (Eq. (5.11)) and $\alpha_g = 4307 \times 4\pi\varepsilon_0 a_0^3$ is the polarisability of the ground state [218]. The dashed line shows the expected transition shift with this value of $\Delta\alpha$. The empty red and filled blue data points were measured during the same experimental run with two classes of atoms in different tweezer depths; Fig. 5.11(b) shows the excitation spectrum from which we extract these points. The black points were obtained with all tweezers in the array at the same depth.

5.8 Rydberg-Rydberg interactions

Rydberg atoms can interact with other Rydberg atoms either by van der Waals interactions, which scale with the interatomic distance as R_{aa}^{-6}, or via resonant dipole-dipole interactions, which scale with the interatomic distance as R_{aa}^{-3}. In this

section, we use the high sensitivity of the van der Waals interaction to precisely measure the distance R_{aa} between two Rydberg atoms. This is a precursor to the measurements of interactions between Rydberg atoms and polar molecules that are discussed in Chs 6 and 7.

Figure 5.12(a) shows the energies of two atoms as a function of interatomic distance R_{aa}. We consider the system where each atom can either be in the ground state $|g\rangle = |1, +1\rangle$ or the Rydberg state $|s\rangle$. To denote pairs states of two atoms we use the notation $|ab\rangle \equiv |a\rangle\,|b\rangle$. In this system, there are four possible pair states: $|gg\rangle$, where both atoms are in the ground state; $|gs\rangle$ and $|sg\rangle$, where one of the atoms is in the Rydberg state and the other is in the ground state; and $|ss\rangle$, where both atoms are in the Rydberg state. The pair states $|gs\rangle$ and $|sg\rangle$ are degenerate. When the atoms are sufficiently separated (i.e. as $R_{aa} \to \infty$), the energy levels are separated by multiples of the energy difference E_s between the states $|g\rangle$ and $|s\rangle$. Relative to the energy of $|ss\rangle$, the states $|gs\rangle$ and $|sg\rangle$ have energy $-E_s$ and the state $|gg\rangle$ has energy $-2E_s$.

The pair state $|ss\rangle$ exhibits long-range interactions resulting from the non-resonant exchange of virtual photons between the atoms [50]. This means that as the atoms are brought together, there is an energy shift which, at long range, is well described as

$$\Delta E = -\frac{C_6}{R_{aa}^6}\,, \tag{5.14}$$

where C_6 is the van der Waals interaction coefficient.[15] We calculate the potential of $|ss\rangle$ with `pairinteraction` [316] and fit it with Eq. (5.14) to obtain $C_6/h \approx -24.7\,\mathrm{GHz}/\mu\mathrm{m}^6$ for this pair state. The van der Waals interaction coefficient scales incredibly strongly with principal quantum number: $C_6 \propto n^{11}$ [50]. For example, for the pair state $|dd\rangle$, $C_6/h \approx 7\,\mathrm{THz}/\mu\mathrm{m}^6$.[16]

The interaction shift ΔE is often used to engineer *Rydberg blockade*. This phenomenon occurs when ΔE is large enough to preclude excitation to a pair state such as $|ss\rangle$. Consider tuning the combined energy of the excitation lasers to be equal to the energy of the blue arrow shown in Fig. 5.12(a) with $R_{aa} \approx 4\,\mu\mathrm{m}$. The lasers can drive transitions from $|gg\rangle$ to either $|gs\rangle$ or $|sg\rangle$. However, assuming the linewidth $\Delta\nu$ of the Rydberg transition satisfies $\Delta\nu \ll \Delta E/h$, the laser does not have the correct energy to drive the transitions $|gs\rangle \to |ss\rangle$ and $|sg\rangle \to |ss\rangle$ due to

[15] The interactions discussed here are non-resonant because there is not a second pair state that has approximately the energy as $|ss\rangle$ when $R_{aa} \to \infty$. If there were, *resonant* virtual photons could be exchanged between the states [50]. The interaction energy is then best described as $\Delta E = -C_3/R_{aa}^3$, where C_3 is the resonant dipole–dipole interaction coefficient. We return to resonant interactions in Ch. 7, when we engineer them between Rydberg atoms and polar molecules.

[16] The energy shifts of pair states with $\ell \geq 1$ are anisotropic and programs such as `ARC` [304] or `pairinteraction` [316] should be used to calculate the full interaction potentials.

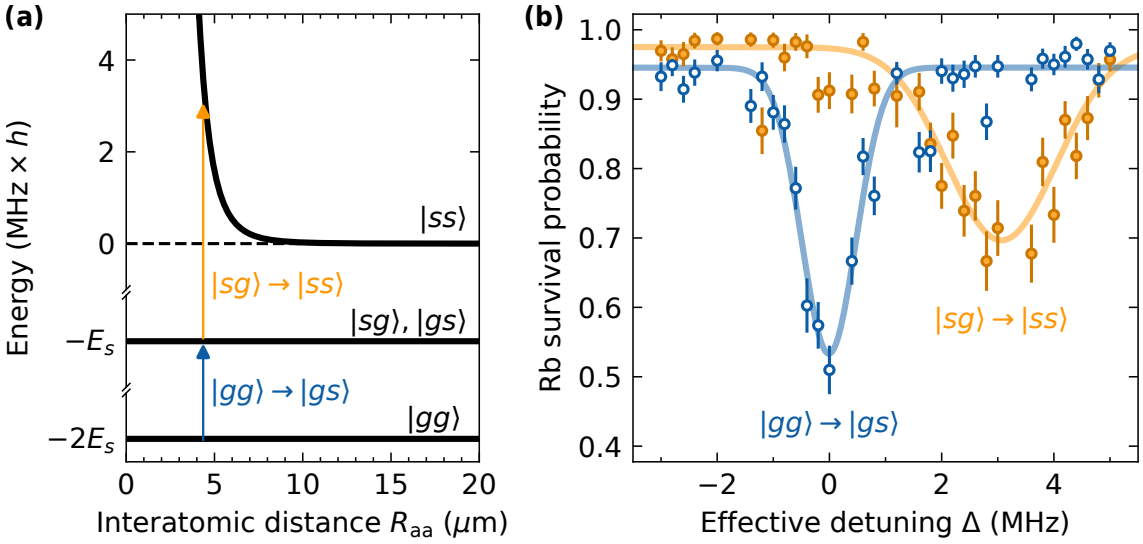

Figure 5.12: van der Waals interactions between Rydberg atoms. (a) Pair potentials for two atoms in states $|g\rangle$ and $|s\rangle$. The van der Waals interactions of the pair state $|ss\rangle$ causes $\sim$ MHz $\times$ h energy shifts for $\sim$ µm separations. **(b)** Interaction shift of the Rydberg transition of one atom caused by the presence of another Rydberg atom. The blue empty points are data from runs where the other atom is not successfully excited (i.e. remains in the state $|g\rangle$); the orange filled points are data from runs where the other atom is excited to state $|s\rangle$ prior to the Rydberg pulse shown here. The detuing is relative to the frequency of the transition $|gg\rangle \rightarrow |gs\rangle$.

the van der Waals energy shift of the state $|ss\rangle$. This principle is fundamental to realising two-qubit interactions in quantum computing or simulation platforms based on Rydberg atoms [48, 76, 198, 339, 340].

It is typical to define a blockade radius r_b at which $\Delta E = h\Delta\nu/2$.[17] Beyond r_b, excitation to the pair state is not precluded by ΔE. In our experiment, typically $\Delta\nu \approx 2\,\mathrm{MHz}$ (see Fig. 5.7(a)), which for the state $|s\rangle$ gives $r_\mathrm{b}^s \approx 5\,\mu\mathrm{m}$ and for the state $|d\rangle$ gives $r_\mathrm{b}^d \approx 14\,\mu\mathrm{m}$. For experiments presented up until now, we have always ensured $R_\mathrm{aa} \gg r_\mathrm{b}$ so that interactions between Rydberg atoms could be ignored whilst using multiple atoms trapped in the arrays of tweezers to increase the rate of data acquisition. We now relax that condition and begin to study interactions involving Rydberg atoms.

We use the strong dependence of the van der Waals interaction on R_aa to precisely measure the distance between two atoms. We begin by preparing two atoms in separate 817 nm tweezers in the state $|g\rangle$. The two tweezers are sourced from the

[17] We define the transition linewidth $\Delta\nu$ as the full width at half maximum (FWHM). Definitions of r_b depend on how $\Delta\nu$ is defined; in any case the blockade radius is not a hard cutoff and experiments typically work with $R_\mathrm{aa} \ll r_\mathrm{b}$ (to strongly blockade excitation to pair states such as $|ss\rangle$) or $R_\mathrm{aa} \gg r_\mathrm{b}$ (to be able to ignore interactions between Rydberg atoms). Using this definition, naively, $r_\mathrm{b} = (2C_6/h\Delta\nu)^{1/6}$. However, Eq. (5.14) begins to break down for short distances and we instead calculate the blockade radius using the pair state potential calculated with `pairinteraction` [316].

same laser and are generated using the 2D AOD (see Sec. 2.2), which means there is no possibility for the misalignment of their foci along the direction of tweezer-light propagation (the z-axis). The position of the tweezers in the xy-plane is set by deflecting the light at the 2D AOD. We have previously calibrated the relationship between the frequency of the RF tones applied to the 2D AOD and the tweezer position in the xy-plane by fitting images of atomic fluorescence such as that shown in Fig. 2.4 [206]. We use this calibration to set the tweezers to be separated along the x-axis by 4.48(3) µm. The tweezers are set to different depths; this allows us to selectively drive either the transition $|gg\rangle \rightarrow |sg\rangle$ or the transition $|gg\rangle \rightarrow |gs\rangle$ as they are no longer degenerate (we set the transition to the state $|gs\rangle$ to be 9.3(2) MHz detuned from the transition to the state $|sg\rangle$). We attempt to excite the first atom to $|s\rangle$ using a two-photon π pulse on the transition $|gg\rangle \rightarrow |sg\rangle$.

We show in Fig. 5.12(b) the probability that the second Rb atom is recovered. The main loss mechanism is the ejection of atoms that are successfully excited to the state $|s\rangle$. Two features appear conditional on the successful excitation of the first Rb atom to $|s\rangle$, which we measure as that atom being lost from its tweezer. If the first atom is not excited to $|s\rangle$, we are able to drive the transition $|gg\rangle \rightarrow |gs\rangle$ (blue empty points). If the excitation of the first atom is successful, we are able to drive the transition $|sg\rangle \rightarrow |ss\rangle$ (orange filled points). This feature is broader than the first because fluctuations in the tweezer separation cause R_{aa} to vary between experimental shots. The difference in energy between these transitions measures ΔE of the pair state $|ss\rangle$. We measure $\Delta E/h = 3.07(14)$ MHz. Using the `pairinteraction` [316], we calculate the pair state potential and convert the measured interaction shift to the interatomic distance $R_{\mathrm{aa}} = 4.48(4)$ µm. This value is in excellent agreement with the expected separation based on our calibration of the 2D AOD.

We use a similar approach to measure the separation in the direction of tweezer-light propagation (the z-axis) between the 817 nm and 1066 nm tweezer arrays. The axial separation is controlled by imprinting a phase pattern corresponding to a Fresnel lens onto the SLM in the 1066 nm path: this moves the axial position of the foci of the 1066 nm tweezers [207]. We repeat the above experiment but this time prepare one atom in an 817 nm tweezer and the other a 1066 nm tweezer. We are unable to observe the interaction-shifted peak for tweezer separations smaller than $\lesssim 3$ µm because ΔE becomes larger than the bandwidths of the AOMs used for the Rydberg pulses. Therefore, we radially displace the tweezers by 3.49(5) µm such that the atomic separation is never smaller than this value.

Figure 5.13 shows the measured interaction shift as a function of the 1066 nm tweezer axial displacement. The relative change in axial position is estimated based

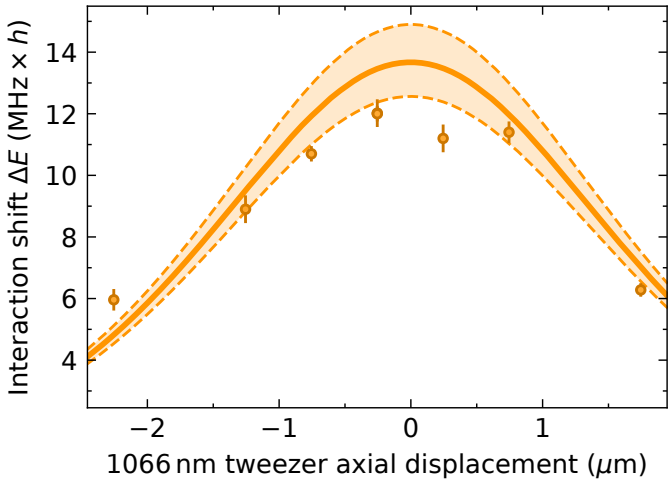

Figure 5.13: Interaction shift of two Rydberg atoms as a function of the axial displacement between the tweezers. Before excitation, one atom is trapped in an 817 nm tweezer and the other is trapped in a 1066 nm tweezer. The tweezers are offset radially by 3.49(5) μm. When the tweezers are overlapped axially, the interaction shift is maximised. The solid line is the expected interaction shift as the axial displacement is varied; the shaded region results from the error on the radial displacement.

on the focal length of the lens applied using the SLM. When the traps are aligned axially, R_{aa} is minimised and ΔE is maximised. We use the `pairinteraction` [316] to calculate the predicted interaction shift as a function of axial displacement given our radial displacement, and fit the measured data with this function. The only free parameter in this fit is the 1066 nm position at which the displacement between the traps along the z-axis is zero; the displacements in Fig. 5.13 are plotted relative to this fitted centre. This fitting procedure returns a value for the overlap position with a 1σ uncertainty of 0.1 μm. Being able to overlap the tweezers with this level of precision is important for the study of interactions between Rydberg atoms and molecules, which generally require smaller distances between particles for their interactions to be significant (see Chs 6 and 7). We have verified the accuracy of this alignment procedure using RbCs molecule formation. Molecule formation is sensitive to the relative overlap of the tweezers as the formation probability is dependent on the probability that the atom pairs occupy the ground state of relative motion (see Sec. 3.2.1). Misalignment of the optical tweezers causes heating during the merging process and hence a reduction in the molecule formation probability.

5.9 Summary

We have shown how we excite individually trapped Rb atoms to the Rydberg states $|s\rangle \equiv |52\mathrm{s}_{1/2}, m_j = -1/2, m_i = +3/2\rangle$ and $|d\rangle \equiv |83\mathrm{d}_{5/2}, m_j = +5/2, m_i = +3/2\rangle$

using a two-photon excitation scheme with lasers at 420 nm and 1013 nm. We have performed spectroscopy of the relevant states and characterised the Rydberg excitation. We detect Rydberg excitation by using optical tweezers to map the excitation onto atom loss. We have measured the dc and ac Stark shifts of the Rydberg atoms and can selectively excite certain atoms by addressing them with optical tweezers of different depths. We have measured the interaction of two adjacent Rydberg atoms and have the necessary tools in place to study their interactions with molecules.

6 Charge-dipole interactions between molecules and Rydberg atoms

The majority of the results in this chapter have been published in Ref. [202].

To engineer a hybrid quantum system of polar molecules and Rydberg atoms, it is important to understand the inter-species interactions. Polar molecules and Rydberg atoms can support electric dipole moments, meaning they are able to interact via the van der Waals and dipole-dipole interactions discussed in the previous chapter. However, their rich structure can give rise to additional interactions. In this chapter, we probe the charge-dipole interaction that can be realised when a molecule is placed approximately within the orbit of the Rydberg electron. We introduce this interaction and elucidate how it can be used to engineer atomic Rydberg blockade. We use species-specific optical tweezers to hold the particles at the requisite sub-micrometre separations and demonstrate the blockade of atomic Rydberg excitation caused by the charge-dipole interaction. This allows for the presence of a molecule to be mapped onto the atomic state.

6.1 Charge-dipole interactions

Polar molecules interact strongly with dc electric fields [41]. The interaction Hamiltonian is $\hat{H}_{\mathrm{dc}} = -\boldsymbol{d} \cdot \boldsymbol{\mathcal{E}}$, where $\boldsymbol{d}$ is the permanent electric dipole moment of the molecule in the molecular frame. For RbCs, the magnitude of $\boldsymbol{d}$ is $d = 1.225\,\mathrm{D}$ [149]. Often, experiments use this interaction to mix different rotational levels of a molecule by applying an external dc electric field [47]. This polarises the molecule, and can be used to engineer tuneable electric dipole moments in the laboratory frame with applications such as simulating quantum magnetism [40, 44, 341].

Here, we consider the case where the electric field is not externally applied, but is that inherent to a Rydberg atom. This field results from contributions from the

positively charged Rydberg core and the negatively charged Rydberg electron. The electric field at position $\boldsymbol{R}$ is

$$\boldsymbol{\mathcal{E}}_r(\boldsymbol{R},\boldsymbol{r}) = \underbrace{\frac{e}{4\pi\varepsilon_0}\frac{\boldsymbol{R}}{|\boldsymbol{R}|^3}}_{\text{core}} + \underbrace{\frac{-e}{4\pi\varepsilon_0}\frac{\boldsymbol{R}-\boldsymbol{r}}{|\boldsymbol{R}-\boldsymbol{r}|^3}}_{\text{electron}}, \tag{6.1}$$

where the first term results from the Rydberg core and the second term is from the Rydberg electron. Here we define the coordinate system such that the Rydberg core is at the origin and the Rydberg electron is at position $\boldsymbol{r}$. The Hamiltonian describing the rotational energy of a polar molecule and charge-dipole interaction between it and the Rydberg atom can be written [109, 111, 342]

$$\hat{H} = hB_\nu \hat{N}^2 - \boldsymbol{d}\cdot\boldsymbol{\mathcal{E}}_r(\boldsymbol{R}_{\text{am}},\boldsymbol{r})\,. \tag{6.2}$$

Here, $\boldsymbol{R}_{\text{am}}$ is the position of the molecule and $\hat{N}$ is the molecular angular momentum operator. This Hamiltonian neglects the molecular hyperfine structure and is valid in the Born-Oppenheimer and rigid-rotor approximations. It represents the dominant interaction for separations R_{am} between the molecule and the Rydberg core on the scale of the radius of the Rydberg atom.[1] The first term is the rigid-rotor Hamiltonian that gives rise to the basis states $|N, M_N\rangle$ with energies $hB_\nu N(N+1)$ (see Sec. 4.1). The second term is from the interaction between the molecular dipole and the electric field of the Rydberg atom. The form of $\boldsymbol{\mathcal{E}}_r(\boldsymbol{R},\boldsymbol{r})$ means that the interaction strength scales as R_{am}^{-2}.

This Hamiltonian can give rise to two distinct regimes, depending on the size of d. For molecules where d is larger than the Fermi-Teller critical dipole moment $d_{\text{c}} \approx 1.639\,\text{D}$ [344], the interaction is strong enough to rip the Rydberg electron from its core and bind it to the molecule. This leaves behind the Rydberg core, which is now a free ion. However, for molecules where $d < d_{\text{c}}$, the interaction is not strong enough for this to occur. In this case, the molecule and Rydberg atom continue to coexist and support a long-range charge-dipole interaction. This interaction gives rise to a rich energy level landscape where, for sub-micrometre separations, energy shifts are predicted to be strong enough to blockade atomic Rydberg excitation when a molecule is present [99, 100]. Furthermore, for Rydberg states with $\ell > 3$, energy shifts are predicted to be large enough to support bound states of the molecule and Rydberg atom pair [109–111]. These bound states are known as giant polyatomic Rydberg molecules (GPRyM) [109, 110] or triatomic

[1] At shorter range when the molecule is deeply inside the orbit of the Rydberg electron, scattering of the electron from the molecule must be considered. This is usually approximated with a Fermi pseudopotential [343]. The details are beyond the scope of this thesis but can be found in the Supplemental Material of Ref. [202].

Table 6.1: Quantum defects for Rb and Cs for $\ell \leq 3$. The given values are for $j = \ell + 1/2$ but depend only weakly on j.

	Rb		Cs	
ℓ	$\delta(\ell)$	$\delta(\ell+1) - \delta(\ell)$	δ	$\delta(\ell+1) - \delta(\ell)$
s	3.13 [309]	-0.48	4.05 [308]	-0.46
p	2.64 [309]	-1.29	3.56 [306]	-1.08
d	1.35 [309]	-1.33	2.47 [308]	-2.43
f	0.02 [310]	-0.02	0.03 [304]	-0.03

ultralong-range Ryderg molecules [111, 112]; here we refer to them as GPRyMs. For RbCs, $d < d_c$ and we are able to study this second regime.

To study the charge-dipole interaction, we choose to use states for which we might experimentally resolve GPRyMs. At first glance this seems problematic: GPRyMs are predicted to occur only for *hydrogenic* Rydberg states (those with with $\ell > 3$) and, with our two-photon excitation scheme (see Sec. 5.2), we can only access Rydberg states with $\ell = 0$ or 2. One way to circumvent this problem would be to perform further transfers between Rydberg states with microwave radiation. However, hydrogenic Rydberg states have quantum defects that are vanishingly small and thus exist in dense manifolds of states which can make populating a specific state challenging.[2] Instead, we use a scheme proposed by González-Férez *et al.* [112], who showed that it is possible to couple to into GPRyM states with two Rydberg excitation lasers starting from an s-state. They propose exploiting near-resonant coupling between pair states of the Rydberg atom and molecule with different principal and rotational quantum numbers in order to excite to GPRyM states. This removes the need to excite a Rydberg atom to a specific hydrogenic state.

To engineer such a near-resonant coupling, we select a Rydberg state ns or nd which has a energy difference from a hydrogenic manifold that is slightly larger than the energy of a molecular rotational state. For example, for a state ns of Rb, we require the energy difference $\Delta E_{\mathrm{Rb}}(n\mathrm{s})$ from a hydrogenic manifold to satisfy

$$\Delta E_{\mathrm{Rb}}(n\mathrm{s}) \equiv |E_{\mathrm{Rb}}(n\mathrm{s}) - E_{\mathrm{Rb}}(n', \ell > 3)| \gtrapprox E_{\mathrm{RbCs}}(N)\,, \tag{6.3}$$

where E_{Rb} is the energy of the Rydberg atom and E_{RbCs} is the energy of the molecule (relative to the rovibrational ground state). Table 6.1 shows the quantum defects $\delta(\ell)$ for Rb and Cs. The binding energy of a Rydberg atom is given by Eq. (5.1) and states with similar effective principal quantum numbers $n^* \equiv n - \delta(\ell)$ have similar energies. For hydrogenic states, $\delta(\ell > 3) \approx 0$. For Rb, $\delta(\mathrm{s}) \approx 3$ and $\delta(\mathrm{d}) \approx 1$,

[2] The negligible quantum defects of Rydberg states with $\ell > 3$ means that they are described well by the Hamiltonian of a hydrogen atom and is precisely why they are termed hydrogenic.

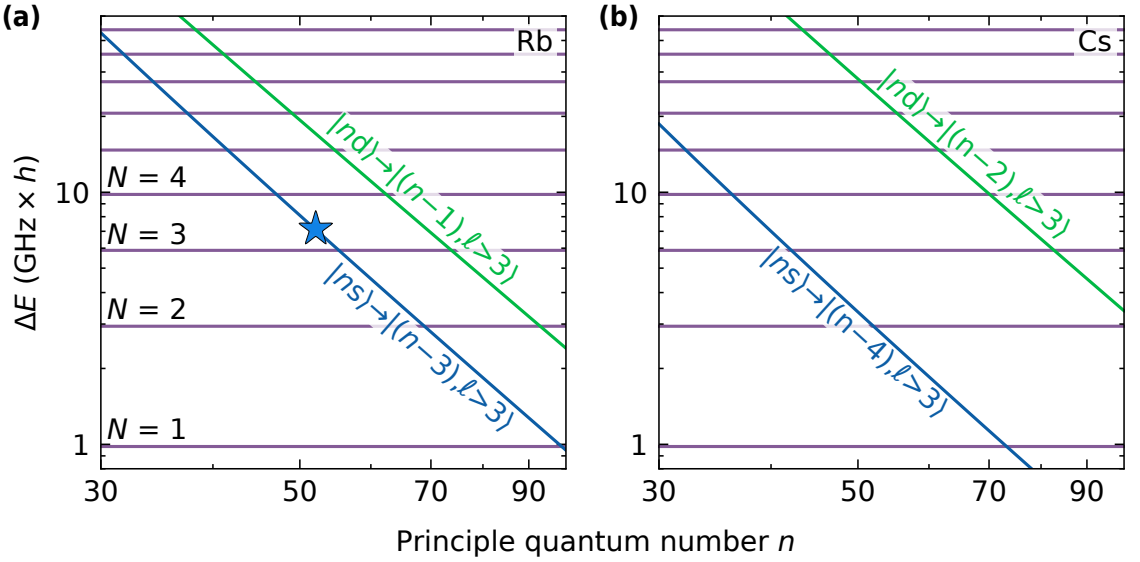

Figure 6.1: Transition energies for Rydberg atoms to neighbouring hydrogenic manifolds. **(a)** Transition energies for Rb Rydberg atoms. The blue (green) line shows the energies for the transition $|ns\rangle \rightarrow |n-3, \ell > 3\rangle$ ($|nd\rangle \rightarrow |n-1, \ell > 3\rangle$). These are the transitions from the states that we can access with our Rydberg excitation lasers. The blue star shows the state $|s\rangle$ that we use to study charge-dipole interactions between Rydberg atoms and molecules. Purple lines show molecular energies relative to the rovibrational ground state. **(b)** Transition energies for Cs Rydberg atoms. The blue (green) line shows the energies for the transition $|ns\rangle \rightarrow |n-4, \ell > 3\rangle$ ($|nd\rangle \rightarrow |n-2, \ell > 3\rangle$). The purples lines are as in (a).

meaning that the neighbouring hydrogenic manifold $n'(\ell > 3)$ for the state ns is that with $n' = n - 3$ and for the state nd is that with $n' = n - 1$. Likewise, for Cs, $\delta(\mathrm{s}) \approx 4$ and $\delta(\mathrm{d}) \approx 2$, so the neighbouring hydrogenic manifolds are those with $n' = n - 4$ and $n' = n - 2$ respectively.

Figure 6.1 shows calculations of ΔE_{Rb} (panel (a)) and ΔE_{Cs} (panel (b)) between states ns (blue) and nd (green) and their neighbouring hydrogenic manifolds $n'(\ell > 3)$ as a function of n. The horizontal lines show the energies of excited rotational states in RbCs. We take the atoms and molecules to be in free space and at zero magnetic and electric fields. This means that, on this scale, the fine and hyperfine splittings are negligible. To be able to experimentally resolve GPRyMs, we choose to work with states where ΔE is just larger than the energy of a molecular state. The blue star in Fig. 6.1(a) highlights the Rb Rydberg state that we choose to work with here, namely the state $|s\rangle \equiv |52\mathrm{s}_{1/2}, m_j = -1/2, m_i = +3/2\rangle$, for which ΔE_{Rb} is just slightly greater than the energy of molecular states with $N = 3$.

Figure 6.2 shows potential energy curves resulting from the charge-dipole interaction close to the pair state $|n = 49, \ell > 3\rangle_{\mathrm{Rb}} |N = 0\rangle_{\mathrm{RbCs}}$. Local minima in the potentials can support bound states and result from the oscillatory nature of the Rydberg electron wavefunction. Notably, the states evolving from this hydrogenic

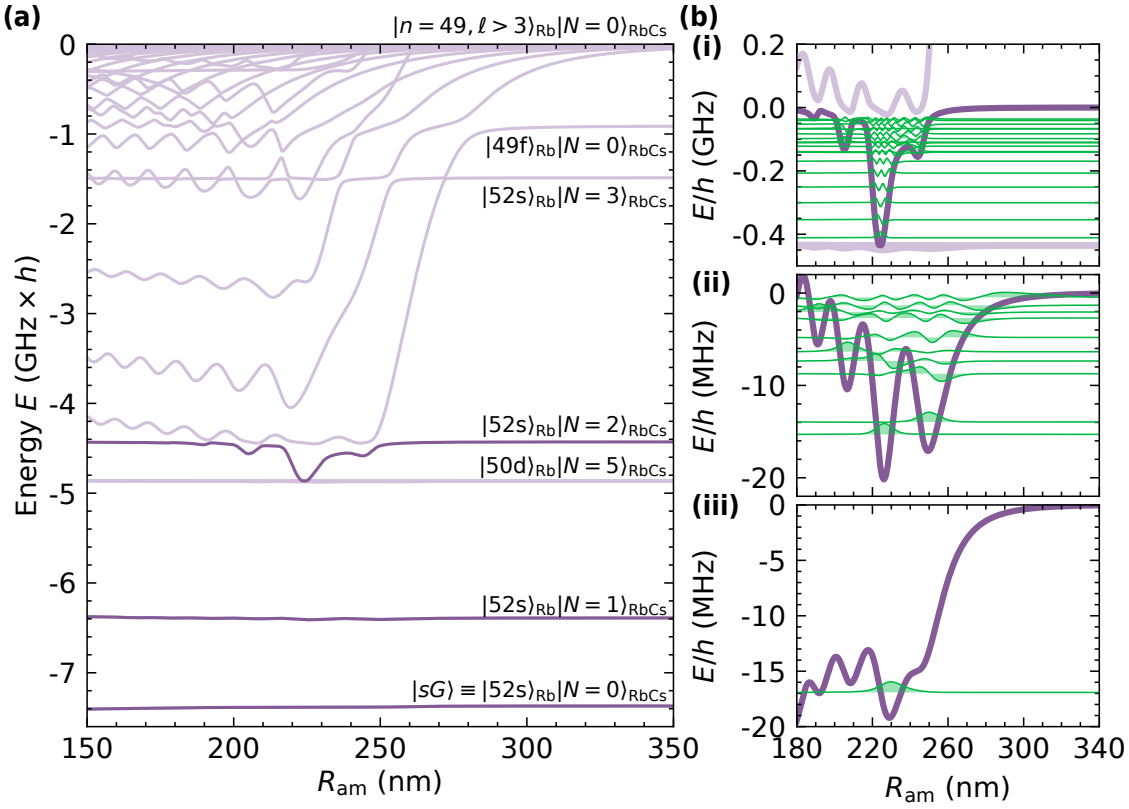

Figure 6.2: Potential energy curves for the Rb+RbCs system close to the $|n = 49, \ell > 3\rangle_{\mathrm{Rb}}|N = 0\rangle_{\mathrm{RbCs}}$ manifold. (a) The energies of pair states as a function of the distance R_{am} between Rydberg core and molecule. Energies are given relative to the energy of the hydrogenic manifold when $R_{\mathrm{am}} \to \infty$. **(b)** Purple lines: potential energy curves evolving from the pair states $|52\mathrm{s}\rangle_{\mathrm{Rb}}|N = 2\rangle_{\mathrm{RbCs}}$ (panel **(i)**), $|52\mathrm{s}\rangle_{\mathrm{Rb}}|N = 1\rangle_{\mathrm{RbCs}}$ (panel **(ii)**), and $|52\mathrm{s}\rangle_{\mathrm{Rb}}|N = 0\rangle_{\mathrm{RbCs}}$ (panel **(iii)**). Energies are given relative to the energy of the pair state when $R_{\mathrm{am}} \to \infty$. Green lines: vibrational wavefunctions of GPRyMs supported by these pair potentials. The wavefunctions have been shifted to the corresponding vibrational energies.

manifold encounter curves where the Rydberg atom in the state $|s\rangle$, to which they are coupled by the charge–dipole interaction [112]. This results in these potential curves acquiring s-wave character, which facilitates the creation of GPRyMs with two-photon Rydberg excitation schemes. The green curves in Fig. 6.2 show the vibrational wavefunctions of such GPRyMs supported by pair states that could be accessed experimentally.[3]

For the remainder of this chapter, we focus on measuring the interaction shift caused by this charge-dipole interaction. We use this interaction shift to engineer atomic Rydberg blockade when a molecule is present. We utilise the pair state $|sG\rangle \equiv |s\rangle_{\mathrm{Rb}}|G\rangle_{\mathrm{RbCs}}$, where $|G\rangle \equiv |N = 0\rangle$ is the rovibrational and hyperfine ground state of RbCs. The potential energy of this pair state is shown in Fig. 6.2(b)(iii). We

[3]These potential energy curves and wavefunctions were calculated by Rosario González-Férez and H. R. Sadeghpour. These calculations use methods that are beyond the scope of this thesis but are detailed in Refs. [109, 111, 202].

note that this pair state supports a single GPRyM (Fig. 6.2(b)(iii), green), which we will aim to observe experimentally in the future.

6.2 RbCs-Rb collisions

For the pair state $|sG\rangle$, the range of the charge-dipole interaction is set by the radius of the Rydberg state. The outermost maximum of the electron probability density for the state $|s\rangle$ occurs at 220 nm. In this section, we discuss how we use our optical tweezer platform to achieve this sub-micrometre interparticle distance.

We begin the experiments discussed here by preparing a Rb atom in an 817 nm tweezer and a RbCs molecule in a 1066 nm tweezer. The RbCs molecule is formed in its rovibrational ground state $|G\rangle$ by magnetoassociation and STIRAP (see Chs 3 and 4). The Rb atom is prepared in the hyperfine ground state $|g\rangle \equiv |5s_{1/2}, f = 1, m_f = +1\rangle$. As a side effect of the molecule formation process, both the Rb atom and the RbCs molecule are primarily prepared in the motional ground state.

To observe blockade, the charge-dipole interaction between the Rydberg atom and the molecule must be greater than the power-broadened transition linewidth. For our system, this is set by the Rabi frequency of 500(3) kHz with which we drive the transition $|g\rangle \rightarrow |s\rangle$ and blockade therefore requires interactions shifts $\gtrsim 1$ MHz. The pair potential plotted in Fig. 6.2(b)(iii) predicts the atom-molecule distance must be below a blockade radius ~ 300 nm to observe this effect, a distance smaller than the beam radii of the individual tweezers (~ 1 μm). One approach to obtaining inter-particle distances smaller than the beam radii of optical tweezers is to load both particles into the same optical tweezer. However, we cannot do this here as the expected lifetime due to collisional loss is < 1 ms [345].

Instead, we utilise species-specific tweezers to realise sub-micrometre separations between particles whilst mitigating collisional loss. The molecule and atom are initially prepared in their respective tweezers of intensities $I_{1066} = 53.8(7)\,\mathrm{kW/cm^2}$ and $I_{817} = 43.9(7)\,\mathrm{kW/cm^2}$. The separation of the *tweezers* is $R_\mathrm{t} = 4\,\mu\mathrm{m}$ along the x-axis. However, analogous to when tweezers containing Rb and Cs are merged together during the molecule formation process (see Sec. 3.4.2), the separation of the *particles* can differ significantly from R_t when the tweezers are close.

Figure 6.3 shows simulations of the behaviour of particles when two traps are merged together along the x-axis. For this simulation, we use the calculated polarisabilities that are tabulated in Table 2.1. In Fig. 6.3(a) we show the potential energy of the particles during the merging. The potentials for different R_t are

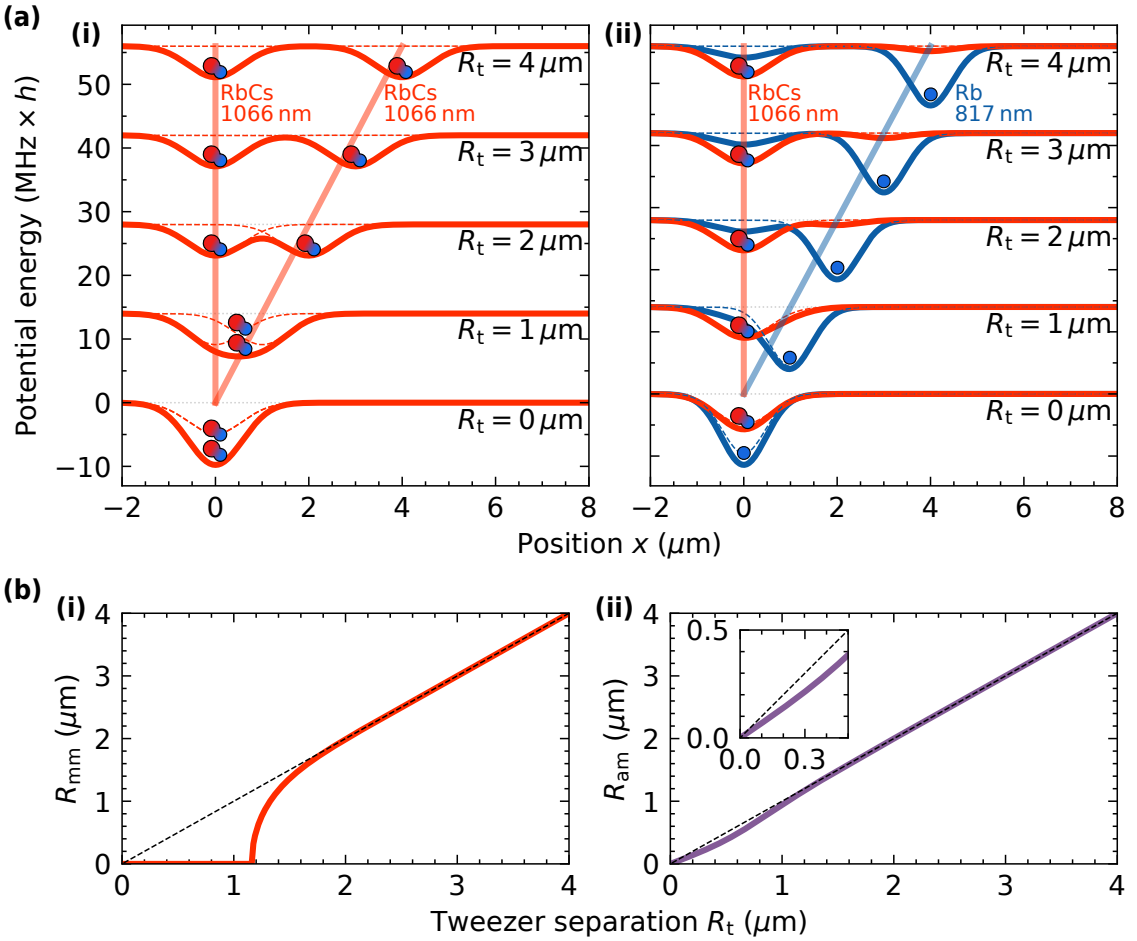

Figure 6.3: Simulations of the merging of traps containing RbCs and Rb. (a) The trapping potentials during the merging process. The solid (dashed) lines show the potential from both tweezers (a single tweezer). The straight lines show the trajectories of the tweezer centres and the potentials are offset for clarity. **(i)** Results for two molecules being merged together. Both molecules are in a 1066 nm tweezer. **(ii)** Results for a molecule and an atom being merged together which are trapped in a 1066 nm and 817 nm tweezer respectively. **(b)** Dependence of the inter-particles distances for the scenarios depicted in (a) as a function of the separation between the centre of the two tweezers R_t. The inset in (b)(ii) shows a zoom to small values of R_t.

offset for clarity. The dashed lines show the potentials resulting from the individual tweezers as the tweezer centres are swept along the bold trajectories. The solid potentials show the combined effect of both tweezers. Fig. 6.3(a)(i) shows the case if we were to start with two molecules both trapped in 1066 nm tweezers that are merged together. When the tweezer separation is less than $R_t \approx 1.2\,\mu m$, the two tweezers no longer satisfy the Rayleigh criterion and a wide single well is formed. At this point, the two molecules come together and the inter-molecule distance R_{mm} drops to zero. Fig. 6.3(b)(i) shows the dependence of R_{mm} on R_t: at separations much larger than the beam waists ($R_t \gg w^{1066}$), $R_{mm} \approx R_t$ (dashed black line). As the Rayleigh criterion is approached, R_{mm} sharply drops to zero. This sharp drop

makes it impractical to realise a stable value of $R_{\mathrm{mm}} \lessapprox w^{1066}$ using two independent tweezers due to fluctuations in the relative tweezer positions, which have a standard deviation of approximately $\sigma(R_{\mathrm{t}}) = 50^{+50}_{-40}$ nm (see Sec. 3.4.2).[4] In contrast, for two particles of different species (here RbCs and Rb), the results are strikingly different. Fig. 6.3(a)(ii) shows the trap potentials during this scenario. The red lines show the potential experienced by RbCs: the solid (dashed) line shows the potential resulting from both tweezers (only the 1066 nm tweezer). The solid (dashed) blue line shows the potential experienced by Rb from both tweezers (only the 817 nm tweezer). The ratio of the polarisabilities at the tweezer wavelengths (see Table 2.1) is $\alpha^{\mathrm{RbCs}}_{1066}/\alpha^{\mathrm{RbCs}}_{817} \approx 4.5$ for RbCs [217] such that the molecule is confined much more strongly by the 1066 nm tweezer than the 817 nm tweezer. Conversely, for Rb this ratio is $\alpha^{\mathrm{Rb}}_{1066}/\alpha^{\mathrm{Rb}}_{817} \approx 1/6.3$ [218] and it is confined predominantly in the 817 nm tweezer. This means that as the tweezers are brought together, each particle is only slightly affected by the other's tweezer. Therefore, the inter-particle separation R_{am} follows the separation between the centre of the tweezers ($R_{\mathrm{am}} \approx R_{\mathrm{t}}$) during most of the merging trajectory. Fig. 6.3(b)(i) shows the dependence of R_{am} on R_{t}: for small distances ~ 100 nm, $R_{\mathrm{am}} < R_{\mathrm{t}}$ albeit only slightly such that R_{am} can still be controlled with reasonable precision.

We investigate loss due to collisions between a Rb atom in the state $|g\rangle$ and a RbCs molecule in the state $|G\rangle$ to verify that we can hold an atom-molecule pair sufficiently close to observe the charge-dipole interaction. Fig. 6.4(a) shows the tweezer sweeps used for this measurement. The atom and molecule tweezers begin separated by 4 µm along the x-axis (panel (i)). We sweep the atom tweezer along the y-axis to a programmed tweezer separation (panel (ii)). The atom tweezer is then swept along the x-axis such that it overlaps with the molecule tweezer in this direction so that the tweezers are separated by R_{t} along the y-axis (panel (iii)). We hold the atom at this position for 9.5 ms before the sweeps are reversed and the particle survival probabilities are measured (panel (iv)).

The survival probabilities of the atom and molecule for different tweezer separations are shown in Fig. 6.4(b). Molecule survival probabilities are obtained using runs in which weakly bound molecules were successfully formed (see Sec. 4.3). The upper panel shows the one-body survival probabilities from runs where *either* the Rb

[4] This is a potential problem for the study of molecule-molecule interactions in optical tweezers, for which $R_{\mathrm{mm}} \sim 500$ nm must be achieved to realise interactions on the scale of $1\,\mathrm{kHz} \times h$ [47]. In future works, we plan to mitigate fluctuations in R_{mm} by transferring molecules to an optical lattice at a magic wavelength λ [98] for which molecules can be stably trapped at distance $R_{\mathrm{mm}} = \lambda/2$ (see Sec. 8.2.2). For quantum information and simulation applications, it is more practical to extend the effective range of molecule-molecule interactions by mediating them with resonant Rydberg atoms (see Ch. 7).

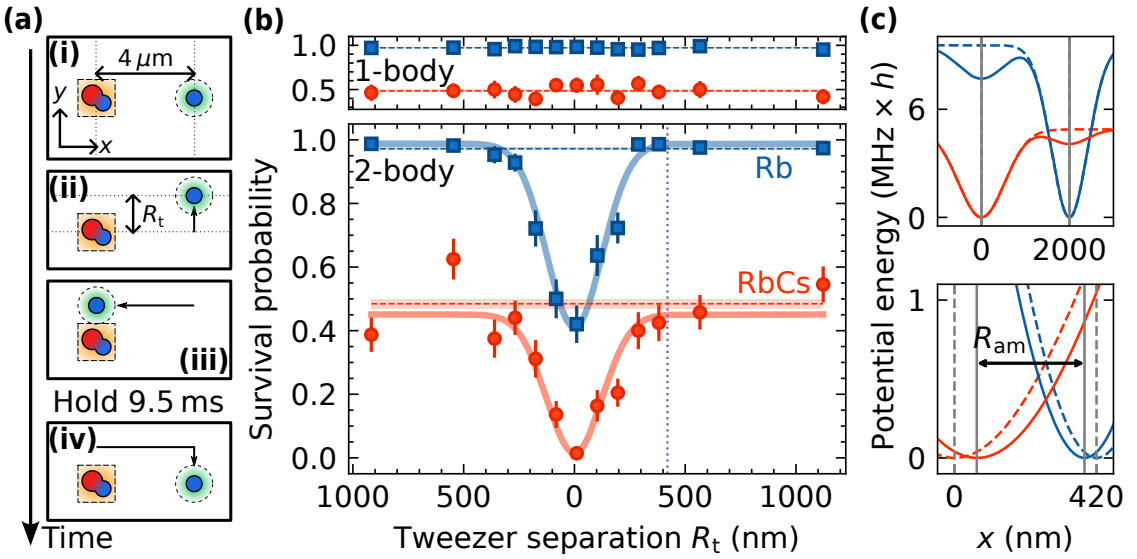

Figure 6.4: Collisions between ground-state RbCs molecules and Rb atoms held in separate species-specific optical tweezers. **(a)** Tweezer positions during the measurement. **(i)** The atom and molecule begin with a separation of 4 μm along the x-axis. The atom (molecule) is stored in an 817 nm (1066 nm) tweezer, shown as a green circle (orange square). **(ii)** The 817 nm tweezer is swept along the y-axis so its separation from the 1066 nm tweezer in this direction is R_t. **(iii)** The 817 nm tweezer is swept along the x-axis to overlap with the 1066 nm tweezer where it is held for 9.5 ms. **(iv)** The 817 nm tweezer is returned to its original position where the particle survival is measured. **(b)** Particle survival probabilities as a function of the tweezer separation R_t. Upper panel: experimental runs where either a single Rb atom (blue squares) or a single RbCs molecule (red circles) is present. Lower panel: runs where both the atom and the molecule are present. The dashed lines (and shaded regions) correspond to the mean values (and errors) from the one-body cases. **(c)** The potential energy of the atom (blue) and molecule (red) resulting from their own tweezer (dashed lines) and both tweezers (solid lines) for $R_t = 2000$ nm (upper panel) and $R_t = 420$ nm (lower panel), relative to the potential minima.

atom *or* the RbCs molecule is present. The atomic survival probability is 97.2(4)% and the molecule survival probability is 48(2)%.[5] By compensating for the return STIRAP efficiency, we predict that a molecule in $|G\rangle$ is present in 53(3)% of runs in which a weakly bound molecule is created. The lower panel in Fig. 6.4(b) shows the two-body survival probabilities for runs in which *both* an atom and a weakly bound molecule are initially prepared. When the tweezers are brought together, the wavefunctions of the particles begin to overlap and collisions cause loss of both the molecule and atom. We observe a reduction in the atom survival probability by 58(6)%, commensurate with the probability a molecule in state $|G\rangle$ is present.

[5]These experiments were performed before the molecule formation stages were fully optimised. For this data, the one-way STIRAP fidelity $\mathcal{F}_{\mathrm{STIRAP}} = 91(1)\%$. Furthermore, magnetoassociation was performed in a deeper 1066 nm tweezer than for most of the experiments presented in Chapter 4, such that loss of molecules in the state $|F\rangle$ prior to STIRAP was significant. These two factors are the primary limit to the molecule survival probability as presented here.

From a Gaussian fit, we find that the loss falls to $1/e^2$ of its maximum value at $R_\mathrm{t} = 250(20)\,\mathrm{nm}$, which meas that we are able to hold the particles sufficiently close to resolve the charge-dipole interaction.

6.3 Rydberg blockade

We now demonstrate the blockade of excitation of a Rb atom to $|s\rangle$ when a RbCs molecule is sufficiently close. As with blockade by an additional Rydberg atom (see Sec. 5.8), this effect occurs due to the energy shift of a pair state being larger than the linewidth of the Rydberg transition. Here we study the pair state $|sG\rangle$, the energy of which is shown in Fig. 6.2(b)(iii). This linewidth of the transition is set by the Rabi frequency with which we excite to $|s\rangle$ (500(3) kHz). Blockade therefore requires interactions shifts $\gtrsim 1\,\mathrm{MHz}$, corresponding to $R_\mathrm{am} \lesssim 300\,\mathrm{nm}$.

To demonstrate blockade, we repeat the routine used to measure collisional loss, but use a shorter hold time of 3 ms when the tweezers are close together. We drive the atomic Rydberg transition $|g\rangle \rightarrow |s\rangle$ during this hold time while the trapping light is still present. Atoms excited to state $|s\rangle$ are anti-trapped and ejected from the tweezers, mapping Rydberg excitation onto atom loss (see Sec. 5.5). The separation between the centre of the tweezers for this measurement is $\mathrm{R_t} = 420(40)\,\mathrm{nm}$; this separation is sufficient to suppress collisional loss (Fig. 6.4(b), purple dotted line). As will be discussed shortly, this equates to an atom-molecule separation of $R_\mathrm{am} = 310(40)\,\mathrm{nm}$ (Fig. 6.4(c), lower panel).

Figure 6.5 shows the blockade of the Rydberg transition of the Rb atom when a RbCs molecule in the state $|G\rangle$ is present. Fig. 6.5(a) shows the survival probability of the Rb atom as the Rydberg pulse duration is varied. For experimental runs where the molecule tweezer is empty (green circles), we observe Rabi oscillations between states $|g\rangle$ and $|s\rangle$ with a fitted frequency of $\Omega = 500(3)\,\mathrm{kHz}$. The observed damping is primarily caused by laser phase noise. In contrast, for runs where a molecule in the state $|G\rangle$ is present (purple squares), we observe a suppression of the excitation to the state $|s\rangle$. Here, the molecule is sufficiently close to the atom that the energy shift of the pair state $|sG\rangle$ due to the charge-dipole interaction is significant and excitation during the Rydberg pulse is blockaded. The frequency of the residual Rabi oscillations is almost identical to that for the unblockaded case. This is due to the sharp onset of the interaction shown in Fig. 6.2(b)(iii) combined with shot-to-shot variations in the relative alignment of the tweezers. For runs with the largest separations, the energy shift is smaller than the Rabi frequency of the Rydberg transition leading to a signal at the unshifted Rabi frequency.

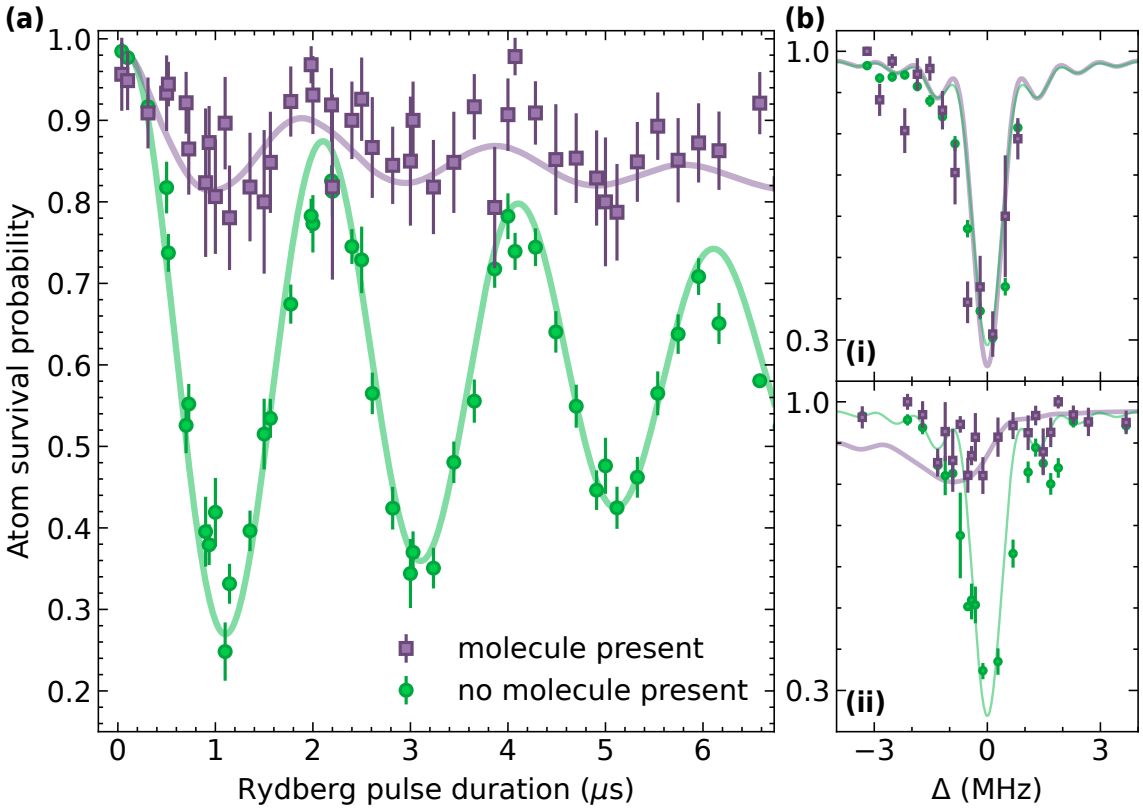

Figure 6.5: Rydberg blockade due to the charge-dipole interaction between an atom and polar molecule. (a) Survival probability of the Rb atom as a function of the Rydberg pulse duration for $R_{\mathrm{am}} = 310(40)$ nm. Atoms excited to $|s\rangle$ are ejected from the trap and lost. Events are post-selected on the detection of a molecule in $|G\rangle$ (purple squares) or unsuccessful formation of a molecule (green circles). The solid lines show the results of simulations using the Lindblad master equation using our estimated atom-molecule separation. (b) Rb atom survival probability as a function of the effective detuning Δ using a 1 µs pulse for $R_{\mathrm{am}} = 700(40)$ nm (panel **(i)**) and $R_{\mathrm{am}} = 310(40)$ nm (panel **(ii)**). The detuning is defined relative to the transition centre in the absence of a molecule. Symbols are as in (a) and solid lines show the results of simulations using the estimated atom-molecule separations.

Figure 6.5(b) shows the effect of changing the atom-molecule separation R_{am} on the Rydberg blockade. For this experiment, we fix the pulse duration to approximate a π pulse and scan the effective detuning Δ of the light driving the Rydberg transition. For $R_{\mathrm{am}} = 700(40)$ nm, shown in Fig. 6.5(b)(i), the charge-dipole interaction is negligible. Here, the dominant interaction is van der Waals, leading to a shift of ~ 0.1 kHz [346]. Consequently, the presence of a molecule does not affect the Rydberg excitation. However, for $R_{\mathrm{am}} = 310(40)$ nm, shown in Fig. 6.5(b)(ii), the presence of a molecule leads to an observed shift of the Rydberg transition to lower energy, as expected. The transition is significantly broadened due to the sensitivity of the charge-dipole interaction to the atom-molecule separation. The broadening causes a concomitant reduction in the signal amplitude.

The dynamics of the atom-molecule system are extremely sensitive to small

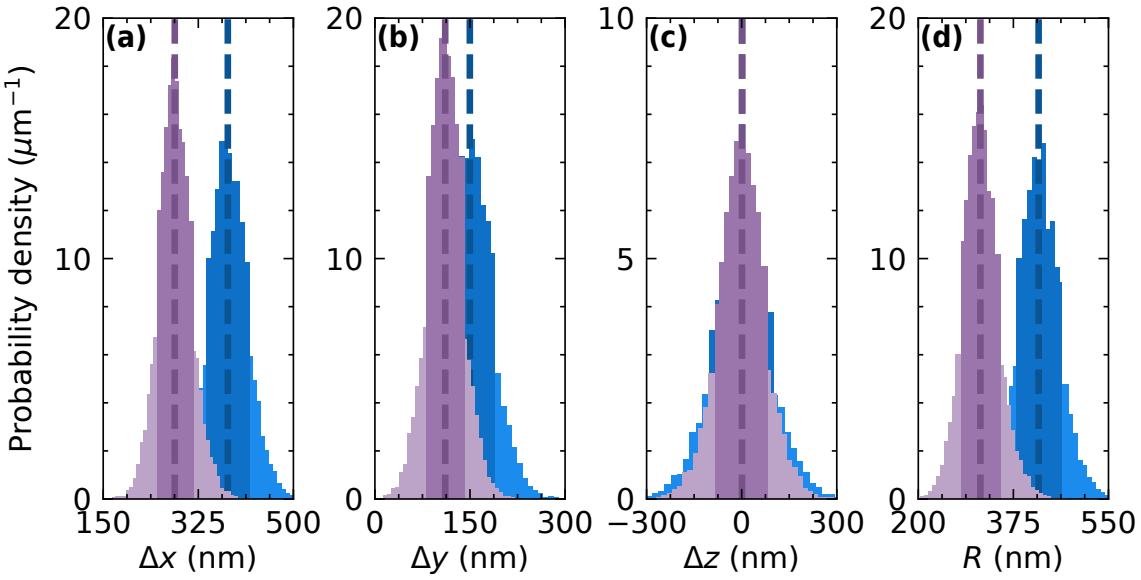

Figure 6.6: Results of the atom-molecule separation simulation for the experiment shown in Fig. 6.5(a). The probability distributions of the tweezer displacements (blue) and atom-molecule displacements (purple) are shown along the three experimental axes (panels **(a)**-**(c)**) and the inter-particle axis (panel **(d)**). The best estimate for each parameter is taken to be equal to the mean of the distribution (indicated by the dashed lines) and the associated systematic uncertainty is read from the 1σ bounds (shown as the darker shaded regions).

changes in the separation R_{am} between atom and molecule. Therefore, a good estimate of R_{am} is critical for the simulations to accurately reproduce the observed dynamics. The relative alignment of the tweezers can drift on the order of $\sim 100\,\mathrm{nm}$ on the timescale of days as laboratory conditions such as the humidity and temperature fluctuate. We correct for this by, immediately after obtaining the data shown in Fig. 6.5, repeating collision measurements like that shown in Fig. 6.4(b) to measure the radial separations between the centre of the tweezers. For the experimental runs where the atom and molecule were close (Fig. 6.5(a) and (b)(i)), we measure the tweezer separations in the x- and y-axes as $\{\Delta x_{\mathrm{t}}, \Delta y_{\mathrm{t}}\} = \{380(40), 150(40)\}\,\mathrm{nm}$ respectively. For experimental runs where the atom and molecule were further apart (Fig. 6.5(b)(ii)), we measure $\{\Delta x_{\mathrm{t}}, \Delta y_{\mathrm{t}}\} = \{40(100), 760(30)\}\,\mathrm{nm}$. The separation in the axial direction is much more stable and we estimate that $\Delta z_{\mathrm{t}} = 0(100)\,\mathrm{nm}$ for all experimental runs.[6] For these separations, the numbers in parentheses represent the systematic uncertainties resulting from the fit of the collision measurements and the distance calibrations of the 2D AOD used to control the position of the 817 nm tweezer (see Sec. 5.5)

To estimate the corresponding atom-molecule displacements $\{\Delta x_{\mathrm{am}}, \Delta y_{\mathrm{am}}, \Delta z_{\mathrm{am}}\}$ and their systematic uncertainties we use a Monte Carlo method. For each iteration

[6]The tweezers were aligned axially with the measurement shown in Fig. 5.13 approximately a week prior to the measurements presented here.

of the Monte Carlo method, the tweezer displacements along each axis are sampled from normal distributions with the means equal to our best estimates and standard deviations equal to the associated systematic uncertainties on these values. The three-dimensional potential landscape is calculated for both the atom and molecule, and each are placed at their potential minima. The tweezer and atom-molecule separations are then calculated. With 10^4 iterations, we find that when the molecule and atom are held close, $\{\Delta x_{\mathrm{am}}, \Delta y_{\mathrm{am}}, \Delta z_{\mathrm{am}}\} = \{280(40), 110(30), 0(80)\}$ nm, $R_{\mathrm{t}} = 420(40)$ nm, and $R_{\mathrm{am}} = 310(40)$ nm. The best estimate for each parameter is taken to be equal to the mean of its distribution and the associated systematic uncertainty is read from the 1σ bounds; the distributions from this simulation are shown in Fig. 6.6. For experimental runs where the atom and molecule were further apart, we find that $\{\Delta x_{\mathrm{am}}, \Delta y_{\mathrm{am}}, \Delta z_{\mathrm{am}}\} = \{40(90), 690(40), 0(110)\}$ nm, $R_{\mathrm{t}} = 770(30)$ nm, and $R_{\mathrm{am}} = 700(40)$ nm.

In these simulations, we use the calculated polarisabilities for each species that are listed in Table 2.1. Accurately calculating the polarisability of the RbCs molecule is more challenging compared to calculating the polarisabilities of alkali-metal atoms like Rb and Cs because of the more complex energy level structure of the molecule. For example, Blackmore *et al.* [291] measured the isotropic polarisability of the RbCs vibrational ground state to be $2.02(4) \times 10^3 \times 4\pi\varepsilon_0 a_0^3$ at a wavelength of 1064.513 nm. This measured value is $\sim 10\%$ higher than the calculated value of $1.8 \times 10^3 \times 4\pi\varepsilon_0 a_0^3$ [217]. In our calculations we have incorporated this uncertainty in the molecule polarisability. For example, for the experiment presented in Fig. 6.5(a), we find that when the RbCs polarisabilities at both wavelengths are scaled by 10% there is no significant change to R_{am}. When the ratio between the two polarisabilities is scaled by 10% the change to R_{am} is on the order of $\sim 2\%$, which is much less than the uncertainty resulting from the systematic uncertainties on the tweezer displacements.

The solid lines in Fig. 6.5 show results of simulations of the dynamics of the system.[7] The system is simulated by solving the Lindblad master equation

$$\dot{\rho} = -i[\mathcal{H}, \rho] + \mathcal{L}[\rho]\,, \tag{6.4}$$

where $\mathcal{L}$ is the Lindblad superoperator, ρ is the density matrix, and $\mathcal{H} \equiv H_{\mathrm{a}} + H_{\mathrm{m}} + V(R_{\mathrm{am}})$ is the model Hamiltonian describing the atom-molecule system. H_{a} and H_{m} are the uncoupled, single particle Hamiltonians corresponding to the atom and molecule respectively and $V(R_{\mathrm{am}})$ is the interaction potential between the atom and the molecule. The atom is approximated as a two-level system with Rabi frequency Ω and detuning Δ from the transition $|g\rangle \rightarrow |s\rangle$. The interaction shift for the pair

[7] These simulations were performed by Archie C. Baldock.

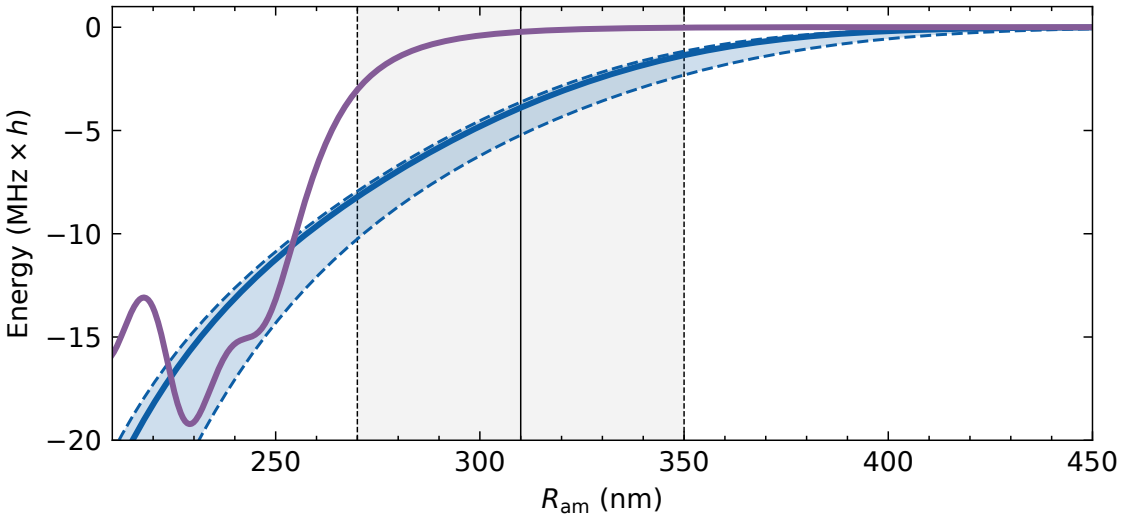

Figure 6.7: Energy shift of the pair state $|sG\rangle$ as a function of the separation R_{am} between the Rb Rydberg atom and RbCs molecule. The blue line shows the result obtained by averaging the interaction using a Gaussian window with standard deviation of 53 nm: this energy is used for the simulation of the system dynamics. The shaded blue region shows the range of potentials obtained when averaging with a standard deviation between 50.3(4) nm and 65.2(6) nm. The purple line shows the energy shift for no averaging. The shaded vertical region highlights the range of R_{am} relevant to the blockade measurements presented here.

state $|gG\rangle$ is negligible for the values of R_{am} in our experiments, so the only non-zero interaction term in the simulation is the energy shift of the pair state $|sG\rangle$. We neglect spontaneous emission from the state $|s\rangle$ as this occurs on timescales longer than the dynamics studied here (the blackbody-limited lifetime for the state $|s\rangle$ is $\tau_s^{(300)} = 70\,\mu s$, see Sec. 5.5).

To reproduce the observed dynamics in the absence of a molecule, we find it important to include dephasing from the Rydberg lasers. We achieve this using Lindblad operators $-\frac{1}{2}\gamma\rho_{gs}$ and $-\frac{1}{2}\gamma\rho_{sg}$ which incorporate the decay of the coherences between the ground and Rydberg states. Using the measured Rabi frequency, we empirically find a value for $\gamma = 0.1\,\text{MHz}$ that matches the observed dynamics in the absence of a molecule. This corresponds to phase noise resulting from the stabilisation of the excitation lasers to the ULE cavity and in future could be suppressed using established techniques [347–349].

When solving the dynamics for the atom-molecule system, we take into account the finite wavefunction spread of the atom and molecule. As the atom and molecule are predominantly prepared in the motional ground state of their respective tweezers, we average the interaction between $|s\rangle$ and $|G\rangle$ over the ground state wavefunction of relative motion. For this, we calculate the confinement length for relative motion $\beta_{rel} \equiv (1/2\pi)\sqrt{h/\mu\nu}$, where $\mu = m_{Rb}m_{RbCs}/(m_{Rb} + m_{RbCs})$ is the reduced mass of the atom-molecule pair and ν is the trap frequency for relative motion (see Eq. (3.1)).

For the tweezer intensities used here, the trap frequencies resulting from just a species' own tweezer are $\{\nu_{\mathrm{Rb},x}, \nu_{\mathrm{Rb},y}, \nu_{\mathrm{Rb},z}\} = \{78(2), 70(1), 15.6(4)\}$ kHz for Rb and $\{\nu_{\mathrm{RbCs},x}, \nu_{\mathrm{RbCs},y}, \nu_{\mathrm{RbCs},z}\} = \{26.8(4), 23.9(3), 5.3(1)\}$ kHz for RbCs. The traps are primarily separated along the two radial directions, and considering just these two directions (i.e. $\nu_j = \sqrt{\nu_{j,x}\nu_{j,y}}$ for species j), we obtain $\beta_{\mathrm{rel}} = 50.3(4)$ nm. In contrast, if we consider all three directions (i.e. $\nu_j = \sqrt[3]{\nu_{j,x}\nu_{j,y}\nu_{j,z}}$ for species j), we find that $\beta_{\mathrm{rel}} = 65.2(6)$ nm. We expect that the true value of β_{rel} is between these two cases. The blue region in Fig. 6.7 shows the effect of averaging the energy shift of the pair state $|sG\rangle$ with a Gaussian window where the standard deviation is between these two values of β_{rel}. The purple line shows the unaveraged potential and the solid blue line shows the energy shift obtained with $\beta = 53$ nm that is used in the simulations of the dynamics.

When simulating the system, we take into account shot-to-shot fluctuations in the alignment of the tweezers. We have independently measured the relative drift of the tweezers have a standard deviation of approximately 50 nm in the radial directions (along the x- and y- axes, see Sec. 3.4.2). We are unable to perform these measurements in the axial direction (along the z-axis) with the same precision due to much larger confinement lengths in this direction and take the estimate of the radial drift for this axis as well. Our estimate for the standard deviations in tweezer separations is therefore $\{\sigma_x, \sigma_y, \sigma_z\} = \{50, 50, 50\}$ nm. We incorporate this drift into the simulations of the dynamics by repeating the simulation for 200 iterations. For each iteration of the simulation, we randomly sample $\{\Delta x_{\mathrm{am}}, \Delta y_{\mathrm{am}}, \Delta z_{\mathrm{am}}\}$ from a normal distribution. We construct the distribution using our best estimate of the atom-molecule separation as the mean and our estimate of the shot-to-shot fluctuations in the tweezer separations as the standard deviation of the distribution. We calculate R_{am} and solve Eq. (6.4); the results of these iterations are then averaged for each time or detuning.

To map the results of the simulations of the dynamics onto the results of the experiments, we include state preparation and measurement errors. Following the approach of de Léséleuc *et al.* [350], we include terms η, ϵ, and ϵ' with each term measured experimentally. The term η accounts for preparation errors and corresponds to the probability the atom was not prepared in the state $|g\rangle$. We find that for this experimental sequence, $\eta = 0.13$ which is predominantly limited by Raman scattering from the optical tweezers in which the atom is held during the molecule formation stages. The term ϵ accounts for loss of atoms in the state $|g\rangle$ which were not excited to the state $|s\rangle$. We measure $\epsilon = 0.02$, limited by collisions with background gas particles in the vacuum chamber. Finally, $\epsilon' = 0.06$ accounts for the probability that an atom in the state $|s\rangle$ decays before it is lost from the optical tweezer (see

Sec. 5.5). We convert the probability $\tilde{P}_g$ that the atom populates the state $|g\rangle$ (obtained from the simulations) into the experimentally measured atom-survival probability P_g using [350]

$$P_g = \eta(1-\varepsilon) + (1-\eta)(1-\varepsilon)\left[\tilde{P}_g + \varepsilon'\tilde{P}_s\right], \tag{6.5}$$

where $\tilde{P}_s$ is the population of state $|s\rangle$ that we also obtain from solving Eq. (6.4).

We find that the results of our simulations (Fig. 6.5, solid lines) are in good agreement with the experimental data. Our simulations reproduce the fact that there are residual Rabi oscillations in the presence of a molecule, corresponding to runs in which the atom-molecule separation was larger than the blockade radius. Furthermore, the simulations predict that when varying Δ in the blockaded case, there is a broadening of the transition due to fluctuations in R_{am} which causes a reduction in the signal amplitude. The exception to this agreement is the appearance of a shoulder in the simulation results shown in Fig. 6.5(b)(ii) which is highly sensitive to fluctuations in R_{am}: we find that small changes of R_{am} on the scale of $\sim 10\,\mathrm{nm}$ can cause large changes is the simulated behaviour.

6.4 Summary

We have demonstrated blockade of the excitation of Rb to the Rydberg state $|s\rangle$ due to the charge-dipole interaction with a RbCs molecule in the rovibrational ground state. To realise this regime, we hold the atom and molecule at a distance of $R_{\mathrm{am}} = 310(40)\,\mathrm{nm}$ with species-specific tweezers such that significant collisional loss is avoided. This represents the first observation of a charge-dipole induced shift in an ultracold setting and opens up many new research directions. In particular, we have highlighted the potential to photoassociate GPRyMs using this platform, which the calculations presented here predict exist for separations $R_{\mathrm{am}} \sim 220$ nm.

7 Resonant dipole-dipole interactions between molecules and Rydberg atoms

In this chapter, we explore how resonant dipole-dipole interactions can be engineered between Rydberg atoms and molecules. These interactions are promising for quantum information and simulation applications because they extend to longer range than the charge-dipole interactions discussed in Ch. 6. We begin with a discussion of the theory of these interactions and explore how they could mediate interactions and quantum gates between molecules. We detail how to choose molecular and atomic transitions that are resonant. We perform microwave spectroscopy of these transitions and present preliminary observations of atomic Rydberg blockade caused by resonant dipole-dipole interactions with a nearby molecule.

7.1 Dipole-dipole interactions

To realise longer-range interactions between molecules and Rydberg atoms, we engineer resonant dipole-dipole interactions between pairs of atoms and molecules. Analogous to dipole-dipole interactions between two Rydberg atoms [50], these interactions give rise to an energy shift

$$\Delta E = -\frac{C_3}{R_{\mathrm{am}}^3}\,, \tag{7.1}$$

where R_{am} is the atom-molecule separation and C_3 is the resonant dipole–dipole interaction coefficient.

Following the approach of Wang *et al.* [101] and Zhang & Tarbutt [102], we consider a hybrid system composed of molecules and Rydberg atoms. The components of this system are shown in Fig 7.1(a). The molecules and (ground-state) atoms are trapped in species-specific optical tweezers that can be dynamically moved. The relevant atomic states are the ground state $|g\rangle$ and two Rydberg states, here labelled

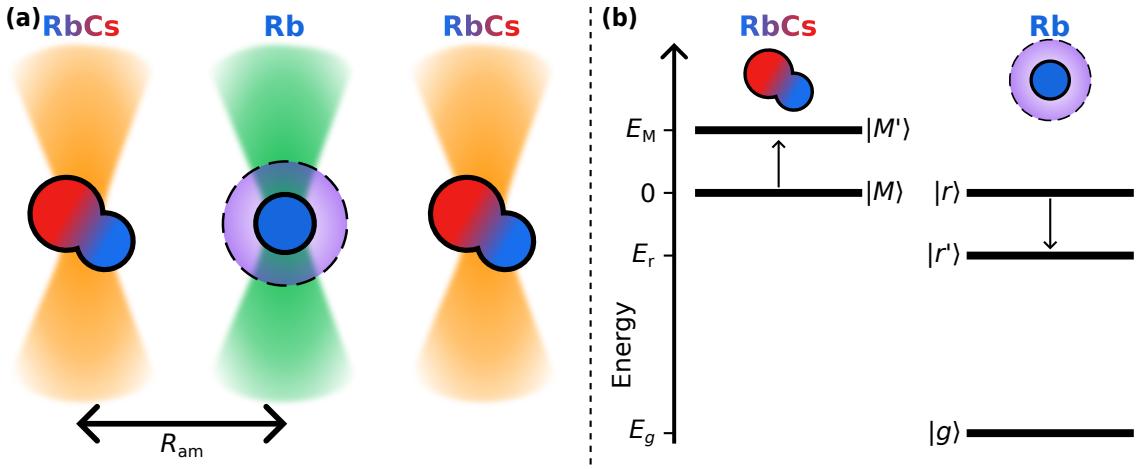

Figure 7.1: A hybrid quantum system of molecules and Rydberg atoms. (a) The physical system considered here. A Rb Rydberg atom is equidistant between two trapped RbCs molecules. The atom-molecule separation is R_{am}. **(b)** Energy levels required for resonant interactions between molecules and Rydberg atoms. Resonant energy exchange can occur when there is an atomic transition $|r\rangle \to |r'\rangle$ with equal and opposite energy to a molecular transition $|M\rangle \to |M'\rangle$.

$|r\rangle$ and $|r'\rangle$, for which there is an allowed one-photon transition $|r\rangle \to |r'\rangle$. The relevant states in the molecule are two rotational states, here labelled $|M\rangle$ and $|M'\rangle$, that also have an allowed one-photon transition $|M\rangle \to |M'\rangle$.

To engineer resonant dipole-dipole interactions, the molecular and Rydberg transitions must be resonant with each other (i.e. their energies must be equal and opposite). This is achieved, for example, if the pair states $|rM\rangle \equiv |r\rangle_{\text{Rb}} |M\rangle_{\text{RbCs}}$ and $|r'M'\rangle \equiv |r'\rangle_{\text{Rb}} |M'\rangle_{\text{RbCs}}$ are degenerate as $R_{\text{am}} \to \infty$. In the following discussion, we take this to be the case and denote the energy of the transition $|M\rangle \to |M'\rangle$ as E_{M} and of the transition $|r\rangle \to |r'\rangle$ as E_{r} (E_{r} has opposite sign to E_{M}). The energy levels of the system are shown in Fig 7.1(b). The resonance condition can be written as requiring that $E_{\text{M}} + E_{\text{r}} = 0$. We take the energy of the single-particle states $|M\rangle$ and $|r\rangle$ to be zero and assume that the effective detuning Δ when driving the Rydberg excitation $|g\rangle \to |r\rangle$ is zero.

The Hamiltonian describing the hybrid system is [102]

$$\hat{H} = \sum_a \hat{H}_a^{\text{a}} + \sum_m \hat{H}_m^{\text{M}} + \sum_a \hat{H}_a^{\text{al}} + \frac{1}{2} \sum_i \sum_j \hat{H}_{ij}^{\text{DD}} . \tag{7.2}$$

Here,

$$\hat{H}_a^{\text{a}} = E_{\text{r}} |r'\rangle \langle r'| + E_g |g\rangle \langle g| \tag{7.3}$$

is the single-particle Hamiltonian for Rydberg atom a and

$$\hat{H}_m^{\text{M}} = E_{\text{M}} |M'\rangle \langle M'| \tag{7.4}$$

is the single-particle Hamiltonian for molecule m. E_g is the energy of the state $|g\rangle$. The atom-light interaction for atom a is

$$\hat{H}_a^{\mathrm{al}} = \frac{1}{2}h\Omega\left(|g\rangle\langle r| + |r\rangle\langle g|\right) , \tag{7.5}$$

the effect of which is to couple the ground state $|g\rangle$ to the Rydberg state $|r\rangle$ with Rabi frequency Ω. For these three terms, the sums in Eq. (7.2) run over all atoms and molecules in the system.

We assume that the only interactions between particles in the system are resonant dipole-dipole interactions. The Hamiltonian representing this interaction between particles i and j is [71, 101]

$$\hat{H}_{ij}^{\mathrm{DD}} = \frac{1}{2}V_{ij}^{\mathrm{DD}}\left(\hat{\sigma}_i^+\hat{\sigma}_j^- + \hat{\sigma}_i^+\hat{\sigma}_j^-\right) , \tag{7.6}$$

where $\hat{\sigma}_i^+$ is the Pauli raising operator for particle i. If particle i is a molecule, this operator transfers molecules in the state $|M\rangle$ to the state $|M'\rangle$, and if particle i is a Rydberg atom, it transfers atoms in the state $|r'\rangle$ to the state $|r\rangle$. The corresponding lowering operator $\hat{\sigma}_i^-$ has the opposite effect. The sum involving H_{ij}^{DD} in Eq. (7.2) runs over all pairs of particles and the coefficient of $1/2$ compensates for the double counting of these pairs. The effect of this Hamiltonian is to transfer an excitation with energy $|E_{\mathrm{M}}| = |E_{\mathrm{r}}|$ between the particles. The atomic ground state $|g\rangle$ is far off resonant and, therefore, does not participate in this interaction.

The strength of the dipole-dipole interaction between two particles i and j is given by

$$V_{ij}^{\mathrm{DD}} = \frac{d_i d_j}{4\pi\varepsilon_0 R^3} . \tag{7.7}$$

Here, R is the distance between the particles and d_i is the TDM between the relevant states in particle i (the states $|M\rangle$ and $|M'\rangle$ for molecules and the states $|r\rangle$ and $|r'\rangle$ for atoms). For typical polar molecules $d \sim 1\,\mathrm{D}$ [47] and for typical Rydberg states in alkali atoms $d \sim 10\,\mathrm{kD}$ [101, 304]. This means that we can ignore molecule-molecule interactions and, by enforcing the restriction that we excite only a single atom to a Rydberg state, consider just interactions between molecules and Rydberg atoms.

These resonant dipole-dipole interactions mean that Rydberg atoms can be used to mediate quantum gates between molecules. Such a gate is approximately $d_{\mathrm{r}}/d_{\mathrm{M}} \sim 10^4$ times faster than a raw molecule-molecule gate, where d_{r} (d_{M}) is the TDM of the Rydberg atom (molecules). For example, Wang *et al.* [101] showed that, for a system where a single atom is halfway between a pair of molecules (see

Fig 7.1(a)), it is possible to realise the entangling gate [101]

$$\begin{pmatrix} -1 & 0 & 0 & 0 \\ 0 & 0 & 1 & 0 \\ 0 & 1 & 0 & 0 \\ 0 & 0 & 0 & 1 \end{pmatrix} \tag{7.8}$$

in the basis $\{|MgM\rangle, |MgM'\rangle, |M'gM\rangle, |M'gM'\rangle\}$ by performing a 2π pulse with the Rydberg excitation light. Here the states of the system are written as e.g. $|M'gM\rangle$, by which we mean that the first molecule is in the state $|M'\rangle$, the atom is in the state $|g\rangle$, and the second molecule is in the state $|M\rangle$. This gate performs the exchange $|MgM'\rangle \leftrightarrow |M'gM\rangle$, such that, if the states $|M\rangle$ and $|M'\rangle$ are used to encode quantum information, this information is transferred between molecules. This particular gate requires the Rabi frequency for Rydberg excitation to be [101]

$$\Omega = \sqrt{\frac{2}{4k^2-1}}\frac{V_{\mathrm{Mr}}^{\mathrm{DD}}}{h} \tag{7.9}$$

for positive integer k. For $k = 1$, this corresponds to $\Omega = \sqrt{2/3}V_{\mathrm{Mr}}^{\mathrm{DD}}/h$ such that the strong molecule-Rydberg interactions set the timescale of the dynamics, which can be on the order of $\sim 1\,\mathrm{MHz}$ for $R_{\mathrm{am}} \sim 1\,\mu\mathrm{m}$.

7.2 Choice of states

To realise resonant interactions, we require a pair of transitions that satisfy the resonance condition $E_{\mathrm{M}} + E_{\mathrm{r}} = 0$. For typical transitions between Rydberg states in alkali atoms, E_{r} is in the microwave regime. This makes a rotational transition in the molecule the natural choice to realise resonant exchange.

We prepare RbCs molecules in the rovibrational and hyperfine ground state $|G\rangle$ at magnetic field $B_0 = 181.699(1)\,\mathrm{G}$ (see Ch. 4). For this chapter, we drive σ^+ transitions from this state so that we remain in spin-stretched states, which have well defined projections of rotational angular momentum and nuclear spin [280], and label these states $|N, M_N\rangle$. Allowed rotational transitions are those with $|\Delta N| = 1$. $|G\rangle \equiv |0, 0\rangle$ and a σ^+ transition is one where $\Delta M_N = \Delta N$.

Choosing to remain in the spin-stretched states offers several advantages. Firstly, the nuclear spins of the constituent atoms act as spectators and can be ignored. Secondly, the composition of the state remains constant as a function of magnetic field, which eliminates potential complications when tuning the transition energies to satisfy the resonance condition. Furthermore, molecules in these states have maximal dipole moments which maximises interaction strengths.

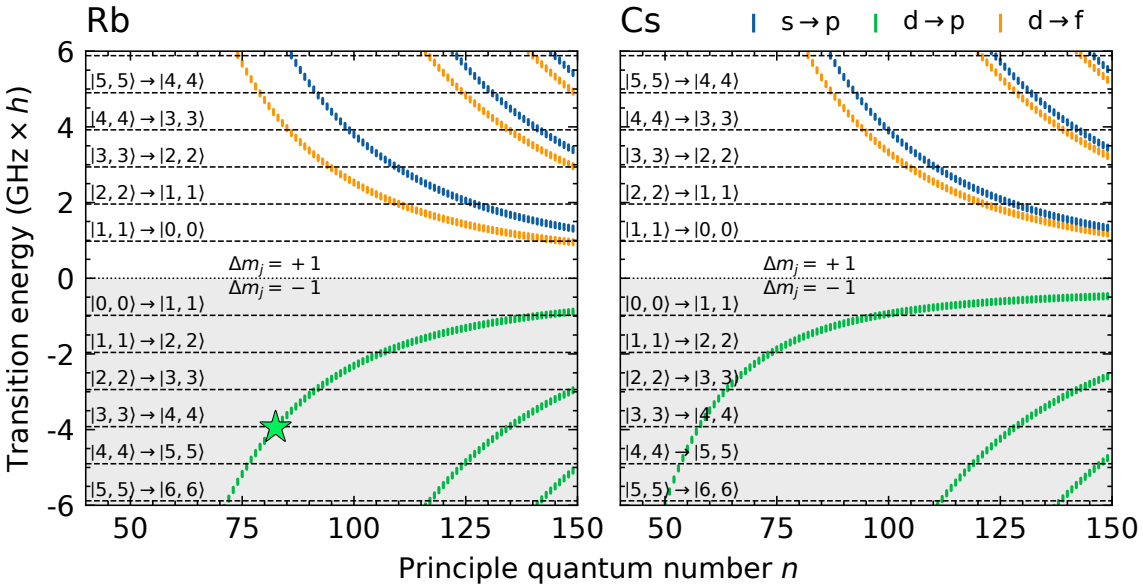

Figure 7.2: Atomic Rydberg transitions near resonant with molecular transitions. The points show the energies E_r of stretched Rydberg transitions accessible when using a two-photon excitation scheme. The extent of each point shows the tuneability of that transition with a magnetic field in the range $150\,\mathrm{G} \leq B \leq 250\,\mathrm{G}$. The horizontal lines show $-E_M$ for the labelled molecular transitions. The resonance condition is satisfied when an atomic transition crosses a molecular transition. The green star highlights the atomic transition $|d\rangle \rightarrow |p\rangle$ that we use to engineer resonant interactions.

We consider Rydberg states of Rb and Cs that could be used to satisfy the resonance condition. When choosing pairs of Rydberg states, the transition between them must be electric-dipole allowed. Explicitly, this means that the transition satisfies $|\Delta\ell| = 1$, $|\Delta j| \leq 1$, and $|\Delta m_j| \leq 1$.[1] There is no selection rule on the change in principal quantum number Δn; this allows a large range of transition energies to be realised. As with the molecule, to avoid the state composition changing with magnetic field, we choose to stay in stretched states with maximal $|m_j + m_i|$ (i.e. $m_j = \pm j = \pm(\ell + s)$, where $s = 1/2$ is the electron spin, and $m_i = \pm i$). The selection rules for the Rydberg transitions then simplify to $\Delta\ell = \Delta j = \Delta m_j = \pm 1$. The Rydberg excitation scheme used in our experiment places a further limitations on the initial Rydberg state $|r\rangle$: we excite Rb atoms from the manifold $5s_{1/2}$ to Rydberg states with two photons such that we can excite to Rydberg states ns or nd (those with $\ell = 0$ or 2). For Cs, we consider the case where a similar two-photon excitation scheme is used to excite atoms from the manifold $6s_{1/2}$ to Rydberg states ns or nd.

In Fig. 7.2, we plot the energy E_r of allowed transitions $|r\rangle \rightarrow |r'\rangle$ for Rb (left panel) and Cs (right panel). The energies are shown as a function of n and are calculated with `ARC` [304]. The vertical extent of each transition shows the range

[1] Additionally, $m_j = 0 \rightarrow 0$ is not allowed if $\Delta j = 0$.

of E_r achievable by tuning the magnetic field in the range $150\,\mathrm{G} \leq B \leq 250\,\mathrm{G}$.[2] In our system, the quantisation axis is set by the magnetic field and during the exchange of resonant photons the quantity $M_N + m_j$ is conserved. Therefore, for an allowed resonant exchange, Δm_j in the Rydberg atom must be equal and opposite to ΔM_N in the molecule (i.e. $\Delta m_j = -\Delta M_N$). Conservation of energy further restricts this condition. For example, molecular transitions with $\Delta M_N = \Delta N = +1$ have $E_\mathrm{M} > 0$. To satisfy both the resonance condition $E_\mathrm{M} + E_\mathrm{r} = 0$ and the condition $\Delta m_j = -\Delta M_N$, for $E_\mathrm{r} < 0$ we only consider transitions with $\Delta\ell = \Delta j = \Delta m_j = -1$ (d $\rightarrow$ p transitions (green)). Similarly, for $E_\mathrm{r} > 0$ we consider only transitions with $\Delta\ell = \Delta j = \Delta m_j = +1$ (either s $\rightarrow$ p (blue) or d $\rightarrow$ f (orange) transitions). The dashed horizontal lines on the figure show $-E_\mathrm{M}$ for stretched molecular transitions up to $|5, +5\rangle \leftrightarrow |6, +6\rangle$: when a Rydberg transition crosses the one of these molecular transitions, the transition pair satisfies the resonance condition $E_\mathrm{M} + E_\mathrm{r} = 0$.

To understand the shape of the curves in Fig. 7.2, we consider the energy structure of a Rydberg atom. The binding energy E^B of a Rydberg electron in free space is given by Eq. (5.1). The energy of the Rydberg transition $|r\rangle \rightarrow |r'\rangle$ is $E_\mathrm{r} = E^\mathrm{B}_{r'} - E^\mathrm{B}_r$. By expanding this equation in powers of δ/n, we expect that $|E_\mathrm{r}| \propto n^{-3}$ for $\{\Delta n, \delta, \delta'\} \ll n$. When fitting the Rb d $\rightarrow$ p branch marked by the green star in Fig. 7.2, we find that this exponent is $-2.63(1)$ for the range of n shown.

The energy of the Rydberg transitions gets smaller as the difference between the quantum defects tends to an integer. As an example, we consider the case where two Rydberg states with an allowed transition between them are degenerate such that $E_\mathrm{r} = 0$. This occurs when $E^\mathrm{B}_{r'} = E^\mathrm{B}_r \implies (n' - \delta')^2 = (n - \delta)^2$. Here n (n') is the principal quantum number and δ (δ') is the quantum defect of the state $|r\rangle$ ($|r'\rangle$). Therefore, $E_\mathrm{r} = 0$ when $\Delta n = \Delta\delta \equiv \delta' - \delta$.[3] As n and n' are positive integers, Δn is an integer. However, there is no selection rule for Δn. This means that whenever $\Delta\delta$ is an integer, there will be an allowed transition with $E_\mathrm{r} = 0$. As $\Delta\delta$ becomes further from an integer, $|E_\mathrm{r}|$ becomes larger. This is seen in the data presented in Fig. 7.2: for a given value of n, the transition with the smallest $|E_\mathrm{r}|$ is a Cs d $\rightarrow$ p transition. It is for this transition that $\Delta\delta$ is closest to an integer (see the $\delta(\ell + 1) - \delta(\ell)$ values in Table 6.1) and the value of $\Delta n = +1$ for this transition is the nearest integer to

[2] For simplicity, here we ignore the diamagnetic shifts of the Rydberg states. Including the diamagnetic term typically corrects the calculated values of E_r for these stretched transitions on the order of $\sim 100\mathrm{MHz} \times h$. Therefore, it is important to include the diamagnetic term once a transition candidate has been chosen.

[3] Mathematically, we can also have $E_\mathrm{r} = 0$ when $2n + \Delta n = \delta' + \delta$. However, this results in the effective principal quantum number $n^* \equiv n - \delta$ of one of the states being negative which is unphysical.

$\Delta\delta = \delta(\mathrm{p}) - \delta(\mathrm{d}) = 1.08$.

For a given molecular transition $|M\rangle \rightarrow |M'\rangle$, there can exist multiple Rydberg transitions $|r\rangle \rightarrow |r'\rangle$ for which the resonance condition $E_\mathrm{M} + E_\mathrm{r} = 0$ is satisfied. These are shown in Fig. 7.2 where multiple Rydberg transitions cross some molecular transitions. To choose the best Rydberg transition for a given molecular transition, we use a cost function $C = n^4/d_\mathrm{r}$. For each molecular transition, we select the atomic transition with the lowest value of C. This cost function is somewhat arbitrary, but we choose to strongly favour small values of n to maximise the Rabi frequency with which we can drive the transition $|g\rangle \rightarrow |r\rangle$ (which scales as n^{-3}, see Sec. 5.2) and minimise the impact of dc Stark shifts caused by stray electric fields in the science cell (which scale as n^7, see Sec. 5.6). For similar n, the cost function prefers transitions with large values of d_r to maximise $V_\mathrm{Mr}^\mathrm{DD}$. We exclude transitions for which the resonance condition cannot be satisfied in the magnetic field range $150\,\mathrm{G} \leq B \leq 250\,\mathrm{G}$: this means that we do not significantly have to change the magnetic field from the molecule-formation field. We denote the magnetic field at which the resonance condition is satisfied as B_res.[4] Stretched Rydberg transitions with minimal C for the states $|M\rangle$ up to $|5, +5\rangle$ in RbCs are shown in Table 7.1 for Rb and Cs atoms. This table also includes the zero-temperature and blackbody-limited lifetimes $\tau^{(0)}$ and $\tau^{(300)}$ at 300 K for each Rydberg state $|r\rangle$.

We choose to use the RbCs transition $|3, +3\rangle \rightarrow |4, +4\rangle$ and the stretched transition between the 83d and 84p manifolds of Rb. Explicitly, this transition is between the state $|d\rangle \equiv |83\mathrm{d}_{5/2}, m_j = +5/2, m_i = +3/2\rangle$ and the state $|p\rangle \equiv |84\mathrm{p}_{3/2}, m_j = +3/2, m_i = +3/2\rangle$. This choice strikes a reasonable balance between the experimental challenges of exciting an atom to a Rydberg state with relatively high n and the necessity to transfer the molecule from the state $|G\rangle$ to the state $|3, +3\rangle$ with successive microwave pulses. We note that the RbCs transition $|2, +2\rangle \rightarrow |3, +3\rangle$ and the stretched transition between the 64d and 65p manifolds of Cs have a lower value of C and require less microwave pulses for molecular state preparation. However, we do not currently have the lasers required for Rydberg excitation of Cs. In future, we will also to study resonant interactions between RbCs and Cs with this choice of states.

[4] Again, here we calculate B_res by considering only the linear Zeeman shift of the Rydberg states. This means that the true value of B_res can shift on the order of $\sim 10\,\mathrm{G}$ for these stretched transitions when including the diamagnetic contribution to the Zeeman shift. This is will be included shortly when a transition pair has been chosen.

Table 7.1: Transition pairs suitable for resonant dipole-dipole interactions between RbCs molecules and Rb or Cs Rydberg atoms. For each molecular transition $|N, M_N\rangle \to |N', M'_N\rangle$ we give the Rydberg transition $n\ell \to n'\ell'$ which has minimal C. Only stretched Rydberg states with $m_j = j = \ell + s$, where $s = 1/2$, are considered. Tabulated quantities are as described in the text.

RbCs molecule		Rb Rydberg atom					
Transition $\lvert N, M_N\rangle \to \lvert N', M'_N\rangle$	E_M/h (MHz)	Transition $n\ell \to n'\ell'$	B_res (G)	d_r (kD)	$C/10^6$ (1/kD)	$\tau^{(0)}$ (ms)	$\tau^{(300)}$ (ms)
$\lvert 0,0\rangle \to \lvert 1,+1\rangle$	980	138d → 139p	154.7	40.7	8.9	2.8	0.75
$\lvert 1,+1\rangle \to \lvert 0,0\rangle$	-980	143d → 142f	156.7	44.4	9.4	3.1	0.82
$\lvert 1,+1\rangle \to \lvert 2,+2\rangle$	1961	106d → 107p	184.6	23.9	5.3	1.2	0.41
$\lvert 2,+2\rangle \to \lvert 1,+1\rangle$	-1961	109d → 108f	163.6	25.7	5.5	1.3	0.44
$\lvert 2,+2\rangle \to \lvert 3,+3\rangle$	2941	91d → 92p	165.2	17.5	3.9	0.78	0.29
$\lvert 3,+3\rangle \to \lvert 2,+2\rangle$	-2941	94d → 93f	162.1	19.1	4.1	0.86	0.31
$\lvert 3,+3\rangle \to \lvert 4,+4\rangle$	3921	83d → 84p	237.5	14.5	3.3	0.59	0.23
$\lvert 4,+4\rangle \to \lvert 3,+3\rangle$	-3921	85d → 84f	168.5	15.6	3.4	0.63	0.25
$\lvert 4,+4\rangle \to \lvert 5,+5\rangle$	4902	125d → 125p	230.3	0.4	640	2.0	0.60
$\lvert 5,+5\rangle \to \lvert 4,+4\rangle$	-4902	79d → 78f	211.8	13.4	2.9	0.51	0.21
$\lvert 5,+5\rangle \to \lvert 6,+6\rangle$	5882	72d → 73p	240.6	10.9	2.5	0.38	0.17
RbCs molecule		Cs Rydberg atom					
Transition $\lvert N, M_N\rangle \to \lvert N', M'_N\rangle$	E_M/h (MHz)	Transition $n\ell \to n'\ell'$	B_res (G)	d_r (kD)	$C/10^6$ (1/kD)	$\tau^{(0)}$ (ms)	$\tau^{(300)}$ (ms)
$\lvert 0,0\rangle \to \lvert 1,+1\rangle$	980	96d → 97p	167.1	20.9	4.1	0.54	0.26
$\lvert 1,+1\rangle \to \lvert 0,0\rangle$	-980	—	—	—	—	—	—
$\lvert 1,+1\rangle \to \lvert 2,+2\rangle$	1961	73d → 74p	156.2	11.9	2.4	0.23	0.13
$\lvert 2,+2\rangle \to \lvert 1,+1\rangle$	-1961	120d → 118f	154.3	27.9	7.4	1.1	0.45
$\lvert 2,+2\rangle \to \lvert 3,+3\rangle$	2941	64d → 65p	225.7	9.0	1.9	0.15	0.091
$\lvert 3,+3\rangle \to \lvert 2,+2\rangle$	-2941	104d → 102f	169.3	20.9	5.6	0.69	0.32
$\lvert 3,+3\rangle \to \lvert 4,+4\rangle$	3921	58d → 59p	248.9	7.4	1.5	0.11	0.070
$\lvert 4,+4\rangle \to \lvert 3,+3\rangle$	-3921	94d → 92f	166.6	17.0	4.6	0.50	0.24
$\lvert 4,+4\rangle \to \lvert 5,+5\rangle$	4902	119d → 119p	210.1	4.4	45	1.0	0.44
$\lvert 5,+5\rangle \to \lvert 4,+4\rangle$	-4902	87d → 85f	158.7	14.5	4.0	0.40	0.20
$\lvert 5,+5\rangle \to \lvert 6,+6\rangle$	5882	112d → 112p	234.5	3.9	40	0.86	0.38

7.3 Microwave spectroscopy

Having chosen to use the Rydberg transition $|d\rangle \rightarrow |p\rangle$ and the molecular transition $|3,+3\rangle \rightarrow |4,+4\rangle$, we now consider how to tune the transitions to satisfy the resonance condition $E_{\mathrm{M}} + E_{\mathrm{r}} = 0$. For the molecular transition, $E_{\mathrm{M}} \approx 3921\,\mathrm{MHz} \times h$.

Figure 7.3 shows the energies of Rydberg states close to the manifold $83\mathrm{d}_{5/2}$ as a function of magnetic field. The lines show state energies calculated with `pairinteraction` [316]. We show states with $\ell \leq 6$ and do not include the hyperfine structure. The energies are relative to the state $|d\rangle$ at zero magnetic field and we assume that there is zero electric field. The Hamiltonian describing the interaction of the atom with the magnetic field $\boldsymbol{B}$ is [316]

$$\hat{H}_B = \underbrace{-\hat{\boldsymbol{\mu}} \cdot \boldsymbol{B}}_{\text{linear}} + \underbrace{\frac{1}{8m_{\mathrm{e}}} |\hat{\boldsymbol{d}} \times \boldsymbol{B}|^2}_{\text{diamagnetic}}, \tag{7.10}$$

where $\hat{\boldsymbol{\mu}} = -\mu_{\mathrm{B}}(g_\ell \hat{\boldsymbol{\ell}} + g_s \hat{\boldsymbol{s}})$ is the magnetic dipole operator and $\hat{\boldsymbol{d}} = e\hat{\boldsymbol{r}}$ is the electric dipole operator. Here, $\hat{\boldsymbol{\ell}}$ ($\hat{\boldsymbol{s}}$) is the orbital (spin) angular momentum operator and g_ℓ (g_s) is the associated Landé factor. $\hat{\boldsymbol{r}}$ is the operator corresponding to the position of the Rydberg electron relative to the atomic nucleus. The first term in Eq. (7.10) gives rise to the linear Zeeman shift and the second term is the diamagnetic interaction. For ground-state atoms, the diamagnetic term is negligible for fields less than a few tesla and is usually ignored. However, the radius of Rydberg atoms $\langle \hat{\boldsymbol{r}} \rangle \propto n^2$ [50], meaning that the diamagnetic term scales as n^4. For Rydberg states with $n \approx 83$, the diamagnetic shift becomes significant for fields $B \gtrsim 10\,\mathrm{G}$.

The diamagnetic shift is quadratic, meaning that it always shifts states to higher energy. Furthermore, it mixes states with the same m_j. In Fig. 7.3, we highlight certain states that are eigenstates in the region where the linear shift dominates; these states are labelled $|j, m_j\rangle$ and evolve from the manifolds labelled as $n\ell$. As the magnetic field is increased, the eigenstates become mixed states where the components have different j but the same m_j. As an example, we consider the state $|83\mathrm{d}_{5/2}, m_j = +1/2\rangle$ which is an eigenstate at low fields. The intensity of the orange colour of a state $|\psi\rangle$ in Fig. 7.3 shows the overlap $\left|\langle\psi|83\mathrm{d}_{5/2}, +1/2\rangle\right|^2$. As the magnetic field increases, the diamagnetic term couples states of different m_j. This causes the probability amplitude of the state $|83\mathrm{d}_{5/2}, +1/2\rangle$ to be distributed across the eigenstates that evolve from the low-field states $|83\mathrm{d}_{3/2}, +1/2\rangle$ and $|83\mathrm{d}_{5/2}, +1/2\rangle$. This can be seen in Fig. 7.3, where there are two states that are coloured orange at high field. This effect happens for all states in this field range, with the exception of stretched states. Stretched states have a unique value of m_j for a given n and ℓ and

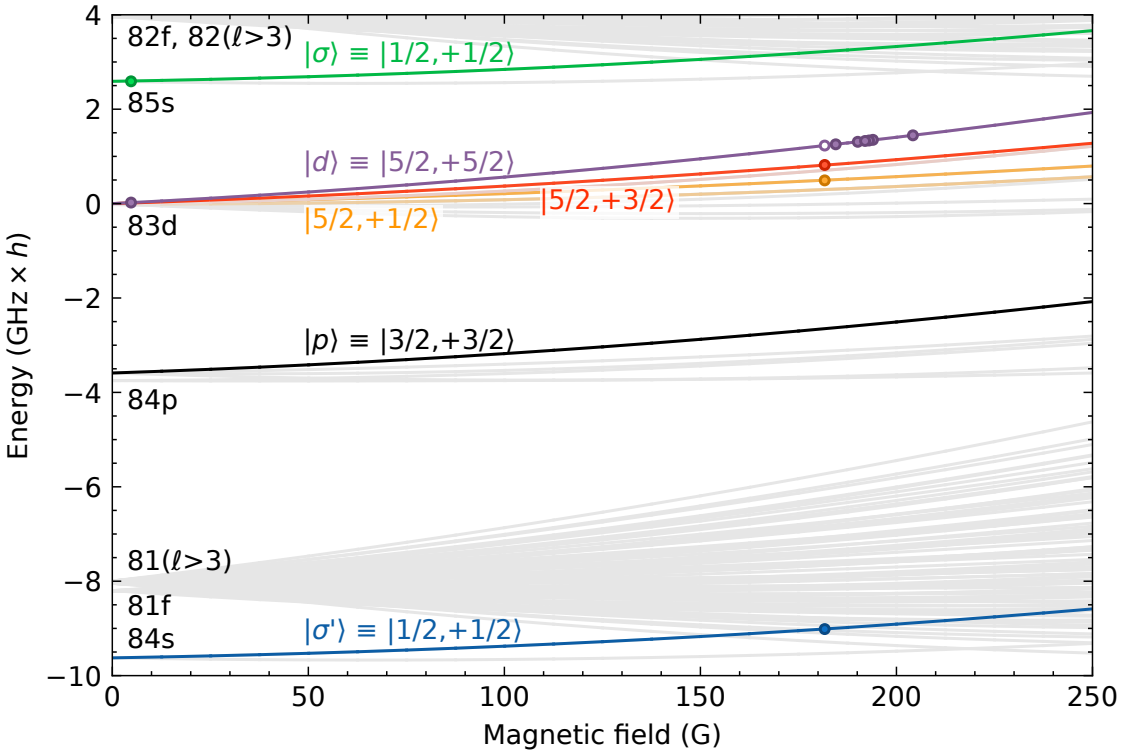

Figure 7.3: Effect of a magnetic field on Rydberg states with $\ell \leq 6$ around the state $|d\rangle$. Lines show the calculated state energies. The intensities of the highlighted states show their overlaps with the low-field states that are labelled $|j, mj\rangle$. Data points show measured energies which are referenced to the purple empty point.

therefore do not mix with other states. Their state composition is uniform for all fields in this range and it is this that makes them ideal to work with.

The data points in Fig. 7.3 show measured energies of Rydberg states that we can access with our two-photon excitation scheme. The error bars are smaller than the size of the points; typical errors are on the order of $\sim 100\,\text{kHz} \times h$ and are obtained from fitted features such as that shown in Fig. 5.7(a). We measure the energy difference between the states by recording the frequencies of the Rydberg EOMs and AOMs (see Sec. 2.5) at which we are on resonance with the transition $|g\rangle \rightarrow |r\rangle$. When comparing points at different magnetic fields, we account for linear Zeeman shift of the ground manifold $5s_{1/2}$ [211]. We do not necessarily eliminate the differential light shifts caused by the excitation lasers (see Eq. (5.6)) as these are also on the order of $\sim 100\,\text{kHz} \times h$, which is much smaller than the energy scale shown here. We expect that the accuracy of these measurements are limited by these two errors and unaccounted dc Stark shifts from stray electric fields that are probably on the order of $\sim 1\,\text{MHz} \times h$ (see Sec. 5.6). We plot the data points in Fig. 7.3 by referencing all points to the empty purple point, which is set to lie exactly on the calculated purple line. We measure energy differences rather than the absolute

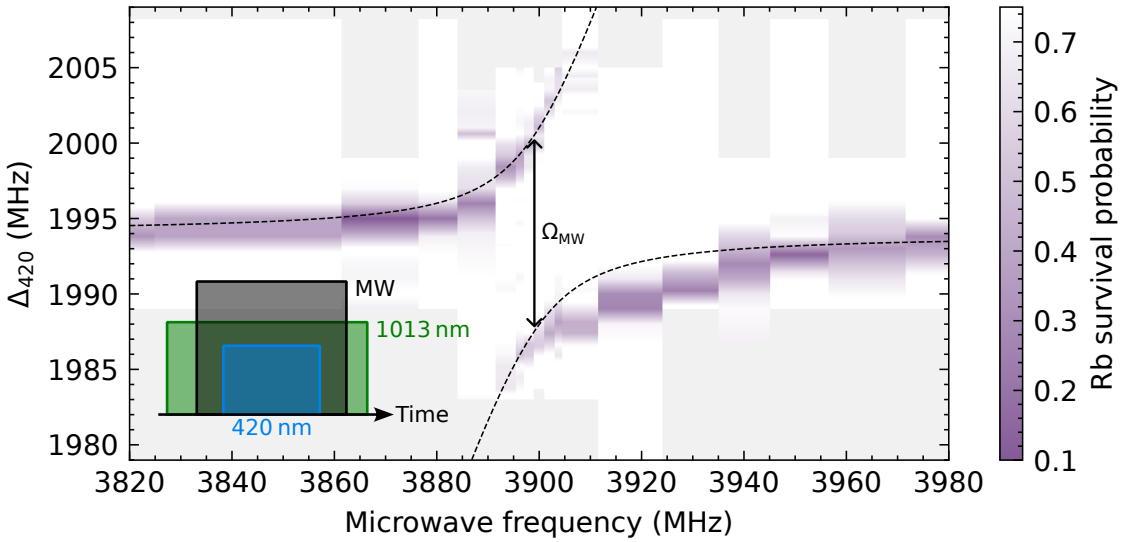

Figure 7.4: Dressed energy landscape when coupling states $|d\rangle$ and $|p\rangle$ with microwaves. The Rb survival probability is shown as a function of the 420 nm laser detuning Δ_{420} and the microwave frequency. More intense purple represents lower probability of survival. Light grey indicates a lack of data. The points are linearly interpolated along the vertical axis of the plot. The dashed lines are a guide to the eye. The inset shows the relevant experimental timings (not to scale).

energies because our highest precision wavemeter[5] has a quoted accuracy of ± 0.2 parts per million, which corresponds to $\sim 200\,\text{MHz} \times h$ on the two-photon Rydberg transitions.

To engineer resonant interactions, we use the Rydberg states $|d\rangle$ (Fig 7.3, purple line) and $|p\rangle$ (Fig 7.3, black line). We are unable to measure the energy of states in the manifold 84p using the method with which we obtain the points in Fig. 7.3 because we cannot couple to p-states with our two-photon excitation scheme. Instead, we perform spectroscopy of this manifold by driving one-photon transitions to it from the states $|d\rangle$ and $|\sigma'\rangle \equiv |84s_{1/2}, m_j = +1/2, m_i = +1/2\rangle$. We excite to the state $|\sigma'\rangle$ with the same excitation scheme that was used to access the state $|\sigma\rangle$ in Sec. 5.6. The photons that couple the states $|d\rangle$ and $|\sigma'\rangle$ with the state $|p\rangle$ are in the microwave regime and we denote the Rabi frequency with which we drive these transitions as Ω_{MW}. We produce this microwave radiation with the Rb antenna described in Sec. 2.1. The resonant frequency of this antenna is approximately 6.8 GHz. However, due to the large TDMs of the Rydberg transitions, we find that we can drive them with Rabi frequencies on the order of $\sim 1\,\text{MHz} \times h$ with microwave powers $< -20\,\text{dBm}$, even though they are up to a few gigahertz detuned from the antenna's resonant frequency.

First, we perform spectroscopy using Autler-Townes splitting of the Rydberg

[5]Bristol Instruments 671A-NIR

transitions $|g\rangle \rightarrow |d\rangle$ and $|g\rangle \rightarrow |\sigma'\rangle$ which occurs when resonant microwaves are applied. The physical picture for this is as described in Sec 5.4, but the dressing field is the microwave field and the weak probe is the two-photon excitation pulse. When the microwaves are resonant, the Rydberg excitation transition splits into two, with the frequency difference between the transitions equal to Ω_{MW}. This spectroscopy method is ideal because we require only that the Rabi frequency of the two-photon Rydberg excitation $\Omega \ll \Omega_{\mathrm{MW}}$. We are not sensitive to the exact value of Ω_{MW}, which is difficult to predict due to the power and polarisation of the microwaves that make it through the metal vacuum chamber to the atoms being hard to calculate.[6] The relevant experimental timings are as shown in the inset of Fig. 7.4. Atoms are prepared in the relevant ground state $|g\rangle$ ($|5\mathrm{s}_{1/2}, f = 2, m_f = +2\rangle$ for excitation to $|d\rangle$ or $|5\mathrm{s}_{1/2}, f = 1, m_f = +1\rangle$ for excitation to $|\sigma'\rangle$) at 181.699(1) G. We switch on the 1013 nm light, then the microwave radiation. Finally, we pulse the 420 nm light for a duration that would drive approximately a π pulse on a transition $|g\rangle \rightarrow |r\rangle$ in the absence of microwave dressing.

Figure 7.4 shows the dressed state landscape when exciting to the Rydberg state $|d\rangle$. When exciting to the Rydberg state, the atom is lost most of the time (see Sec 5.5). The vertical axis shows the effect of varying the effective detuning Δ of the Rydberg excitation pulse. We vary Δ by changing the detuning of the 420 nm light Δ_{420}, which we reference to the same cavity mode as in Fig. 5.2(b)(ii). The horizontal axis shows the effect of varying the microwave frequency. In the absence of microwaves, the bare transition $|g\rangle \rightarrow |d\rangle$ is at $\Delta_{420} \approx 1994$ MHz. When microwaves are applied, the states are dressed. The energies $E_{\pm}$ of the dressed states relative to the state $|d\rangle$ are given by Eq. (5.9) with the detuning and Rabi frequency now those of the microwaves relative to the transition $|d\rangle \rightarrow |p\rangle$. When the microwaves are resonant, the dressed states are split by $h\Omega_{\mathrm{MW}}$. The dashed lines are a guide to the eye, and show calculated values of $E_{\pm}$ if the resonant microwave frequency equals 3899 MHz and $\Omega_{\mathrm{MW}} = 13$ MHz. We note that the state $|p\rangle$ is lower in energy that the state $|d\rangle$; this means that a *higher* microwave frequency gives a *lower* detuning.

We use this method to perform spectroscopy of transitions from the states $|d\rangle$ and $|\sigma'\rangle$. For each state, we set the effective detuning of the Rydberg excitation lasers to be zero and apply microwaves during the excitation pulse. When the microwaves are resonant, the states are dressed and shifted from the bare state by $\pm h\Omega_{\mathrm{MW}}/2$, which precludes Rydberg excitation. Correspondingly, the survival probability of the atoms increases. We show the results of this spectroscopy in Fig. 7.5. Fig. 7.5(a) shows the relevant energy landscape at 181.699 G. The energies are relative to that

[6] For reference, microwave radiation of frequency ~ 3 GHz has a wavelength ~ 10 cm. This is of the same scale as the metallic vacuum chamber, which causes many unpredictable reflections.

of the state $|d\rangle$ at this field and the transitions that we drive are the vertical arrows. Fig. 7.5(b) shows measurements of transitions from the state $|d\rangle$. The magnetic field is $B_0 = 181.699(1)$ G. The purple feature shows the transition $|d\rangle \rightarrow |p\rangle$ and the grey feature shows the transition $|d\rangle \rightarrow |82\mathrm{f}_{7/2}, m_j = +7/2\rangle$. For each peak we set the microwave power (i.e. set Ω_{MW}) to give a clear feature that is not saturated. Fig. 7.5(c) shows measurements of the transitions $|\sigma'\rangle \rightarrow |84\mathrm{p}_j, m_j\rangle$. The lower panel shows zoomed regions of the upper panel and are labelled j, m_j.

The dashed vertical lines in Fig. 7.5(b)-(c) show the calculated frequencies of the transitions from Fig. 7.3 at 181.699 G. For this calculation, we assume that there is zero electric field. For the transitions $|\sigma'\rangle \rightarrow |84\mathrm{p}_j, m_j\rangle$, we measure the transition at lower frequencies than calculated. In contrast, the measured frequency for the transition $|d\rangle \rightarrow |p\rangle$ is higher than calculated. The difference between the measured and calculated frequencies are within ±15–20 MHz. We also observe a shift and broadening of the transition $|d\rangle \rightarrow |82\mathrm{f}_{7/2}, 7/2\rangle$. We expect that these discrepancies are due to a stray electric field in the science cell, leading to a dc Stark shift of the transitions.[7] The dotted lines in Fig. 7.5(b)-(c) show the calculated frequencies of the transitions when an electric field of strength 50 mV/cm is perpendicular to the magnetic field. These calculated frequencies are much closer to the observed transition frequencies. As the states with $\ell > 0$ are anisotropic, the angle between the electric and magnetic fields affects the dc Stark shifts, but they are always this order of magnitude for this field strength. We do not plot the dc Stark shifted transition $|d\rangle \rightarrow |82\mathrm{f}_{7/2}, 7/2\rangle$ because this is highly anisotropic and depends significantly on the angle between the fields. We note that this stray field is approximately double that reported in Sec. 5.6. These measurements were performed approximately three months after those presented in Fig. 5.10 and no LIAD was performed during this time. Therefore, we expect that the surface charge buildup could have been significant, changing the stray electric field. In future we plan to remeasure and null this stray field.

To observe resonant dipole-dipole interactions, we tune the energy of the transitions with the magnetic field in order to satisfy the resonance condition $E_{\mathrm{M}} + E_{\mathrm{r}} = 0$. Using `diatomic-py` [290], we calculate the magnetic moments of the molecular states $|3, +3\rangle$ and $|4, +4\rangle$ at 181.699 G to be $5.335\mu_{\mathrm{N}}$ and $5.329\mu_{\mathrm{N}}$ respectively.[8] Therefore,

[7] The transition $|d\rangle \rightarrow |p\rangle$ being higher in frequency than expected and the transitions $|\sigma'\rangle \rightarrow |84\mathrm{p}_j, m_j\rangle$ being lower than expected could also be explained if the manifold 84p is lower in energy than expected. However, a shift on this scale not caused by stray fields would require a modification in the quantum defect of approximately one part in 10^3, well above the experimental uncertainty of approximately one part in 10^6 reported by Li *et al.* [309] and this is therefore highly unlikely to be the cause.

[8] As the states $|3, +3\rangle$ and $|4, +4\rangle$ are stretched, their magnetic moment is constant with magnetic field.

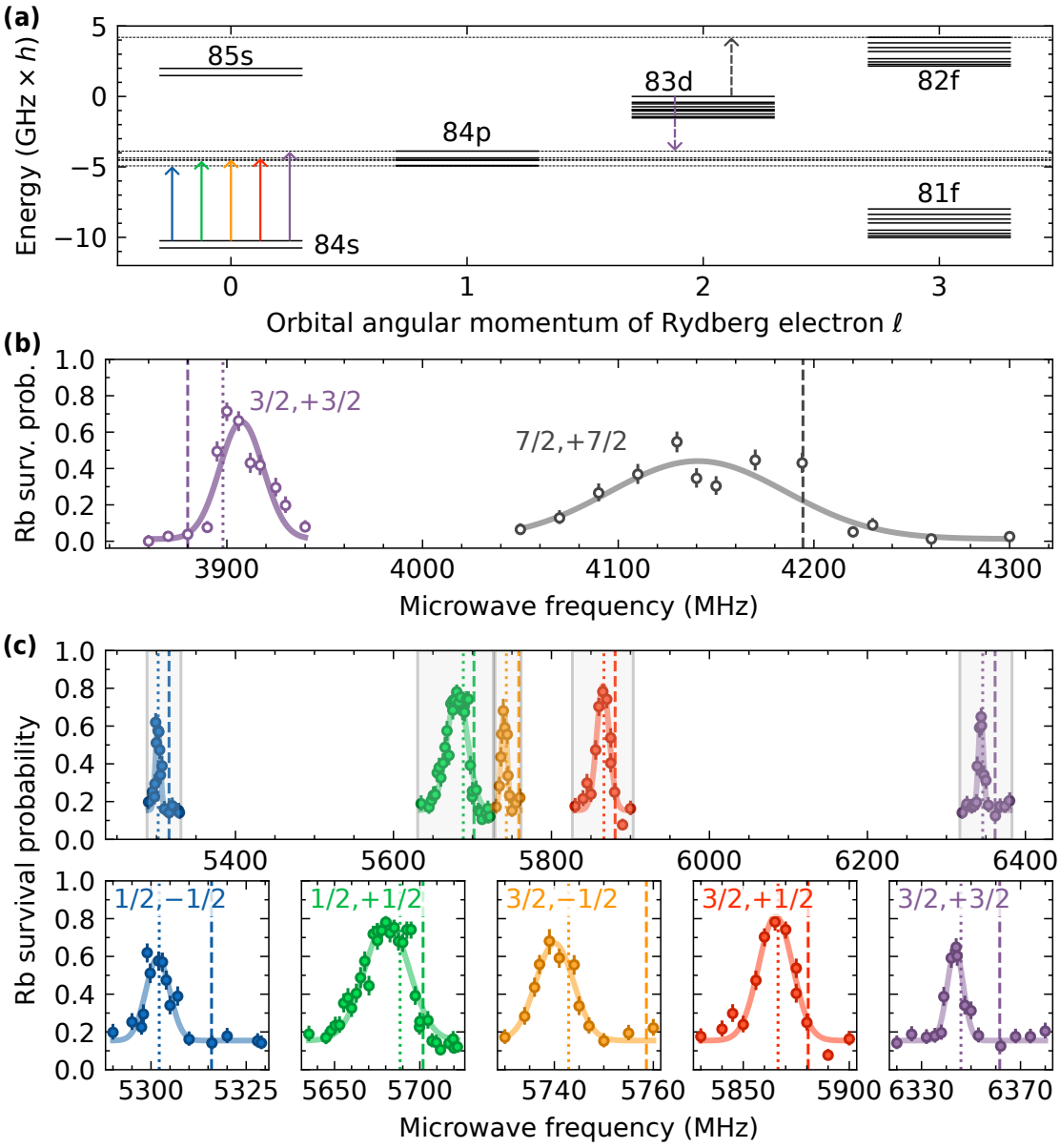

Figure 7.5: Autler-Townes spectroscopy of transitions between Rydberg states. (a) Rydberg energy landscape at 181.699 G. Energies are given relative to that of the state $|d\rangle$. **(b)** Transitions from the state $|d\rangle$. Purple: the transition $|d\rangle \rightarrow |p\rangle$. Grey: the transition $|d\rangle \rightarrow |82\mathrm{f}_{7/2}, 7/2\rangle$. **(c)** The transitions $|\sigma'\rangle \rightarrow |84\mathrm{p}_j, m_j\rangle$. The lower panel shows zoomed regions of the upper panel and are labelled j, m_j. For (b) and (c), dashed (dotted) vertical lines show calculated frequencies for the transitions with zero electric field (an electric field of 50 mV/cm perpendicular to the magnetic field).

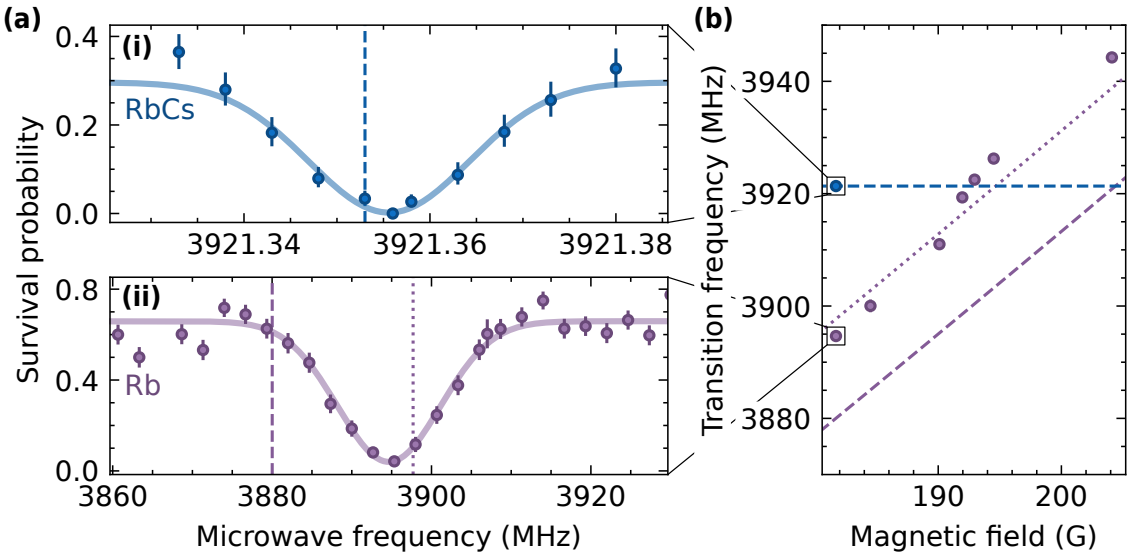

Figure 7.6: Tuning Rydberg atom and molecule into resonance with a magnetic field. **(a)** Microwave spectroscopies for **(i)** the RbCs transition $|3,+3\rangle \rightarrow |4,+4\rangle$ and **(ii)** the Rb Rydberg transition $|d\rangle \rightarrow |p\rangle$ at 181.699(1) G. For both measurements, the molecule and atom are prepared in the initial state and an approximate π pulse is applied (here we use pulse durations 34 µs and 50 ns respectively). **(b)** Tuning of the transition frequencies with magnetic field. The colours are the same as in (a). For both panels, the dashed purple (blue) line shows the expected frequency of the atomic (molecular) transition when there is zero electric field. The dotted purple line shows the calculated frequency of the atomic transition when there is an electric field of 50 mV/cm perpendicular to the magnetic field.

the differential magnetic moment of the transition $|3,+3\rangle \rightarrow |4,+4\rangle$ is approximately $6 \times 10^{-3}\mu_N = 5\,\mathrm{Hz/G} \times h$. For our purposes, we neglect the Zeeman shift of this transition and consider E_M to be constant.

In contrast, E_r is highly tuneable with magnetic field. Although we operate in a field regime where the diamagnetic shift of the Rydberg states is significant, at a given field we are still able to calculate a linear magnetic moment for each state. This linear approximation is valid for small changes in magnetic field $\Delta B \ll B$. Using `pairinteraction` [316], we calculate that, at 181.699 G, the magnetic moments of the states $|d\rangle$ and $|p\rangle$ are $6.7\mu_B$ and $5.4\mu_B$ respectively. Therefore, the differential magnetic moment of the transition $|d\rangle \rightarrow |p\rangle$ is approximately $1.3\mu_B \approx 1.8\,\mathrm{MHz/G} \times h$.

In Fig. 7.6 we show the tuning of E_r with magnetic field. Fig. 7.6(a) shows an example of microwave spectroscopy on the RbCs transition $|3,+3\rangle \rightarrow |4,+4\rangle$ to measure E_M (panel (i)) or on the Rb transition $|d\rangle \rightarrow |p\rangle$ to measure E_r (panel (ii)) at B_0. For both of these measurements, we prepare the particle in the initial state and apply approximately a π pulse to drive the relevant transition. Explicitly, for the measurement of E_M, we prepare molecules in the state $|G\rangle$ and perform the transfer $|G\rangle \rightarrow |1,+1\rangle \rightarrow |2,+2\rangle \rightarrow |3,+3\rangle$ with a series of π pulses (see Sec. 4.5). The spectroscopy pulse (of duration 34 µs) is applied before transferring molecules in

the state $|3,+3\rangle$ back to the state $|G\rangle$, from which atom pairs are recovered. When the spectroscopy pulse is resonant with the transition $|3,+3\rangle \rightarrow |4,+4\rangle$, molecules are removed from the state $|3,+3\rangle$ and therefore atom pairs are not recovered at the end of the experimental sequence. The measurement of E_r is similar. We first prepare atoms in the state $|g\rangle$ and drive the two-photon transition $|g\rangle \rightarrow |d\rangle$. We apply the spectroscopy pulse (of duration 50 ns) and then return atoms in the state $|d\rangle$ back to the state $|g\rangle$. When the spectroscopy pulse is resonant with the transition $|d\rangle \rightarrow |p\rangle$, atoms are transferred to the state $|p\rangle$. These atoms are not returned to the ground state with the final pulse and therefore are ejected from the tweezer.

For this measurement, the molecules are trapped in 1066 nm tweezers of intensity $I_{1066} = 3.07\,\mathrm{kW/cm^2}$. This is the same intensity used for most of the molecular spectroscopy presented in Ch. 4. The atomic spectroscopy with Rb in 817 nm tweezers of intensity $I_{817} = 3.09(5)\,\mathrm{kW/cm^2}$. We expect that this intensity causes an ac Stark shift of $46(1)\,\mathrm{kHz} \times h$ for the Rydberg states. However, we expect that the differential shift of the transition $|d\rangle \rightarrow |p\rangle$ is much less than this because the polarisability α_r (see Eq. (5.11)) is approximately the same for all Rydberg states. Nevertheless, for this measurement we turn the tweezers off for the Rydberg excitation. After the second Rydberg π pulse, the trap quickly turns back on to eject atoms that are still in a Rydberg state.

The vertical lines in Fig. 7.6(a) show the calculated transition frequencies. As in Fig. 7.5, for the atomic transition we show two calculations. The dashed line shows the predicted transition frequency when there is zero electric field and the dotted line shows the predicted transition frequency when there is an electric field of 50 mV/cm perpendicular to the magnetic field.

Figure 7.6(b) shows how the frequencies of these transitions change with magnetic field. The frequency of the molecular (atomic) transition is shown in blue (purple). On this scale, the frequency of the molecular transition is effectively constant. We measure the frequency of the atomic transition as a function of magnetic field by repeating the measurement shown in Fig. 7.6(a)(ii); these frequencies are shown as the purple data points. The dashed and dotted lines are as in Fig. 7.6(a). The resonance field B_res is that where two lines cross and the resonance condition $E_\mathrm{M} + E_\mathrm{r} = 0$ is satisfied.[9] At zero electric field we expect that $B_\mathrm{res} = 204.2\,\mathrm{G}$. In our system we expect that $B_\mathrm{res} = 192.5\,\mathrm{G}$: we obtain this value by linearly interpolating the purple data points and seeing where this crosses the blue dashed line.

[9]We have implicitly defined the frequency of transition i as $\nu_i \equiv |E_i|/h$ throughout this work. This means that even though $E_\mathrm{r} < 0$ for the transition $|d\rangle \rightarrow |p\rangle$, the transition frequency is still positive. We do this because when applying microwave radiation (for which we can set the frequency ν) we can drive transitions with energy $\pm h\nu$.

7.4 Rydberg blockade

Figure 7.7(a) shows a calculation of the energy shift ΔE caused the resonant dipole-dipole interaction of a Rb Rydberg atom and a RbCs molecule.[10] The interaction shift is shown as a function of the atom-molecule separation R_{am}. For this calculation, the hyperfine structure of the atom and molecule have been ignored. In the limit $R_{\mathrm{am}} \to \infty$, the eigenstates of the system are uncoupled pair states $|r\rangle_{\mathrm{Rb}} |N, M_N\rangle_{\mathrm{RbCs}}$. At finite R_{am}, the dipole-dipole interaction mixes pair states of the same $m_j + M_N$. For example, the interaction couples the states $|d\rangle_{\mathrm{Rb}} |3, +3\rangle_{\mathrm{RbCs}}$ and $|p\rangle_{\mathrm{Rb}} |4, +4\rangle_{\mathrm{RbCs}}$. For this discussion, we label each eigenstate by the quantum numbers of the state that it adiabatically evolves into as $R_{\mathrm{am}} \to \infty$.

The blue curves show eigenstates evolving from the RbCs rotational manifold with $N = 3$. Similarly, the green curves show eigenstates evolving from the rotational manifold with $N = 4$. Each manifold has $2N + 1$ states because the quantum number M_N runs from $-N$ to $+N$. States of the same $m_j + M_N$ are coupled by the dipole-dipole interaction. Explicitly, this means that each blue eigenstate (evolving from a state $|d\rangle_{\mathrm{Rb}} |3, M_N\rangle_{\mathrm{RbCs}}$) has a corresponding green eigenstate (which evolves from the state $|p\rangle_{\mathrm{Rb}} |4, M'_N = M_N + 1\rangle_{\mathrm{RbCs}}$). Each pair of eigenstates is approximately symmetric around $\Delta E = 0$. There are two eigenstates for which ΔE is negligible. These evolve from the states $|p\rangle_{\mathrm{Rb}} |4, -3\rangle_{\mathrm{RbCs}}$ and $|p\rangle_{\mathrm{Rb}} |4, -4\rangle_{\mathrm{RbCs}}$ and show no significant dipole-dipole energy shift because their corresponding states ($|d\rangle_{\mathrm{Rb}} |3, -4\rangle_{\mathrm{RbCs}}$ and $|d\rangle_{\mathrm{Rb}} |3, -5\rangle_{\mathrm{RbCs}}$ respectively) to which they could couple does not exist (as $|M_N| \not> N$).

The size of the energy shift ΔE is proportional to the TDMs of the atomic and molecular transitions (see Eq. (7.7)). The molecular transition with the largest TDM is the stretched molecular transition $|3, +3\rangle \to |4, +4\rangle$. Therefore, ΔE is largest for the eigenstates evolving from $|d\rangle_{\mathrm{Rb}} |3, +3\rangle_{\mathrm{RbCs}}$ and $|p\rangle_{\mathrm{Rb}} |4, +4\rangle_{\mathrm{RbCs}}$. These two states are shown in bold in Fig. 7.7(a). The splitting between these states is $\sim 10\,\mathrm{MHz} \times h$ for $R_{\mathrm{am}} \sim 0.8\,\mu\mathrm{m}$. This energy scale sets how stringently we must satisfy the resonance condition in order to observe resonant dipole-dipole interactions. To observe resonant behaviour, we need $|E_{\mathrm{M}} + E_{\mathrm{r}}| \lesssim 10\,\mathrm{MHz} \times h$. This corresponds to needing the magnetic field to be tuned to within $\sim 5\,\mathrm{G}$ of B_{res}, which is approximately 192.5 G in our system.

We probe the resonant dipole-dipole interactions using an experimental sequence similar to that used in Sec. 6.3 to study charge-dipole interactions. We begin with two Rb atoms and one Cs atom, each individually trapped in tweezers at wavelength

[10] These potential energy curves were calculated by Pablo Fernández-Mayo Yelo and Rosario González-Férez.

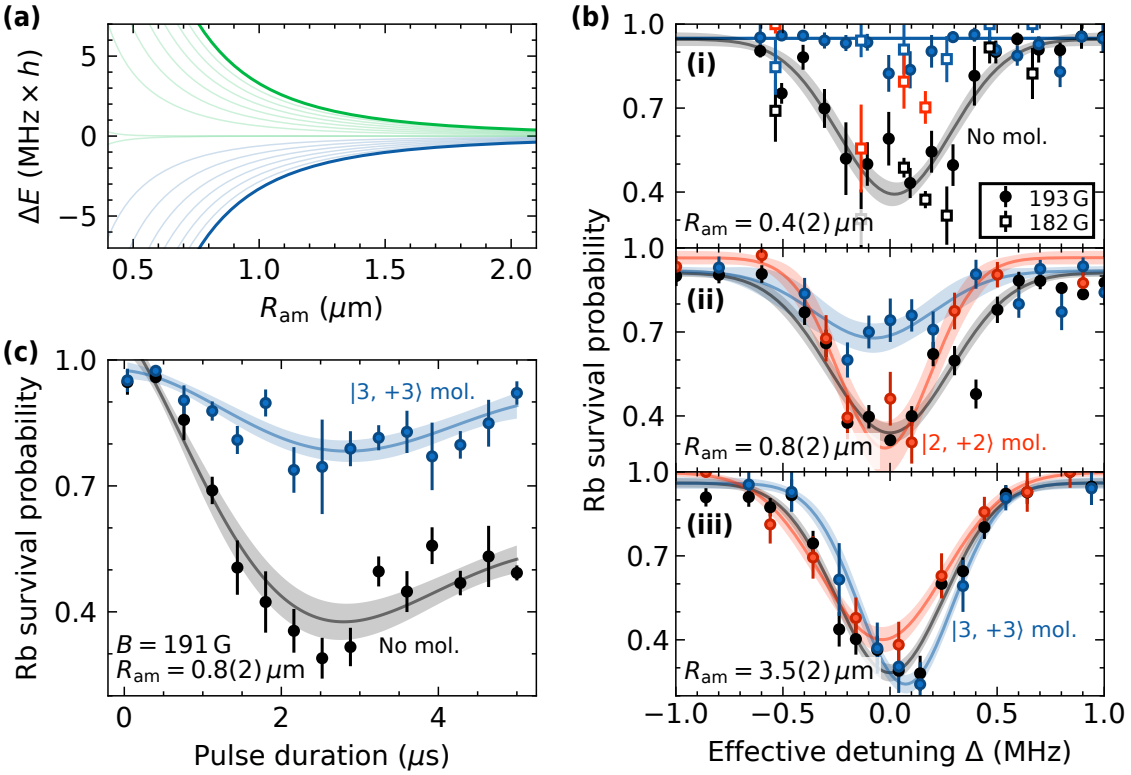

Figure 7.7: Rydberg blockade due to resonant dipole-dipole interactions between an atom and a polar molecule. (a) Calculated interaction shift ΔE between a Rb Rydberg atom and a RbCs molecule. The curves in blue (green) show ΔE for states evolving from the states $|d\rangle_{\mathrm{Rb}}\,|3, M_N\rangle_{\mathrm{RbCs}}$ ($|p\rangle_{\mathrm{Rb}}\,|4, M'_N\rangle_{\mathrm{RbCs}}$). **(b)** Effect of changing the atom-molecule separation R_{am}. Panels **(i)**, **(ii)**, and **(iii)** show data obtained for R_{am} of 0.4(2) µm, 0.8(2) µm, and 3.5(2) µm respectively. The filled circles show data obtained at 193 G and the empty squares show data obtained at 182 G. Blue and red points are from experimental runs where a molecule is successfully formed and later recovered. Blue (red) points are taken with microwave pulses that ideally transfer the molecules to the state $|3, +3\rangle$ ($|2, +2\rangle$) before the Rydberg excitation. Black points are from runs where no molecule was present. The solid lines are fits to Gaussians and the shaded regions show the errors extracted from the fits. **(c)** Blockaded excitation at $R_{\mathrm{am}} = 0.8(2)$ µm and magnetic field 191 G. The data points are coloured the same as in (b).

817 nm and 1066 nm respectively. We merge one of the Rb tweezers into the Cs tweezer and attempt to form a molecule in the state $|G\rangle$ with magnetoassociation and STIRAP. If the molecule formation is successful, this prepares a RbCs molecule and a Rb atom that are trapped in their own tweezers separated by 4 µm along the x-axis, as shown in Fig. 6.4(a)(i). If molecule formation is unsuccessful, the molecule detection scheme (see Sec. 4.3) removes the atom pair from the molecule tweezer, leaving only the additional Rb atom in its 817 nm tweezer . We perform successive microwave transfers to prepare the molecule in a chosen rotational state before moving the atom tweezer to realise a programmed atom-molecule separation R_{am}. We attempt to excite the atom to the Rydberg state $|d\rangle$ before moving the

atom tweezer back to its initial position, disassociating the molecule, and measuring the particle survival probabilities.

For this experiment, we excite to the Rydberg state $|d\rangle$ from the hyperfine ground state $|5s_{1/2}, f = 1, m_f = +1\rangle$.[11] This is in contrast to the experiments presented until now, where we excite to the state $|d\rangle$ from the state $|5s_{1/2}, f = 2, m_f = +2\rangle$ using the excitation scheme shown in Fig. 5.2(a)(ii). This is because, in order to form molecules, the Rb atoms are prepared in the state $|5s_{1/2}, f = 1, m_f = +1\rangle$ after Raman sideband cooling (see Sec. 2.3.2). For typical tweezer depths, the differential ac Stark shift of the hyperfine transition $|5s_{1/2}, f = 1, m_f = +1\rangle \rightarrow |5s_{1/2}, f = 2, m_f = +2\rangle$ is $\sim 1\,\mathrm{kHz} \times h$ so we cannot prepare the two Rb atoms in different hyperfine states. A solution to this would be to perform the spin flip $|5s_{1/2}, f = 1, m_f = +1\rangle \rightarrow |5s_{1/2}, f = 2, m_f = +2\rangle$ at high magnetic field *after* the molecule has been formed. This is precisely what we do when detecting molecule formation errors mid-sequence (see Sec. 4.8), where we perform this spin flip with ARP by using microwaves to couple the two hyperfine states. However, we find that connecting the requisite microwave amplifier to our Rb antenna causes the Rydberg transitions to significantly shift and rapidly dephase, probably due to spontaneous emission from the amplifier. Therefore, we cannot use ARP to perform the spin flip in this routine, so we excite from the state $|5s_{1/2}, f = 1, m_f = +1\rangle$.

In Fig. 7.7(b) we show the effect of changing the effective detuning Δ of the Rydberg excitation lasers for different separations R_{am} between the atom and molecule. We show data for $R_{\mathrm{am}} = 0.4(2)\,\mu\mathrm{m}$ (panel (i)), $R_{\mathrm{am}} = 0.8(2)\,\mu\mathrm{m}$ (panel (ii)), and $R_{\mathrm{am}} = 3.5(2)\,\mu\mathrm{m}$ (panel (iii)). Circular filled data points are measured with $B = 193\,\mathrm{G}$ and square empty points are measured with $B = 182\,\mathrm{G}$. Blue and red data points show data obtained from experimental runs in which molecule formation and recovery was successful. The blue points show data from a routine in which a series of microwave π pulses are applied to perform the molecular state transfers $|G\rangle \rightarrow |1, +1\rangle \rightarrow |2, +2\rangle \rightarrow |3, +3\rangle$ prior to the Rydberg excitation. The red points show data from a routine in which the last of these pulses is removed so that molecules are ideally prepared in the state $|2, +2\rangle$. We apply the Rydberg pulse before transferring the molecules back to $|G\rangle$ from which they are disassociated and atom pairs are recovered. The data points show the chance of the additional Rb atom (that we attempt to excite to the Rydberg state) surviving at the end of the routine. Atoms that are excited to $|d\rangle$ are typically lost whilst atoms are not excited typically survive.

[11] The Rydberg state that we can access by driving two σ^+ transitions from the state $|5s_{1/2}, f = 1, m_f = +1\rangle$ is actually a different hyperfine state to the state $|d\rangle$ discussed so far because it has $m_i = +1/2$ rather than $m_i = +3/2$. However, we do not experimentally resolve the hyperfine coupling for the state $|d\rangle$ and the calculations presented in Fig. 7.7 ignore it entirely. Therefore, for simplicity, we continue to use the state label $|d\rangle$ for this Rydberg state.

The black points show data from experimental runs in which molecule formation was unsuccessful. The solid lines show Gaussian fits to the data and the shaded regions show the error on these fits. The detunings are relative to the fitted centres from the data obtained when molecule formation was unsuccessful.

We observe three distinct behaviours for the different values of R_{am}. For short distances, the interaction is dominated by the charge-dipole interaction that was discussed in Ch. 6. This occurs when $R_{\mathrm{am}} \lesssim \langle \hat{r} \rangle$, where $\langle \hat{r} \rangle$ is the radius of the orbit of the Rydberg electron. For the state $|d\rangle$, $\langle \hat{r} \rangle \sim 0.5\,\mu\mathrm{m}$. Therefore, for the data shown in Fig. 7.7(b)(i), where $R_{\mathrm{am}} = 0.4(2)\,\mu\mathrm{m}$, the molecule is within the Rydberg electron orbital. This means that the charge-dipole interaction is sufficiently strong to blockade Rydberg excitation, even when the molecule and atom are not resonant with each other. For this reason, we observe suppressed Rydberg excitation whenever a molecule is present, whether this be in the resonant case (blue filled circles) or the non-resonant cases (blue empty squares and red points).

In the other extreme, R_{am} can be sufficiently large that, even when interactions are resonant, the interaction shift is too small to sufficiently blockade the Rydberg excitation. This happens when $R_{\mathrm{am}} \gg r_{\mathrm{b}}$, where, as in Sec. 5.8, the blockade radius r_{b} is the distance at which the interaction shift $\Delta E = h\Delta\nu/2$ for transition linewidth $\Delta\nu$. Here, $\Delta\nu \approx 1\,\mathrm{MHz}$, and the interaction potential shown in Fig 7.7(a) predicts that the blockade radius $r_{\mathrm{b}} \approx 1.9\,\mu\mathrm{m}$ for these interactions. Therefore, for the data shown in Fig 7.7(b)(iii), where $R_{\mathrm{am}} = 3.5(2)\,\mu\mathrm{m}$, we expect no significant Rydberg blockade, even in the resonant case. This is precisely we observe: all data sets, including the resonant case where the molecule is prepared in the state $|3, +3\rangle$ at 193 G (blue points), are similar to the case in which no molecule is present.

For intermediate values of R_{am}, we observe a difference between the resonant and non-resonant cases. This is shown in Fig. 7.7(b)(ii) where $R_{\mathrm{am}} = 0.8(2)\,\mu\mathrm{m}$. When a molecule is prepared in the state $|2, +2\rangle$ (red points), the dominant interactions are van der Waals and interaction shift is negligible. However, when the molecule is prepared in the state $|3, +3\rangle$ (blue points), the resonant dipole-dipole interactions dominate and the energy shift ΔE is approximately $5\,\mathrm{MHz} \times h$ (see Fig 7.7(a)). This is sufficient to blockade Rydberg excitation.

In Fig 7.7(c) we show the effect of changing the pulse time when the excitation lasers are resonant with the Rydberg transition in the case where there is no molecule. In runs where molecules are formed, the atom-molecule separation $R_{\mathrm{am}} = 0.8(2)\,\mu\mathrm{m}$ and the molecules are ideally transferred to the state $|3, +3\rangle$ with microwave pulses prior to the Rydberg excitation pulse. The magnetic field is $B = 191\,\mathrm{G}$. When the molecule is present, we observe partial Rydberg blockade: the contrast in the Rabi oscillations is approximately 0.2, compared to approximately 0.6 for the experimental

runs in which molecules were not formed. This is consistent with the amplitudes of the corresponding features in Fig. 7.7(b)(ii). We fit both sets of data points with Eq. (5.10) and extract a mean Rabi frequency $\langle\Omega\rangle = 160(20)\,\mathrm{kHz}$. This is significantly reduced from the Rabi frequency shown in Fig. 5.7(b) because here we excite from a non-stretched hyperfine state. This reduction in Rabi frequency limits the excitation fidelity.

The most likely reason for observing only partial blockade is imperfect state transfer of the molecule to the state $|3,+3\rangle$. This means that in some of the experimental runs in which we think there is a molecule in the state $|3,+3\rangle$, there is not. This manifests as partial blockade with the same Rabi frequency as the unblockaded case. This is in contrast to regime that we would observe if the molecular state preparation was perfect, but the interaction shift was not sufficiently large to completely blockade the Rydberg excitation (i.e. $\Delta E \approx h\Delta\nu/2$). We would then expect to drive the Rydberg transition with slightly off-resonant light with a detuning Δ. This would also result in Rabi oscillations with the contrast reduced by a factor $\widetilde{\Omega}/\Omega$, where the effective Rabi frequency $\widetilde{\Omega} = \sqrt{\Omega^2 + \Delta^2}$. However, in this regime, we would expect the Rabi frequency of the partially blockaded interactions to be scaled by the observed contrast (i.e. $\widetilde{\Omega} \approx (0.6/0.2)\Omega$), which is not what we observe. We do not expect fluctuations in the relative alignment of the tweezers to be significant here because the distances are much larger than the tweezer fluctuations, unlike the experiment presented in Sec. 6.3.

We are currently upgrading the experiment to allow us to excite Rydberg atoms from the hyperfine state $|5\mathrm{s}_{1/2}, f = 2, m_f = +2\rangle$ in this experimental sequence. To remove the need to use ARP for the hyperfine spin flip (which requires the problematic microwave amplifier), we plan to perform the spin flip using the Raman beams (see Sec. 2.3.2). These beams drive this spin flip during the atomic cooling sequence that takes place at low magnetic field (4.78 G). We cannot currently use these lasers to perform the spin flip at high magnetic fields ($\sim 200\,\mathrm{G}$) because the magnetic field noise ($\approx 30\,\mathrm{mG}$) means that there is significant dephasing with the current Rabi frequencies that we achieve with the Raman lasers ($\approx 20\,\mathrm{kHz}$). We plan to significantly the increasing the power of the Raman lasers so that they can be used for this spin flip at high fields whilst not suffering from this dephasing.

7.5 Summary

We have presented preliminary measurements of the blockade of atomic Rydberg excitation due to the resonant dipole-dipole interaction between a Rydberg atom

and a polar molecule. We have shown how pairs of atomic and molecular states can be chosen in order to engineer these interactions. We performed microwave spectroscopy of the transitions between these states and showed how they can be tuned into resonance with an applied magnetic field. These resonant interactions will be crucial to the implement molecule-molecule gates mediated by Rydberg atoms, which we aim to study in the near future.

8 Conclusion

Some of the results in this chapter have been published in Ref. [203].

In this thesis, we have described the development of a hybrid quantum system of ultracold polar molecules and Rydberg atoms. This system has great promise for quantum science applications. In this chapter, we briefly summarise our results and provide an outlook to future work.

8.1 Summary

We have demonstrated the efficient assembly, manipulation, and readout of individually trapped RbCs molecules in optical tweezers. We have introduced mergoassociation, a new method for molecule formation that is applicable for systems with large interspecies interactions where particles are tightly confined. In our system, the efficiency of molecule formation by mergoassociation is comparable to that of magnetoassociation, and mergoassociation can be used to access bound states that would otherwise be inaccessible at our starting magnetic fields. Mergoassociation will be effective even in systems that do not possess Feshbach resonances suitable for magnetoassociation [278].

We use STIRAP to transfer weakly bound molecules to the ground state and have developed a toolbox for their control. The overall efficiency for the conversion of an atom pair to a ground-state molecule is 48(2)% and the majority of formed molecules are in the motional ground state. We have implemented global and local microwave control of the rotational states of molecules in small arrays, using optical tweezers to address specific molecules. We map the rotational state of molecules onto atomic position in a novel multi-state readout scheme. Furthermore, we have implemented a scheme for molecule rearrangement where we detect and eliminate molecule-formation errors to prepare defect-free arrays.

We have coherently excited individually trapped Rb atoms to Rydberg states.

Similarly to the molecular addressing, we exploit ac Stark shifts caused by the optical tweezers to selectively excite only certain atoms. We use the Rydberg atoms as sensitive probes for the electric and magnetic fields in our experiment. Using Rydberg-Rydberg interactions, we have precisely measured the distance between optical tweezers.

We have demonstrated blockade of the transition to the Rb Rydberg state $|52s\rangle$ due to the charge-dipole interaction with a RbCs molecule in the rovibrational ground state. To realise this blockade, we use species-specific tweezers to set the atom-molecule separation to 310(40) nm. The observed excitation dynamics are in good agreement with simulations using calculated interaction potentials. This represents the first observation of a charge-dipole induced shift in an ultracold setting.

Finally, we have engineered resonant dipole-dipole interactions between a polar molecule and a Rb atom in the Rydberg state $|83d\rangle$. We have detailed how to choose pairs of resonant transitions. We have presented spectroscopy of these transitions and shown how they can be tuned to resonance with a magnetic field. We have observed the partial blockade of Rydberg excitation due to these resonant interactions when the atom-molecule separation is set to 0.8(2) µm. These interactions will allow us to implement molecule-molecule quantum gates that are mediated by Rydberg atoms in the near future [101, 102].

8.2 Outlook

The work presented in this thesis provides a foundation for exciting experiments with individually trapped molecules and atoms. Here, we outline ongoing and upcoming research directions for the experiment.

8.2.1 Magic tweezers

The primary limitation to coherence times when we drive molecular transitions is their differential light shifts. Typically, molecules are trapped in tweezers where the differential light shift is approximately $100\,\mathrm{kHz} \times h$. The molecules are predominantly formed in the motional ground state, so most of the fluctuations in the potential experienced by them is from shot-to-shot fluctuations in the tweezer intensity. From independent characterisations of the tweezers, we expect these fluctuations are on the order of a percent. This leads to the transition frequency fluctuating on the scale of kilohertz and, for Rabi frequencies of 10 to 100 kHz, leads to a Rabi coherence time on the order of tens of milliseconds. If these differential light shifts were to be eliminated, the coherence times would be significantly longer. This can be achieved

by trapping the molecules in magic-wavelength traps. Furthermore, an array of molecules trapped in magic-wavelength tweezers would have identical transition frequencies, eliminating the dephasing discussed in Sec. 4.7.

A magic-wavelength trap for molecules has recently been demonstrated by Gregory *et al.* [98] in the RbCs bulk-gas experiment at Durham. The trapping wavelength ($\lambda = 1145\,\text{nm}$) is chosen such that the anisotropic polarisability of the molecule is zero. This eliminates differential light shifts between molecular states. Gregory *et al.* achieved a Ramsey coherence time of $0.78(4)\,\text{s}$, and extended this to $> 1.4\,\text{s}$ using a single spin-echo pulse. These coherence times are limited by the large linewidth of their magic-trapping laser. We are currently implementing and characterising magic-wavelength tweezers in our experiment. Our trapping laser is locked to a ULE cavity like that to which we lock the STIRAP and Rydberg lasers (see Sec. 2.5) to achieve a much smaller linewidth. Therefore, we expect to achieve coherence times exceeding that demonstrated by Gregory *et al.*.

8.2.2 Optical lattice

We plan to study dipole-dipole interactions between individually trapped molecules. For this interaction to be experimentally resolvable (i.e. on the kilohertz scale), an inter-molecule separation of approximately 500 nm is required [47]. Currently, molecules in our experiment are trapped in tweezers at wavelength 1066 nm with micrometre-scale beam waists, as shown in Fig. 8.1(a). If we move two of these tweezers to separations of approximately 1 µm, they no longer satisfy the Rayleigh criterion and a wide single well is formed. The molecule-molecule separation quickly drops to zero (see Sec. 6.2), which makes it impractical to achieve stable sub-micrometre separations. This would cause dipole-dipole interactions to rapidly dephase or molecules to be lost from collisions when their separation drops to zero.

We plan to implement an optical lattice to pin the molecules at sub-micrometre separations. We will form a one-dimensional lattice from the same 1145 nm light used to form the magic-wavelength tweezers. This lattice will be in the xy-plane (perpendicular to the direction of tweezer light propagation), as shown in Fig. 8.1(b). Potential minima will be formed at separations of $\lambda/2$, and we will operate in the regime where the lattice depth is larger than that of the tweezers. The tweezers will confine the molecules in all directions, and the lattice will pin the molecule-molecule separation at approximately 570 nm. This separation, combined with the magic trapping of the molecules, will provide the ideal environment to study dipole-dipole interactions between pairs of individually trapped molecules.

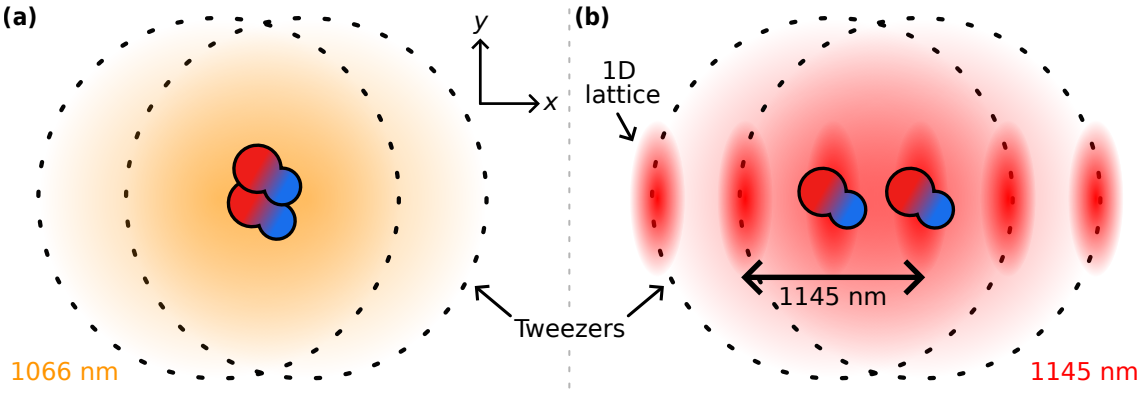

Figure 8.1: Planned trapping scheme for the study of dipole-dipole interactions between individually trapped molecules. (a) Currently, molecules are trapped in 1066 nm tweezers with beam waists of approximately a micrometre. This makes it impractical to achieve fixed sub-micrometre separations between molecules. **(b)** We plan to trap molecules in magic-wavelength tweezers at $\lambda = 1145$ nm. To pin the inter-molecular separation, we will implement a magic-wavelength optical lattice that will provide potential minima separated by $\lambda/2$.

8.2.3 Larger arrays and Rydberg-mediated detection

We plan to scale the number of optical tweezers in our arrays in order to trap a greater number of molecules and atoms. The amount of molecules that we can form and the performance of our molecule rearrangement protocol (see Sec. 4.8) is limited by laser power. Currently, we use approximately 1 W of 1066 nm light and 100 mW of 817 nm light, with which we are able to assemble and rearrange an array of molecules starting from six atom pairs. However, our 1066 nm laser is capable of outputting 50 W and laser sources with output powers of 2 W at 817 nm are readily available. Therefore, a 20-fold increase in the array size is realisable in the short term and we note that higher power laser sources exceeding 100 W [351, 352] are available for further scaling in the long term.

In Fig. 8.2(a) we show the results of a Monte Carlo simulation of the performance of the rearrangement scheme discussed in Sec. 4.8 with 120 atom pairs initially trapped, corresponding to the anticipated 20-fold increase in laser power. The simulation is the same as that discussed in Sec. 4.8, but with a larger array of traps. The blue symbols show the predicted performance for molecule recovery probability $P_r = 68\%$; the value we measured in the rearrangement routine using six atom pairs. The green symbols show the performance that would be achieved if the molecule recovery probability were improved to $P_r = 88\%$. This latter value requires the infidelity in the hyperfine-state preparation to be reduced to 2% and the STIRAP efficiency increased to 99%. Both improvements are feasible in the near term by changing the wavelength of the Rb tweezer to be further detuned (to reduce Raman scattering) and by suppressing phase noise on the STIRAP lasers using

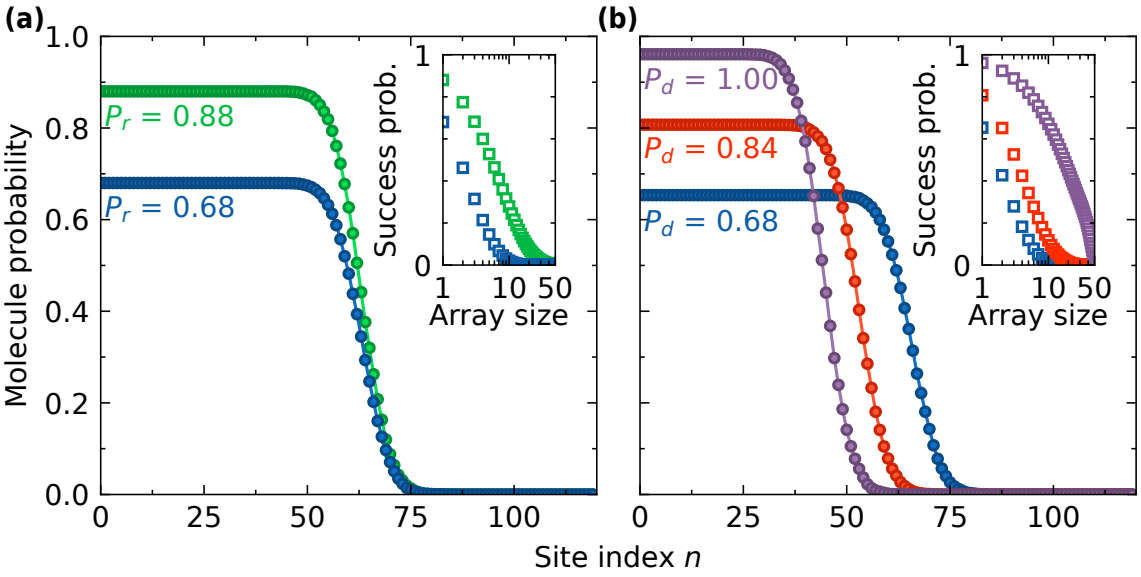

Figure 8.2: Prospects for scaling the molecule rearrangement protocol to larger array sizes. The performance is simulated using a Monte Carlo method starting with an array of 120 atom pairs. The main plots show the probability of an atom pair being recovered from a molecule in site index n when *not* post-selecting on molecule formation. The insets show the probability of recovering a defect-free array of a given size. **(a)** Rearrangement performance for different molecule recapture probabilities P_r. **(b)** Rearrangement performance using direct detection of ground-state molecules with probability P_d, rather than the detection of the failure to form molecules.

feed-forward techniques [348, 349]. In both cases, the effect of non-unity P_r is to cause false-positive errors when a weakly bound molecule is formed but subsequently lost, decreasing the average number of molecules in the array. The inset in Fig. 8.2(a) shows the probability of preparing a defect-free array, which reduces with array size s proportional to $(P_r)^s$, as we observed experimentally with the smaller array.

As an aside, we note that increasing the laser power available for tweezer generation will allow an increase in the number of rotational states that can be readout using the scheme detailed in Sec. 4.6. There is no fundamental limit to the number of states that can be readout with our detection scheme; we need only to have enough laser power to generate the required number of detection arrays.

Developing the capability to non-destructively detect molecules in the ground state would greatly enhance the prospect of large defect-free arrays of RbCs molecules. Currently, as the assembled molecules cannot be directly imaged, detection is limited to measuring only when a molecule has been formed. Consequently, we cannot correct for the subsequent loss of molecules. This leads to a significant drop in the probability of preparing a defect-free array when scaling to larger systems. To overcome this limitation, we propose to exploit the long-range interactions between molecules and Rydberg atoms discussed in Chs 6 and 7 to detect molecules in

ground-state directly. We will use the blockade of the atomic Rydberg excitation when a molecule is present to infer the presence of molecules from the failure to excite atoms to a Rydberg state [100–102, 353].

In Fig. 8.2(b) we show the expected recovery of atom pairs from molecules in a sorted array using the proposed Rydberg atom scheme. Here we use $P_r = 68\%$, the effect of which is now to reduce the average trap occupancy *before* rearrangement as detection can be performed after all the lossy molecule formation stages. The simulation is similar to that for Fig. 8.2(b) (see Sec. 4.8), but a trap is now occupied prior to rearrangement if $x_n < P_f P_r / \mathcal{F}_{\text{STIRAP}}$, where $P_f = 53\%$ is the assumed molecule formation probability and $\mathcal{F}_{\text{STIRAP}} = 96.4\%$ is the STIRAP fidelity. We show the results of simulations using different values of the molecule detection probability P_d. We expect P_d to be dominated by false-positive errors due to imperfect transfer to the atomic Rydberg state when no molecule is present. We incorporate this into the simulation by assigning each site with a second random number y_n between 0 and 1, such that if $y_n > P_d$ on an unoccupied site, we simulate a false-positive error in the detection by using this trap during the rearrangement even though it is unoccupied. As before, we repeat this simulation for 500 initialisations of the array and determine the average occupancy of each site in the array. The limiting factor to atom pair recovery is now the reverse STIRAP transfer $\mathcal{F}_{\text{STIRAP}}$ with which we scale the recovery probability of all the traps in the array. Non-unity detection fidelities P_d do not cause molecule loss but instead result in unoccupied molecule traps being inserted into the final array. This reduces the average occupancy of "filled" traps while increasing the length of the array that is "filled". The total number of molecules in the array is the same for all P_d shown here. These simulations suggest that a Rydberg excitation fidelity of $> 84\,\%$, less than we currently achieve (see Sec. 5.5), will enable the preparation of defect-free arrays of tens of assembled molecules.

The upgrades to our experiment described above will allow the formation of defect-free arrays of molecules comparable in size to those demonstrated with directly-cooled molecules. For comparison, stochastic loading probabilities of $\sim 35\%$ are typical for an array of CaF molecules in optical tweezers [69]. The rearrangement of such molecules has been demonstrated to obtain defect-free arrays of up to 16 molecules with a probability > 0.6 for a reported single-particle rearrangement fidelity of 97.4(1)% and a state-preparation fidelity of 82.4(11)% [70]. In this work, the probability to convert an atom pair into a ground state molecule is 48(2)% and the direct detection of ground-state molecules will allow for a rearrangement fidelity limited by the STIRAP fidelity (currently 96.4(1)%). All molecules formed in this experiment occupy a single internal state. Furthermore, for assembled molecules

such as RbCs, the molecule inherits the motional state of the center of mass of the atom pair from which it is assembled. As only atom pairs in the ground state of relative motion are converted into molecules, the formed molecules usually occupy the three-dimensional motional ground state. We estimate that this is true for 56(6)% of the molecules formed in our experiment (see Sec. 4.2). This efficiency is comparable to the 54(18)% occupancy of the three-dimensional motional ground state achieved after Raman sideband cooling of CaF molecules in optical tweezers [135, 136].

8.2.4 Rydberg-mediated quantum gates

In additional to using the Rydberg atoms to detect molecules, we will use them to mediate high-fidelity entangling gates between molecules [101, 102]. We will prototype a hybrid network where quantum information can be transferred between individually trapped molecules using Rydberg atoms. The molecules will act as long-lived quantum memories that encode information in their rotational states, allowing for tests of high-dimension quantum computing [47, 59, 60] and quantum simulation [44, 47, 74]. This will build on the partial blockade caused by resonant interactions that we have shown in this work. We are currently limited by the fidelities with which we can prepare atoms and molecules in the requisite states, and have begun work to increase these.

8.2.5 Molecule-Rydberg interactions and giant molecules

Our hybrid platform provides the ideal environment to study interactions between Rydberg atoms and molecules in an ultracold setting. Previously, these interactions have largely been studied in scattering experiments [161] where the energy-level spacings between high n Rydberg states are much smaller than the translational collision energies [354]. These experiments were typically described by models that consider the scattering of the molecule from the Rydberg electron and core independently [355], and state-resolved imaging proved a challenge [354]. To overcome this, resonant energy transfer has been exploited to perform Rydberg atom-enabled spectroscopy of molecules [106]. This is a versatile tool for exploring the structures of molecules and has been used in room-temperature [104] or cold [105] settings. We now have the ideal test bed to test this technique in ultracold regime where the particles can be placed in delicate quantum states before interacting.

As probe of these interactions, we will aim to photoassociate GPRyMs [109–112]. Spectroscopy of these giant molecules will enable sensitive probing of the

energy landscapes caused by charge-dipole interactions between the molecule and the Rydberg atom. Both the Rydberg core and electron affect these energy levels, allowing interactions between molecules and the entire Rydberg atom to be probed at ultra-low energies. The ability to synthesise GPRyMs will open up further study into their properties such as their polarisabilities and lifetimes, which will be enhanced if it proves possible to trap them.

8.2.6 Studies of interspecies energy transfer

Looking further ahead, our platform could be used to simulate the behaviour of a wide range of quantum systems that demonstrate interspecies energy exchange. For example, in a biological setting, Förster resonance energy transfer occurs between light-sensitive molecules through nonradiative dipole–dipole coupling [356]. Our hybrid system is ideal for studying quantum effects, such as decoherence, that occur during such energy transfer [357]. Alternatively, one could simulate photosynthesis where absorbed energy is transferred to the photosynthetic reaction centre with near-unity efficiency. A debate is ongoing as to whether quantum coherence is responsible for this high efficiency [358, 359]. Our hybrid platform is ideal for simulating such interspecies energy transfer in a fully quantum setting which may shed some light on this process.

8.3 Concluding remarks

In this thesis, we have detailed the formation of a hybrid quantum system of ultracold molecules and Rydberg atoms. This platform promises to be a powerful and versatile tool for exploring for new quantum science. There are many exciting research avenues to embark down, and the future of *Team Tweezer* is bright.

Glossaries

Acronyms

1D AOD one-dimensional AOD 2.1, 2.2

2D AOD two-dimensional AOD 1.5, 2.1–2.3, 5.8, 6.3

AMO atomic, molecular, and optical 1.3, 2.6

AOD acousto-optic deflector 2.2, 2.3, 3.4

AOM acousto-optic modulator 2.2, 2.3, 2.5, 4.2, 5.3–5.5, 5.8, 7.3

AR anti-reflection 2.1, 2.3, 2.4, 5.2

ARP adiabatic rapid passage 4.8, 5.3, 7.4

AWG arbitrary waveform generator 1.5, 2.2, 2.6

CIR confinement-induced resonance 3.2

DAC digital-to-analogue converter 5.6

DDS direct digital synthesiser 1.5, 2.5

EMCCD electron-multiplying charge-coupled device 2.1, 2.3, 2.6

EOM electro-optic modulator 2.3, 2.5, 5.3, 5.4, 7.3

FIFO first-in, first-out 2.6

GPRyM giant polyatomic Rydberg molecule 6.1, 6.4, 8.2

HWP half-wave plate 2.3, 5.2

IR infrared 5.2

LIAD light-induced atomic desorption 5.6, 7.3

MOT magneto-optical trap 2.1, 2.3

MWG microwave generator 1.5, 2.6

NA numerical aperture 2.2

PBS polarising beam splitter 2.3, 2.5

PDH Pound-Drever-Hall 2.5, 5.3

QWP quarter-wave plate 2.5

RF radiofrequency 2.2, 2.3, 4.5, 5.8

ROI region of interest 2.6

SLM spatial light modulator 1.5, 2.1–2.3, 2.6, 5.8

STIRAP stimulated Raman adiabatic passage 1.5, 2.3–2.5, 4.2–4.8, 5.2, 6.2, 7.4, 8.1, 8.2

TDM transition dipole moment 4.4, 4.5, 5.2, 7.1, 7.3, 7.4

ULE ultra-low expansion 1.5, 2.5, 4.1, 5.2–5.4, 6.3, 8.2

UV ultraviolet 2.5, 5.2, 5.6

Fundamental physical constants

Symbols are generally defined in the relevant places in the text, with the exception of fundamental physical constants. The fundamental physical constants that are used in the text are listed here alongside the 2022 CODATA recommended values [360].

Quantity	Symbol	Value
Bohr magneton	μ_B	$9.274\,010\,065\,7(29) \times 10^{-24}\,\mathrm{J/T}$
	μ_B/h	$1.399\,624\,491\,71(44)\,\mathrm{MHz/G}$
Bohr radius	a_0	$5.291\,772\,105\,44(82) \times 10^{-11}\,\mathrm{m}$
Boltzmann constant	k_B	$1.380\,649 \times 10^{-23}\,\mathrm{J/K}$

Quantity	**Symbol**	**Value**
	k_B/h	$20.836\,619\,12\ldots$ MHz/mK
Electron mass	m_e	$9.109\,383\,713\,9(28) \times 10^{-31}$ kg
Elementary charge	e	$1.602\,176\,634 \times 10^{-19}$ C
Nuclear magneton	μ_N	$5.050\,783\,739\,3(16) \times 10^{-27}$ J/T
	μ_N/h	$762.259\,321\,88(24)$ Hz/G
Planck constant	h	$6.626\,070\,15 \times 10^{-34}$ J/Hz
		$4.135\,667\,696\ldots \times 10^{-15}$ eV/Hz
Speed of light in vacuum	c	$2.997\,924\,58 \times 10^{8}$ m/s
Unified atomic mass unit	u	$1.660\,539\,068\,92(52) \times 10^{-27}$ kg
Vacuum electric permittivity	ε_0	$8.854\,187\,818\,8(14) \times 10^{-12}$ F/m

Bibliography

[1] R. P. Feynman, *Simulating physics with computers*, Int. J. Theor. Phys **21**, 467 (1982).

[2] S. Lloyd, *Universal quantum simulators*, Science **273**, 1073 (1996).

[3] I. Buluta and F. Nori, *Quantum simulators*, Science **326**, 108 (2009).

[4] J. I. Cirac and P. Zoller, *Goals and opportunities in quantum simulation*, Nat. Phys. **8**, 264 (2012).

[5] I. M. Georgescu, S. Ashhab, and F. Nori, *Quantum simulation*, Rev. Mod. Phys. **86**, 153 (2014).

[6] S. Somaroo, C. H. Tseng, T. F. Havel, R. Laflamme, and D. G. Cory, *Quantum simulations on a quantum computer*, Phys. Rev. Lett. **82**, 5381 (1999).

[7] M. A. Nielsen and I. L. Chuang, *Quantum computation and quantum information* (Cambridge University Press, Cambridge, 2000).

[8] J. Preskill, *Quantum computing in the NISQ era and beyond*, Quantum **2**, 79 (2018).

[9] P. Shor, "Algorithms for quantum computation: discrete logarithms and factoring", in Proc. 35 Annu. Symp. Found. Comput. Sci. (1994), pp. 124–134.

[10] L. K. Grover, "A fast quantum mechanical algorithm for database search", in Proc. 28 Annu. ACM Symp. Theor. Comput. (1996), pp. 212–219.

[11] D. P. DiVincenzo, *The physical implementation of quantum computation*, Fortschr. Phys. **48**, 771 (2000).

[12] I. Buluta, S. Ashhab, and F. Nori, *Natural and artificial atoms for quantum computation*, Rep. Prog. Phys. **74**, 104401 (2011).

[13] H. Häffner, C. Roos, and R. Blatt, *Quantum computing with trapped ions*, Phys. Rep. **469**, 155 (2008).

[14] R. Blatt and C. F. Roos, *Quantum simulations with trapped ions*, Nat. Phys. **8**, 277 (2012).

[15] C. D. Bruzewicz, J. Chiaverini, R. McConnell, and J. M. Sage, *Trapped-ion quantum computing: Progress and challenges*, Appl. Phys. Rev. **6**, 021314 (2019).

[16] C. Monroe, W. C. Campbell, L.-M. Duan, Z.-X. Gong, A. V. Gorshkov, P. W. Hess, R. Islam, K. Kim, N. M. Linke, G. Pagano, P. Richerme, C. Senko, and N. Y. Yao, *Programmable quantum simulations of spin systems with trapped ions*, Rev. Mod. Phys. **93**, 025001 (2021).

[17] H.-L. Huang, D. Wu, D. Fan, and X. Zhu, *Superconducting quantum computing: a review*, Sci. China Inf. Sci. **63**, 180501 (2020).

[18] S. Bravyi, O. Dial, J. M. Gambetta, D. Gil, and Z. Nazario, *The future of quantum computing with superconducting qubits*, J. Appl. Phys **132**, 160902 (2022).

[19] O. Ezratty, *Perspective on superconducting qubit quantum computing*, Eur. Phys. J. A **59**, 94 (2023).

[20] M. J. Hartmann, *Quantum simulation with interacting photons*, J. Opt. **18**, 104005 (2016).

[21] J. Wang, F. Sciarrino, A. Laing, and M. G. Thompson, *Integrated photonic quantum technologies*, Nat. Photonics **14**, 273 (2020).

[22] H.-S. Zhong, H. Wang, Y.-H. Deng, M.-C. Chen, L.-C. Peng, Y.-H. Luo, J. Qin, D. Wu, X. Ding, Y. Hu, P. Hu, X.-Y. Yang, W.-J. Zhang, H. Li, Y. Li, X. Jiang, L. Gan, G. Yang, L. You, Z. Wang, L. Li, N.-L. Liu, C.-Y. Lu, and J.-W. Pan, *Quantum computational advantage using photons*, Science **370**, 1460 (2020).

[23] G. Moody, V. J. Sorger, D. J. Blumenthal, P. W. Juodawlkis, W. Loh, C. Sorace-Agaskar, A. E. Jones, K. C. Balram, J. C. F. Matthews, A. Laing, M. Davanco, L. Chang, J. E. Bowers, N. Quack, C. Galland, I. Aharonovich, M. A. Wolff, C. Schuck, N. Sinclair, M. Lončar, T. Komljenovic, D. Weld, S. Mookherjea, S. Buckley, M. Radulaski, S. Reitzenstein, B. Pingault, B. Machielse, D. Mukhopadhyay, A. Akimov, A. Zheltikov, G. S. Agarwal, K. Srinivasan, J. Lu, H. X. Tang, W. Jiang, T. P. McKenna, A. H. Safavi-Naeini, S. Steinhauer, A. W. Elshaari, V. Zwiller, P. S. Davids, N. Martinez, M. Gehl, J. Chiaverini, K. K. Mehta, J. Romero, N. B. Lingaraju, A. M. Weiner, D. Peace, R. Cernansky, M. Lobino, E. Diamanti, L. T. Vidarte, and R. M. Camacho, *2022 roadmap on integrated quantum photonics*, J. Phys. Photonics **4**, 012501 (2022).

[24] E. Pelucchi, G. Fagas, I. Aharonovich, D. Englund, E. Figueroa, Q. Gong, H. Hannes, J. Liu, C.-Y. Lu, N. Matsuda, J.-W. Pan, F. Schreck, F. Sciarrino, C. Silberhorn, J. Wang, and K. D. Jöns, *The potential and global outlook of integrated photonics for quantum technologies*, Nat. Rev. Phys. **4**, 194 (2022).

[25] R. K. Ramakrishnan, A. B. Ravichandran, A. Mishra, A. Kaushalram, G. Hegde, S. Talabattula, and P. P. Rohde, *Integrated photonic platforms for quantum technology: a review*, ISSS J. Micro Smart Syst. **12**, 83 (2023).

[26] J. Gray, A. Bayat, R. K. Puddy, C. G. Smith, and S. Bose, *Unravelling quantum dot array simulators via singlet-triplet measurements*, Phys. Rev. B **94**, 195136 (2016).

[27] T. Hensgens, T. Fujita, L. Janssen, X. Li, C. J. Van Diepen, C. Reichl, W. Wegscheider, S. Das Sarma, and L. M. K. Vandersypen, *Quantum simulation of a Fermi–Hubbard model using a semiconductor quantum dot array*, Nature **548**, 70 (2017).

[28] Y. P. Kandel, H. Qiao, S. Fallahi, G. C. Gardner, M. J. Manfra, and J. M. Nichol, *Coherent spin-state transfer via Heisenberg exchange*, Nature **573**, 553 (2019).

[29] H. Qiao, Y. P. Kandel, S. K. Manikandan, A. N. Jordan, S. Fallahi, G. C. Gardner, M. J. Manfra, and J. M. Nichol, *Conditional teleportation of quantum-dot spin states*, Nat. Commun. **11**, 3022 (2020).

[30] Y. P. Kandel, H. Qiao, S. Fallahi, G. C. Gardner, M. J. Manfra, and J. M. Nichol, *Adiabatic quantum state transfer in a semiconductor quantum-dot spin chain*, Nat. Commun. **12**, 2156 (2021).

[31] C. J. van Diepen, T.-K. Hsiao, U. Mukhopadhyay, C. Reichl, W. Wegscheider, and L. M. K. Vandersypen, *Quantum simulation of antiferromagnetic Heisenberg chain with gate-defined quantum dots*, Phys. Rev. X **11**, 041025 (2021).

[32] M. Kiczynski, S. K. Gorman, H. Geng, M. B. Donnelly, Y. Chung, Y. He, J. G. Keizer, and M. Y. Simmons, *Engineering topological states in atom-based semiconductor quantum dots*, Nature **606**, 694 (2022).

[33] M. Baranov, M. Dalmonte, G. Pupillo, and P. Zoller, *Condensed matter theory of dipolar quantum gases*, Chem. Rev. **112**, 5012 (2012).

[34] N. Y. Yao, M. P. Zaletel, D. M. Stamper-Kurn, and A. Vishwanath, *A quantum dipolar spin liquid*, Nat. Phys. **14**, 405 (2018).

[35] A. M. Kaufman and K.-K. Ni, *Quantum science with optical tweezer arrays of ultracold atoms and molecules*, Nat. Phys. **17**, 1324 (2021).

[36] T. Lahaye, C. Menotti, L. Santos, M. Lewenstein, and T. Pfau, *The physics of dipolar bosonic quantum gases*, Rep. Prog. Phys. **72**, 126401 (2009).

[37] S. Baier, M. J. Mark, D. Petter, K. Aikawa, L. Chomaz, Z. Cai, M. Baranov, P. Zoller, and F. Ferlaino, *Extended Bose-Hubbard models with ultracold magnetic atoms*, Science **352**, 201 (2016).

[38] L. Chomaz, I. Ferrier-Barbut, F. Ferlaino, B. Laburthe-Tolra, B. L. Lev, and T. Pfau, *Dipolar physics: a review of experiments with magnetic quantum gases*, Rep. Prog. Phys **86**, 026401 (2023).

[39] L. Su, A. Douglas, M. Szurek, R. Groth, S. F. Ozturk, A. Krahn, A. H. Hébert, G. A. Phelps, S. Ebadi, S. Dickerson, F. Ferlaino, O. Marković, and M. Greiner, *Dipolar quantum solids emerging in a Hubbard quantum simulator*, Nature **622**, 724 (2023).

[40] R. Barnett, D. Petrov, M. Lukin, and E. Demler, *Quantum magnetism with multicomponent dipolar molecules in an optical lattice*, Phys. Rev. Lett. **96**, 190401 (2006).

[41] L. D. Carr, D. DeMille, R. V. Krems, and J. Ye, *Cold and ultracold molecules: science, technology and applications*, New J. Phys. **11**, 055049 (2009).

[42] A. V. Gorshkov, S. R. Manmana, G. Chen, J. Ye, E. Demler, M. D. Lukin, and A. M. Rey, *Tunable superfluidity and quantum magnetism with ultracold polar molecules*, Phys. Rev. Lett. **107**, 115301 (2011).

[43] W. Lechner and P. Zoller, *From classical to quantum glasses with ultracold polar molecules*, Phys. Rev. Lett. **111**, 185306 (2013).

[44] M. L. Wall, K. R. A. Hazzard, and A. M. Rey, "Quantum magnetism with ultracold molecules", in *From atomic to mesoscale* (World Scientific, Singapore, 2015) Chap. 1, pp. 3–37.

[45] J. L. Bohn, A. M. Rey, and J. Ye, *Cold molecules: progress in quantum engineering of chemistry and quantum matter*, Science **357**, 1002 (2017).

[46] T. P. Softley, *Cold and ultracold molecules in the twenties*, Proc. R. Soc. A: Math. Phys. Eng. Sci. **479**, 20220806 (2023).

[47] S. L. Cornish, M. R. Tarbutt, and K. R. A. Hazzard, *Quantum computation and quantum simulation with ultracold molecules*, Nat. Phys. **20**, 730 (2024).

[48] M. Saffman, T. G. Walker, and K. Mølmer, *Quantum information with Rydberg atoms*, Rev. Mod. Phys. **82**, 2313 (2010).

[49] M. Saffman, *Quantum computing with atomic qubits and Rydberg interactions: progress and challenges*, J. Phys. B **49**, 202001 (2016).

[50] C. S. Adams, J. D. Pritchard, and J. P. Shaffer, *Rydberg atom quantum technologies*, J. Phys. B **53**, 012002 (2019).

[51] A. Browaeys and T. Lahaye, *Many-body physics with individually controlled Rydberg atoms*, Nat. Phys. **16**, 132 (2020).

[52] X. Wu, X. Liang, Y. Tian, F. Yang, C. Chen, Y.-C. Liu, M. K. Tey, and L. You, *A concise review of Rydberg atom based quantum computation and quantum simulation*, Chin. Phys. B **30**, 020305 (2021).

[53] M. Morgado and S. Whitlock, *Quantum simulation and computing with Rydberg-interacting qubits*, AVS Quantum Sci. **3**, 023501 (2021).

[54] D. DeMille, *Quantum computation with trapped polar molecules*, Phys. Rev. Lett. **88**, 067901 (2002).

[55] S. F. Yelin, K. Kirby, and R. Côté, *Schemes for robust quantum computation with polar molecules*, Phys. Rev. A **74**, 050301(R) (2006).

[56] J. Zhu, S. Kais, Q. Wei, D. Herschbach, and B. Friedrich, *Implementation of quantum logic gates using polar molecules in pendular states*, J. Chem. Phys. **138**, 024104 (2013).

[57] K.-K. Ni, T. Rosenband, and D. D. Grimes, *Dipolar exchange quantum logic gate with polar molecules*, Chem. Sci. **9**, 6830 (2018).

[58] M. Hughes, M. D. Frye, R. Sawant, G. Bhole, J. A. Jones, S. L. Cornish, M. R. Tarbutt, J. M. Hutson, D. Jaksch, and J. Mur-Petit, *Robust entangling gate for polar molecules using magnetic and microwave fields*, Phys. Rev. A **101**, 062308 (2020).

[59] V. V. Albert, J. P. Covey, and J. Preskill, *Robust encoding of a qubit in a molecule*, Phys. Rev. X **10**, 031050 (2020).

[60] R. Sawant, J. A. Blackmore, P. D. Gregory, J. Mur-Petit, D. Jaksch, J. Aldegunde, J. M. Hutson, M. R. Tarbutt, and S. L. Cornish, *Ultracold polar molecules as qudits*, New J. Phys. **22**, 013027 (2020).

[61] R. V. Krems, *Cold controlled chemistry*, Phys. Chem. Chem. Phys. **10**, 4079 (2008).

[62] B. R. Heazlewood and T. P. Softley, *Towards chemistry at absolute zero*, Nat. Rev. Chem. **5**, 125 (2021).

[63] Y. Liu and K.-K. Ni, *Bimolecular chemistry in the ultracold regime*, Annu. Rev. Phys. Chem. **73**, 73 (2022).

[64] S. Schiller and V. Korobov, *Tests of time independence of the electron and nuclear masses with ultracold molecules*, Phys. Rev. A **71**, 032505 (2005).

[65] C. Chin, V. V. Flambaum, and M. G. Kozlov, *Ultracold molecules: new probes on the variation of fundamental constants*, New J. Phys. **11**, 055048 (2009).

[66] J. J. Hudson, D. M. Kara, I. J. Smallman, B. E. Sauer, M. R. Tarbutt, and E. A. Hinds, *Improved measurement of the shape of the electron*, Nature **473**, 493 (2011).

[67] V. Andreev, D. G. Ang, D. DeMille, J. M. Doyle, G. Gabrielse, J. Haefner, N. R. Hutzler, Z. Lasner, C. Meisenhelder, B. R. O'Leary, C. D. Panda, A. D. West, E. P. West, X. Wu, and A. C. M. E. Collaboration, *Improved limit on the electric dipole moment of the electron*, Nature **562**, 355 (2018).

[68] T. S. Roussy, L. Caldwell, T. Wright, W. B. Cairncross, Y. Shagam, K. B. Ng, N. Schlossberger, S. Y. Park, A. Wang, J. Ye, and E. A. Cornell, *An improved bound on the electron's electric dipole moment*, Science **381**, 46 (2023).

[69] Y. Bao, S. S. Yu, L. Anderegg, E. Chae, W. Ketterle, K.-K. Ni, and J. M. Doyle, *Dipolar spin-exchange and entanglement between molecules in an optical tweezer array*, Science **382**, 1138 (2023).

[70] C. M. Holland, Y. Lu, and L. W. Cheuk, *On-demand entanglement of molecules in a reconfigurable optical tweezer array*, Science **382**, 1143 (2023).

[71] B. Yan, S. A. Moses, B. Gadway, J. P. Covey, K. R. A. Hazzard, A. M. Rey, D. S. Jin, and J. Ye, *Observation of dipolar spin-exchange interactions with lattice-confined polar molecules*, Nature **501**, 521 (2013).

[72] J.-R. Li, K. Matsuda, C. Miller, A. N. Carroll, W. G. Tobias, J. S. Higgins, and J. Ye, *Tunable itinerant spin dynamics with polar molecules*, Nature **614**, 70 (2023).

[73] L. Christakis, J. S. Rosenberg, R. Raj, S. Chi, A. Morningstar, D. A. Huse, Z. Z. Yan, and W. S. Bakr, *Probing site-resolved correlations in a spin system of ultracold molecules*, Nature **614**, 64 (2023).

[74] B. Sundar, B. Gadway, and K. R. A. Hazzard, *Synthetic dimensions in ultracold polar molecules*, Sci. Rep. **8**, 3422 (2018).

[75] D. Jaksch, J. I. Cirac, P. Zoller, S. L. Rolston, R. Côté, and M. D. Lukin, *Fast quantum gates for neutral atoms*, Phys. Rev. Lett. **85**, 2208 (2000).

[76] M. D. Lukin, M. Fleischhauer, R. Cote, L. M. Duan, D. Jaksch, J. I. Cirac, and P. Zoller, *Dipole blockade and quantum information processing in mesoscopic atomic ensembles*, Phys. Rev. Lett. **87**, 037901 (2001).

[77] L. Isenhower, E. Urban, X. L. Zhang, A. T. Gill, T. Henage, T. A. Johnson, T. G. Walker, and M. Saffman, *Demonstration of a neutral atom controlled-*NOT *quantum gate*, Phys. Rev. Lett. **104**, 010503 (2010).

[78] T. Wilk, A. Gaëtan, C. Evellin, J. Wolters, Y. Miroshnychenko, P. Grangier, and A. Browaeys, *Entanglement of two individual neutral atoms using Rydberg blockade*, Phys. Rev. Lett. **104**, 010502 (2010).

[79] H. Levine, A. Keesling, G. Semeghini, A. Omran, T. T. Wang, S. Ebadi, H. Bernien, M. Greiner, V. Vuletić, H. Pichler, and M. D. Lukin, *Parallel implementation of high-fidelity multiqubit gates with neutral atoms*, Phys. Rev. Lett. **123**, 170503 (2019).

[80] P. Shor, "Fault-tolerant quantum computation", in Proc. 37 Annu. Symp. Found. Comput. Sci. (1996), pp. 56–65.

[81] A. Steane, *Multiple-particle interference and quantum error correction*, Proc. R. Soc. A: Math. Phys. Eng. Sci. **452**, 2551 (1996).

[82] E. Dennis, A. Kitaev, A. Landahl, and J. Preskill, *Topological quantum memory*, J. Math. Phys. **43**, 4452 (2002).

[83] D. Bluvstein, S. J. Evered, A. A. Geim, S. H. Li, H. Zhou, T. Manovitz, S. Ebadi, M. Cain, M. Kalinowski, D. Hangleiter, J. P. Bonilla Ataides, N. Maskara, I. Cong, X. Gao, P. Sales Rodriguez, T. Karolyshyn, G. Semeghini, M. J. Gullans, M. Greiner, V. Vuletić, and M. D. Lukin, *Logical quantum processor based on reconfigurable atom arrays*, Nature **626**, 58 (2024).

[84] M. Wallquist, K. Hammerer, P. Rabl, M. Lukin, and P. Zoller, *Hybrid quantum devices and quantum engineering*, Phys. Scr. **2009**, 014001 (2009).

[85] T. Duty, *Towards superconductor-spin ensemble hybrid quantum systems*, Physics **80**, 3 (2010).

[86] Z.-L. Xiang, S. Ashhab, J. Q. You, and F. Nori, *Hybrid quantum circuits: superconducting circuits interacting with other quantum systems*, Rev. Mod. Phys. **85**, 623 (2013).

[87] M. Aspelmeyer, T. J. Kippenberg, and F. Marquardt, *Cavity optomechanics*, Rev. Mod. Phys. **86**, 1391 (2014).

[88] G. Kurizki, P. Bertet, Y. Kubo, K. Mølmer, D. Petrosyan, P. Rabl, and J. Schmiedmayer, *Quantum technologies with hybrid systems*, Proc. Natl. Acad. Sci. **112**, 3866 (2015).

[89] A. Cottet, M. C. Dartiailh, M. M. Desjardins, T. Cubaynes, L. C. Contamin, M. Delbecq, J. J. Viennot, L. E. Bruhat, B. Douçot, and T. Kontos, *Cavity qed with hybrid nanocircuits: from atomic-like physics to condensed matter phenomena*, J. Phys. Condens. Matter **29**, 433002 (2017).

[90] A. H. Safavi-Naeini, D. V. Thourhout, R. Baets, and R. V. Laer, *Controlling phonons and photons at the wavelength scale: integrated photonics meets integrated phononics*, Optica **6**, 213 (2019).

[91] D. Lachance-Quirion, Y. Tabuchi, A. Gloppe, K. Usami, and Y. Nakamura, *Hybrid quantum systems based on magnonics*, Appl. Phys. Express **12**, 070101 (2019).

[92] J.-P. Brantut and T. U. Donner, *Quantum simulation with atoms and photons*, SPG Mitt. **67**, 25 (2022).

[93] E. Guardado-Sanchez, B. M. Spar, P. Schauss, R. Belyansky, J. T. Young, P. Bienias, A. V. Gorshkov, T. Iadecola, and W. S. Bakr, *Quench dynamics of a Fermi gas with strong nonlocal interactions*, Phys. Rev. X **11**, 021036 (2021).

[94] A. Chotia, B. Neyenhuis, S. A. Moses, B. Yan, J. P. Covey, M. Foss-Feig, A. M. Rey, D. S. Jin, and J. Ye, *Long-lived dipolar molecules and Feshbach molecules in a 3D optical lattice*, Phys. Rev. Lett. **108**, 080405 (2012).

[95] J. W. Park, Z. Z. Yan, H. Loh, S. A. Will, and M. W. Zwierlein, *Second-scale nuclear spin coherence time of ultracold $^{23}Na^{40}K$ molecules*, Science **357**, 372 (2017).

[96] S. Burchesky, L. Anderegg, Y. Bao, S. S. Yu, E. Chae, W. Ketterle, K.-K. Ni, and J. M. Doyle, *Rotational coherence times of polar molecules in optical tweezers*, Phys. Rev. Lett. **127**, 123202 (2021).

[97] P. D. Gregory, J. A. Blackmore, S. L. Bromley, J. M. Hutson, and S. L. Cornish, *Robust storage qubits in ultracold polar molecules*, Nat. Phys. **17**, 1149 (2021).

[98] P. D. Gregory, L. M. Fernley, A. L. Tao, S. L. Bromley, J. Stepp, Z. Zhang, S. Kotochigova, K. R. A. Hazzard, and S. L. Cornish, *Second-scale rotational coherence and dipolar interactions in a gas of ultracold polar molecules*, Nat. Phys. **20**, 415 (2024).

[99] E. Kuznetsova, S. T. Rittenhouse, H. R. Sadeghpour, and S. F. Yelin, *Rydberg atom mediated polar molecule interactions: a tool for molecular-state conditional quantum gates and individual addressability*, Phys. Chem. Chem. Phys. **13**, 17115 (2011).

[100] E. Kuznetsova, S. T. Rittenhouse, H. R. Sadeghpour, and S. F. Yelin, *Rydberg-atom-mediated nondestructive readout of collective rotational states in polar-molecule arrays*, Phys. Rev. A **94**, 032325 (2016).

[101] K. Wang, C. P. Williams, L. R. B. Picard, N. Y. Yao, and K.-K. Ni, *Enriching the quantum toolbox of ultracold molecules with Rydberg atoms*, PRX Quantum **3**, 030339 (2022).

[102] C. Zhang and M. R. Tarbutt, *Quantum computation in a hybrid array of molecules and Rydberg atoms*, PRX Quantum **3**, 030340 (2022).

[103] T. M. Graham, M. Kwon, B. Grinkemeyer, Z. Marra, X. Jiang, M. T. Lichtman, Y. Sun, M. Ebert, and M. Saffman, *Rydberg-mediated entanglement in a two-dimensional neutral atom qubit array*, Phys. Rev. Lett. **123**, 230501 (2019).

[104] F. Jarisch and M. Zeppenfeld, *State resolved investigation of Förster resonant energy transfer in collisions between polar molecules and Rydberg atoms*, New J. Phys. **20**, 113044 (2018).

[105] K. Gawlas and S. D. Hogan, *Rydberg-state-resolved resonant energy transfer in cold electric-field-controlled intrabeam collisions of NH_3 with Rydberg He atoms*, J. Phys. Chem. Lett. **11**, 83 (2020).

[106] S. Patsch, M. Zeppenfeld, and C. P. Koch, *Rydberg atom-enabled spectroscopy of polar molecules via Förster resonance energy transfer*, J. Phys. Chem. Lett. **13**, 10728 (2022).

[107] B. Zhao, A. W. Glaetzle, G. Pupillo, and P. Zoller, *Atomic Rydberg reservoirs for polar molecules*, Phys. Rev. Lett. **108**, 193007 (2012).

[108] S. D. Huber and H. P. Büchler, *Dipole-interaction-mediated laser cooling of polar molecules to ultracold temperatures*, Phys. Rev. Lett. **108**, 193006 (2012).

[109] S. T. Rittenhouse and H. R. Sadeghpour, *Ultracold giant polyatomic Rydberg molecules: coherent control of molecular orientation*, Phys. Rev. Lett. **104**, 243002 (2010).

[110] S. T. Rittenhouse, M. Mayle, P. Schmelcher, and H. R. Sadeghpour, *Ultralong-range polyatomic Rydberg molecules formed by a polar perturber*, J. Phys. B **44**, 184005 (2011).

[111] R. González-Férez, H. R. Sadeghpour, and P. Schmelcher, *Rotational hybridization, and control of alignment and orientation in triatomic ultralong-range Rydberg molecules*, New J. Phys. **17**, 013021 (2015).

[112] R. González-Férez, S. T. Rittenhouse, P. Schmelcher, and H. R. Sadeghpour, *A protocol to realize triatomic ultralong range Rydberg molecules in an ultracold KRb gas*, J. Phys. B **53**, 074002 (2020).

[113] W. D. Phillips, *Nobel lecture: laser cooling and trapping of neutral atoms*, Rev. Mod. Phys. **70**, 721 (1998).

[114] M. R. Tarbutt, *Laser cooling of molecules*, Contemp. Phys. **59**, 356 (2018).

[115] E. S. Shuman, J. F. Barry, D. R. Glenn, and D. DeMille, *Radiative force from optical cycling on a diatomic molecule*, Phys. Rev. Lett. **103**, 223001 (2009).

[116] E. S. Shuman, J. F. Barry, and D. DeMille, *Laser cooling of a diatomic molecule*, Nature **467**, 820 (2010).

[117] J. F. Barry, E. S. Shuman, E. B. Norrgard, and D. DeMille, *Laser radiation pressure slowing of a molecular beam*, Phys. Rev. Lett. **108**, 103002 (2012).

[118] J. F. Barry, D. J. McCarron, E. B. Norrgard, M. H. Steinecker, and D. DeMille, *Magneto-optical trapping of a diatomic molecule*, Nature **512**, 286 (2014).

[119] D. J. McCarron, E. B. Norrgard, M. H. Steinecker, and D. DeMille, *Improved magneto–optical trapping of a diatomic molecule*, New J. Phys. **17**, 035014 (2015).

[120] E. B. Norrgard, D. J. McCarron, M. H. Steinecker, M. R. Tarbutt, and D. DeMille, *Submillikelvin dipolar molecules in a radio-frequency magneto-optical trap*, Phys. Rev. Lett. **116**, 063004 (2016).

[121] M. H. Steinecker, D. J. McCarron, Y. Zhu, and D. DeMille, *Improved radio-frequency magneto-optical trap of SrF molecules*, ChemPhysChem **17**, 3664 (2016).

[122] D. J. McCarron, M. H. Steinecker, Y. Zhu, and D. DeMille, *Magnetic trapping of an ultracold gas of polar molecules*, Phys. Rev. Lett. **121**, 013202 (2018).

[123] M. T. Hummon, M. Yeo, B. K. Stuhl, A. L. Collopy, Y. Xia, and J. Ye, *2D magneto-optical trapping of diatomic molecules*, Phys. Rev. Lett. **110**, 143001 (2013).

[124] M. Yeo, M. T. Hummon, A. L. Collopy, B. Yan, B. Hemmerling, E. Chae, J. M. Doyle, and J. Ye, *Rotational state microwave mixing for laser cooling of complex diatomic molecules*, Phys. Rev. Lett. **114**, 223003 (2015).

[125] V. Zhelyazkova, A. Cournol, T. E. Wall, A. Matsushima, J. J. Hudson, E. A. Hinds, M. R. Tarbutt, and B. E. Sauer, *Laser cooling and slowing of CaF molecules*, Phys. Rev. A **89**, 053416 (2014).

[126] B. Hemmerling, E. Chae, A. Ravi, L. Anderegg, G. K. Drayna, N. R. Hutzler, A. L. Collopy, J. Ye, W. Ketterle, and J. M. Doyle, *Laser slowing of CaF molecules to near the capture velocity of a molecular MOT*, J. Phys. B **49**, 174001 (2016).

[127] S. Truppe, H. J. Williams, N. J. Fitch, M. Hambach, T. E. Wall, E. A. Hinds, B. E. Sauer, and M. R. Tarbutt, *An intense, cold, velocity-controlled molecular beam by frequency-chirped laser slowing*, New J. Phys. **19**, 022001 (2017).

[128] L. Anderegg, B. L. Augenbraun, E. Chae, B. Hemmerling, N. R. Hutzler, A. Ravi, A. Collopy, J. Ye, W. Ketterle, and J. M. Doyle, *Radio frequency magneto-optical trapping of CaF with high density*, Phys. Rev. Lett. **119**, 103201 (2017).

[129] H. J. Williams, S. Truppe, M. Hambach, L. Caldwell, N. J. Fitch, E. A. Hinds, B. E. Sauer, and M. R. Tarbutt, *Characteristics of a magneto-optical trap of molecules*, New J. Phys. **19**, 113035 (2017).

[130] S. Truppe, H. J. Williams, M. Hambach, L. Caldwell, N. J. Fitch, E. A. Hinds, B. E. Sauer, and M. R. Tarbutt, *Molecules cooled below the Doppler limit*, Nat. Phys. **13**, 1173 (2017).

[131] H. J. Williams, L. Caldwell, N. J. Fitch, S. Truppe, J. Rodewald, E. A. Hinds, B. E. Sauer, and M. R. Tarbutt, *Magnetic trapping and coherent control of laser-cooled molecules*, Phys. Rev. Lett. **120**, 163201 (2018).

[132] L. W. Cheuk, L. Anderegg, B. L. Augenbraun, Y. Bao, S. Burchesky, W. Ketterle, and J. M. Doyle, *Λ-enhanced imaging of molecules in an optical trap*, Phys. Rev. Lett. **121**, 083201 (2018).

[133] L. Anderegg, B. L. Augenbraun, Y. Bao, S. Burchesky, L. W. Cheuk, W. Ketterle, and J. M. Doyle, *Laser cooling of optically trapped molecules*, Nat. Phys. **14**, 890 (2018).

[134] C. M. Holland, Y. Lu, and L. W. Cheuk, *Bichromatic imaging of single molecules in an optical tweezer array*, Phys. Rev. Lett. **131**, 053202 (2023).

[135] Y. Lu, S. J. Li, C. M. Holland, and L. W. Cheuk, *Raman sideband cooling of molecules in an optical tweezer array*, Nat. Phys. **20**, 389 (2024).

[136] Y. Bao, S. S. Yu, J. You, L. Anderegg, E. Chae, W. Ketterle, K.-K. Ni, and J. M. Doyle, *Raman sideband cooling of molecules in an optical tweezer array to the 3D motional ground state*, Phys. Rev. X **14**, 031002 (2024).

[137] J. Lim, J. R. Almond, M. A. Trigatzis, J. A. Devlin, N. J. Fitch, B. E. Sauer, M. R. Tarbutt, and E. A. Hinds, *Laser cooled YbF molecules for measuring the electron's electric dipole moment*, Phys. Rev. Lett. **120**, 123201 (2018).

[138] I. Kozyryev, L. Baum, K. Matsuda, B. L. Augenbraun, L. Anderegg, A. P. Sedlack, and J. M. Doyle, *Sisyphus laser cooling of a polyatomic molecule*, Phys. Rev. Lett. **118**, 173201 (2017).

[139] L. Baum, N. B. Vilas, C. Hallas, B. L. Augenbraun, S. Raval, D. Mitra, and J. M. Doyle, *1D magneto-optical trap of polyatomic molecules*, Phys. Rev. Lett. **124**, 133201 (2020).

[140] B. L. Augenbraun, Z. D. Lasner, A. Frenett, H. Sawaoka, C. Miller, T. C. Steimle, and J. M. Doyle, *Laser-cooled polyatomic molecules for improved electron electric dipole moment searches*, New J. Phys. **22**, 022003 (2020).

[141] D. Mitra, N. B. Vilas, C. Hallas, L. Anderegg, B. L. Augenbraun, L. Baum, C. Miller, S. Raval, and J. M. Doyle, *Direct laser cooling of a symmetric top molecule*, Science **369**, 1366 (2020).

[142] N. Fitch and M. Tarbutt, "Laser-cooled molecules", in *Advances In Atomic, Molecular, and Optical Physics*, Vol. 70 (Academic Press, London, 2021) Chap. 3, pp. 157–262.

[143] B. L. Augenbraun, L. Anderegg, C. Hallas, Z. D. Lasner, N. B. Vilas, and J. M. Doyle, "Direct laser cooling of polyatomic molecules", in *Advances in Atomic, Molecular, and Optical Physics*, Vol. 72 (Academic Press, London, 2023) Chap. 2, pp. 89–182.

[144] T. Köhler, K. Góral, and P. S. Julienne, *Production of cold molecules via magnetically tunable feshbach resonances*, Rev. Mod. Phys. **78**, 1311 (2006).

[145] C. Chin, R. Grimm, P. Julienne, and E. Tiesinga, *Feshbach resonances in ultracold gases*, Rev. Mod. Phys. **82**, 1225 (2010).

[146] K.-K. Ni, S. Ospelkaus, M. H. G. de Miranda, A. Pe'er, B. Neyenhuis, J. J. Zirbel, S. Kotochigova, P. S. Julienne, D. S. Jin, and J. Ye, *A high phase-space-density gas of polar molecules*, Science **322**, 231 (2008).

[147] M.-G. Hu, Y. Liu, D. D. Grimes, Y.-W. Lin, A. H. Gheorghe, R. Vexiau, N. Bouloufa-Maafa, O. Dulieu, T. Rosenband, and K.-K. Ni, *Direct observation of bimolecular reactions of ultracold KRb molecules*, Science **366**, 1111 (2019).

[148] T. Takekoshi, M. Debatin, R. Rameshan, F. Ferlaino, R. Grimm, H.-C. Nägerl, C. R. Le Sueur, J. M. Hutson, P. S. Julienne, S. Kotochigova, and E. Tiemann, *Towards the production of ultracold ground-state RbCs molecules: Feshbach resonances, weakly bound states, and the coupled-channel model*, Phys. Rev. A **85**, 032506 (2012).

[149] P. K. Molony, P. D. Gregory, Z. Ji, B. Lu, M. P. Köppinger, C. R. Le Sueur, C. L. Blackley, J. M. Hutson, and S. L. Cornish, *Creation of ultracold $^{87}Rb^{133}Cs$ molecules in the rovibrational ground state*, Phys. Rev. Lett. **113**, 255301 (2014).

[150] P. K. Molony, P. D. Gregory, A. Kumar, C. R. Le Sueur, J. M. Hutson, and S. L. Cornish, *Production of ultracold $^{87}Rb^{133}Cs$ in the absolute ground state : Complete characterisation of the STIRAP transfer*, ChemPhysChem **17**, 3811 (2016).

[151] J. W. Park, S. A. Will, and M. W. Zwierlein, *Ultracold dipolar gas of fermionic $^{23}Na^{40}K$ molecules in their absolute ground state*, Phys. Rev. Lett. **114**, 205302 (2015).

[152] F. Seeßelberg, N. Buchheim, Z.-K. Lu, T. Schneider, X.-Y. Luo, E. Tiemann, I. Bloch, and C. Gohle, *Modeling the adiabatic creation of ultracold polar* ^{23}Na^{40}K *molecules*, Phys. Rev. A **97**, 013405 (2018).

[153] H. Yang, D.-C. Zhang, L. Liu, Y.-X. Liu, J. Nan, B. Zhao, and J.-W. Pan, *Observation of magnetically tunable Feshbach resonances in ultracold $^{23}Na^{40}K+^{40}K$ collisions*, Science **363**, 261 (2019).

[154] K. K. Voges, P. Gersema, M. Meyer zum Alten Borgloh, T. A. Schulze, T. Hartmann, A. Zenesini, and S. Ospelkaus, *Ultracold gas of bosonic $^{23}Na^{39}K$ ground-state molecules*, Phys. Rev. Lett. **125**, 083401 (2020).

[155] M. Guo, B. Zhu, B. Lu, X. Ye, F. Wang, R. Vexiau, N. Bouloufa-Maafa, G. Quéméner, O. Dulieu, and D. Wang, *Creation of an ultracold gas of ground-state dipolar $^{23}Na^{87}Rb$ molecules*, Phys. Rev. Lett. **116**, 205303 (2016).

[156] T. M. Rvachov, H. Son, A. T. Sommer, S. Ebadi, J. J. Park, M. W. Zwierlein, W. Ketterle, and A. O. Jamison, *Long-lived ultracold molecules with electric and magnetic dipole moments*, Phys. Rev. Lett. **119**, 143001 (2017).

[157] W. B. Cairncross, J. T. Zhang, L. R. Picard, Y. Yu, K. Wang, and K.-K. Ni, *Assembly of a rovibrational ground state molecule in an optical tweezer*, Phys. Rev. Lett. **126**, 123402 (2021).

[158] I. Stevenson, A. Z. Lam, N. Bigagli, C. Warner, W. Yuan, S. Zhang, and S. Will, *Ultracold gas of dipolar nacs ground state molecules*, Phys. Rev. Lett. **130**, 113002 (2023).

[159] R. Wynar, R. S. Freeland, D. J. Han, C. Ryu, and D. J. Heinzen, *Molecules in a Bose-Einstein condensate*, Science **287**, 1016 (2000).

[160] C. McKenzie, J. Hecker Denschlag, H. Häffner, A. Browaeys, L. E. E. de Araujo, F. K. Fatemi, K. M. Jones, J. E. Simsarian, D. Cho, A. Simoni, E. Tiesinga, P. S. Julienne, K. Helmerson, P. D. Lett, S. L. Rolston, and W. D. Phillips, *Photoassociation of sodium in a Bose-Einstein condensate*, Phys. Rev. Lett. **88**, 120403 (2002).

[161] T. F. Gallagher, *Rydberg atoms* (Cambridge University Press, Cambridge, 1994).

[162] S. K. Dutta, J. R. Guest, D. Feldbaum, A. Walz-Flannigan, and G. Raithel, *Ponderomotive optical lattice for Rydberg atoms*, Phys. Rev. Lett. **85**, 5551 (2000).

[163] S. Kuhr, W. Alt, D. Schrader, I. Dotsenko, Y. Miroshnychenko, A. Rauschenbeutel, and D. Meschede, *Analysis of dephasing mechanisms in a standing-wave dipole trap*, Phys. Rev. A **72**, 023406 (2005).

[164] T. Monz, P. Schindler, J. T. Barreiro, M. Chwalla, D. Nigg, W. A. Coish, M. Harlander, W. Hänsel, M. Hennrich, and R. Blatt, *14-qubit entanglement: creation and coherence*, Phys. Rev. Lett. **106**, 130506 (2011).

[165] J. Preskill, *Sufficient condition on noise correlations for scalable quantum computing*, 2012, arXiv:1207.6131 [quant-ph].

[166] A. G. Fowler and J. M. Martinis, *Quantifying the effects of local many-qubit errors and nonlocal two-qubit errors on the surface code*, Phys. Rev. A **89**, 032316 (2014).

[167] C. E. Bradley, J. Randall, M. H. Abobeih, R. C. Berrevoets, M. J. Degen, M. A. Bakker, M. Markham, D. J. Twitchen, and T. H. Taminiau, *A ten-qubit solid-state spin register with quantum memory up to one minute*, Phys. Rev. X **9**, 031045 (2019).

[168] J. M. Boter, X. Xue, T. Krähenmann, T. F. Watson, V. N. Premakumar, D. R. Ward, D. E. Savage, M. G. Lagally, M. Friesen, S. N. Coppersmith, M. A. Eriksson, R. Joynt, and L. M. K. Vandersypen, *Spatial noise correlations in a Si/SiGe two-qubit device from Bell state coherences*, Phys. Rev. B **101**, 235133 (2020).

[169] C. D. Wilen, S. Abdullah, N. A. Kurinsky, C. Stanford, L. Cardani, G. D'Imperio, C. Tomei, L. Faoro, L. B. Ioffe, C. H. Liu, A. Opremcak, B. G. Christensen, J. L. DuBois, and R. McDermott, *Correlated charge noise and relaxation errors in superconducting qubits*, Nature **594**, 369 (2021).

[170] I. I. Beterov and M. Saffman, *Rydberg blockade, Förster resonances, and quantum state measurements with different atomic species*, Phys. Rev. A **92**, 042710 (2015).

[171] K. Singh, S. Anand, A. Pocklington, J. T. Kemp, and H. Bernien, *Dual-element, two-dimensional atom array with continuous-mode operation*, Phys. Rev. X **12**, 011040 (2022).

[172] K. Singh, C. E. Bradley, S. Anand, V. Ramesh, R. White, and H. Bernien, *Mid-circuit correction of correlated phase errors using an array of spectator qubits*, Science **380**, 1265 (2023).

[173] S. Anand, C. E. Bradley, R. White, V. Ramesh, K. Singh, and H. Bernien, *A dual-species Rydberg array*, 2024, arXiv:2401.10325 [quant-ph].

[174] A. D. Bounds, N. C. Jackson, R. K. Hanley, R. Faoro, E. M. Bridge, P. Huillery, and M. P. A. Jones, *Rydberg-dressed magneto-optical trap*, Phys. Rev. Lett. **120**, 183401 (2018).

[175] I. S. Madjarov, J. P. Covey, A. L. Shaw, J. Choi, A. Kale, A. Cooper, H. Pichler, V. Schkolnik, J. R. Williams, and M. Endres, *High-fidelity entanglement and detection of alkaline-earth Rydberg atoms*, Nat. Phys. **16**, 857 (2020).

[176] A. W. Young, W. J. Eckner, W. R. Milner, D. Kedar, M. A. Norcia, E. Oelker, N. Schine, J. Ye, and A. M. Kaufman, *Half-minute-scale atomic coherence and high relative stability in a tweezer clock*, Nature **588**, 408 (2020).

[177] N. C. Jackson, R. K. Hanley, M. Hill, F. Leroux, C. S. Adams, and M. P. A. Jones, *Number-resolved imaging of ^{88}Sr atoms in a long working distance optical tweezer*, SciPost Phys. **8**, 038 (2020).

[178] S. Saskin, J. T. Wilson, B. Grinkemeyer, and J. D. Thompson, *Narrow-line cooling and imaging of ytterbium atoms in an optical tweezer array*, Phys. Rev. Lett. **122**, 143002 (2019).

[179] J. T. Wilson, S. Saskin, Y. Meng, S. Ma, R. Dilip, A. P. Burgers, and J. D. Thompson, *Trapping alkaline earth Rydberg atoms optical tweezer arrays*, Phys. Rev. Lett. **128**, 033201 (2022).

[180] R. Grimm, M. Weidemüller, and Y. B. Ovchinnikov, "Optical dipole traps for neutral atoms", in *Advances In Atomic, Molecular, and Optical Physics*, Vol. 42 (Academic Press, London, 2000), pp. 95–170.

[181] N. Schlosser, G. Reymond, I. Protsenko, and P. Grangier, *Sub-poissonian loading of single atoms in a microscopic dipole trap*, Nature **411**, 1024 (2001).

[182] N. Schlosser, G. Reymond, and P. Grangier, *Collisional blockade in microscopic optical dipole traps*, Phys. Rev. Lett. **89**, 023005 (2002).

[183] D. Bluvstein, H. Levine, G. Semeghini, T. T. Wang, S. Ebadi, M. Kalinowski, A. Keesling, N. Maskara, H. Pichler, M. Greiner, V. Vuletić, and M. D. Lukin, *A quantum processor based on coherent transport of entangled atom arrays*, Nature **604**, 451 (2022).

[184] Y. Miroshnychenko, W. Alt, I. Dotsenko, L. Förster, M. Khudaverdyan, D. Meschede, D. Schrader, and A. Rauschenbeutel, *An atom-sorting machine*, Nature **442**, 151 (2006).

[185] W. Lee, H. Kim, and J. Ahn, *Three-dimensional rearrangement of single atoms using actively controlled optical microtraps*, Opt. Express **24**, 9816 (2016).

[186] D. Barredo, S. de Léséleuc, V. Lienhard, T. Lahaye, and A. Browaeys, *An atom-by-atom assembler of defect-free arbitrary two-dimensional atomic arrays*, Science **354**, 1021 (2016).

[187] M. Endres, H. Bernien, A. Keesling, H. Levine, E. R. Anschuetz, A. Krajenbrink, C. Senko, V. Vuletic, M. Greiner, and M. D. Lukin, *Atom-by-atom assembly of defect-free one-dimensional cold atom arrays*, Science **354**, 1024 (2016).

[188] H. C. Nägerl, D. Leibfried, H. Rohde, G. Thalhammer, J. Eschner, F. Schmidt-Kaler, and R. Blatt, *Laser addressing of individual ions in a linear ion trap*, Phys. Rev. A **60**, 145 (1999).

[189] D. D. Yavuz, P. B. Kulatunga, E. Urban, T. A. Johnson, N. Proite, T. Henage, T. G. Walker, and M. Saffman, *Fast ground state manipulation of neutral atoms in microscopic optical traps*, Phys. Rev. Lett. **96**, 063001 (2006).

[190] C. Zhang, S. L. Rolston, and S. Das Sarma, *Manipulation of single neutral atoms in optical lattices*, Phys. Rev. A **74**, 042316 (2006).

[191] C. Knoernschild, X. L. Zhang, L. Isenhower, A. T. Gill, F. P. Lu, M. Saffman, and J. Kim, *Independent individual addressing of multiple neutral atom qubits with a micromirror-based beam steering system*, Appl. Phys. Lett. **97**, 134101 (2010).

[192] H. Labuhn, S. Ravets, D. Barredo, L. Béguin, F. Nogrette, T. Lahaye, and A. Browaeys, *Single-atom addressing in microtraps for quantum-state engineering using Rydberg atoms*, Phys. Rev. A **90**, 023415 (2014).

[193] J. T. Merrill, S. C. Doret, G. Vittorini, J. P. Addison, and K. R. Brown, *Transformed composite sequences for improved qubit addressing*, Phys. Rev. A **90**, 040301 (2014).

[194] S. Crain, E. Mount, S. Baek, and J. Kim, *Individual addressing of trapped $^{171}Yb^{+}$ ion qubits using a microelectromechanical systems-based beam steering system*, Appl. Phys. Lett. **105**, 181115 (2014).

[195] T. Xia, M. Lichtman, K. Maller, A. W. Carr, M. J. Piotrowicz, L. Isenhower, and M. Saffman, *Randomized benchmarking of single-qubit gates in a 2D array of neutral-atom qubits*, Phys. Rev. Lett. **114**, 100503 (2015).

[196] C. Weitenberg, M. Endres, J. F. Sherson, M. Cheneau, P. Schauß, T. Fukuhara, I. Bloch, and S. Kuhr, *Single-spin addressing in an atomic Mott insulator*, Nature **471**, 319 (2011).

[197] H. Labuhn, D. Barredo, S. Ravets, S. de Léséleuc, T. Macrì, T. Lahaye, and A. Browaeys, *Tunable two-dimensional arrays of single Rydberg atoms for realizing quantum ising models*, Nature **534**, 667 (2016).

[198] H. Bernien, S. Schwartz, A. Keesling, H. Levine, A. Omran, H. Pichler, S. Choi, A. S. Zibrov, M. Endres, M. Greiner, V. Vuletić, and M. D. Lukin, *Probing many-body dynamics on a 51-atom quantum simulator*, Nature **551**, 579 (2017).

[199] S. J. Evered, D. Bluvstein, M. Kalinowski, S. Ebadi, T. Manovitz, H. Zhou, S. H. Li, A. A. Geim, T. T. Wang, N. Maskara, H. Levine, G. Semeghini, M. Greiner, V. Vuletić, and M. D. Lukin, *High-fidelity parallel entangling gates on a neutral-atom quantum computer*, Nature **622**, 268 (2023).

[200] H. J. Manetsch, G. Nomura, E. Bataille, K. H. Leung, X. Lv, and M. Endres, *A tweezer array with 6100 highly coherent atomic qubits*, 2024, arXiv:2403.12021 [quant-ph].

[201] D. K. Ruttley, A. Guttridge, S. Spence, R. C. Bird, C. R. Le Sueur, J. M. Hutson, and S. L. Cornish, *Formation of ultracold molecules by merging optical tweezers*, Phys. Rev. Lett. **130**, 223401 (2023).

[202] A. Guttridge, D. K. Ruttley, A. C. Baldock, R. González-Férez, H. R. Sadeghpour, C. S. Adams, and S. L. Cornish, *Observation of Rydberg blockade due to the charge-dipole interaction between an atom and a polar molecule*, Phys. Rev. Lett. **131**, 013401 (2023).

[203] D. K. Ruttley, A. Guttridge, T. R. Hepworth, and S. L. Cornish, *Enhanced quantum control of individual ultracold molecules using optical tweezer arrays*, PRX Quantum **5**, 020333 (2024).

[204] R. V. Brooks, A. Guttridge, M. D. Frye, D. K. Ruttley, S. Spence, J. M. Hutson, and S. L. Cornish, *Feshbach spectroscopy of Cs atom pairs in optical tweezers*, New J. Phys. **24**, 113051 (2022).

[205] S. Spence, R. V. Brooks, D. K. Ruttley, A. Guttridge, and S. L. Cornish, *Preparation of ^{87}Rb and ^{133}Cs in the motional ground state of a single optical tweezer*, New J. Phys. **24**, 103022 (2022).

[206] R. V. Brooks, "Control and collisions of ^{87}Rb and ^{133}Cs atoms in optical tweezers", PhD thesis (Durham University, 2022).

[207] S. J. Spence, "Assembling single RbCs molecules with optical tweezers", PhD thesis (Durham University, 2023).

[208] M. W. Gempel, T. Hartmann, T. A. Schulze, K. K. Voges, A. Zenesini, and S. Ospelkaus, *Versatile electric fields for the manipulation of ultracold nak molecules*, New J. Phys. **18**, 045017 (2016).

[209] R. S. Bloom, "Few-body collisions in a quantum gas mixture of ^{40}K and ^{87}Rb atoms", PhD thesis (University of Colorado, 2014).

[210] O. J. Wales, "Splitting and recombination of bright-solitary-matter waves", PhD thesis (Durham University, 2019).

[211] D. A. Steck, *Rubidium 87 D line data*, available online at http://steck.us/alkalidata, (revision 2.3.3, 2024).

[212] J. Mitroy, M. S. Safronova, and C. W. Clark, *Theory and applications of atomic and ionic polarizabilities*, J. Phys. B **43**, 202001 (2010).

[213] R. H. Leonard, A. J. Fallon, C. A. Sackett, and M. S. Safronova, *High-precision measurements of the ^{87}RbD-line tune-out wavelength*, Phys. Rev. A **92**, 052501 (2015).

[214] A. Ratkata, P. D. Gregory, A. D. Innes, A. J. Matthies, L. A. McArd, J. M. Mortlock, M. S. Safronova, S. L. Bromley, and S. L. Cornish, *Measurement of the tune-out wavelength for ^{133}Cs at 880 nm*, Phys. Rev. A **104**, 052813 (2021).

[215] P. J. Mohr and W. D. Phillips, *Dimensionless units in the SI*, Metrologia **52**, 40 (2014).

[216] I. Mills, *On the units radian and cycle for the quantity plane angle*, Metrologia **53**, 991 (2016).

[217] R. Vexiau, D. Borsalino, M. Lepers, A. Orbán, M. Aymar, O. Dulieu, and N. Bouloufa-Maafa, *Dynamic dipole polarizabilities of heteronuclear alkali dimers: optical response, trapping and control of ultracold molecules*, Int. Rev. Phys. Chem. **36**, 709 (2017).

[218] P. Barakhshan, A. Marrs, A. Bhosale, B. Arora, R. Eigenmann, and M. S. Safronova, *Portal for high-precision atomic data and computation*, available online at https://www.udel.edu/atom, (version 2.0, 2020).

[219] C. S. Adams and I. G. Hughes, *Optics f2f: From Fourier to Fresnel* (Oxford University Press, Oxford, 2018).

[220] T. A. Savard, K. M. O'Hara, and J. E. Thomas, *Laser-noise-induced heating in far-off resonance optical traps*, Phys. Rev. A **56**, R1095 (1997).

[221] A. M. Kaufman, B. J. Lester, and C. A. Regal, *Cooling a single atom in an optical tweezer to its quantum ground state*, Phys. Rev. X **2**, 041014 (2012).

[222] J. D. Thompson, T. G. Tiecke, A. S. Zibrov, V. Vuleti ć, and M. D. Lukin, *Coherence and Raman sideband cooling of a single atom in an optical tweezer*, Phys. Rev. Lett. **110**, 133001 (2013).

[223] B. Albrecht, Y. Meng, C. Clausen, A. Dareau, P. Schneeweiss, and A. Rauschenbeutel, *Fictitious magnetic-field gradients in optical microtraps as an experimental tool for interrogating and manipulating cold atoms*, Phys. Rev. A **94**, 061401 (2016).

[224] B. Richards, E. Wolf, and D. Gabor, *Electromagnetic diffraction in optical systems, II. Structure of the image field in an aplanatic system*, Proc. R. Soc. Lond. A **253**, 358 (1959).

[225] S. Bergamini, B. Darquié, M. Jones, L. Jacubowiez, A. Browaeys, and P. Grangier, *Holographic generation of microtrap arrays for single atoms by use of a programmable phase modulator*, J. Opt. Soc. Am. B **21**, 1889 (2004).

[226] H. Kim, W. Lee, H.-g. Lee, H. Jo, Y. Song, and J. Ahn, *In situ single-atom array synthesis using dynamic holographic optical tweezers*, Nat. Commun. **7**, 13317 (2016).

[227] D. Barredo, V. Lienhard, S. de Léséleuc, T. Lahaye, and A. Browaeys, *Synthetic three-dimensional atomic structures assembled atom by atom*, Nature **561**, 79 (2018).

[228] D. Kim, A. Keesling, A. Omran, H. Levine, H. Bernien, M. Greiner, M. D. Lukin, and D. R. Englund, *Large-scale uniform optical focus array generation with a phase spatial light modulator*, Opt. Lett. **44**, 3178 (2019).

[229] K.-N. Schymik, V. Lienhard, D. Barredo, P. Scholl, H. Williams, A. Browaeys, and T. Lahaye, *Enhanced atom-by-atom assembly of arbitrary tweezer arrays*, Phys. Rev. A **102**, 063107 (2020).

[230] S. Ebadi, T. T. Wang, H. Levine, A. Keesling, G. Semeghini, A. Omran, D. Bluvstein, R. Samajdar, H. Pichler, W. W. Ho, S. Choi, S. Sachdev, M. Greiner, V. Vuletić, and M. D. Lukin, *Quantum phases of matter on a 256-atom programmable quantum simulator*, Nature **595**, 227 (2021).

[231] E. D. Black, *An introduction to Pound–Drever–Hall laser frequency stabilization*, Am. J. Phys. **69**, 79 (2001).

[232] L. Conti, M. D. Rosa, and F. Marin, *High-spectral-purity laser system for the auriga detector optical readout*, J. Opt. Soc. Am. B **20**, 462 (2003).

[233] H. Zhen, H. Ye, X. Liu, D. Zhu, H. Li, Y. Lu, and Q. Wang, *Widely tunable reflection-type fabry-perot interferometer based on relaxor ferroelectric poly(vinylidenefluoride-chlorotrifluoroethylene-trifluoroethylene)*, Opt. Express **16**, 9595 (2008).

[234] J. I. Thorpe, K. Numata, and J. Livas, *Laser frequency stabilization and control through offset sideband locking to optical cavities*, Opt. Express **16**, 15980 (2008).

[235] P. D. Gregory, P. K. Molony, M. P. Köppinger, A. Kumar, Z. Ji, B. Lu, A. L. Marchant, and S. L. Cornish, *A simple, versatile laser system for the creation of ultracold ground state molecules*, New J. Phys. **17**, 055006 (2015).

[236] M. P. Köppinger, "Creation of ultracold RbCs molecules", PhD thesis (Durham University, 2014).

[237] R. Legaie, "Coherent control of Rydberg atoms using sub-kHz linewidth excitation lasers", PhD thesis (University of Strathclyde, 2020).

[238] T. P. Wiles, "Dynamics of bright solitary matter-waves", PhD thesis (Durham University, 2013).

[239] J. M. Brown and A. Carrington, *Rotational spectroscopy of diatomic molecules*, Cambridge Molecular Science (Cambridge University Press, 2003).

[240] T. Takekoshi, L. Reichsöllner, A. Schindewolf, J. M. Hutson, C. R. Le Sueur, O. Dulieu, F. Ferlaino, R. Grimm, and H.-C. Nägerl, *Ultracold dense samples of dipolar RbCs molecules in the rovibrational and hyperfine ground state*, Phys. Rev. Lett. **113**, 205301 (2014).

[241] M. P. Köppinger, D. J. McCarron, D. L. Jenkin, P. K. Molony, H.-W. Cho, S. L. Cornish, C. R. Le Sueur, C. L. Blackley, and J. M. Hutson, *Production of optically trapped ^{87}RbCs Feshbach molecules*, Phys. Rev. A **89**, 033604 (2014).

[242] C. J. Joachain, *Quantum collision theory* (North-Holland, Netherlands, 1975).

[243] J. Dalibard, "Collisional dynamics of ultra-cold atomic gases", in *Bose-Einstein Condensation in Atomic Gases*, Vol. 140 (Società Italiana di Fisica, Varenna, 1998), pp. 321–349.

[244] D. Blume and C. H. Greene, *Fermi pseudopotential approximation: two particles under external confinement*, Phys. Rev. A **65**, 043613 (2002).

[245] E. L. Bolda, E. Tiesinga, and P. S. Julienne, *Effective-scattering-length model of ultracold atomic collisions and Feshbach resonances in tight harmonic traps*, Phys. Rev. A **66**, 013403 (2002).

[246] Z. Idziaszek and T. Calarco, *Analytical solutions for the dynamics of two trapped interacting ultracold atoms*, Phys. Rev. A **74**, 022712 (2006).

[247] A. J. Moerdijk, B. J. Verhaar, and A. Axelsson, *Resonances in ultracold collisions of ^{6}Li, ^{7}Li, and ^{23}Na*, Phys. Rev. A **51**, 4852 (1995).

[248] J. T. Zhang, Y. Yu, W. B. Cairncross, K. Wang, L. R. B. Picard, J. D. Hood, Y.-W. Lin, J. M. Hutson, and K.-K. Ni, *Forming a single molecule by magnetoassociation in an optical tweezer*, Phys. Rev. Lett. **124**, 253401 (2020).

[249] M. Olshanii, *Atomic scattering in the presence of an external confinement and a gas of impenetrable bosons*, Phys. Rev. Lett. **81**, 938 (1998).

[250] T. Bergeman, M. G. Moore, and M. Olshanii, *Atom-atom scattering under cylindrical harmonic confinement: numerical and analytic studies of the confinement induced resonance*, Phys. Rev. Lett. **91**, 163201 (2003).

[251] J. P. Kestner and L.-M. Duan, *Anharmonicity-induced resonances for ultracold atoms and their detection*, New J. Phys. **12**, 053016 (2010).

[252] S. Sala and A. Saenz, *Theory of inelastic confinement-induced resonances due to the coupling of center-of-mass and relative motion*, Phys. Rev. A **94**, 022713 (2016).

[253] H. Moritz, T. Stöferle, K. Günter, M. Köhl, and T. Esslinger, *Confinement induced molecules in a 1D Fermi gas*, Phys. Rev. Lett. **94**, 210401 (2005).

[254] E. Haller, M. Gustavsson, M. J. Mark, J. G. Danzl, R. Hart, G. Pupillo, and H.-C. Nägerl, *Realization of an excited, strongly correlated quantum gas phase*, Science **325**, 1224 (2009).

[255] G. Lamporesi, J. Catani, G. Barontini, Y. Nishida, M. Inguscio, and F. Minardi, *Scattering in mixed dimensions with ultracold gases*, Phys. Rev. Lett. **104**, 153202 (2010).

[256] G. Zürn, F. Serwane, T. Lompe, A. N. Wenz, M. G. Ries, J. E. Bohn, and S. Jochim, *Fermionization of two distinguishable fermions*, Phys. Rev. Lett. **108**, 075303 (2012).

[257] D. Capecchi, C. Cantillano, M. J. Mark, F. Meinert, A. Schindewolf, M. Landini, A. Saenz, F. Revuelta, and H.-C. Nägerl, *Observation of confinement-induced resonances in a 3D lattice*, Phys. Rev. Lett. **131**, 213002 (2023).

[258] S. Sala, G. Zürn, T. Lompe, A. N. Wenz, S. Murmann, F. Serwane, S. Jochim, and A. Saenz, *Coherent molecule formation in anharmonic potentials near confinement-induced resonances*, Phys. Rev. Lett. **110**, 203202 (2013).

[259] X. He, K. Wang, J. Zhuang, P. Xu, X. Gao, R. Guo, C. Sheng, M. Liu, J. Wang, J. Li, G. V. Shlyapnikov, and M. Zhan, *Coherently forming a single molecule in an optical trap*, Science **370**, 331 (2020).

[260] A. M. Kaufman, B. J. Lester, C. M. Reynolds, M. L. Wall, M. Foss-Feig, K. R. A. Hazzard, A. M. Rey, and C. A. Regal, *Two-particle quantum interference in tunnel-coupled optical tweezers*, Science **345**, 306 (2014).

[261] A. M. Kaufman, B. J. Lester, M. Foss-Feig, M. L. Wall, A. M. Rey, and C. A. Regal, *Entangling two transportable neutral atoms via local spin exchange*, Nature **527**, 208 (2015).

[262] R. Stock, I. H. Deutsch, and E. L. Bolda, *Quantum state control via trap-induced shape resonance in ultracold atomic collisions*, Phys. Rev. Lett. **91**, 183201 (2003).

[263] M. Krych and Z. Idziaszek, *Controlled collisions of two ultracold atoms in separate harmonic traps*, Phys. Rev. A **80**, 022710 (2009).

[264] J. P. Covey, S. A. Moses, M. Gärttner, A. Safavi-Naini, M. T. Miecnikowski, Z. Fu, J. Schachenmayer, P. S. Julienne, A. M. Rey, D. S. Jin, and J. Ye, *Doublon dynamics and polar molecule production in an optical lattice*, Nat. Commun. **7**, 11279 (2016).

[265] L. Reichsöllner, A. Schindewolf, T. Takekoshi, R. Grimm, and H.-C. Nägerl, *Quantum engineering of a low-entropy gas of heteronuclear bosonic molecules in an optical lattice*, Phys. Rev. Lett. **118**, 073201 (2017).

[266] M. Debatin, T. Takekoshi, R. Rameshan, L. Reichsöllner, F. Ferlaino, R. Grimm, R. Vexiau, N. Bouloufa, O. Dulieu, and H.-C. Nägerl, *Molecular spectroscopy for ground-state transfer of ultracold RbCs molecules*, Phys. Chem. Chem. Phys. **13**, 18926 (2011).

[267] H. Jeffreys, *An invariant form for the prior probability in estimation problems*, Proc. R. Soc. Lond. A **186**, 453 (1946).

[268] L. D. Brown, T. T. Cai, and A. DasGupta, *Interval estimation for a binomial proportion*, Stat. Sci. **16**, 101 (2001).

[269] T. T. Cai, *One-sided confidence intervals in discrete distributions*, J. Stat. Plan. Inference **131**, 63 (2005).

[270] A. G. A. Schindewolf, "Quantum engineering of a low-entropy sample of RbCs molecules in an optical lattice", PhD thesis (University of Innsbruck, 2018).

[271] R. V. Brooks, S. Spence, A. Guttridge, A. Alampounti, A. Rakonjac, L. A. McArd, J. M. Hutson, and S. L. Cornish, *Preparation of one ^{87}Rb and one ^{133}Cs atom in a single optical tweezer*, New J. Phys. **23**, 065002 (2021).

[272] F. Diedrich, J. C. Bergquist, W. M. Itano, and D. J. Wineland, *Laser cooling to the zero-point energy of motion*, Phys. Rev. Lett. **62**, 403 (1989).

[273] L. R. Liu, J. D. Hood, Y. Yu, J. T. Zhang, N. R. Hutzler, T. Rosenband, and K.-K. Ni, *Building one molecule from a reservoir of two atoms*, Science **360**, 900 (2018).

[274] J. T. Zhang, "Assembling an array of polar molecules with full quantum-state control", PhD thesis (Harvard University, 2021).

[275] L. R. Liu, J. D. Hood, Y. Yu, J. T. Zhang, K. Wang, Y.-W. Lin, T. Rosenband, and K.-K. Ni, *Molecular assembly of ground-state cooled single atoms*, Phys. Rev. X **9**, 021039 (2019).

[276] Y. B. Band and Y. Avishai, "Approximation methods", in *Quantum Mechanics with Applications to Nanotechnology and Information Science* (Academic Press, London, 2013) Chap. 7, pp. 303–366.

[277] R. C. Bird, C. R. Le Sueur, and J. M. Hutson, *Making molecules by mergoassociation: Two atoms in adjacent nonspherical optical traps*, Phys. Rev. Res. **5**, 043086 (2023).

[278] A. Guttridge, M. D. Frye, B. C. Yang, J. M. Hutson, and S. L. Cornish, *Two-photon photoassociation spectroscopy of CsYb: Ground-state interaction potential and interspecies scattering lengths*, Phys. Rev. A **98**, 022707 (2018).

[279] C. Fellows, R. Gutterres, A. Campos, J. Vergès, and C. Amiot, *The RbCs $X^1\Sigma^+$ ground electronic state: new spectroscopic study*, J. Mol. Spectrosc. **197**, 19 (1999).

[280] P. D. Gregory, J. Aldegunde, J. M. Hutson, and S. L. Cornish, *Controlling the rotational and hyperfine state of ultracold $^{87}Rb^{133}Cs$ molecules*, Phys. Rev. A **94**, 041403 (2016).

[281] K. Bergmann, H. Theuer, and B. Shore, *Coherent population transfer among quantum states of atoms and molecules*, Rev. Mod. Phys. **70**, 1003 (1998).

[282] N. V. Vitanov, A. A. Rangelov, B. W. Shore, and K. Bergmann, *Stimulated Raman adiabatic passage in physics, chemistry, and beyond*, Rev. Mod. Phys. **89**, 015006 (2017).

[283] G. S. Vasilev, A. Kuhn, and N. V. Vitanov, *Optimum pulse shapes for stimulated Raman adiabatic passage*, Phys. Rev. A **80**, 013417 (2009).

[284] P. D. Gregory, J. A. Blackmore, J. Aldegunde, J. M. Hutson, and S. L. Cornish, *ac Stark effect in ultracold polar $^{87}Rb^{133}Cs$ molecules*, Phys. Rev. A **96**, 021402 (2017).

[285] J. A. Blackmore, "Coherence and collisions in ultracold ^{87}Rb^{133}Cs molecules", PhD thesis (Durham University, 2020).

[286] P. Scholl, A. L. Shaw, R. B.-S. Tsai, R. Finkelstein, J. Choi, and M. Endres, *Erasure conversion in a high-fidelity Rydberg quantum simulator*, Nature **622**, 273 (2023).

[287] C. He, X. Nie, V. Avalos, S. Botsi, S. Kumar, A. Yang, and K. Dieckmann, *Efficient creation of ultracold ground state $^6Li^{40}K$ polar molecules*, Phys. Rev. Lett. **132**, 243401 (2024).

[288] O. Dulieu, Private communication.

[289] J. A. Blackmore, P. D. Gregory, S. L. Bromley, and S. L. Cornish, *Coherent manipulation of the internal state of ultracold $^{87}Rb^{133}Cs$ molecules with multiple microwave fields*, Phys. Chem. Chem. Phys. **22**, 27529 (2020).

[290] J. A. Blackmore, P. D. Gregory, J. M. Hutson, and S. L. Cornish, *Diatomic-py: a Python module for calculating the rotational and hyperfine structure of $^1\Sigma$ molecules*, Comput. Phys. Commun. **282**, 108512 (2023).

[291] J. A. Blackmore, R. Sawant, P. D. Gregory, S. L. Bromley, J. Aldegunde, J. M. Hutson, and S. L. Cornish, *Controlling the ac Stark effect of RbCs with dc electric and magnetic fields*, Phys. Rev. A **102**, 053316 (2020).

[292] A. Micheli, G. Brennen, and P. Zoller, *A toolbox for lattice-spin models with polar molecules*, Nat. Phys. **2**, 341 (2006).

[293] J. P. Covey, L. D. Marco, Ó. L. Acevedo, A. M. Rey, and J. Ye, *An approach to spin-resolved molecular gas microscopy*, New J. Phys. **20**, 043031 (2018).

[294] S. Kotochigova and E. Tiesinga, *Ab initio relativistic calculation of the RbCs molecule*, J. Chem. Phys. **123**, 174304 (2005).

[295] M. Debatin, "Creation of ultracold RbCs ground-state molecules", PhD thesis (University of Innsbruck, 2013).

[296] Y. Liu, M.-G. Hu, M. A. Nichols, D. Yang, D. Xie, H. Guo, and K.-K. Ni, *Precision test of statistical dynamics with state-to-state ultracold chemistry*, Nature **593**, 379 (2021).

[297] R. Raussendorf and H. J. Briegel, *A one-way quantum computer*, Phys. Rev. Lett. **86**, 5188 (2001).

[298] H. J. Briegel, D. E. Browne, W. Dür, R. Raussendorf, and M. Van den Nest, *Measurement-based quantum computation*, Nat. Phys. **5**, 19 (2009).

[299] M. P. Fisher, V. Khemani, A. Nahum, and S. Vijay, *Random quantum circuits*, Annu. Rev. Condens. Matter Phys. **14**, 335 (2023).

[300] M. Kwon, M. F. Ebert, T. G. Walker, and M. Saffman, *Parallel low-loss measurement of multiple atomic qubits*, Phys. Rev. Lett. **119**, 180504 (2017).

[301] M. Martinez-Dorantes, W. Alt, J. Gallego, S. Ghosh, L. Ratschbacher, Y. Völzke, and D. Meschede, *Fast nondestructive parallel readout of neutral atom registers in optical potentials*, Phys. Rev. Lett. **119**, 180503 (2017).

[302] M. Martinez-Dorantes, W. Alt, J. Gallego, S. Ghosh, L. Ratschbacher, and D. Meschede, *State-dependent fluorescence of neutral atoms in optical potentials*, Phys. Rev. A **97**, 023410 (2018).

[303] N. Šibalić and C. S. Adams, *Rydberg physics*, 2399-2891 (IOP Publishing, Bristol, 2018).

[304] N. Šibalić, J. D. Pritchard, C. S. Adams, and K. J. Weatherill, *Arc: an open-source library for calculating properties of alkali Rydberg atoms*, Comput. Phys. Commun. **220**, 319 (2017).

[305] C.-J. Lorenzen and K. Niemax, *Quantum defects of the $n^2P_{1/2,3/2}$ levels in ^{39}K I and ^{85}Rb I*, Phys. Scr. **27**, 300 (1983).

[306] C.-J. Lorenzen and K. Niemax, *Precise quantum defects of ns, np and nd levels in Cs I*, Z. Phys. A **315**, 127 (1984).

[307] P. Goy, J. Liang, M. Gross, and S. Haroche, *Quantum defects and specific-isotopic-shift measurements in ns and np highly excited states of lithium: exchange effects between Rydberg and core electrons*, Phys. Rev. A **34**, 2889 (1986).

[308] K.-H. Weber and C. J. Sansonetti, *Accurate energies of ns, np, nd, nf, and ng levels of neutral cesium*, Phys. Rev. A **35**, 4650 (1987).

[309] W. Li, I. Mourachko, M. W. Noel, and T. F. Gallagher, *Millimeter-wave spectroscopy of cold Rb Rydberg atoms in a magneto-optical trap: quantum defects of the ns, np, and nd series*, Phys. Rev. A **67**, 052502 (2003).

[310] J. Han, Y. Jamil, D. V. L. Norum, P. J. Tanner, and T. F. Gallagher, *Rb nf quantum defects from millimeter-wave spectroscopy of cold ^{85}Rb Rydberg atoms*, Phys. Rev. A **74**, 054502 (2006).

[311] K. Afrousheh, P. Bohlouli-Zanjani, J. A. Petrus, and J. D. D. Martin, *Determination of the ^{85}Rb ng-series quantum defect by electric-field-induced resonant energy transfer between cold Rydberg atoms*, Phys. Rev. A **74**, 062712 (2006).

[312] B. Sanguinetti, H. O. Majeed, M. L. Jones, and B. T. H. Varcoe, *Precision measurements of quantum defects in the $nP_{3/2}$ Rydberg states of ^{85}Rb*, Journal of Physics B: Atomic, Molecular and Optical Physics **42**, 165004 (2009).

[313] M. Mack, F. Karlewski, H. Hattermann, S. Höckh, F. Jessen, D. Cano, and J. Fortágh, *Measurement of absolute transition frequencies of ^{87}Rb to nS and nD Rydberg states by means of electromagnetically induced transparency*, Phys. Rev. A **83**, 052515 (2011).

[314] J. Deiglmayr, H. Herburger, H. Saßmannshausen, P. Jansen, H. Schmutz, and F. Merkt, *Precision measurement of the ionization energy of Cs I*, Phys. Rev. A **93**, 013424 (2016).

[315] K. Moore, A. Duspayev, R. Cardman, and G. Raithel, *Measurement of the Rb g-series quantum defect using two-photon microwave spectroscopy*, Phys. Rev. A **102**, 062817 (2020).

[316] S. Weber, C. Tresp, H. Menke, A. Urvoy, O. Firstenberg, H. P. Büchler, and S. Hofferberth, *Calculation of Rydberg interaction potentials*, J. Phys. B **50**, 133001 (2017).

[317] E. Brion, L. H. Pedersen, and K. Mølmer, *Adiabatic elimination in a lambda system*, J. Phys. A **40**, 1033 (2007).

[318] S. de Léséleuc, "Quantum simulation of spin models with assembled arrays of Rydberg atoms", PhD thesis (Université Paris-Saclay, 2018).

[319] E. Gomez, S. Aubin, L. A. Orozco, and G. D. Sprouse, *Lifetime and hyperfine splitting measurements on the 7s and 6p levels in rubidium*, J. Opt. Soc. Am. B **21**, 2058 (2004).

[320] C. Glaser, F. Karlewski, J. Kluge, J. Grimmel, M. Kaiser, A. Günther, H. Hattermann, M. Krutzik, and J. Fortágh, *Absolute frequency measurement of rubidium $5S-6P$ transitions*, Phys. Rev. A **102**, 012804 (2020).

[321] A. Tauschinsky, R. Newell, H. B. van Linden van den Heuvell, and R. J. C. Spreeuw, *Measurement of ^{87}Rb Rydberg-state hyperfine splitting in a room-temperature vapor cell*, Phys. Rev. A **87**, 042522 (2013).

[322] F. Pokorny, "A microwave dressed Rydberg ion", PhD thesis (Stockholm University, 2020), p. 123.

[323] K. C. Younge, S. E. Anderson, and G. Raithel, *Rydberg-atom trajectories in a ponderomotive optical lattice*, New J. Phys. **12**, 113036 (2010).

[324] A. Osterwalder and F. Merkt, *Using high Rydberg states as electric field sensors*, Phys. Rev. Lett. **82**, 1831 (1999).

[325] J. A. Sedlacek, A. Schwettmann, H. Kübler, R. Löw, T. Pfau, and J. P. Shaffer, *Microwave electrometry with Rydberg atoms in a vapour cell using bright atomic resonances*, Nat. Phys. **8**, 819 (2012).

[326] H. Fan, S. Kumar, J. Sedlacek, H. Kübler, S. Karimkashi, and J. P. Shaffer, *Atom based RF electric field sensing*, J. Phys. B **48**, 202001 (2015).

[327] J. P. Shaffer and H. Kübler, "A read-out enhancement for microwave electric field sensing with Rydberg atoms", in *Quantum Technologies*, Vol. 10674 (SPIE, Bellingham, 2018), p. 106740C.

[328] D. H. Meyer, Z. A. Castillo, K. C. Cox, and P. D. Kunz, *Assessment of Rydberg atoms for wideband electric field sensing*, J. Phys. B **53**, 034001 (2020).

[329] F. Ripka, H. Amarloo, J. Erskine, C. Liu, J. Ramirez-Serrano, J. Keaveney, G. Gillet, H. Kübler, and J. P. Shaffer, "Application-driven problems in Rydberg atom electrometry", in *Optical and Quantum Sensing and Precision Metrology*, Vol. 11700 (SPIE, Bellingham, 2021), 117002Y.

[330] A. Duspayev, R. Cardman, D. A. Anderson, and G. Raithel, *High-angular-momentum Rydberg states in a room-temperature vapor cell for dc electric-field sensing*, Phys. Rev. Res. **6**, 023138 (2024).

[331] L. Béguin, A. Vernier, R. Chicireanu, T. Lahaye, and A. Browaeys, *Direct measurement of the van der Waals interaction between two Rydberg atoms*, Phys. Rev. Lett. **110**, 263201 (2013).

[332] L. A. Jones, J. D. Carter, and J. D. D. Martin, *Rydberg atoms with a reduced sensitivity to dc and low-frequency electric fields*, Phys. Rev. A **87**, 023423 (2013).

[333] D. W. Booth, J. Isaacs, and M. Saffman, *Reducing the sensitivity of Rydberg atoms to dc electric fields using two-frequency ac field dressing*, Phys. Rev. A **97**, 012515 (2018).

[334] A. Khadjavi, A. Lurio, and W. Happer, *Stark effect in the excited states of Rb, Cs, Cd, and Hg*, Phys. Rev. **167**, 128 (1968).

[335] Z. Lai, S. Zhang, Q. Gou, and Y. Li, *Polarizabilities of Rydberg states of Rb atoms with n up to 140*, Phys. Rev. A **98**, 052503 (2018).

[336] J. Bai, S. Bai, X. Han, Y. Jiao, J. Zhao, and S. Jia, *Precise measurements of polarizabilities of cesium nS Rydberg states in an ultra-cold atomic ensemble*, New J. Phys. **22**, 093032 (2020).

[337] A. Gozzini, F. Mango, J. H. Xu, G. Alzetta, F. Maccarrone, and R. A. Bernheim, *Light-induced ejection of alkali atoms in polysiloxane coated cells*, Nuovo Cimento D **15**, 709 (1993).

[338] L. Torralbo-Campo, G. D. Bruce, G. Smirne, and D. Cassettari, *Light-induced atomic desorption in a compact system for ultracold atoms*, Sci. Rep. **5**, 14729 (2015).

[339] V. Lienhard, S. de Léséleuc, D. Barredo, T. Lahaye, A. Browaeys, M. Schuler, L.-P. Henry, and A. M. Läuchli, *Observing the space- and time-dependent growth of correlations in dynamically tuned synthetic Ising models with antiferromagnetic interactions*, Phys. Rev. X **8**, 021070 (2018).

[340] S. Ebadi, A. Keesling, M. Cain, T. T. Wang, H. Levine, D. Bluvstein, G. Semeghini, A. Omran, J.-G. Liu, R. Samajdar, X.-Z. Luo, B. Nash, X. Gao, B. Barak, E. Farhi, S. Sachdev, N. Gemelke, L. Zhou, S. Choi, H. Pichler, S.-T. Wang, M. Greiner, V. Vuletić, and M. D. Lukin, *Quantum optimization of maximum independent set using Rydberg atom arrays*, Science **376**, 1209 (2022).

[341] J. A. Blackmore, L. Caldwell, P. D. Gregory, E. M. Bridge, R. Sawant, J. Aldegunde, J. Mur-Petit, D. Jaksch, J. M. Hutson, B. E. Sauer, M. R. Tarbutt, and S. L. Cornish, *Ultracold molecules for quantum simulation: rotational coherences in CaF and RbCs*, Quantum Sci. Technol. **4**, 014010 (2018).

[342] J. P. Shaffer, S. T. Rittenhouse, and H. R. Sadeghpour, *Ultracold Rydberg molecules*, Nat. Commun. **9**, 1965 (2018).

[343] A. Omont, *On the theory of collisions of atoms in Rydberg states with neutral particles*, J. Phys. France **38**, 1343 (1977).

[344] E. Fermi and E. Teller, *The capture of negative mesotrons in matter*, Phys. Rev. **72**, 399 (1947).

[345] P. D. Gregory, J. A. Blackmore, F. M. D, L. M. Fernley, S. L. Bromley, J. M. Hutson, and S. L. Cornish, *Molecule–molecule and atom–molecule collisions with ultracold RbCs molecules*, New J. Phys. **23**, 125004 (2021).

[346] V. Olaya, J. Pérez-Ríos, and F. Herrera, *C_6 coefficients for interacting Rydberg atoms and alkali-metal dimers*, Phys. Rev. A **101**, 032705 (2020).

[347] H. Levine, A. Keesling, A. Omran, H. Bernien, S. Schwartz, A. S. Zibrov, M. Endres, M. Greiner, V. Vuleti ć, and M. D. Lukin, *High-fidelity control and entanglement of Rydberg-atom qubits*, Phys. Rev. Lett. **121**, 123603 (2018).

[348] L. Li, W. Huie, N. Chen, B. DeMarco, and J. P. Covey, *Active cancellation of servo-induced noise on stabilized lasers via feedforward*, Phys. Rev. Appl. **18**, 064005 (2022).

[349] Y.-X. Chao, Z.-X. Hua, X.-H. Liang, Z.-P. Yue, L. You, and M. K. Tey, *Pound-Drever-Hall feedforward: laser phase noise suppression beyond feedback*, Optica **11**, 945 (2024).

[350] S. de Léséleuc, D. Barredo, V. Lienhard, A. Browaeys, and T. Lahaye, *Analysis of imperfections in the coherent optical excitation of single atoms to Rydberg states*, Phys. Rev. A **97**, 053803 (2018).

[351] C. Dixneuf, G. Guiraud, Y.-V. Bardin, Q. Rosa, M. Goeppner, A. Hilico, C. Pierre, J. Boullet, N. Traynor, and G. Santarelli, *Ultra-low intensity noise, all fiber 365 W linearly polarized single frequency laser at 1064 nm*, Opt. Express **28**, 10960 (2020).

[352] F. Wellmann, M. Steinke, P. Wessels, N. Bode, F. Meylahn, B. Willke, L. Overmeyer, J. Neumann, and D. Kracht, *Performance study of a high-power single-frequency fiber amplifier architecture for gravitational wave detectors*, Appl. Opt. **59**, 7945 (2020).

[353] M. Zeppenfeld, *Nondestructive detection of polar molecules via Rydberg atoms*, EPL **118**, 13002 (2017).

[354] H. Song, D. Dai, G. Wu, C. C. Wang, S. A. Harich, M. Y. Hayes, X. Wang, D. Gerlich, X. Yang, and R. T. Skodje, *Chemical reaction dynamics of Rydberg atoms with neutral molecules: A comparison of molecular-beam and classical trajectory results for the H(n)+D2→HD+D(n') reaction*, J. Chem. Phys. **123**, 074314 (2005).

[355] E. Fermi, *Sopra lo spostamento per pressione delle righe elevate delle serie spettrali*, Nuovo Cimento **11**, 157 (1934).

[356] R. M. Clegg, "Förster resonance energy transfer—FRET what is it, why do it, and how it's done", in *FRET and FLIM techniques*, Vol. 33, Laboratory Techniques in Biochemistry and Molecular Biology (Elsevier, Amsterdam, 2009) Chap. 1, pp. 1–57.

[357] P. C. Nelson, *The role of quantum decoherence in FRET*, Biophys. J. **115**, 167 (2018).

[358] P. Ball, *Is photosynthesis quantum-ish?*, Phys. World **31(4)**, 44 (2018).

[359] E. Altman, K. R. Brown, G. Carleo, L. D. Carr, E. Demler, C. Chin, B. DeMarco, S. E. Economou, M. A. Eriksson, K.-M. C. Fu, M. Greiner, K. R. A. Hazzard, R. G. Hulet, A. J. Kollár, B. L. Lev, M. D. Lukin, R. Ma, X. Mi, S. Misra, C. Monroe, K. Murch, Z. Nazario, K.-K. Ni, A. C. Potter, P. Roushan, M. Saffman, M. Schleier-Smith, I. Siddiqi, R. Simmonds, M. Singh, I. Spielman, K. Temme, D. S. Weiss, J. Vučković, V. Vuletić, J. Ye, and M. Zwierlein, *Quantum simulators: architectures and opportunities*, PRX Quantum **2**, 017003 (2021).

[360] E. Tiesinga, P. J. Mohr, D. B. Newell, and B. N. Taylor, *The 2022 CODATA recommended values of the fundamental physical constants*, available online at https://physics.nist.gov/cuu/Constants/index.html, (revision 9.0, 2024).